UNIVERSIDADE DE ÉVORA

STRONG GROUND MOTION SIMULATIONS AND ASSESSMENT OF INFLUENCE OF MODEL PARAMETERS ON WAVEFORMS

Ekaterina Zadonina

Thesis submitted to University of Évora for the degree of Masters in Earth, Atmosphere and Space Sciences

Supervisor: Prof. Dr. Bento Caldeira

2010

UNIVERSIDADE DE ÉVORA

Masters in Earth, Atmosphere and Space Sciences

STRONG GROUND MOTION SIMULATIONS AND ASSESSMENT OF INFLUENCE OF MODEL PARAMETERS ON WAVEFORMS

Masters thesis

Ekaterina Zadonina

19 1 𝒹65

Supervisor: Prof. Dr. Bento Caldeira

2010

Table of contents

SIMULAÇÕES DE MOVIMENTOS FORTES E AVALIAÇÃO DA INFLUÊNCIA DOS PARÂMETROS DO MODELO POR COMPARAÇÃO DAS FORMAS DE ONDA

Resumo

A modelação de movimentos sísmicos intensos em campo próximo é um importante instrumento da sismologia moderna, usado nos estudos de sismologia e risco sísmico. Existem várias abordagens para calcular os movimentos do solo produzido por fontes sísmicas finitas. Neste trabalho utilizámos um algoritmo de diferenças finitas, desenvolvido para estruturas 3D e modelos cinemáticos de fonte, para calcular os movimentos da Terra em campo próximo produzidos por um evento real. Os sismogramas sintéticos e as correspondentes formas de onda registadas são quantitativamente comparados para justificar o modelo usado. Foram também ensaiado o efeito das variações de alguns parâmetros que caracterizam a fonte e a estrutura (velocidade de ruptura, dimensão e geometria, modelo de velocidade), sobre as formas de onda. Os resultados obtidos mostraram, em geral, boa concordância entre os dados observados e sintéticos e revelam a diferente capacidade que os parâmetros envolvidos têm para influenciar as formas de onda obtidas.

Summary

Modeling near-field ground motion is an important and helpful tool of modern seismology. It helps in studies of seismic events and mitigation of seismic hazards. Several approaches are widely used to obtain synthetic ground motion for a finite earthquake source. In our work we use a finite-difference algorithm, developed for 3D structures and kinematic source models, to compute near-field ground motions from a real moderate event with pre-existing slip distribution model. Lately, synthetic seismograms are quantitatively compared with observed waveforms from near-field seismic stations on order to justify created model. Moreover, we independently changed several source parameters (rupture velocity, source dimension and geometry), and structure (velocity model) to evaluate their influence on the waveforms. Here we also applied quantitative comparison of seismograms. Obtained results showed generally good agreement in magnitudes of motion between observed and synthetic data, and revealed effect of different model parameters on the waveforms.

Acknowledgments

Introduction

Ground motion modeling is an important and useful instrument of modern seismology that may provide valuable information about seismic events and Earth structure that helps to mitigate seismic risks.

However, synthesizing seismograms requires appropriate scientific method and defining many parameters of the source and media, which differently affect the final result. It is believed that variations in these parameters may lead to significantly different seismograms. To study this problem we synthesized waveforms from a moderate earthquake for which observed strong ground motions, a source rupture model and structure models existed. We studied various ground motion modeling techniques and decided to use finite-difference method based algorithm to calculate strong ground motion in all three directions for particular sites near epicenter of the event. Based on obtained results, we then numerically estimated the influence of some of the used parameters by their reasonable modifications in order to understand how it would affect obtained waveforms.

For waveform synthesis we used 2D/3D elastic finite-difference wave propagation code E3D (Larsen & Schultz, 1995) based on the elastodynamic formulation of the wave equation on a staggered grid. This code gave us the opportunity to perform all needed manipulations using computer cluster of University of Évora. For quantitative comparison of signals we used misfit criteria proposed by Kristeková et.al (2006).

This thesis is presented in three chapters. The first chapter is presented by brief review of history of seismology, the state of the art of existing methods for ground motion modeling and some methods for quantitative waveform comparison.

The second chapter contains information about data that were used in this work and describes applied methodology.

The third chapter presents obtained results and their analysis.

Chapter I. Historical review and state of the art

Since ancient time people were trying to understand and explain the nature of one of the most devastating disaster – earthquakes. The works of authors of classical antiquity who theorized about the natural causes of earthquakes already in the fifth century B.C. are lost but known based on accounts by Aristotle or Seneca. Aristotle himself was one of the first to attempt an explanation of earthquakes based on natural phenomena. He postulated that winds within the earth whipped up the occasional shaking of the earth's surface. During the Middle Ages and the early modern times no new concepts about earthquake mechanisms and causes had been developed. For the long time, empirical observations of the effects of earthquakes were rare. In 1750, England was uncharacteristically rocked by a series of five strong earthquakes. These earthquakes were followed on Sunday, November 1, 1755, by a catastrophic shock and tsunami that killed an estimated 70,000 people, leveling the city of Lisbon, Portugal. This event marks the beginning of the modern era of seismology, prompting numerous studies into the effects, locations, and timing of earthquakes. For the hundreds of years past since this event, study of earthquakes inexorably increases and its methods advanced. In the 1850s, 60s, and 70s, were made cornerstone efforts in seismology. Robert Mallet, an engineer, measured the velocity of seismic waves in the earth using explosions of gunpowder. His idea was to look for variations in seismic velocity that would indicate variations in the properties of the earth. English scientist, Robert Mallet was also one of the first to estimate the depth of an earthquake underground. In Italy, Luigi Palmieri invented an electromagnetic seismograph that was the first seismic instruments capable of routinely detecting earthquakes imperceptible to human beings. Many fundamental advances in seismology would be made in the late 1800s and early 1900s. Three English scientists, John Milne, James Ewing, and Thomas Gray, working at the Imperial College of Tokyo, invented the first seismic instruments sensitive enough to be used in the scientific study of earthquakes. In the United States, Grove Karl Gilbert, after studying the fault scarp from the 1872 Owens Valley, California earthquake, concluded that the faults were a primary feature of earthquakes, not a secondary one. Before that people thought that earthquakes were the result of underground explosions and that faults were only a result of the explosion, not a primary feature of earthquakes.

Harry Fielding Reid after examining the fault trace of the 1906 San Francisco earthquake deduced that earthquakes were the result of the gradual buildup of stresses within the earth occurring over many years. This stress is due to distant forces and is eventually released violently during an earthquake, allowing the earth to rapidly rebound after years of accumulated strain.

In 1886 Japanese geologist Seikei Sekiya became the first person to be appointed as a professor in seismology; he was also one of the first people to quantitatively analyze seismic recordings from earthquakes.

All great scientific achievements and developments in seismology were made in order to understand nature of this phenomenon and prevent its devastating effects. During the years, many scientists work on methods to predict earthquakes. However, nowadays earthquake prediction mostly operates with percentage possibilities of earthquake occurrence for the following several decades. The best working technique to avoid catastrophic consequences of earthquakes is to be well prepared for them. To do that it is necessary to study and model potential seismic sources in populated areas and their effect in the region. Though earthquakes can make significant damage in the areas far from the epicenter, harm in the immediate vicinity of the source is always much more severe, which makes mitigation of seismic hazards in this regions a subject of great importance. This is the main concern of strong ground motion seismology.

I-1. Strong ground motion modeling

Strong motion seismology was established by earthquake engineers. Two pioneers in this area are Kyoji Suyehiro (1877–1932) and John R. Freeman (1855–1932). The first was a member of the Japanese Imperial Academy and Professor of Applied Mechanics at Tokyo Imperial University and after the Tokyo earthquake of 1923, when the Japanese government set up the Earthquake Research Institute at Tokyo University, was appointed its first director, created multi-pendulum recorder named by author "seismic vibration analyzer" and made a lot of remarkable conclusions based on observations that lately was formulated as "soil-structure interaction". The second was an American civil and hydraulic engineer, who first emphasized the need to develop and deploy accelerographs to measure strong earthquake ground motion and convinced the USC&GS to build a multi-pendulum Mechanical Vibration Analyzer. John R. Freeman, who was among the first to recognize the importance of monitoring ground motion at close distances from seismic sources. And, thought the first instrumental records of seismic motion date back to the 1890s, thanks to his personal efforts, the first strong ground motion records from the Long Beach, California earthquake were obtained in 1933 by the instruments specifically designed for recording strong motion and installed in 1931 (Trifunac, 2003; Trifunac, 2008).

From engineering point of view strong ground motion study is concerned with the understanding of the characteristics – peaks of ground acceleration and frequencies on which they occur, epicentral distance and site conditions – and effects of potentially damaging earthquake ground motions. Numerical calculations that involve these characteristics allow to conduct seismic hazards and to improve earthquake engineering design (Papageorgiou, 1997). Despite the similar objective of seismic hazards assessment, seismologist who works in strong motion seismology mainly concern with study of seismic source and rupture process and use different techniques and models rather than engineers.

Seismologists became involved in strong motion seismology after 1966 Parkfield earthquake that provided ground motion records in immediate vicinity of the earthquake fault (Oakeshott et al, 1966; McEvilly et al, 1967; Cloud & Perez, 1967; Housner & Trifunac, 1967; Tsai & Patton, 1973; Levy & Mal, 1976; Aki, 1982). Scientific seismological community felt the urgent to characterize destructive ground motions occurred in immediate vicinity from the source. Since then, numerous

theoretical works on simulating strong motion have been carried out, starting with the use of a simple kinematic model assuming source as a point (Müller, 1969; Tsai & Patton, 1972; Anderson, 1973; Trifunac, 1974; Abramovici & Gal-Ezer, 1978) or as a fault plane (Haskell, 1964; Savage, 1966; Aki, 1968; Ward & Valensise, 1989; Olsen et al, 1995; Graves, 1998). In the evolution of methods for calculating synthetic time histories of ground motion, kinematic source models was primarily proposed and are widely used our days due to their ease of application. Lately, after Kostrov derived the first three dimensional analytical solution for a shear stress relaxation on a plane in 1964 (Kostrov, 1964), dynamic models, which incorporate a physical relationship between important faulting parameters of stress drop, slip, rupture velocity, and rise time, are becoming more accessible (Ida, 1973; Beroza & Mikumo, 1996; Nielsen & Olsen, 2000; Oglesby & Day, 2002; Guatteri et al, 2003; Guatteri et al, 2004; Peyrat & Olsen, 2004).

The quantitative prediction of strong ground motion and the physics of earthquake source have been progressing rapidly with the deployment of modern strong-motion network and development of sophisticated computer algorithms for analysis and simulation of ground motion. Through studies of large amount of earthquakes, the simulation technique has been significantly advanced by a number of scientists (Madariaga, 1976; Olsen & Archuleta, 1996; Larsen et al, 1997; Pitarka et al, 2004; Grandin et al, 2007; Grandin et al, 2007). Among the main achievements may be named the capacity to include in calculations more realistic complex medium (Campillo & Bouchon, 1983), the free surface effect (Niazy, 1975; Kawasaki, 1975; Kawasaki et al, 1975; Anderson, 1976; Bouchon & Aki, 1977; Israel & Kovach, 1977; Hartzell, 1978; Archuleta & Frazier, 1978), the effect of a sedimentary layer (Heaton & Helmberger, 1977; Archuleta & Day, 1977; Wiggins et al, 1977; Bouchon, 1979; Bouchon, 1980; Bouchon & Aki, 1980), laterally heterogeneous basin structure (Jacob, 1970; Aki & Richards, 1980), and absorbing boundary condition (Lindman, 1975; Clayton & Engquist, 1977; Chang & McMechan, 1989; Festa & Nielsen, 2003; Yang et al, 2003).

Seismic wave simulation requires high-performance algorithms for numerical solution of the second-order elastodynamic equation for the displacements in the medium. During the years, various methods was proposed and applied for this purpose including the most widely implemented finite-difference method (Boore, 1972), finite element method (Lysmer & Drake, 1972; Hulbert & Hughes, 1990; Toshinawa & Ohmachi, 1992; Richter, 1994), spectral element method (Faccioli et al, 1996; Komatitsch & Vilotte, 1998) or combination of different methods (Kummer et al, 1987).

Finite-difference method (FDM) was one of the first to be applied and, with significant additions and improvements, is commonly used nowadays thanks to straight-forward implementation, relatively low computational requirements and high efficiency.

I-2. Finite-difference method

For many mathematical and physical problems it is required to approximate solutions to differential equations, i.e., to find a function (or some discrete approximation to this function) which satisfies a given relationship between various of its derivatives on some given region of space and/or time, along with some boundary conditions along the edges of this domain. In general this is a difficult problem and only rarely can an analytic formula be found for the solution. A FDM proceeds by replacing the derivatives in the differential equations by finite-difference approximations. This gives a large algebraic system of equations to be solved in place of the differential equation, something that is easily solved on a computer.

Generally, analytical methods fail when:

1. The partial differential equations are not linear and can't be linearized without seriously affecting the result.

2. The solution region is complex.

3. The boundary conditions are of mixed types.

4. The boundary conditions are time-dependent.

5. The medium is inhomogeneous or anisotropic.

To obtain solutions in these cases FDM is often used. It was developed by A. Thom in the 1920s under the title "the method of square" to solve nonlinear hydrodynamic equations. As it was mentioned before, the finite-difference techniques are based upon the approximations that permit replacing differential equations by finite-difference equations. These finite-difference approximations are algebraic in form, and the solutions are related to grid points. Thus, a finite-difference solution basically involves three steps:

1. Dividing the solution domain into grids of nodes.

2. Approximating the given differential equation by finite-difference equivalence that relates the solutions to grid points.

3. Solving the difference equations subject to the prescribed boundary conditions and/or initial conditions.

Seismologists began using FDM to solve wave propagation problems some 40 years ago. In 1968 was developed an algorithm that allows obtaining of theoretical seismograms for the horizontal and the vertical components of displacement for homogeneous media (Alterman & Kornfeld, 1968; Alterman & Karal, 1968). With the

rapid advance of computer technologies, 3D seismic simulation on a large scale becomes affordable. FDMs (Kelly et al, 1976; Virieux, 1984; Virieux, 1986; Dablain, 1986; Igel et al, 1995; Graves, 1996; Pitarka, 1999; Moczo et al, 2002; Kristek & Moczo, 2006) are widely used in 3D seismic modeling due to their simplicity for computer code.

As mentioned before, FDM is used to find numerical solution of the second-order elastodynamic equation for the displacements in the medium. In a 3D anisotropic medium, the wave equations that describe the elastic wave propagation are written as equation of momentum conservation

$$\rho \frac{\partial^2 u_i}{\partial t^2} = \frac{\partial \sigma_{ij}}{\partial x_j} + f_i \qquad (I\text{-}1)$$

and stress-strain relation

$$\sigma_{ij} = \frac{1}{2} c_{ijkl} \left(\frac{\partial u_k}{\partial u_l} + \frac{\partial u_l}{\partial u_k} \right) \qquad (I\text{-}2)$$

where subscripts i, j, k and l take the values of 1, 2, and 3; $\rho = \rho(x, y, z)$ is the density; u_i and f_i denote the displacement component and the source force component respectively in the i-th direction; and x_1, x_2 and x_3 are x, y and z directions, respectively. σ_{ij} are the second-order stress tensors, c_{ijkl} are the fourth-order tensors of elastic constants that satisfy the symmetrical conditions $c_{ijkl} = c_{jilk} = c_{ijlk} = c_{klij}$ and may be up to 21 independent elastic constants for a 3D anisotropic case. Especially for the isotropic and transversely isotropic case, the 21 independent elastic constants are reduced to two Lamé constants (λ and μ) and five constants ($c_{11}, c_{13}, c_{33}, c_{44}$ and c_{66}).

This equation can be formulated into a set of first-order differential equations by first differentiating equation (I-2) with respect to time and then substituting the velocitycomponentsv_x, v_y, v_z for the time-differentiated displacements $\partial_t(u_x, u_y, u_z)$. The resulting sets of equations are given by

$$\partial_t v_x = b\left(\partial_x \tau_{xx} + \partial_y \tau_{xy} + \partial_z \tau_{xz} + f_x \right)$$

$$\partial_t v_y = b\left(\partial_x \tau_{xy} + \partial_y \tau_{yy} + \partial_x \tau_{yz} + f_y \right) \qquad (I\text{-}3)$$

$$\partial_t v_z = b\left(\partial_x \tau_{xz} + \partial_y \tau_{yz} + \partial_z \tau_{zz} + f_z \right)$$

Here $b = \frac{1}{\rho}$ is the buoyancy and τ_{ij} are the stress components. Stress-strain relation transform into following set of equations:

$$\partial_t \tau_{xx} = (\lambda + 2\mu)\partial_x v_x + \lambda \left(\partial_y v_y + \partial_z v_z \right)$$

$$\partial_t \tau_{yy} = (\lambda + 2\mu)\partial_y v_y + \lambda (\partial_x v_x + \partial_z v_z)$$

$$\partial_t \tau_{zz} = (\lambda + 2\mu)\partial_x v_x + \lambda(\partial_y v_y + \partial_z v_z) \qquad \text{(I-4)}$$

$$\partial_t \tau_{xy} = \mu(\partial_y v_x + \partial_x v_y)$$

$$\partial_t \tau_{xz} = \mu(\partial_z v_x + \partial_x v_z)$$

$$\partial_t \tau_{yz} = \mu(\partial_z v_y + \partial_y v_z)$$

These systems of equations are easily solved nowadays using a staggered-grid finite-difference technique (Virieux, 1986; Lavander, 1988; Randall, 1989). Fig. I-1 shows the grid layout for staggered-grid formulation, a unit cell consists of the wavefield variables and media parameters that are defined at a specific node, as shown in the top portion of the figure. The model space is then made up of series of repeated unit cells that occupy a 3D volume of space. The indices (i, j, k) represent values of the spatial coordinates (x, y, z), respectively, and the grid spacing h is defined as the length between the centers of two adjacent grid cells. This model is in the basin of nowadays algorithms for ground motion simulations, such as E3D, for example.
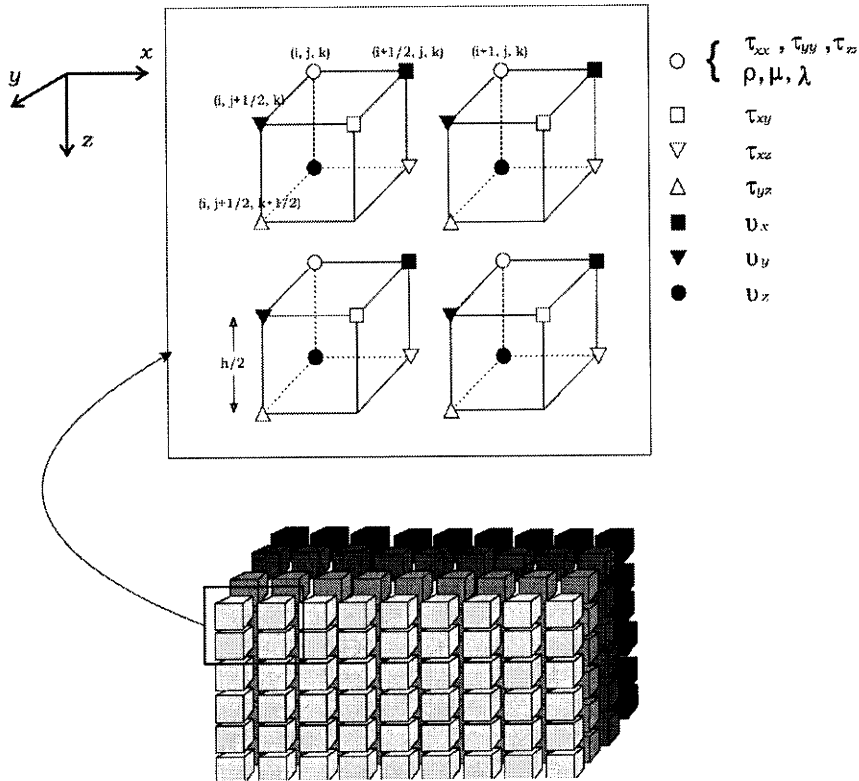
Fig. I-1. The grid layout for staggered-grid formulation

This scheme was widely used by seismologist for years, but, unfortunately, it suffered from "grid dispersion" near large gradient of the wave field, or when too-coarse computational grids are used. For realistic applications (Frankel, 1993; Olsen& Archuleta, 1996; Pitarka & Irikura, 1996a; Pitarka & Irikura, 1996b; Aoi & Fujiwara, 1999), balancing of the trade-off between numerical dispersion and computational cost turned out to be rather difficult. For classical second-order centered FDMs, at least 15 points must be used for the wavelength corresponding to the upper half-power

frequency (Kelly et al, 1976; Alford et al, 1974). Virieux (1984; 1986) proposed a velocity-stress staggered-grid scheme in which the first-order equations were used instead of the second-order equations. Levander (1988) extended the staggered-grid scheme to a fourth-order approximation. It allows reducing of grid dispersion and anisotropy. This can also be achieved by using fourth-order centered schemes both in space and time, based on modified wave-equation techniques (Dablain, 1986; Bayliss et al, 1986). Another difficulty with finite differences is their inability to implement free-surface conditions with the same accuracy as in the interior regions of the model and their lack of geometrical flexibility. However, some techniques can incorporate surface topography in finite-difference simulations by using methods based on grid deformation to match exactly the free surface relief (Tessmer et al, 1992; Hestholm & Ruud, 1994). It is effective for relatively smooth topography but has limitations for steep topography. Other methods employ a rectangular grid and generalize the free surface condition (Jih et al, 1988; Frankel & Leith, 1992; Robertsson, 1996; Ohminato & Chouet, 1997). Combined with the staggered grid formulation, they often remain limited to simple geometrical transformations and may affect the stability criterion in the case of grid-deformation techniques, or they require up to 15 grid points per shortest wavelength in the case of vacuum-to-solid techniques, which puts some limitations for narrow free-surface structures.

An efficient solution is to use method called a multigrid, variable-grid, or discontinuous-grid method. The discontinuous-grid approach allows to vary the discretization of the model and the wave field as required by the velocity structure. Compared to a standard uniform finite-difference grid approach, this method saves a considerable amount of memory and computations. Several seismological studies describing the discontinuous grid approach have been reported (Moczo, 1989; Jastram & Tessmer, 1994; Moczo, 1996; De Lilla, 1997). This approach enables to handle rough topography efficiently and was widely implemented by seismologist.

In this work the long-period motions (<1.4 Hz) from the moderate event were numerically calculated using the 3D FDM for broad-band stations, located in immediate vicinity from the fault. For our modeling, we used the finite-difference code, E3D (Larsen & Schultz, 1995), which is accurate to fourth-order in space and to second-order in time. It utilizes a regularly spaced, staggered grid for six stress and three velocity components. A free surface boundary condition and absorbing boundary conditions (Clayton & Engquist, 1977) were used.

I-3. Quantitative comparison of signals

The synthesis of seismograms for a particular event in order to assess influence of model parameters on results requires capacity to make fair quantitative comparison of the results with original data. Although the simple visual comparison of two signals could be useful in some cases, it is obvious that it cannot provide proper quantification and characterization of the difference between the seismograms. Sometimes the misfit of two seismograms is evaluated using following formula:

$$D(t) = s(t) - s_{ref}(t) \qquad (I-5)$$

Here $s(t)$ is the tested seismogram, $s_{ref}(t)$ is the reference seismogram, and t is time. $D(t)$ shows a time dependent difference between two seismograms. It is clear that it can provide very misleading information. The simplest example is a pure time shift of two identical signals. In this case $D(t)$ would be large without any reasonable explanation for the difference.

Sometimes it is necessary to investigate and show dependence of the misfit between two solutions on some important parameter(s) as, for example, epicentral distance, Poisson's ratio, grid spacing, time step, parameters of source and medium. In such cases it is reasonable to characterize the misfit by a proper single valued integral quantity. A simple integral criterion corresponding to the difference seismogram $D(t)$ may be defined as

$$MD = \frac{\sum_t |s(t) - s_{ref}(t)|}{\sum_t |s_{ref}(t)|} \qquad (I-6)$$

A more commonly used misfit criterion (Geller & Takeuchil, 1995) is the RMS (root mean square) misfit defined as

$$RMS = \sqrt{\frac{\sum_t |s(t) - s_{ref}(t)|}{\sum_t |s_{ref}(t)|^2}} \qquad (I-7)$$

However, these three criteria do not clarify the cause of misfit between two signals. They are unable to properly characterize it.

Considering some time signal as a reference, it is clear that some modifications of the signal can be more visible and understandable in the time domain, some others in the frequency domain. Some modifications in whole or part signal can change only/mainly amplitudes or envelope, some others can change only/mainly phase. At the same time, the most complete and informative characterization of a signal can be

obtained by its decomposition in the time-frequency plane, that is, by its time-frequency representation (TFR). The TFR enables us to see the time evolution of the spectral content. It seems quite natural to define misfit criteria based on the TFR, that is, time-frequency dependent criteria. From the time-frequency signal or misfit representation it is then easy to obtain time- or frequency-dependent quantities by projecting the TFR onto either of two domains. It is also possible to naturally define single-valued quantities based on the TFR.

In 2006 the misfit criteria based on the time-frequency representation of the seismograms obtained as the continuous wavelet transform with the analyzing Morlet wavelet was proposed (Kristeková et al, 2006). Equations presented in that work allow obtaining time-frequency envelope and phase misfits, time-dependent envelope and phase misfits, frequency-dependent envelope and phase misfits, and single-valued envelope and phase misfits.

The continuous wavelet transform (CWT) of signal $s(t)$ is defined by

$$CWT_{(a,b)}\{s(t)\} = \frac{1}{\sqrt{|a|}} \int_{-\infty}^{\infty} s(t)\Psi * \frac{(t-b)}{a} dt \qquad \text{(I-8)}$$

Here t is time, a is the scale parameter, b is the translational parameter, and Ψ is the analyzing wavelet. The scale parameter a is inversely proportional to frequency f. As analyzing wavelet any progressive in both the time domain and the frequency domain wavelet could be considered. Continuous waveletsare functions used by the continuous wavelet transform. These functions are defined asanalytical expressions, as functions either of time or of frequency. Most of the continuous wavelets are used for both wavelet decomposition and composition transforms.

For different applications various continuous wavelets was invented, such as Morlet wavelet and Mexican hat wavelet and their modifications, Shannon wavelet, Hermitian wavelet, Beta wavelet and some others. In this work was used complex Morlet wavelet (Fig. I-2). It is a complex wavelet which can be decomposed in two parts, one for the real part, and the other for the imaginary part.
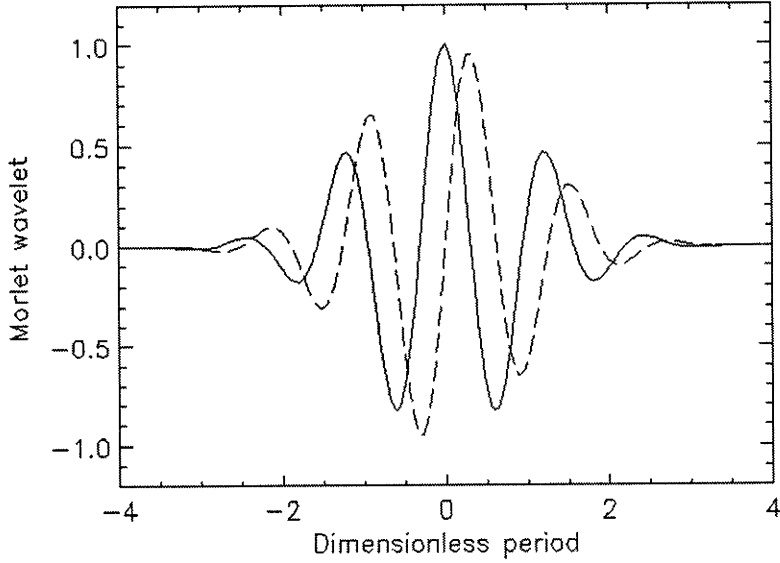
Fig. I-2. Complex Morlet wavelet: solid line presents real part, dashed line shows imaginary part

In view of that scale parameter a depends on frequency f as $f = {\omega_0}/{2\pi a}$, the TFR of signal $s(t)$ can be defined as

$$W(t,f) = CWT_{(a,b)}\{s(t)\}; \quad a = {\omega_0}/{2\pi f}, b = t \qquad (I\text{-}9)$$

Considering the TFR of both the original and referential signals as $W(t,f)$ and $W_{ref}(t,f)$ and N_T and N_F as the numbers of time and frequency samples in the time-frequency plane, respectively, a local time-frequency envelope difference defined as

$$\Delta E(t,f) = |W(t,f)| - |W_{ref}(t,f)| \qquad (I\text{-}10)$$

and a local time-frequency phase difference defined as

$$\Delta P(t,f) = |W_{ref}(t,f)| \frac{\{Arg[W(t,f)] - Arg[W_{ref}(t,f)]\}}{\pi} \qquad (I\text{-}11)$$

After that, envelope and phase misfits dependent on both time and frequency can be defined as following:

time-frequency envelope misfit (TFEM)

$$TFEM(t,f) = \frac{\Delta E(t,f)}{max_{t,f}(|W_{ref}(t,f)|)} \qquad (I\text{-}12)$$

time-frequency phase misfit (TFPM)

$$TFPM(t,f) = \frac{\Delta P(t,f)}{max_{t,f}(|W_{ref}(t,f)|)} \qquad (I\text{-}13)$$

$TFEM(t,f)$ characterizes the difference between the envelopes of the two signals as a function of time and frequency. Analogously, $TFPM(t,f)$ characterizes the difference between the phases of the two signals as a function of time and frequency. Both

18

differences are normalized with respect to the maximum absolute TFR value of the reference signal.

These misfit criteria were used in this work as criteria for quantitative comparison of synthetic waveforms for objectives that was defined before.

Chapter II. Data and methodology description

II-1. Description of the data

The main goal of this master student work was to gain theoretical knowledge and practical skills in seismic source modeling and waveform synthesis. In order to achieve this goal, after revision of theoretical basins of source modeling and waveform synthesis, it was decided to apply them for strong ground motion waveform synthesis of actual moderate event using its source geometry and slip distribution along with regional velocity structure as input parameters. Further, we planned to assess influence of different model parameters on simulated strong-motion waveforms.

As a moderate seismic event that could provide us with near-field strong-motion data we decide on using the Alum Rock earthquake that occurred near the junction of the Hayward and Calaveras faults in the San Francisco Bay, California, on October 31, 2007 at approximately 8:04 p.m. PDT (Fig. II-1).The Calaveras and Hayward faults are major components of the San Andreas Fault system in the San Francisco Bay region. This system forms the plate tectonic boundary between the North American Plate and the Pacific Plate. Geodetic monitoring of the Calaveras fault indicates about 6 mm/yr, but further south near Hollister the long-term offset rate of about 17 mm/year. Historic earthquakes on the Calaveras fault and instrumental seismicity suggest that this fault ruptures in moderate sized earthquakes ($M_w 5 - 6.5$) that occur on time scales of decades (rather than larger earthquakes that occur on time scales of hundreds of years). The fault is also known to be creeping aseismically along much of its length, which may contribute to the release of stress. The interaction between the Calaveras and Hayward faults produces region of complex deformation and is usually considered as a single system for developing rupture scenarios for seismic hazard assessments. Moreover, recent studies of seismicity, geological, and geophysical data in the region (Ponce et al, 2004; Williams et al, 2005) reviled that the Hayward fault at depths below 6 km connects in a simple way to the Calaveras fault as a structure following the Mission Seismic Trend. The San Francisco Bay area is one of the most well studied seismically active regions and it is densely covered with digital stations, including short period, strong motion and broadband sensors.
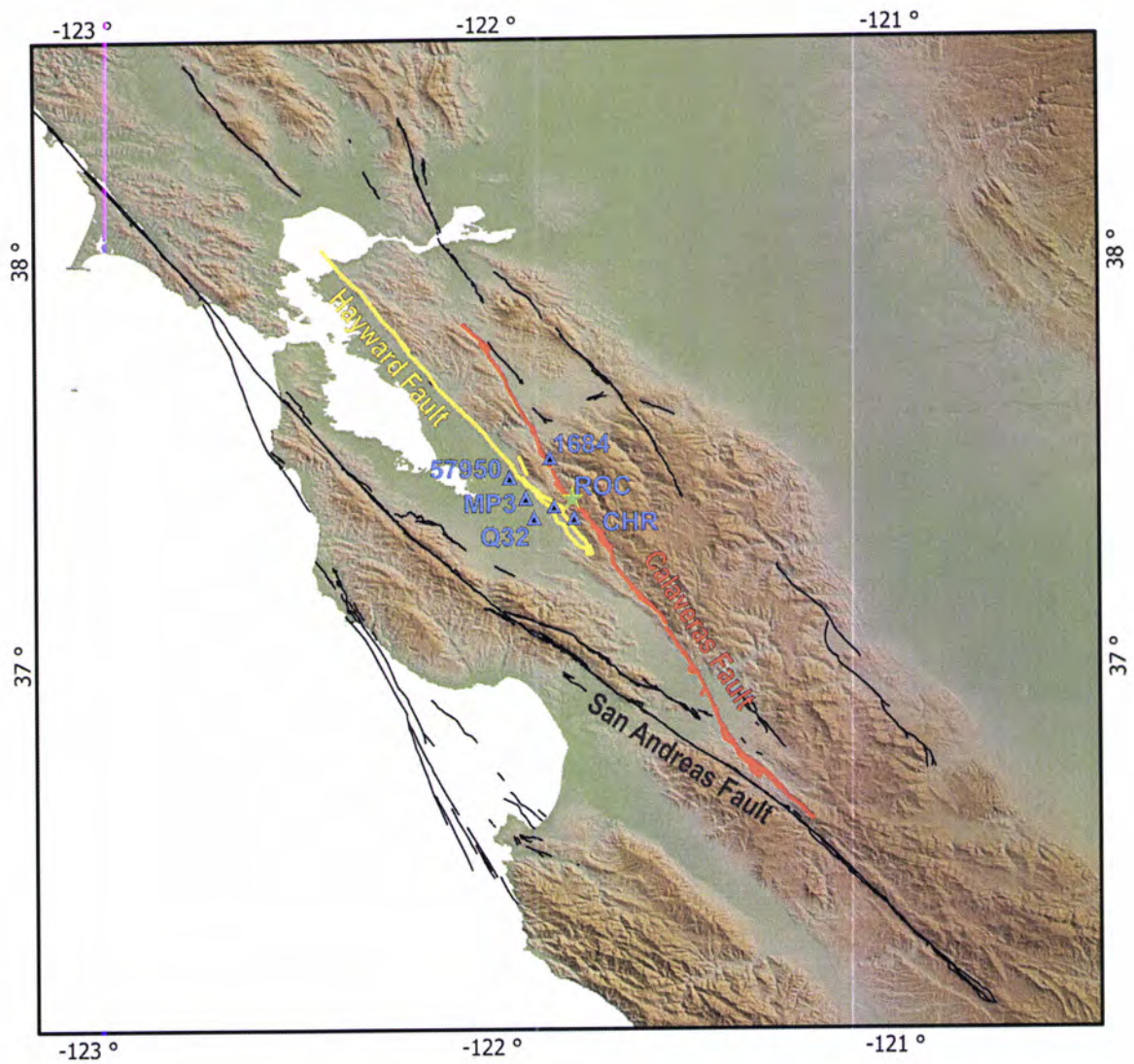
Fig. II-1. Area of interest – San Francisco Bay; Hayward Fault shown in yellow; Calaveras Fault shown in red; San Andreas Fault shown in black. Blue triangles represent locations of broad-band seismic stations that provided us with strong-motion waveforms. Green star marks epicenter of selected even.

The Alum Rock earthquake had $M_w = 5.4$ and its focal mechanism indicated right-lateral strike-slip. It was the largest event occurred in the region since the 1989 Loma Prieta earthquake ($M_w = 6.9$) and caused stress changes in the Calaveras Fault and the nearby Hayward Fault. Ground shaking was felt in the epicentral region, in San Francisco, Oakland and some other areas to the North with over 60,000 felt reports. Parts of the Bay Area felt the shaking for up to 15 seconds. Strike, dip and rake angles were estimated as 323°, 87°, and 180° respectively (Fig. II-2) and hypocenter of the event located at a depth of 9.2 km.

| Tangential | Radial | Vertical |

/FARB BK.DH.LP20SYN/data.286 Max Amp=8.49e-03 cm
VR=79.4

/CVS BK.LP20SYN/data.320 Max Amp=2.15e-02 cm
VR=93.0

/MCCM BK.DH.LP20SYN/data.309 Max Amp=1.69e-02 cm
VR=91.1

/CMB BK.DH.LP20SYN/data.61 Max Amp=1.71e-02 cm
VR=84.2

/PKD BK.DH.LP20SYN/data.146 Max Amp=1.99e-02 cm
VR=88.3

/KCC BK.DH.LP20SYN/data.92 Max Amp=5.82e-03 cm
VR=75.3

Strike=233 ; 323
Rake =-3 ; -180
Dip =90 ; 87
Mo =1.85e+24
Mw =5.4
Percent DC=98
Percent CLVD=2
Percent ISO=0
Variance=1.03e-06
Var. Red=8.77e+01
RES/Pdc.=1.05e-08

Fig. II-2. Moment tensor solution for the Alum Rock earthquake from the web-site of Berkeley Seismological Laboratory (http://seismo.berkeley.edu/~peggy/AlumRock.htm)

The strong motion seismograms for the earthquake were obtained on the web-site of Center for Engineering Strong Motion Data (http://www.strongmotioncenter.org/). We picked six broad-band strong ground motion stations that provided us with good azimuthal coverage and were located in the distance range from 5.4 to 14 km from the epicenter (Fig. II-1, Table II-1).

Code/ID of the station	Epicentral distance, km
ROC	5.4
CHR	6.6
MP3	10.3
1684	10.4
Q32	10.8
57950	14

Table II-1.Epicentral distance of the stations (http://www.strongmotioncenter.org/)

Four of these stations belong to USGC network, one - to CGS network, and one - to CHR network. For each station we were provided with three components of ground motions – North, East and Upward. Waveforms were presented in a form of standard tape format for CSMIP strong-motion data tapes Volume 2. A Volume 2 file contains

22

the instrument and base-line corrected data. For each of the channels, the file has three headers – alphanumeric text header, integer header, and real-value header, followed by the acceleration time series, the velocity time series, and the displacement time series.

Subsequently, a slip distribution model of selected event was required. Unfortunately, slip distribution wasn't available as dataset. It was obtained from the report of the Berkeley Seismological Laboratory (Hellweg et al, 2007) (Fig. II-3).

Finally, a velocity model was required for the region of interest. In our work we used the very detailed 1D velocity model (Aagaard et al, 2008). It follows the average depth variations in the structure and we adapted it for 3D media (Table II-2).
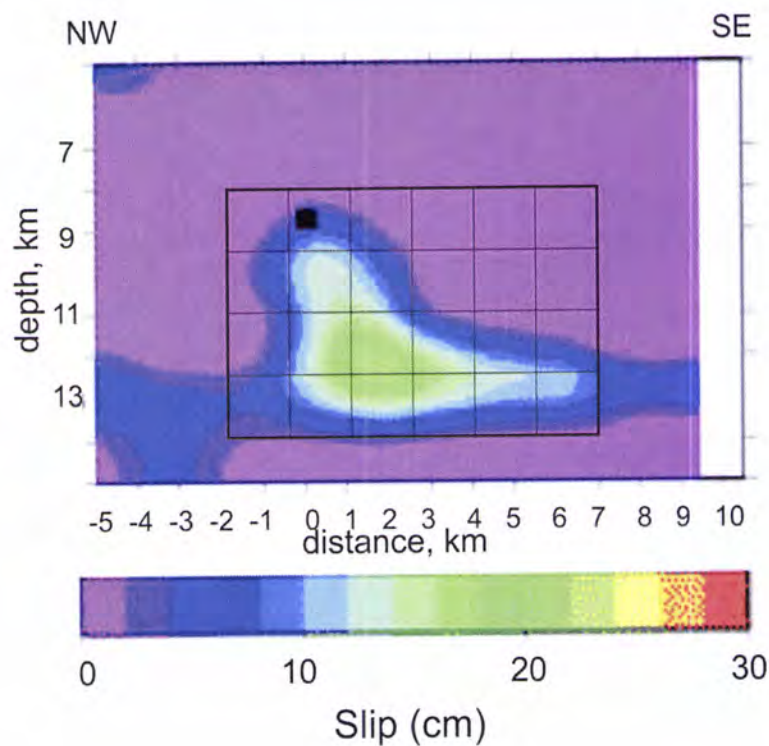
Fig. II-3. Slip distribution obtained by Hellweg et al. (2007). Black grid covers the asperity where the maximum slip occurred. It was selected for simulations as finite fault slip model.

The decision to use of 1D velocity model was justified by the choice of finite-difference code. E3D algorithm that we used in our work for waveform synthesis allows to input a velocity model into the grid by several ways. First way is to present velocity model as a sequence of blocks that could be specified by velocities of P- and S-waves in particular layer, its density, vertical gradient, P/S ration, Q value for P and/or S wave attenuation, central frequency of attenuation curve and starting and ending position of block in all three directions. Second way allows to present velocity model as "vfile"

23

which defines a grid-based velocity file with the same description of the model as in "block" type. And the last way is to define a 3D polygon velocity file through type "poly3d". It allows input a velocity model via 3D polygon solids. However, the documentation on using this option currently is not provided by algorithm developers. In our case, we preferred to use precise 1D velocity model extended to 3D medium and described by the line type "block" that is easy to set and modify in working process if necessary. We also combined first six layers of proposed velocity model in one layer because it was originally very detailed and minimum velocity of the model would be too small for calculations.

Width of the layer, m	V_p, km/s	V_s, km/s	ρ, g/cm^3
2	1,7	0,35	2
4	1,8	0,55	2,1
6	1,8	0,8	2,1
8	1,9	0,9	2,1
10	2	1	2,2
70	2,4	1,1	2,3
100	2,6	1,2	2,4
300	3	1,4	2,45
500	3,6	1,95	2,5
500	4,2	2,3	2,55
1000	4,8	2,8	2,6
500	5,25	3	2,62
2000	5,6	3,25	2,65
2000	5,9	3,41	2,7
2000	6,15	3,55	2,75
8000	6,35	3,62	2,85
8000	7	4,1	3

Table II-2. 1D Velocity model by Aagaard (2008). First six layers were combined in the same layer with width of 100 m, V_p equals 2.4 km/sec, V_s equals 1.1 km/sec and density equals 2.3 g/cm^3

II-2. Methodology

The main goal of this work was to simulate ground motion waveforms produced by the seismic source in the immediate vicinity from the epicenter, and then compare obtained synthetic seismograms with actual data from the field measurements during the earthquake in order to justify the model we originally set. Further, we planned to modify independently various parameters of the model and proceeded simulations with these modifications in order to recognize their effect on waveforms in terms of phase and envelope misfits. The data processing chart is presented on the Fig. II-4.
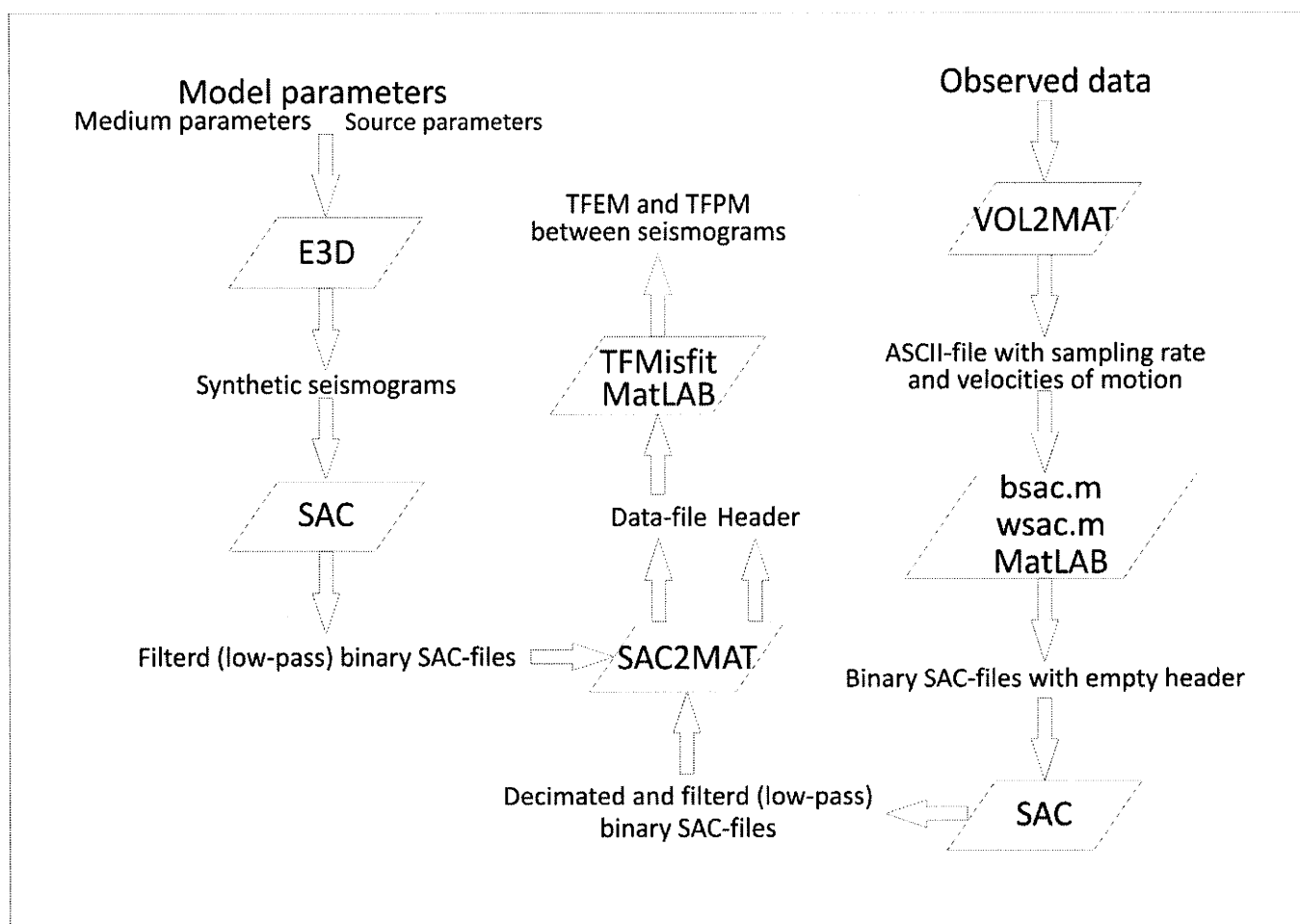
Fig. II-4. Data processing chart

A very important part of working process was to select approach, method and algorithm that would be used for simulations. From the varieties of available wave simulating algorithms, we stopped on finite-difference code that works with kinematic source model – E3D (Larsen & Schultz, 1995). E3D algorithm was developed by Shawn Larsen in 1992. It is an explicit 2D/3D elastic finite-difference wave propagation code used for the modeling of seismic waves. It is 4th-order accurate in space and 2nd-

25

order accurate in time and based on the elastodynamic formulation of the wave equation on a staggered grid (Madariaga, 1976; Virieux, 1986; Lavander, 1988). The grid is staggered in both space and time and regularly spaced. The computed variables at each node are the velocities and the components of the stress tensor. Input consists of a single parameter file containing information about run-time options, grid structure, time stepping parameters, source functions, velocity model, and output options. Various data also can be input from separate files. Output could be seismograms (SAC format), images (floating point), and run-time visualization. This code allow to implement such features as absorbing (non-reflecting) boundary conditions, sponge boundary conditions, stress-free surface conditions, multiple sources, attenuation, topography (2D), 1D static grid refinement, hybridization, parallelization (shared memory/message passing), run-time visualization, SAC output, image output and pure acoustic modeling option (for efficiency). This code is installed on the CGE cluster (ROMULO) and is widely implemented by the research team of Internal Geophysics/Seismology of CGE for waveform simulations.

We intended to simulate long-period waveforms for three components of six near-field seismic stations, because simulation of high frequencies requires much more precise description of the rupture process and structure model then the one we had and necessitates more complicated approach (stochastic approach). By comparing the computed motions with recorded motions, we were able to assess how well we can reproduce the recorded shaking relative to the uncertainty in the earthquake source. In order to quantitatively assess the effect of uncertainties in some model parameters on synthetic waveforms, we then made reasonable changes in these parameters. Hence, we used two different velocity models of the region (Aagaard et al, 2008; Waldhauser & Ellsworth, 2002), modified strike angle (15^0 in both directions with the same hypocenter location), dip angle (10^0 in both directions), rupture velocity (2.8, 3.1 km/sec) and length of the fault (13.5 km). Results of simulations through modified parameter of the model were later compared with results obtained via original model using quantitative misfit criteria (Kristeková et al, 2006). That would give us a chance to assess effect produced by parameters modification not only in amplitudes of motion, but also in phases.

a. Observed data processing

Observed strong ground motion, although they were preprocessed, required further processing. So as to complete data processing, we had to convert data from Volume 2 format to SAC format for further operations with seismograms.

SAC is an abbreviation for Seismic Analysis Code. It is a general purpose interactive program designed for the study of sequential signals, especially time-series data. It is a strong analysis tool used by research seismologists in the detailed study of seismic events. Analysis capabilities include general arithmetic operations, Fourier transforms, three spectral estimation techniques, IIR and FIR filtering, signal stacking, decimation, interpolation, correlation, and seismic phase picking. It is very useful and powerful tool for processing seismic data.

By means of creating a simple feature (vol2mat) in FORTRAN 77, we formed ASCII-file that contained sampling rate and magnitudes of the velocity for each chosen station. To complete transformation from Volume 2 to SAC format we applied MATLAB utilities called rsac.m and wsac.m created by Michael Thorne (http://web.utah.edu/thorne/) that allows add empty header to ASCII-file and write a binary file in SAC format.

After that obtained binary files were treated in SAC: time series, with instrument effect deconvolved, were decimated to the same sampling rate (DELTA) of 0.5 seconds and were cut from first wave arrival to twenty second. These parameters will be used later for ground motion simulations. Moreover, data were filtered with low-pass filter for frequencies up to 1.4 Hz for the reason that the maximum frequency of the seismic wave that can be correctly simulated using further proposed model is considered to be equal f_{cell} from the following condition:

$$f_{cell} < v_{min}/5h \qquad \text{(II-1)}$$

In this inequality f_{cell} is the minimum of all frequencies calculated for each unit cell, v_{min} and h are minimum wave speed and grid spacing respectively.

Afterwards, processed SAC-files were split by sac2mat.m utility (http://case.caltech.edu/useful/matlab/sac2mat.m) in 2 arrays of file header and data that later will be used for time-frequency comparisons of original observed signal with synthetic data.

b.   Waveforms synthesis

The first step of simulations was to develop a model that includes parameters related to the source and velocity model that will be later processed using E3D code. Besides that, E3D requires information about grid (dimensions and step of the grid (in km)), timing (total duration of seismogram, time step (in seconds) and number of points) and output files.

The grid parameters in E3D had to be set using "grid" line type that defines the grid dimensions, parameters, and some run time options. As was said before, the E3D code use finite-difference staggered grid for simulations. It means that the simulated state variables are spatially staggered from one another. Fig. II-5 illustrates their distribution in grid nods. The velocities presented as V_x, V_y, and V_z, and the stress tensor presented as components T_{nn} (corresponds to the normal stresses T_{xx}, T_{yy}, T_{zz}), T_{xy}, T_{xz}, T_{yz}. V_x is considered as the reference point for each virtual node and the other variables are staggered by 1/2 grid point from this reference point. To set the grid parameters we had to specify the variables of the "grid" line type. That parameters were x, y, z and dh that are dimensions of the grid in East, North and depth directions and grid spacing in kilometers respectively. Simulation of seismic waves in the immediate vicinity of the source didn't require large grid, so the explored volume was limited to a box 80 km long (East direction), 60 km wide (North direction) and 25 km deep. The E3D code implements nonreflecting boundary condition, which let us defined narrow boundaries for the media and significantly reduces computational and memory storage requirements.
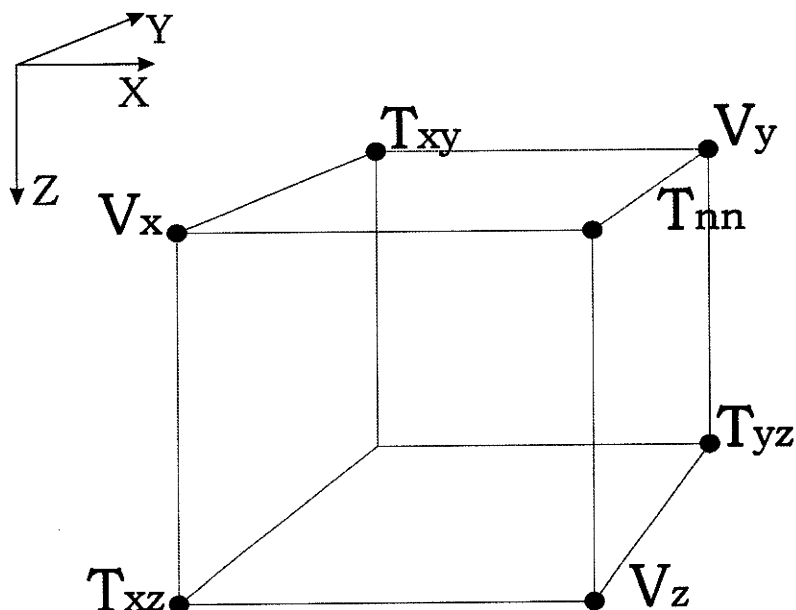
Fig. II-5. Left-handed coordinate system and state variables distribution in E3D code

28

To set the grid parameters we had to specify the variables of the "grid" line type. That parameters were x, y, z and dh that are dimensions of the grid in East, North and vertical downward directions and grid spacing in kilometers respectively. Simulation of seismic waves in the immediate vicinity of the source didn't require large grid, so the explored volume was limited to a box 80 km long (East direction), 60 km wide (North direction) and 25 km deep. The E3D code implements nonreflecting boundary condition, which let us defined narrow boundaries for the media and significantly reduces computational and memory storage requirements. Grid spacing, as well as time-step increment, was set to satisfy the Courant condition that required for stability of solution:

$$dt < factor * dh/V_{max} \qquad \text{(II-2)}$$

Here dt is a time-step of the output simulated seismogram, V_{max} is the maximum velocity in the model (P-wave velocity) and $factor$ is a constant that for 3D case equals 0.494. To satisfy this stability criterion, we put dh as 0.15 km.

The other important parameters that could be specified in E3D algorithm are physical model and mechanisms of propagating grid. In our studies, we used elastic model which is *a priori* physical model of the code. A propagating grid is an option useful for problems run on massively parallel processors, is unnecessary in our simulations and set as "active=0".

After the grid parameters were defined it was necessary to input the finite-difference timing parameters. "Time" line type required to set time-step increment dt and number of time-steps t. Time-step increment dt was set as 0.005 seconds. It is important to point out that according to calculated Courant condition using V_{max} of originally used velocity model (Aagaard et al, 2008) dt has to be less than 0.01058 seconds. But for alternative velocity model (Waldhauser & Ellsworth, 2002) which V_{max} is greater dt has to be less than 0.00928 seconds. Thus, in order to satisfy both of these requirement and use appropriate and convenient value for further manipulations with waveforms it was decided to set dt as 0.005 seconds. Value of time increment is in agreement (though it was not necessary) with time-step increment of the source-time function that was used for simulations. The number of time-steps was set as 4000 which resulted in 20 seconds of total time of simulated seismograms. We assumed based on the total rupture duration (estimated 2.9 seconds) that study of 15 seconds after first arrival of strong-motion synthetic seismograms and comparison of them with original

data from the strong-motion stations would be sufficient and would allow to make conclusions about fairness of the proposed model.

An appropriate velocity model is a factor of great importance in waveform simulations. In our work we used the 1D velocity model for short-period simulations (Aagaard et al, 2008) adapted for 3D media. Parameters of the velocity model were specified using line type "block". We set P- and S-waves velocities, density for each layer and its top and bottom depth according to the model. Hence, in our work we used layered velocity structure.

The ground motion from earthquakes is often predicted based on finite-fault modeling, in which the fault plane is discretized into small independently rupturing subfaults; the radiation from all subfaults is summed at the observation point. Description of seismic source in E3D can be performed using several source types including multiple sources. In our case we used this option to include multiple sources into the same run to present the source as a set of subfaults that have some joint borders and in total represent the entire finite fault.

Geometry of the source fault plane – strike, dip and rake –was considered as 323°, 90°, and 180° respectively according to moment tensor solution. Based on the slip distribution (Hellweg et al, 2007), the source was defined as a finite fault plane 9 km in length by 6 km in width (the area is restricted by the black grid on the Fig. II-3). This is the part of the fault that suffered from the significant amount of slip. The fault plane was divided on subfaults 1.5 km by 1.5 km in dimensions and each subfaultis presented as independent seismic source with its own coordinates and depth of center-top of its plane, geometry, location of the hypocenter, amplitude, velocity of rupture, source-time function file and start-time. Some of these parameters are equals for different subfaults (geometry, location of the hypocenter on the plane (always in the center of subfault), velocity of rupture and source-time function file). However, coordinates of center-top of subfaults, amplitude and start-time were calculated separately for each subfault.

Coordinates of the center-top of subfaults were calculated using geographic coordinates and depth of the earthquake hypocenter and the fault geometry. The hypocenter of the event was placed in the middle of the grid (40 km in the x direction and 30 km in the y direction) on the appropriate depth and other coordinates were calculated with respect to it. Upper edge of the higher row of subfaults located on the depth of 8 km, upper edge of the lower row of subfaults – on the depth of 14 km.

Coordinate in x direction, km	Coordinate in y direction, km	Depth of the top-center, km
39,10	31,20	8,0
40,00	30,00	8,0
40,90	28,80	8,0
41,80	27,60	8,0
42,70	26,40	8,0
43,60	25,20	8,0

Table II-2. Coordinates of center-top of the first row of subfaults

Table II-2 contains coordinates of center-top of the first row of subfaults. Since the dip angle of the fault equals 90^0 the coordinates of center-tops of other rows would be equal to corresponding coordinates of the upper row. For total of four rows, depth to the upper edges of subfaults was 8, 9.5, 11 and 12.5 km respectively. The initial point of rupture locates at the depth of 9.2 km.

The amplitude parameter of source relates to total scalar seismic moment that corresponds to specific subfault. It will be multiplied with the input source time-history. The source amplitude is defined by the "amp" attribute of the source line-type. It is required, although it can be equal 0.

Amplitude attribute had to be calculated for each subfault independently since the slip on the fault was considered nonuniform. To calculate it we used formula proposed in E3D code manual (Larsen & Schultz, 1995):

$$amp = M_0/N_p/\int STH \qquad \text{(II-3)}$$

M_0 is a desired seismic moment, $\int STH$ is an integral of source time history and N_p is a parameter that represents the number of points on the fault plane and has to be calculated due to the following formula:

$$N_p = \left(\frac{MAX(abs(x_2-x_1),abs(y_2-y_1))}{dh} + 1\right) * \left(W/dh + 1\right) \qquad \text{(II-4)}$$

In the formula (II-4) x_1, y_1, x_2, y_2 are the coordinates at the ends of the fault, W is a fault width and dh is grid spacing. It is needed to point that this formula is only fair in case of vertical fault that is not aligned with the grid. For a non-vertical fault, W in theabove equations has to be substituted with $Z_{top} - Z_{bot}$ for faults dipping greater than 45^0, or with the horizontal distance representing the projection of the fault width to the

31

surface for faults dipping less than 45^0. Z_{top} and Z_{bot} are the depths of upper and lower borders of the fault.

Another difficulty was to obtain magnitude of the slip in each particular cell of the grid. It was necessary in order to obtain seismic moment M_0 that is required to calculate the amplitude of source. The amount of slip in centimeters was calculated for each cell by using the color bar. We decided to apply the following formula:

$$S_i = \frac{\sum N_j * P_j}{100} \qquad \text{(II-5)}$$

Here S_i is a slip in centimeters for the subfault i, N_j is amount of slip marked by particular color j, and P_j is a percentage of this color in the subfault. Slip distribution in centimeters was calculated with this formula for each subfault. Maximum slip equals 17.9 cm (which is consistence with data presented in the report of the Berkeley Seismological Laboratory (Hellweg et al, 2007)).

Earthquakes are often thought to follow self-similar scaling in which the source dimensions are scale-invariant, that is, events of different sizes cannot be distinguished except by a scale factor (Scholz, 1990). Using the relation between seismic moment and the source dimensions

$$M_0 = \mu L W D \qquad \text{(II-6)}$$

where μ is the rigidity of cracking rocks, L and W are length and width of subfault respectively and D is a calculated slip we obtained seismic moments for each and every subfault, and after that calculated amplitude of source following formula (II-3).

Rupture does not occur on the surface of finite fault at the same time; it radiates from initial point in the hypocenter. To reach this effect in our simulations, it was necessary to set start time shift for each subfault. It was calculated individually. First, we calculated the total duration of the rupture following the empirical relation (Caldeira, 2007):

$$T_r = 10^{0.657 * M_w - 3.182}, \text{ for } M_w \leq 7 \qquad \text{(II-7)}$$

Here M_w is a moment magnitude and in our case equal to 5.4. Hence, T_r equals 2.9 sec. We also set the velocity of rupture as 3 km/sec based on the assumption that it is equal to 0.8 of S-wave velocity or 0.5 of P-wave velocity (Larsen & Schultz, 1995) and that seismic source located on the depth between 8 and 14 km (Fig. II-2, Table II-1).

Afterwards, we calculated the time that it takes for rupture to travel from initial point to the center of each particular sublault. That gave us start time shift for each all subfaults.

Then, assuming that, according to E3D manual, the rupture will propagate in a circular pattern outward from the hypocenter and defining the hypocenter, we calculated the time that it would take for the rupture to propagate from hypocenter to reach center of each subfault center.

Source time function (STF) is the earthquake source signal produced by faulting. The STF in earthquakes can be modeled by mathematic functions that typically are symmetric and evolves in time, first increasing and after decreasing. The time interval where the evolution increases is called "rise time". Real faults give rise to a very complicated source time functions. However, for calculations simple form signals are usually used. In our simulations, we used the same simple triangular source time function for each subfault (Fig. II-6). Total time of rupture for each subfault was estimate as 0.25 seconds, using dimensions of the subfault and rupture velocity. During the simulations, this signal presented by SAC-file got multiplied by calculated amplitude of signal.
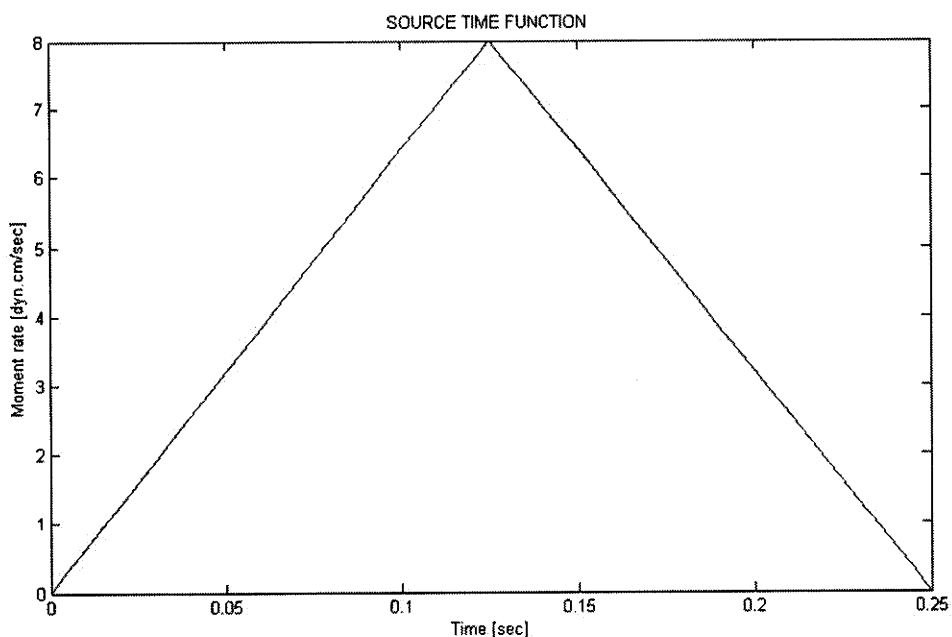
Fig. II-6. Triangular source-time function

The sites on the surface for which seismic signals were computed correspond to locations near-field seismic stations that provided us with actual observed seismograms. Their positions on the surface of the grid were calculated from their geographic

coordinates and ratio degree/km for their region of location. As an output we obtained one seismogram for each of three channels of all six stations in SAC format.

Afterwards, these results were filtered using low-pass filter (f<1.4 Hz) and then quantitatively compared with processed observed data through MATLAB algorithm that generated time-frequency envelope and phase misfits between signals and constructed visualizations of results of comparison.

c.   Influence of model parameters assessment

Usage of adequate model parameters is a matter of great importance in terms of ground motion synthesis and it is not easy to calibrate them and take all the factors into account in order to obtain reasonable results. Besides, while we were searching for information and model parameters to set we realized that different information sources for the same seismic event gave different values of some parameters. Hence, after obtaining the results of simulations based on original model we decided independently modify several of its parameters in reasonable limits ant check quantitatively how it would affect envelope and phase of waveform in time-frequency domain.

To assess our results we use the misfit criteria for quantitative comparison of seismograms (Kristeková et al, 2006) and based on the time-frequency representation of seismograms obtained as a continuous wavelet transform with a Morlet wavelet. In our work we apply the time-frequency envelope misfit and time-frequency phase misfit.

It was decided to test five parameters of the source model: strike angle, dip angle, length of the fault plane, and rupture velocity. We also decided to substitute original velocity model with other model of the region (Waldhauser & Ellsworth, 2002). It is 1D velocity model for P-waves used for routine location by the NCSN for events on the Hayward and Calaveras Fault (Table II-3). The S-wave velocities were obtained by scaling the corresponding velocities of P-waves by a factor $1/\sqrt{3}$. Densities were calculated for each layer using empirical relations between elastic wave speeds and density in the Earth's crust (Brocher, 2005):

$$\rho\left(\frac{g}{cm^3}\right) = 1.6612 * V_p - 0.4721 * V_p^2 + 0.0671 * V_p^3 - 0.0043 *$$

$$V_p^4 + 0.000106 * V_p^5 \text{(II-8)}$$

Here ρ is density and V_p is P-wave velocity in the particular layer.

Top of layer, km	V_p, km/s	V_s, km/s	ρ, g/cm^3
0	3,77	2,18	2,36
1	4,64	2,68	2,48
3	5,34	3,08	2,58
6	5,75	3,32	2,66
14	6,22	3,59	2,76
25	7,98	4,61	3,27

Table II-3. Velocity model that was used for simulations as alternative to originally set

(Waldhauser & Ellsworth, 2002)

Original strike angle of the fault in the model was rotated on 15^0 in both positive and negative directions. Rotation axis was set through the hypocenter point, so its position in the grid remained unchanged. Coordinates of subfaults top-centers were recalculated with respect to new strike angle.

Another source parameter that we decided to test was dip angle. We decided to rotate the fault plane from vertical position in both NE and SW directions by 10^0. We recalculated locations of all subfaults center-top points with respect to the new dip angles. In case of rotation in SW direction we also were forced to change the direction of strike angle by 180^0 without changing rake angle (that brought it to 0^0). Besides, since the fault plane in both cases was not vertical anymore, we ought to recalculate amplitude of sources. It was made following formula (II-3) with corresponding modification of W parameter for N_p in formula (II-4).

The original length of the finite fault plane was assumed as 9 km because it covered main slip asperity on the slip distribution (Fig. II-2). However, we were concern with possibility that extension of fault plane length could lead to significant changes of waveforms. So, we extended the original fault plane by 3 km in north-west direction and 1.5 km in south-east direction. It forced us to recalculate amplitudes for all subfault, though the total seismic moment was preserved.

The last source model parameter to test was rupture velocity. Values of rupture velocity, as well as values of P- and S-waves speeds, depends of the mechanics proprieties of the rocks that forms the fault, and then habitually relates. However, since our fault plane didn't belong to one particular velocity layer, it seemed reasonable to test minimum and maximum of possible rupture velocities. In our case this values equal 2.8 and 3.1 km/sec respectively. In order to incorporate these values into original model, we had to recalculate source time shift for each subfault and change duration of source-time function.

After we finished testing source model parameter, it was decided to use alternative velocity model of the region. It is difficult to overestimate the importance of fair velocity model for waveform simulations. The originally used velocity model was rather detailed and designed for short-period simulations. In contrary, it was agreed to use less precise structure model of the region to see if it would make significant difference in terms of results.

36

Simulated and observed waveforms are presented in appendix, while results of their comparison are presented in the following chapter.

Chapter III. Obtained results and their analysis

The following chapter consists of two principal parts. In the first part we analyze the results of application of FDM and algorithm for strong ground motion synthesis for the Alum Rock earthquake ($M_w = 5.4$) that occurred near the junction of the Hayward and Calaveras faults in the San Francisco Bay, California, on October 31, 2007. We used existing slip distribution for this event obtained through inversion in the Berkeley Seismological Laboratory that was available in the report (Hellweg et al, 2007) (Fig. II-3) and very detailed 1D velocity model of the San Francisco Bay region that was adapted for 3D media (Aagaard et al, 2008) (Table II-2) as input parameters of the model in simulations of waveforms for three channels of six broad-band stations located in the immediate vicinity from the epicenter of the event. Results of simulations were quantitatively compared with observed waveforms using misfit criteria (Kristeková et al, 2006).

The second part contains analysis of the results of study of importance of some parameters of the model involved in waveform synthesis. We present here the visualization and analysis of quantitative comparison of waveforms obtained using original model we set in the first part with waveforms obtained using models with separately and independently modified parameters of original model: – dip angle, strike angle, length of the fault plane, rupture velocity, and velocity model.

In both cases for comparison and visualization we used the developed MATLAB code based on the wavelet transform to quantify the time-frequency envelope and phase misfit (Kristeková et al, 2006). This code, as well as observed and synthetic waveforms and E3D input files of different models are applied in appendix.

III-1. Quantitative comparison of observed and synthetic waveforms

Results of strong ground motion simulation against observed data and misfit between them in envelope and phase in time-frequency domain are presented in the Appendix, in the section A5 (example presented on the Fig. III-1). Synthetic data were obtained using model which parameters were discussed previously (Chapter II) and are presented in Appendix as an input file for E3D algorithm (A2-a).

On the presented figures, a color scale indicates the misfit magnitude. On the pictures misfit presented in parts from one taking reference signal as etalon. We transformed it into percentage by simply multiplying the value by 100 for better understanding. Misfit between the waveforms is inhomogeneous and it is important to point out that for analysis we used only maximum value of misfit. For both envelope and phase misfit positive values indicated with warm colors on color scale. In terms of envelope misfit it signifies that envelope of compared signal exceeded envelop of reference signal. In terms of phase misfit, it indicates that compared signal arrived earlier than reference signal and is shifted in backward direction along the time line with respect to reference signal. Congruently, cold palette shows negative misfit and means that envelope of reference signal exceeded envelop of compared signal. Negative phase misfit indicates that compared signal arrived later than reference signal and is consequently shifted in progressive direction along the time line with respect to reference signal.

Time line is associated with the horizontal axis. Time unites are seconds. Vertical axis for envelop and phase time-frequencies misfit visualizations represents scale parameter a that is in invers dependence from frequency of the signal (Eq. I-9). Thus, the smallest value of scale parameter equals 20 indicates the highest presented frequency (1.4 Hz). Vertical axis for the visualization of two analyzed signals indicates velocity of the motion and presented in m/sec.
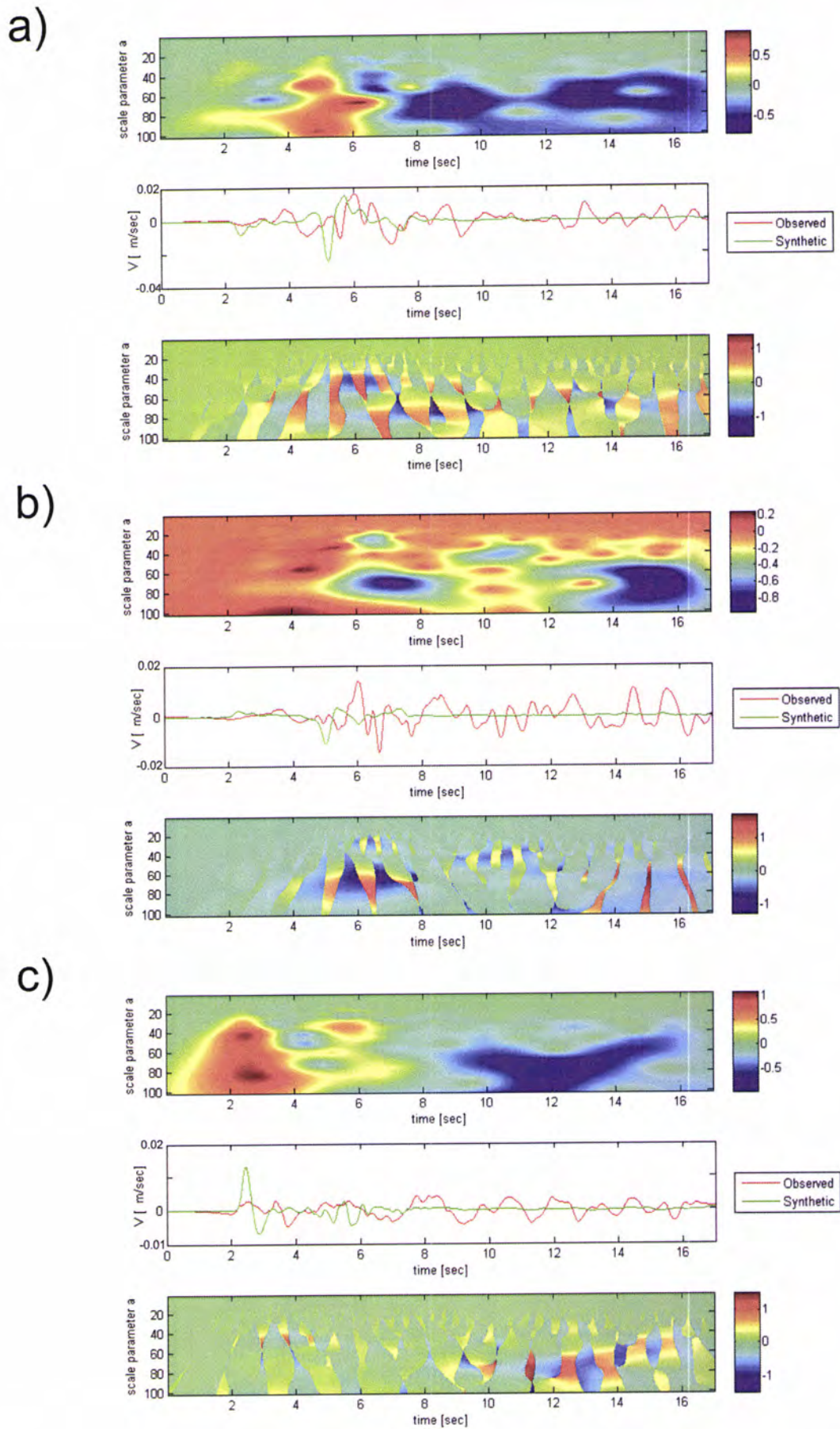
Fig. III-1.Time-frequency envelope misfit (top), comparison of observed and synthetic waveforms (middle) and time-frequency phase misfit (bottom) for the three channels (a – East, b – North, c - Up) of the station 57950

Station	Epicentral distance	Direction of motion	Observed waveform		Synthetic waveform	
			Maximum velocity (m/sec)	Minimum velocity (m/sec)	Maximum velocity (m/sec)	Minimum velocity (m/sec)
57950	14 km	East	0.015899	-0.014521	0.015169	-0.024246
		North	0.013926	-0.014721	0.003435	-0.011311
		Up	0.003987	-0.004843	0.013241	-0.006866
CHR	6.6 km	East	0.087013	-0.071132	0.046486	-0.031226
		North	0.105834	-0.05.6485	0.08.5103	-0.046711
		Up	0.027172	-0.013542	0.009690	-0.013867
MP3	10.3 km	East	0.024228	-0.022915	0.044063	-0.068273
		North	0.022084	-0.023885	0.046261	-0.028371
		Up	0.005209	-0.005908	0.015372	-0.007968
Q32	10.8 km	East	0.044501	-0.042279	0.047462	-0.072689
		North	0.040803	-0.040256	0.098770	-0.062763
		Up	0.006494	-0.007161	0.003506	-0.002213
ROC	5.4 km	East	0.029518	-0.058605	0.091114	-0.107964
		North	0.059710	-0.033989	0.098247	-0.059114
		Up	0.007456	-0.009603	0.003096	-0.002359
1684	10.4 km	East	0.017198	-0.015110	0.025219	-0.067559
		North	0.006597	-0.006842	0.000198	-0.000511
		Up	0.003140	-0.004489	0.001884	-0.003432

Table III-1-1. Maximum and minimum velocities of observed and synthetic waveforms.

We compared and analyzed 15 seconds of the observed and synthetic signals after first wave arrival. Visualization of time-frequency envelope and phase misfits revealed significant deviations of the modeled signal from the observed.

For the eastern component we obtained negative misfit in envelope for the stations CHR and 1684 that reaches 60% and 200% respectively. Though misfit is significant for the station CHR, we obtained the best fit in shape between the signals for the eastern and the northern components of this station. For the eastern component of the other stations (57950, MP3, Q32 and ROC), we obtained positive misfit on the duration of first two seconds (up to 50%, 150%, 100% and 90% respectively) and negative misfit for the following 13 seconds (up to 50%, 100%, 90% and 50% respectively).

For the northern component of the stations 57950, CHR and 1684 comparison of waveforms displayed negative envelope misfit up to 80%, 40% and 80% respectively. Envelope misfit between observed and simulated waveforms for the northern

component of another three stations MP3, Q32 and ROC is more complex. It is positive (up to 50%, 100% and 50% respectively) during the first 2-4 seconds and negative (up to 100%, 90% and 50% respectively) afterwards.

Comparison of waveform for the vertical component of the stations CHR, Q32 and ROC displayed negative envelope misfit up to 80%, 90% and 90% respectively. Envelope misfit between observed and simulated waveforms for the vertical component of another three stations 57950, MP3 and 1684 appeared positive (up to 100%, 120% and 40% respectively) during the first 2-3 seconds and negative (up to 100%, 100% and 80% respectively) afterwards.

Phase misfit for all the channels of all six stations appears significant, shows both positive and negative values and varies from 100% to 150%.

Despite the high values of the misfit between observed and synthetic data both in envelope and phase we obtained consistency on the polarity of the first motion for all presented stations. Moreover and most importantly, velocity peaks are generally in the same greatness order (Table III-1). Generally, results of performed strong ground motion simulations could be considered as reasonable.

It is clear that no model is able to exactly describe such complicated process as ground motion produced by seismic event. All methods created for that purpose are based on many important assumptions, simplifications and approximations in such parts of the process as physical and mathematical basis of the method, models of earth structure and seismic rupture. Thus, synthetic ground motion data never precisely matches actual observed data. In our case, the source of misfit between observed and synthetic signals besides imperfections related to limitations of the method could be, for example, the fact that we were not able to take into account regional topography.

Misfit also could be a result of major inaccuracies in source and structure models: used velocity model didn't take into account lateral variations of the velocity or site effects, and rupture model could be a source of inaccuracies because it was reconstructed by inversion method that can coverage to local minima (Bersenev, 2003).

It is also possible, that some model parameters that we used require thoughtful reassessment. In order to understand how dramatically variations on some model parameters could affect synthetic waveform we independently modified their values, simulated new waveforms, compared the results with data obtained using original model and presented results in the following section.

III-2. Quantitative comparison of originally synthesized waveforms with waveforms obtained using models with independently modified parameters

As mentioned before, modeling of a ground motions is a complex task that implies consideration of larg number of parameters of source and structure that could vary from one informational source to another.

Here we presented analisis of results of quantitative comparison of originally synthesized waveforms with waveforms obtained using models with independently modified) dip angle, b) strike angle, c) fault plane length, d) rupture velocity and e) velocity model. Results of comparison presented in Appendix in section A6

a. Comparison of originally synthesized waveforms with waveforms obtained using models with modified dip angle

We considered two modification of dip angle of the original model that was set as 90^0. It was modified by 10^0 in both directions which leads us to two models with following parameters: i) dip angle=80^0 (fault plane dipping in the north-east direction) and ii) dip angle=80^0 (fault plane dipping in the south-west direction). In the last case we also had to modify strike and rake angle by 180^0 of the fault plane in order to follow the standard technique when the strike angle always has to be taken so that the dip angle is dipping to the right of the strike. Strike angle than equals to 143^0 and rake angle equals 0^0.

i. Obtained results revealed that decrease of the dip angle by 10^0 involve significant changes in envelope and phase of the signal.

For the eastern component of the stations CHR and 1684 we obtained positive misfit in envelope between compared signals up to 20% and 15% correspondingly. For the stations MP3, Q32 and ROC negative misfit between the signals (up to 5%, 20% and 10% respectively) alternates with positive misfit (15%, 10% and 10% respectively). For the stations 57950 insignificant negative envelope misfit between the signals (about 5%) alternated bypositive misfit (up to 20%) that is followed by negative misfit (up to 10%) on higher frequencies.

For the northern component of the stations 57950 and CHR we obtainednegative misfit in envelope between compared signals up to 15% alternates with positive misfit that riches 10% in both cases. For the stations MP3, Q32 and ROC negative misfit between the signals (up to 20%) followed by episodic positive misfit on high frequencies that reaches 10%. For the station 1684 insignificant positive envelope misfit

(about 2.5%) alternated bynegative misfit (up to 10%) that is followed by positive misfit (up to 10%).

Comparison of the signals for the vertical component of the stations 57950, CHR and MP3 revealed that negative misfit in envelope up to 20%, 40% and 20% respectivelyalternated by positive misfit that riches 30%, 10% and 12%. For the stations, Q32 and ROC negative misfit between the signals (up to 40% and 45% correspondingly) appear on low frequencies and alternated bypositive misfit on higher frequencies that reaches about 25%. For the station 1684 positive envelope misfit that reaches 60% alternated by negative misfit (up to 60%).

Phase misfit between reference and comparison signals for all component of all six stations appeared to be insignificant.

ii. Differences in envelop and phase between reference and comparison signals produced by proposed changes in the original model are dramatic. Comparison of the signals revealed that all the comparison signals have opposite polarity. It appears that mainly it is the effect of nodal plane changes due to dip angle modification.

Comparison of the signals revealed positive envelope misfit for both horizontal and vertical channels of the stations 57950, MP3, Q32 and ROC with different degree of significance. In some cases it alternated by negative misfit, but visual comparison of the waveforms suggests that it occurred due to differences in polarity of the signals.

For the station 1684 positive envelope misfit was obtained for the horizontal channels, though the vertical component revealed negative misfit for about 3 seconds after first arrival alternated by positive misfit.

For the station CHR comparison of the waveforms for both horizontal channels displayed negative envelope misfit. For the vertical component of this station misfit between the signals appeared positive.

Visualisation of phase misfit suggested that it is dramatic for all compared pairs of signals, but visual comparison of the waveforms revealed that phase misfit most of the time is insignificant.

b. Comparison of originally synthesized waveforms with waveforms obtained using models with modified strike angle

In order to evaluate the effect of modifications of strike angle on the waveforms we considered following changes in azimuth direction of the rupture with respect to the strike angle of the reference model: i) strike angle $= 308^0$; ii) strike angle $= 338^0$.

i. Envelope and phase misfit between waveforms obtained from reference model and model with decreased strike angle appears to be significant.

For the eastern component of the stations 57950, MP3, Q32, ROC and 1684 negative misfit in envelope (up to 20%, 20%, 60%, 40% and 50%) alternated (partly due to phase difference) with positive envelope misfit (80%, 60%, 20%, 20% and 50% respectively). For the station CHR comparison of the waveforms revealed change in polarity. Visual comparison of the signals suggests decrease in envelop.

Modification of strike angle resulted significant positive misfit between referenceand modified signal modeled for the northern channel of the stations 57950 and 1684 (up to 400% and 100% respectively). For the northern component of the stations MP3, Q32 and ROC envelope misfit between compared waveforms appear negative – up to 80%.The comparison of the waveforms for the stations CHR and 1684 exposed negative misfit in envelope up to 60% alternated by positive misfit that reaches 20%.

Comparison of waveforms for the vertical component of stations 57950, CHR and MP3 revealedcomplicatedpicture for envelope misfit. For the station 57950 negative misfit (up to 60%) appearedon the low frequenciesbetween 2.5 and 5 seconds and alternated by positive misfit (up to 40%) on the higher frequenciesbetween 4 and 8 seconds. For the station CHR episodic negative misfit (up to 50%) alternated by episodic positive misfit (up to 40%) for the all range of frequencies. For the station MP3 negative misfit (up to 55%) appearedon the low frequenciesbetween 2.5 and 4 seconds and alternated by positive misfit (up to 70%) on the higher frequenciesbetween 3 and 7.5 seconds.

Obtained phase misfit between compared signals appeared both negative and positive. Visual examination of waveforms for all stations suggested that comparison signals arrived with delay with respect to reference signals.

ii. Increase of the strike angle by 15^0 caused significant envelopeand phase misfit betweenwaveforms obtained from original and modified models for different stations.

For the eastern component of the stations 57950 and 1684 positive misfit in envelope (up to 40% and 60%) alternated seemingly due to phase difference with negative envelope misfit (20% for both signals). Comparison of the waveforms forthe eastern channel of the station MP3 shown negative envelope misfit (up to 40%) alternated by positive misfit (up to 20%). For the station CHR we obtained positive misfit in envelope (up to 60%). Comparison of the signals obtained from reference and modified models for the stations Q32 and ROC revealed negative envelope misfit up to 60%.

Modification of strike angle resulted in changes in polarity and significant positive misfit between referenceand modified signal modeled for the northern channel of the station 57950. For the northern component of the stations MP3, Q32 and ROC envelope misfit between compared waveforms appear positive – up to 80%, 25% and 40% respectively. Though for the station ROC positive misfit is preceded by negative misfit visual comparison of the waveforms suggested that it occured due to significant misfit in phase. The comparison of the waveforms for the stations CHR and 1684 exposed negative misfit in envelope up to 60%.

Comparison of waveforms for the vertical component of stations Q32, ROC and 1684 displayed changes in polarity of the signal which is consistent with increase of a strike angle by 15^0 and corresponding changes in focal mechanism of the event. Significant positive envelope misfit wasdetectedbetween three pairs of waveforms though partly it occured due to changes in polarity. For the stations CHR and MP3 comparison of waveforms revealed negative misfit up to 60% and 20% correspondingly.

Obtained phase misfit between compared signals appeared both negative and positive. Visual examination of waveforms for all stations suggested that comparison signals arrived with delay with respect to reference signals.

It is clear that strike angle is a parameter that is very perceptive for seismic modeling and its innaccurate definition could be a source of considerablediscrepancies.

c. Comparison of originally synthesized waveforms with waveforms obtained using model with modified fault plane length

As it was mentioned before, we used a slip distribution model of selected event obtained from the report of the Berkeley Seismological Laboratory (Hellweg et al, 2007) (Fig. II-3). Because we didn't use the total area of the rupture presented in the report but only a main asperity as a finite fault plane it gave us opportunity to enlarge its length by 50%. We increased the length of the fault by 3 km in north-west direction and by 1.5 km in south-east direction. We also recalculated the amount of slip for each subfault in order to preserve the total seismic moment.

Proposed changes in length of the original model appeared to have dramatic influence on the waveforms.

First of all, all the waveforms suffered from significant envelope decrease (up to 80%).

Obtained phase misfit between compared signals is generally positive for the components of the stations 57950, CHR and MP3 and reaches 150%. For the station Q32 phase misfit for all three channels is insignificant. For the stations ROC and 1684

phase misfit for both horizontal channels appeared negative (up to 100%) and positive for the vertical channel (up to 100%).

It is important to mention that previously obtained results which were presented at 2010 EGU meeting differ from results presented in this work. It didn't show such dramatic envelope misfit and appeared to be more realistic. That results generally suggested that increase of the fault plane leads to positive envelope misfit between reference and comparison signals. It is possible that we have torevise some parameters of the model that could have been set incorrectly. It is also possible that such big envelope misfit between waveforms could be a result of internal algorithm error.

d. Comparison of originally synthesized waveforms with waveforms obtained using models with modified rupture velocity

Rupture speed is a very important parameter of seismic source and it can provide valuable data for studying the physics of earthquakes. In this study we modified velocity of rupture of reference model in permissible limits (0.5 of P-waves velocity or 0.8 of S-wave velocity). Thus, rupture velocities of modified models are: i) 2.8 km/sec and ii) 3.1 km/sec

i. Decreased rupture velocity of the original model resulted in generally negative envelope misfit for all components of six presented stations.

For the eastern component of the stations 57950, MP3, Q32 and ROC comparison of the waveforms obtained from reference and modified models revealed negative misfit in envelope (up to 8%, 8%, 10% and 8%). For the station CHR and 1684 we found out that negative envelope misfit (up to 6% for both) alternated by positive envelope misfit (up to 2% and 4% respectively) on higher frequencies.

Described modification of rupture velocity resulted inmainly negative envelope misfit between referenceand modified signal modeled for the northern channel of the stations 57950, CHR and 1684 (up to 10%, 6% and 6% respectively) alternated by positive envelope misfit on higher frequencies (5%, 2% and 4%). For the northern component of the stations MP3, Q32 and ROC envelope misfit between compared waveforms appear negative – up to 8%, 10% and 8% respectively.

Comparison of waveforms for the vertical component of stations of all six stations we obtained definitive misfit: 57950 – 15%; CHR – 12%; MP3 – 15%; Q32 – 15%; ROC – 20%; 1684 – 12%.

Obtained phase misfit between compared signals is insignificant, however negative. It means the comparison signal arrived later than reference one because rupture velocity of modified model was smaller.
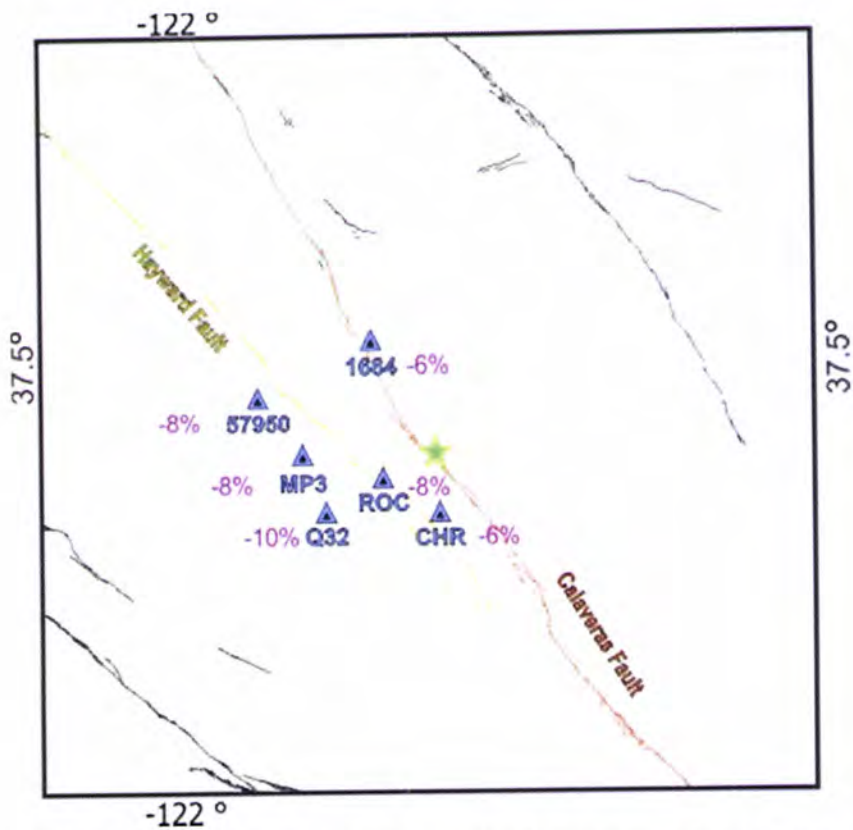
Fig. III-2-d-1. Spatial distribution of broad-band seismic stations and value of envelope misfit occurred due to decrease of initial rupture velocity (3.0 km/sec) by 0.2 km/sec for their eastern channels.
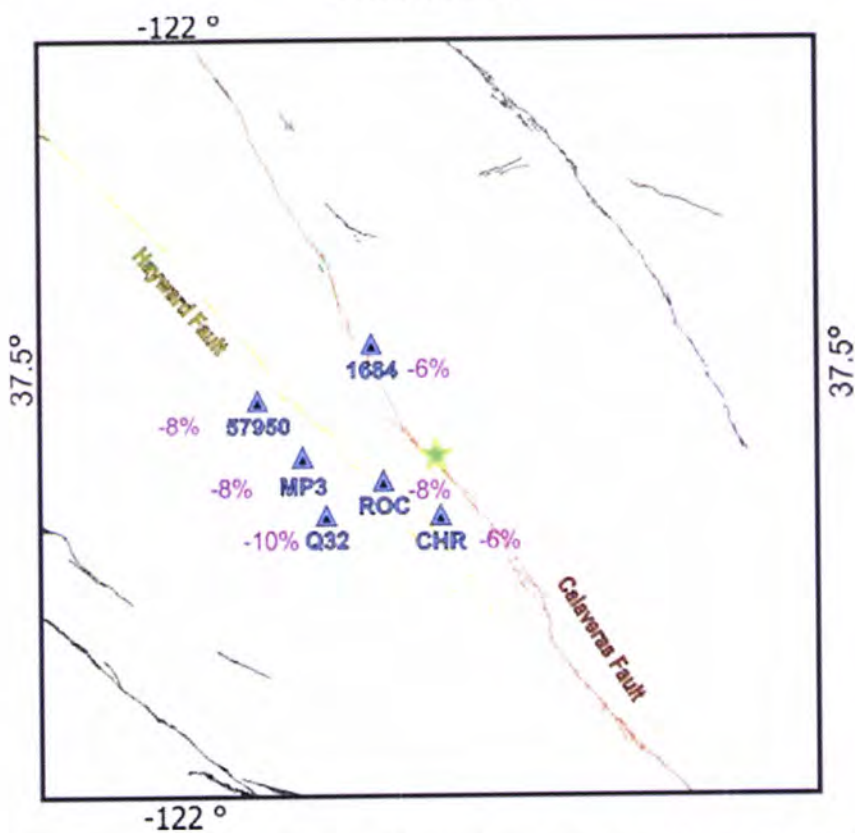
Fig. III-2-d-2. Spatial distribution of broad-band seismic stations and value of envelope misfit occurred due to decrease of initial rupture velocity (3.0 km/sec) by 0.2 km/sec for their northern channels.
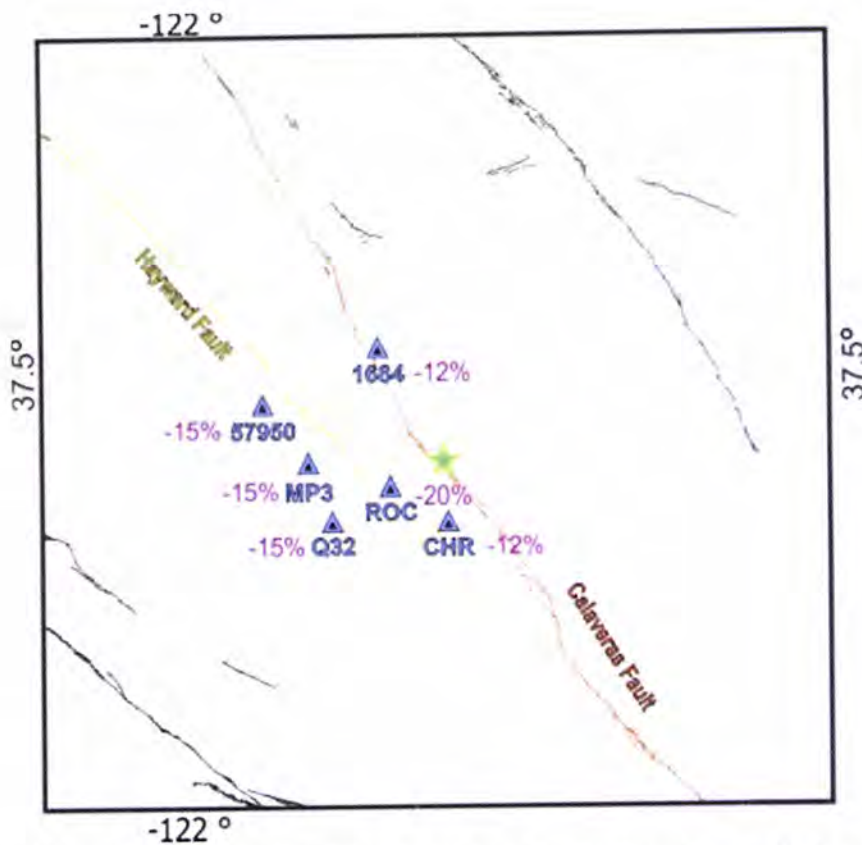
Fig. III-2-d-3. Spatial distribution of broad-band seismic stations and value of envelope misfit occurred due to decrease of initial rupture velocity (3.0 km/sec) by 0.2 km/sec for their vertical channels.

As it can be seen from presented figures effect produced by decrease of rupture velocity of reference model by 0.2 km/sec is not uniform.

The biggest envelope misfit (10%) was detected between the waveforms obtained from reference and modified models for the eastern and the northern channels of the station Q32 located 10.8 km to the South-West form the epicenter. Smaller envelope misfit (8%) was obtained for the eastern and the northern channels of the patch of stations 57950, MP3 and ROC, located 14 km North-West, 10.3 km West and 5.4 km South-West from the epicenter. For both horizontal channels decrease of rupture velocity produced the smallest effect on the envelope of waveforms obtained for the stations CHR and 1684 – 6%. These stations are located 6.6 km South and 10.4 km North-West from the epicenter.

For the vertical channels the biggest envelope misfit (20%) was detected between the waveforms obtained from reference and modified models for the station ROC (5.4 km SW). Smaller envelope misfit (15%) was obtained for the patch of stations 57950, MP3 and Q32 (14 km NW, 10.3 km W and 5.4 km SW respectively). For the vertical channel of the stations CHR and 1684 (6.6 km S and 10.4 km NW) decrease of rupture velocity produced the smallest effect on the envelope of waveforms – 12%.

49

ii. Results of comparison of the waveforms obtained through reference model with the waveforms obtained through modelswith increased rupture velocity appear to be very interesting.

For the eastern component of the stations 57950 and ROC positive changes in rupture velocity resulted in positive misfit in envelope up to 3%alternated by episodic negative envelope misfit of about 1%. For the station CHR and 1684 comparison of the waveforms revealed positive misfit in envelope up to 2.5% and 2% alternated by episodic negative misfit of about 1% and 2% respectively. The comparison of the waveforms for the stations MP3 andQ32displayed positive envelope misfitup to 3% and 4% respectively.

Only for northern component of the stations MP3 and Q32 misfit in envelope isstrictly positive up to 3% and 4% correspondingly. For other stations – 57950, CHR, Q32, ROC and 1684 – positive changes in rupture velocity resulted in positive misfit in envelope (up to 2.5%, 2.5%, 3% and 2% respectively) alternated by episodic negative envelope misfit of about 4%, 1%, 1% and 2% respectively.

Comparison of waveforms for the vertical component of stations 57950 and ROC revealed positive envelope misfit (up to 10% and 12% respectively). For the stations Q32 and 1684 we obtained positive envelope misfit between the waveforms up to 8%. For the station CHR revealed positive misfit up to 7%. For the station MP3 positive envelope misfit (up to 10%) alternated by negative misfit up to 2%.

Obtained phase misfit between compared signals as well as in the case of decreased rupture velocity appeared insignificant. However is is positive which means the comparison signal arrived earlier than reference one. It is consistent with the fact that rupture velocity of modified model was bigger then rupture velocity of reference model.

It was decided to investigate possible relation between rupture velocity modification effect and spatial distribution of the stations. For that reason we created figures illustrated stations spatial distribution and value of misfit occurred due to rupture speed modifications for their three channels. Main faults of the region and epicenter of the seismic event are also on the figures.
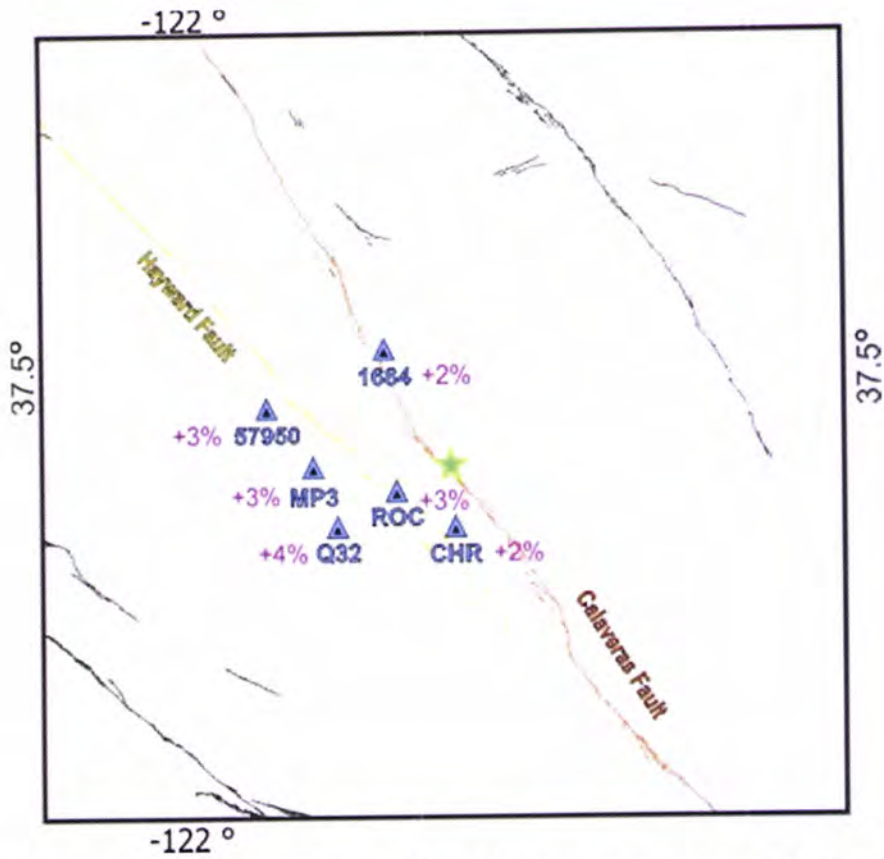
Fig. III-2-d-4. Spatial distribution of broad-band seismic stations and value of envelope misfit occurred due to increase of initial rupture velocity (3.0 km/sec) by 0.1 km/sec for their eastern channels.
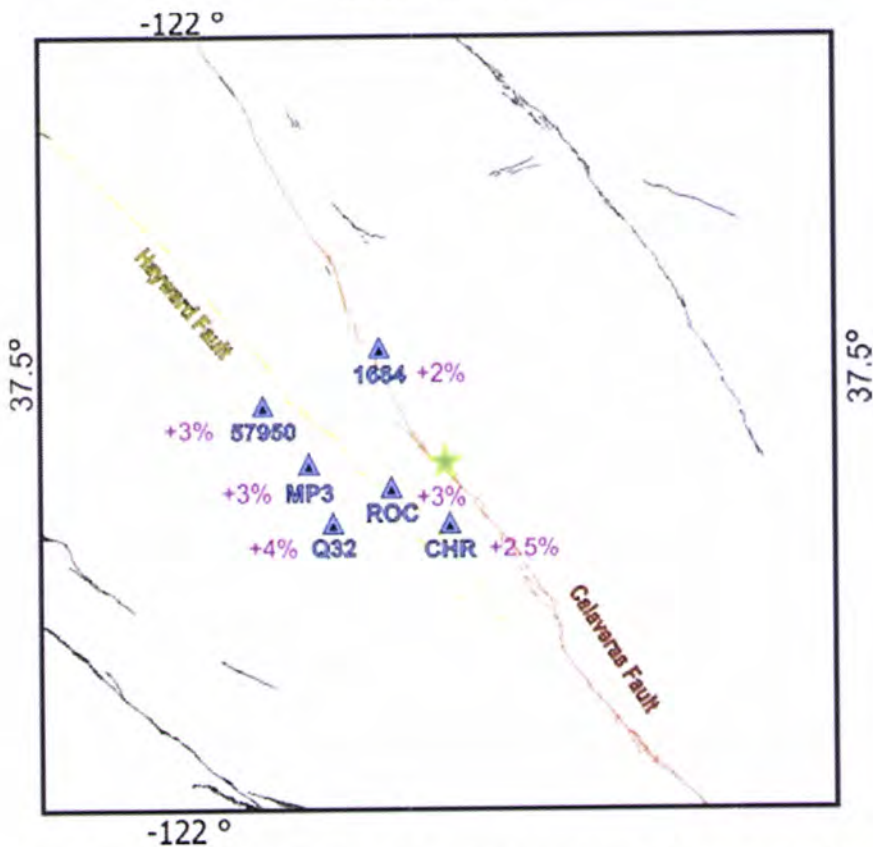
Fig. III-2-d-5. Spatial distribution of broad-band seismic stations and value of envelope misfit occurred due to increase of initial rupture velocity (3.0 km/sec) by 0.1 km/sec for their northern channels.
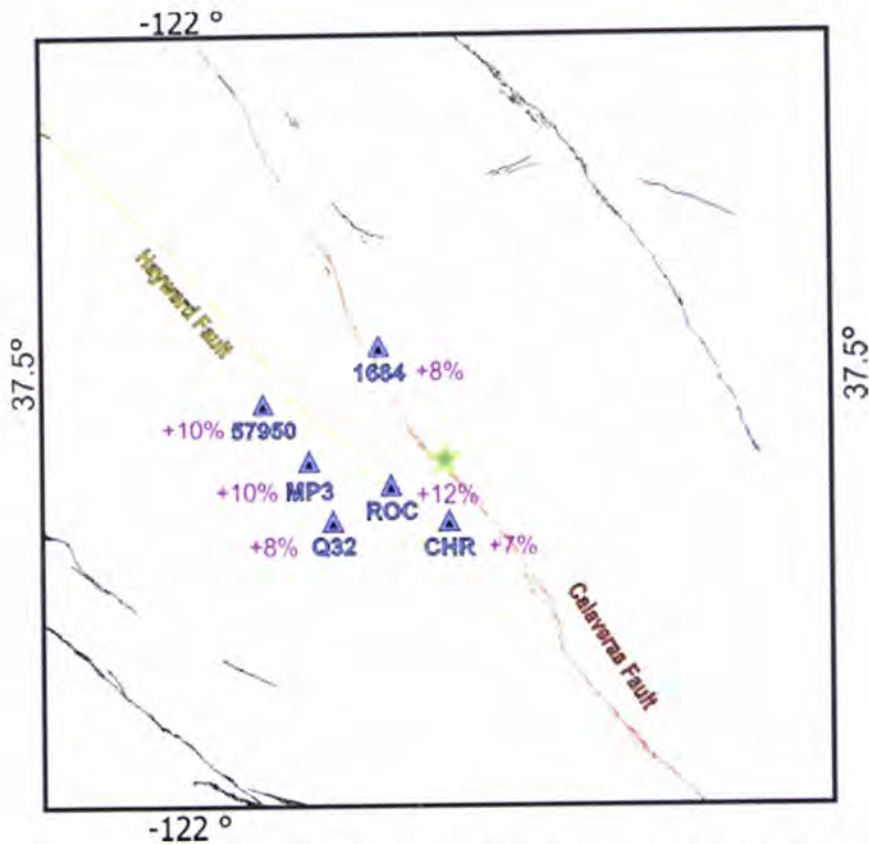
Fig. III-2-d-6. Spatial distribution of broad-band seismic stations and value of envelope misfit occurred due to increase of initial rupture velocity (3.0 km/sec) by 0.1 km/sec for their vertical channels.

The biggest envelope misfit (4%) produced by increase of rupture velocity of the original model by 0.1 km/sec was detected for the eastern and the northern channels of the station Q32 (10.8 km SW). Smaller envelope misfit (3%) was obtained for the eastern and the northern channels of the patch of stations 57950, MP3 and ROC (14 km NW, 10.3 km W and 5.4 km SW). For both horizontal channels increase of rupture velocity produced the smallest effect on the envelope of waveforms obtained for the stations CHR (6.6 km S) and 1684 (10.4 km NW) – 2.5% and 2% correspondingly.

For the vertical channels the biggest envelope misfit (12%) was detected between the waveforms obtained from reference and modified models for the station ROC (5.4 km SW). Smaller envelope misfit (10%) was obtained for the stations 57950 and MP3 (14 km NW and 10.3 km W respectively). For the vertical channel of the stations 1684 (10.4 km NW) and Q32 (10.8 km SW) increase of rupture velocity produced envelope misfit of 8%. For the vertical channel of the stations CHR (6.6 km S) increase of rupture velocity produced the smallest effect on the envelope of waveforms – 7%.

	Misfit (%)	Station code (rupture velocity 2.8 km/sec)	Misfit (%)	Station code (rupture velocity 3.1 km/sec)
Eastern channel	-10	Q32	+4	Q32
	-8	57950, MP3, ROC	+3	57950, MP3, ROC
	-6	CHR, 1684	+2	1684, CHR
Northern channel	-10	Q32	+4	Q32
	-8	57950, MP3, ROC	+3	57950, MP3, ROC
	-6	1684, CHR	+2; +2.5	1684, CHR
Vertical channel	-20	ROC	+10; +12	*57950, MP3*, ROC
	-15	*57950,MP3*, Q32	+8	Q32,
	-12	1684, CHR	+7	CHR, 1684

Table III-2-d-1. Stations grouped by the value of misfit between reference and comparison signals produce by increase and decrease of rupture speed

Based on the obtained results we draw the following conclusions:

1. All stations could be divided into three main groups based on the value of misfit (Table III-2-d-1).

2. Misfit between the reference and comparison signals produced by both increase and decrease of rupture speed of the original model mostly has the same pattern.

3. From station to station, value of misfit between the signals for both horizontal channels is the same in case of rupture velocity decrease. It is also true in case of rupture velocity increase.

4. Misfit between the reference and comparison signals produced by both increas and decrease of rupture speed of the original model for the vertical channel significantly exceeded misfit for both horizontal channels.

Clearly, rupture speed is one of the key parameters to be considered in case of ground motion modeling and has to be taken thoughtfully.

e. **Comparison of originally synthesized waveforms with waveforms obtained using model with alternative velocity model**

An appropriate velocity model is a factor of great importance in waveform simulations. As a velocity model of the reference model we used a very detailed 1D velocity model of the San Francisco Bay region for short-period simulations that follows the average depth variations in the structure and we adapted it for 3D media (Table II-2). It was decided to use two different velocity models of the same region for independent simulation and then quantitatively compare results in order to see how dramatically they would differ. As a velocity model of the comparison model we used

53

1D velocity model for P-waves used for routine location by the NCSN for events on the Hayward and Calaveras Fault (Table II-3). The S-wave velocities were obtained by scaling the corresponding velocities of P-waves by a factor $1/\sqrt{3}$ and densities were calculated for each layer using empirical relations between elastic wave speeds and density in the Earth's crust (II-8). Hence, we used two different velocity models of the region (Aagaard et al, 2008; Waldhauser & Ellsworth, 2002)

Velocity model by Aagaard et al (2008)				Velocity model by Waldhauser & Ellsworth (2002)			
Top of the layer, km	V_p, km/s	V_s, km/s	ρ, g/cm^3	Top of the layer, km	V_p, km/s	V_s, km/s	ρ, g/cm^3
0	2,4	1,1	2,3	0	3.77	2.18	2.36
0.2	3	1,4	2,45				
0.5	3,6	1,95	2,5				
1	4,2	2,3	2,55	1	4.64	2.68	2.48
1.5	4,8	2,8	2,6				
2.5	5,25	3	2,62				
3	5,6	3,25	2,65	3	5.34	3.08	2.58
5	5,9	3,41	2,7	6	5.75	3.32	2.66
7	6,15	3,55	2,75				
9	6,35	3,62	2,85	14	6.22	3.59	2.76
17	7	4,1	3				
-	-	-	-	20	7.98	4.61	3.27

Table III-2-e-1. Reference (Aagaard et al, 2008) and comparison (Waldhauser & Ellsworth, 2002) velocity models

Judging from the obtained results presented in Appendix in section A6 envelope and phase misfit between waveforms obtained from models using different velocity structures of the region appears to be significant.

For the eastern component of the stations CHR, Q32, ROC and 1684 positive misfit in envelope that occurred on higher frequencies (up to 70%, 60%, 60% and 100% respectively) alternated bynegative envelope misfit (50%, 40%, 45% and 40% respectively) on lower frequencies. For the station MP3 comparison of the waveforms revealed negative envelope misfit of 20% with episodic positive misfit on high frequencies. Only for the station 57950 definite positive envelop misfit between compared waveforms was detected on higher frequencies.

Usage of alternative velocity model resulted in significant positive misfit between referenceand modified signals modeled for the northern channel of the stations 57950, CHR, MP3, Q32, ROC and 1684 on higher frequencies (up to 40%, 50%, 80%, 60%, 60% and 90% respectively) alternated by negative misfit (50%, 40%, 20%, 40%, 45% and 40% respectively) on lower frequencies.

Comparison of waveforms for the vertical component of all six stations (57950, CHR, MP3, Q32, ROC and 1684) revealed complicated picture: positive envelope misfit (25%, 150%, 150%, 250% and 200%) alternated by negative envelope misfit (50%, 50%, 40%, 30%, 80% and 50%) for the all range of frequencies.

Obtained phase misfit between compared signals for the eastern component of the station 57950 appeared significant and vary between positive (50%) and negative (150%). For another stations comparison of signals revealed insignificant phase misfit.

For the northern component of the station 57950 and CHR phase misfit vary between positive (50% and 150%) and negative (150% and 50%). For the northern components of another stations phase misfit is insignificant.

For the vertical components of the stations 57950 and MP3 phase misfit vary between positive (50%) and negative (150%). Obtained phase misfit between compared signals for the vertical component of the stations CHR, Q32 and ROC appeared significant and vary between positive (100%) and negative (150%). For the station 1684 phase misfit between waveforms modeled for the vertical component appeared insignificant.

Waveforms obtained from comparison model for the vertical channel of all stations arrived with delay with respect to waveform obtained for the vertical component from original model. For the horizontal channels, delay appeared for the stations 57950, MP3 and Q32. For stations CHR, ROC and 1684 delay between the waveforms obtained for the horizontal channels appeared insignificant.

Importance of velocity model as input parameter for simulations of ground motions could not be overestimated. And usage of appropriate and realistic velocity modelis essential for simulation results. Our results revealed that usage of two different velocity models of the same region could lead to significantly different results in terms of envelop and phase in time-frequency domain.

Conclusions

Strong ground motion modeling is a subject of the great importance for modern seismology. Its contribution in the study of seismic source and seismic risks mitigation is more than significant. It provides abundance of valuable information about seismic event and helps in characterization of the risk.

Apparently, modeling of string ground motion is not an easy process. It requires a lot of components among which can be named:

1. Modeling algorithm that is appropriate for the set goal and have a strong mathematical and physical foundation.
2. Suitable computing capacity.
3. Apt knowledge of the structure.
4. Information about the source that should be as full as possible.

It is important to remember that inadequacies of any of these components could dramatically affect upcoming results. Thus, the main goal of this work was to assess influence of different model parameters on simulated strong-motion waveforms based on gained theoretical knowledge of various existing scientific approaches, methods and algorithms and practical skills in seismic source modeling and waveform synthesis. We applied them for strong ground motion modeling of actual moderate event using its source geometry and slip distribution along with regional velocity structure as input parameters.

We applied FDM and algorithm for ground motion synthesis based on it – 2D/3D elastic finite-difference wave propagation code E3D (Larsen & Schultz, 1995)– for simulation of strong ground motions produced by the Alum Rock earthquake ($M_w = 5.4$) that occurred near the junction of the Hayward and Calaveras faults in the San Francisco Bay, California, on October 31, 2007. We used existing slip distribution for this event obtained through inversion in the Berkeley Seismological Laboratory that was available in the report (Hellweg et al, 2007) (Fig. II-3) and detailed 1D velocity model of the San Francisco Bay region that was adapted for 3D media (Aagaard et al, 2008) (Table II-2) as input parameters of the model in simulations of long-period waveforms for three channels of six broad-band stations located in the immediate vicinity from the epicenter of the event. Results of simulations were quantitatively compared with observed waveforms using MATLAB code that we developed based the wavelet transform to quantify the time-frequency envelope and phase misfit (Kristeková et al, 2006). It is a very advantageous technique that allows compare seismograms in

terms of envelope and phase in time-frequency domain that could be applied for various tasks when quantitative comparison of waveforms is required (for example, in source inversion). Eventually, we studied importance of some parameters of the model involved in waveform synthesis through modeling of waveforms using models with separately and independently modified parameters from original model: – dip angle, strike angle, length of the fault plane, rupture velocity, and velocity model. Later, we quantitatively compared these waveforms with originally obtained and draw some important conclusions about their influence on the waveforms. It helped us realize the significance of their appropriate and thoughtful usage in input models.

Results, obtained during this work, are very inspiring. First of all, comparison of the results of simulations with observed waveforms for corresponding stations revealed that despite the high values of the misfit both in envelope and phase we obtained consistency on the polarity of the first motion for all presented stations. Moreover and most importantly, velocity peaks are generally in the same greatness order (Table III-1). Generally, results of performed strong ground motion simulations could be considered as reasonable. We also draw some conclusion about the reasons that could have affected the results, such as unaccounted regional topography, lateral velocity variations and site effect. Rupture model could also be a source of inaccuracies because it was reconstructed by inversion method (Bersenev, 2003).

Inappropriate choice of parameters could also be a source of misfit. In order to understand how dramatically variations on some model parameters (dip angle, strike angle, length of the fault plane, rupture velocity, and velocity model) could affect synthetic waveform we independently modified their values, simulated new waveforms, compared the results with data obtained using original model.

Results of the tests for dip angle modifications influence on the waveforms revealed:

- Decrease of the dip angle of original model by 10^0 involve significant changes in envelope and phase of the signal. For the horizontal components of some stations both positive and negative envelope misfit reached 20% and often alternated by each other. For the vertical components positive and negative envelope misfit reached 60%. Alternation of positive and negative misfit also occurred in this case. Phase misfit, however, appeared insignificant

- Changes in the dip angle of the original model by 10^0 that leaded to the changes in strike and rake angle that was described previously (Chapter III,

2-a) produced signals with polarity opposite to polarity of original signals for the corresponding stations. Supposedly, it is the effect of nodal plane changes produced by dip angle modification. Comparison of signals modeled for different stations revealed both positive and negative envelope misfit. Visualisation of phase misfit suggested that it is dramatic for all compared pairs of signals, but visual comparison of the waveforms revealed that phase misfit most of the time is insignificant.

Results of the tests for strike angle modifications influence on the waveforms revealed:

- Decrease of the strike angle of the original model by 15^0 resulted in dramatically significant envelope and phase misfit between compared waveforms. For the eastern component negative envelope misfit reached 60%, positive – 80%. For one station opposite polarity was registers. For the northern component negative envelope misfit reached 80%, positive – 400%. For the vertical component negative envelope misfit reached 60%, positive – 70%.Obtained phase misfit between compared signals appeared both negative and positive. Visual examination of waveforms for all stations suggested that comparison signals arrived with delay with respect to reference signals.

- Increase of the strike angle of the original model by 15^0 resulted in both negative and positive envelope misfit between comapared signals that reached 60% for the eastern component of the stations. For the northern component negative envelope misfit reached 60%, positive – 80%. For one station opposite polarity was registers along with significant positive envelop misfit. Comparison of waveforms for the vertical component revealed changes in polarity and significant positive envelope misfit for three stations. This results are in agreement withcorresponding changes in focal mechanism produced by increase of a strike angle by 15^0. Besides that, positive envelope misfit for the vertical component reaches 40%, negative – 60%. Obtained phase misfit between compared signals appeared both negative and positive. Visual examination of waveforms for all stations suggested that comparison signals arrived with delay with respect to reference signals.

It is clear that strike angle is a parameter that is very perceptive for seismic modeling and its inaccurate definition could be a source of considerable discrepancies.

Proposed changes in length of the original model appeared to have dramatic influence on the waveforms:

58

-   For all components of all stations comparison of signals revealed negative envelope misfit up to 80%. Obtained phase misfit between compared signals is generally positive for the components of the stations 57950, CHR and MP3 and reaches 150%. For the station Q32 phase misfit for all three channels is insignificant. For the stations ROC and 1684 phase misfit for both horizontal channels appeared negative (up to 100%) and positive for the vertical channel (up to 100%).

Significant differences between reference and comparison signals forced us to question their fairness. It is possible that we have to revise some parameters of the model that could have been set incorrectly. It is also possible that such big envelope misfit between waveforms could be a result of internal algorithm error.

Manipulations with rupture velocity of the original model revealed that:

-   Decrease of rupture velocity of the original model by 0.2 km/sec resulted in generally negative envelope misfit for all components of six presented stations (up to 10% for the horizontal channels and up to 20% for the vertical channel) that in some cases alternated by positive misfit (up to 4%) on higher frequencies. Obtained phase misfit between compared signals is insignificant, however negative. It means the comparison signal arrived later than reference one because rupture velocity of modified model was smaller.

-   Increase of rupture velocity of the original model by 0.1 km/sec resulted in generally positive envelope misfit. For the horizontal componentspositive envelope misfit reached 4% in some cases alternated by episodicnegative misfit (up to 4%). For the vertical component positive misfit reached 12%. Obtained phase misfit between compared signals is insignificant, however positive. It means the comparison signal arrived earlier than reference one because rupture velocity of modified model was bigger.

We found out based on obtained results that all stations which locations were used in simulations could be divided into three main groups based on the value of misfit (Table III-2-d-1). Values of misfit produced both by increase and decrease of rupture speed of the original model mostly distributed following the same pattern. From station to station, value of misfit between the signals for both horizontal channels is the same in case of rupture velocity decrease. It is also true in case of rupture velocity increase. It also appeared that misfit between the reference and comparison signals produced by both increase and decrease of rupture speed of the original model for the vertical channel significantly exceeded misfit for both horizontal channels.

Performed tests clearly proved that rupture speed is one of the key parameters to be considered in case of ground motion modeling and has to be taken thoughtfully.

Tests performed using velocity model alternative to original one revealed that:

- For the eastern component positive misfit in envelope on higher frequencies reached 100% and alternated bt negative envelope misfit (up to 50%) on lower frequencies. Only for one station was obtained positive envelop misfit between compared waveforms on higher frequencies. Usage of alternative velocity model resulted in significant positive misfit between reference and modified signals on higher frequencies (up to 90%). It alternated by negative misfit (up to 50%) on lower frequencies. Comparison of waveforms for the vertical component of all six stations revealed complicated picture when positive envelope misfit (up to 250%) alternated by negative envelope misfit (up to 80%) for all range of frequencies. Obtained phase misfit between compared signals is very different from station to station: it appeared positive or negative reaching up to 150% or insignificant. However, waveforms obtained from comparison model for the vertical channel of all stations arrived with delay with respect to waveform obtained for the vertical component from original model. For the horizontal channels of some stations was observed delay. Meanwhile, for the horizontal channels of other stations delay between the waveforms appeared insignificant.

Importance of velocity model as input parameter for simulations of ground motions could not be overestimated. And usage of appropriate and realistic velocity model is essential for simulation results. Our results revealed that usage of two different velocity models of the same region could lead to significantly different results in terms of envelop and phase in time-frequency domain.

Eventually, we achieved main goal of presented work and assess influence of some parameters of the model on upcoming result. But most importantly, priceless theoretical knowledge and practical skills were obtained in the process and they would be used and enriched in the future.

Future perspectives

The project "Prediction of seismic ground motions in broadband frequencies for highly populated areas of the Western part of Ibero-Maghrebian zone from remote and local sources" was submitted for FCT fellowship. In the future, it is planned to continue the work on strong ground motion modeling with different and more complicated approaches.

We also plan to write an article based on this work and its results.

References

Aagaard, B. T., T. M. Brocher, D. Dolenc, D. Dreger, R. W. Graves, S. Harmsen, S. Hartzell, S. Larsen, and M. L. Zoback (2008). Ground motion modeling of the 1906 San Francisco earthquake, part I: Validation using the 1989 Loma Prieta earthquake, *Bull. Seism. Soc. Am.* **98**, no. 2, 989-1011.

Abramovici, F. and J. Gal-Ezer (1978). Numerical seismograms for a vertical point-force in a single layer over a half-space, *Bull. Seism. Soc. Am.* **68**, 81-101.

Aki, K. (1968). Seismic displacements near a fault, *J. Geophys. Res.* **73**, 5359-5376.

Aki, K. (1982). Strong ground motion prediction using mathematical modeling techniques, *Bull. Seism. Soc. Am.* **72**, S29-S41.

Aki, K. and P. G. Richards (1980). *Quantitative Seismology, Theory and Methods*, Vols.I and II, W. H. Freeman, San Francisco, California.

Alford, R. M., K. R. Kelly, and D. M. Boore (1974). Accuracy of finite difference modeling of the acoustic wave equation, *Geophysics* **39**, 834–842.

Alterman, Z., and F. C. Karal (1968). Propagation of elastic waves in layered media by finite difference methods, *Bull. Seism. Soc. Am.* **58**, 367–398.

Alterman, Z., and P. Kornfeld (1968). Finite difference solution for pulse propagation in a sphere, *Israel J. Technology* **6**, 138–149.

Anderson, J. (1973). A model source time function for the Parkfield, Califoroia, earthquake, Abstract, Prog. 60th Annual Mtg., *Seism. Soc. Am.*, Golden, Colorado.

Anderson, J. G. (1976). Motions near a shallow rupturing fault: evaluation of the effects due to the free surface, *Geophys. J.* **16**, 575-593.

Aoi, S., and H. Fujiwara (1999). 3D finite-difference method using discontinuous grids, *Bull. Seism. Soc. Am.* **89**, 918–930.

Archuleta, R. J. and G. A. Frazier (1978). Three-dimensional numerical simulations and dynamic faulting in a half-space, *Bull. Seism. Soc. Am.* **68**, 573-598.

Archuleta, R. J. and S. M. Day (1977). Near-field particle motion resulting from a propagating stress relaxation over a fault embedded within a layered medium, *Trans. Am. Geophys. Union* **58**, 445.

Bayliss, A., K. E. Jordan, B. J. LeMesurier, and E. Turkel (1986). A fourth order accurate finite-difference scheme for the computation of elastic waves, *Bull. Seism. Soc. Am.* **76**, 1115–1132.

Beroza, G. C., and T. Mikumo (1996). Short slip duration in dynamic rupture in the presence of heterogeneous fault properties, *J. Geophys. Res.* **101**, 22,449–22,460.

Beresnev, I. A. (2003). Uncertainties in finite-fault slip inversions: To what extent to believe? (A critical review), *Bull. Seism. Soc. Am.* **93**, 2445-2458.

Boore, D. M. (1972). Finite difference methods for seismic-wave propagation in heterogeneous materials, Chapter 5 in *Methods in Computational Physics*, Vol. II, Academic Press (in press).

Bouchon, M. (1979). Predictability of ground displacement and velocity near an earthquake fault. An example: the Parkfield earthquake of 1966, *J. Geophys. Res.* **84**, 6149-6156.

Bouchon, M. (1980). The motion of the ground during an earthquake. 1. The case of a strike slip fault, *J. Geophys. Res.* **85**, 356-366.

Bouchon, M., and K. Aki (1977). Discrete wavenumber representation of seismic source wave fields, *Bull. Seism. Soc. Am.* **67**, 259–277.

Bouchon, M., and K. Aki (1980). Simulation of long-period, near-field motion for the great California earthquake of 1857, *Bull. Seism. Soc. Am.* **70**, 1669–1682.

Brocher, T. M. (2005). Empirical relations between elastic wave speeds and density in the Earth's crust, *Bull. Seism. Soc. Am.* **95**, no. 6, 2081–2092.

Caldeira, B. (2004).Caracterização espaço-temporal da fonte sísmica - Processos de rupture e directividade, *PhD thesis*, Universidade de Évora

Campillo, M and M Bouchon (1983). A theoretical study of the radiation from small strike-slip earthquakes at close distances, *Bull. Seism. Soc. Am.* **73**, 83-96.

Chang, Wen-Fong and G.A. McMechan (1989). Absorbing boundary conditions for 3-D acoustic and elastic finite-difference calculations, *Bull Seism. Soc. Am.* **79**, 211-218.

Clayton, R. and B. Engquist (1977). Absorbing boundary conditions for acoustic and elastic wave equations, *Bull Seism. Soc. Am.* **67**, 1529-1540.

Cloud, W. K. and V. Perez (1967). Accelerograms –Parkfield earthquake, *Bull. Seism. Soc. Am.* **57**.

Dablain, M. A. (1986). The application of high-order differencing to the scalar wave equation, *Geophysics* **51**, 54–66.

De Lilla, A. (1997). Finite difference seismic wave propagation using discontinuous grid sizes, *M. Sc. Thesis*, Massachusetts Institute of Technology.

Faccioli, E., F. Maggio, A. Quarteroni, and A. Tagliani (1996). Spectral domain decomposition methods for the solution of acoustic and elastic wave equations, *Geophysics* **61**, 1160-1174.

Festa, G., and S. Nielsen (2003). PML Absorbing Boundaries, *Bull. Seism. Soc. Am.* **93**, no. 2, 891–903.

Frankel, A. (1993). Three-dimensional simulations of ground motions in the San Bernardino valley, California, for hypothetical earthquakes on the San Andreas fault, *Bull. Seism. Soc. Am.* **83**, 1020–1041.

Frankel, A., and W. Leith (1992). Evaluation of topographic effects on P and S waves of explosions at the northern Novaya Zemlya test site using 3-D numerical simulations, *Geophys. Res. Lett.* **19,** 1887–1890.

Geller, R. J., and N. Takeuchi (1995). A new method for computing highly accurate DSM synthetic seismograms, *Geophys. J. Int.* **123,** 449–470.

Grandin, R., Borges, J. F., Bezzeghoud M., Caldeira, B., Carrilio, F. (2007). Simulation of strong ground motion in SW Iberia for the 1969 February 28 (M_s=8.0) and the 1755 November 1 (M~8.5) earthquakes – I. Velocity model, *Geophys. J. Int.*, Vol. **171**, Issue 3, 1144-1161.

Grandin, R., Borges, J. F., Bezzeghoud M., Caldeira, B., Carrilio, F. (2007). Simulation of strong ground motion in SW Iberia for the 1969 February 28 (Ms=8.0) and the 1755 November 1 (M~8.5) earthquakes – II. Strong ground motion simulations, *Geophys. J. Int.*, Vol. **171**, Issue 2, 807-822.

Graves, R. W. (1996). Simulating seismic wave propagation in 3D elastic media using staggered grid finite differences, *Bull. Seism. Soc. Am.* **86**, 1091–1106.

Graves, R. W. (1998). Three-dimensional finite-difference modeling of the San Andreas fault: Source parameterization and ground-motion levels, *Bull. Seism. Soc. Am.* **88**, 881-897.

Guatteri, M., M. Mai, P. Martin, and G. C. Beroza (2004). A pseudo-dynamic approximation to dynamic rupture models for strong ground motion prediction, *Bull. Seism. Soc. Am.* **94**, 2051–2063.

Guatteri, M., P. M. Mai, G. C. Beroza, and J. Boatwright (2003). Strong ground motion prediction from stochastic-dynamic source models, *Bull. Seism. Soc. Am.* **93**, 301–313.

Hardebeck, J. L., A. J. Michael, and T. M. Brocher (2007). Seismic velocity structure and seismotectonics of the eastern San Francisco Bay region, California, *Bull. Seism. Soc. Am.* **97**, 826–842.

Hartzell, S. H. (1978). Interpretation of earthquake strong ground motion and implications for earthquake mechanism, Ph.D. Dissertation, University of California, San Diego, La Jolla, 269 pp.

Haskell, N. A. (1964). Total energy and energy spectral density of elastic wave radiation from propagating faults, *Bull. Seism. Soc. Am.* **54**, 1811-1841.

Heaton, T. H., and D. V. Helmberger (1977). A study of the strong ground motion of the Borrego Mt., California earthquake, *Bull. Seism. Soc. Am.* **67**, 315-319.

Hellweg, M., A. Chung, D. Dreger, A. Kim and J. Boatwright (2007). Mapping the Rupture of the M_w5.4 Alum Rock Earthquake, report of the Berkeley Seismological Laboratory.

Hestholm, S., and B. Ruud (1994). 2D finite-difference elastic wave modeling including surface topography, *Geophys. Prop.* **42**, 371–390.

Hole, J. A., T. M. Brocher, S. L. Klemperer, T. E. Parsons, H. M. Benz, and K. P. Furlong (2000). Three-dimensional seismic velocity structure of the San Francisco Bay area, *J. Geophys. Res.* **105**, 13,859–13,874.

Housner, G. W. and M. D. Trifunac (1967). Analysis of accelerograms – Parkfield earthquake, *Bull. Seism. Soc. Am.* **57**, 1193-1220.

Hulbert, G. M. and Hughes, T. J. R. (1990). Space-time finite element methods for second-order hyperbolic equations, *Comp. Meth. Appl. Mech. Eng.* **84**, 327-348.

Ida, Y (1973). The maximum acceleration of seismic ground motion, *Bull. Seism. Soc. Am.* **63**, 959-968.

Igel, H., P. Mora, and B. Riollet (1995). Anisotropic wave propagation through finite-difference grids, *Geophysics* **60**, 1203–1216.

Israel, M. and R. L. Kovach (1977). Near-field motions from a propagating strike-slip fault in an elastic half-space, *Bull. Seism. Soc. Am.* **67**, 977-994.

Jacob, K. H. (1970). Three-dimensional seismic ray tracing in a laterally heterogeneous spherical earth, *J. Geophys. Res.* **75**, 6675-6689.

Jastram, C., and E. Tessmer (1994). Elastic modeling on a grid with vertically varying spacing, *Geophys. Prospect.* **42**, 357–370.

Jih, R. S., K. L. McLaughlin, and Z. A. Der (1988). Boundary conditions of arbitrary polygonal topography in elastic finite difference scheme for seismogram generation, *Geophysics*.

Kanamori, H., and L. Rivera (2004). Static and dynamic scaling relations for earthquakes and their implications for rupture speed and stress drop, *Bull. Seism. Soc. Am.* **94**, no. 1, 314–319.

Kawasaki, I. (1975). On the dynamic process of the Parkfield earthquake of June 28, 1966, *J. Phys. Earth* **23**, 127–144.

Kawasaki, I., Y Suzuki, and R. Sato (1975). Seismic waves due to a shear fault in a semi-infinite medium, Part II: Moving source, *J. Phys. Earth* **23**, 43-61.

Kelly, K., R. Ward, S. Treitel, and R. Alford (1976). Synthetic seismograms: a finite-difference approach, *Geophysics* **41**, 2–27.

Komatitsch, D. and J.-P.Vilotte (1998). The spectral element method: an efficient tool to simulate the seismic response of 2D and 3D geological structure, *Bull. Seism. Soc. Am.* **88**, 368-392.

Kostrov, B. V. (1964). Self-similar problems of propagation of shear cracks, *J. Appl. Math. Mech.* **28**, 1077-1087.

Kristek, J., and P. Moczo (2006). On the accuracy of the finite-difference schemes: The 1D elastic problem, *Bull. Seism. Soc. Am.* **96**, 2398–2414.

Kristekova, M., Kristek, J., Moczo, P., Day, S.M., (2006). Misfit criteria for quantitative comparison of seismograms, *Bull. Seism. Soc. Am.* **96(5)**, 1836–1850.

Kummer, B., A. Behle, and F. Dorau (1987). Hybrid modeling of elastic wave propagation in two-dimensional laterally inhomogeneous media, *Geophysics* **52**, 765-771.

Larsen, S. and C.A. Schultz (1995). ELAS3D: 2D/3D elastic finite-difference wave propagation code, Technical Report No. UCRL-MA-121792, 19 pp.

Larsen, S., M. Antolik, D. Dreger, C. Stidham, C. Schultz, A. Lomax, and B. Romanowicz (1997). 3-D models of seismic wave propagation: Simulating scenario earthquakes along the Hayward fault, *Seism. Res. Lett.* **68**, 328.

Levander, A. (1988). Fourth-order finite-difference P-SV seismograms, *Geophysics* **53**, 1425-1436.

Levy, N. A. and A. K. Mal (1976). Calculation of ground motion in a three-dimensional model of the 1966 Parkfield earthquake, *Bull. Seism. Soc. Am.* **66**, 403-423.

Lindman, E. L. (1975). Free-space boundary conditions for the time dependent wave equation, *J. Comput. Phys.* **18**, 66–78.

Lysmer, J. and L. A. Drake (1972). A finite element method for seismology, in *Methods in Computational Physics*, **11**, B. Bolt, Editor, 181-216, Academic Press, New York.

Madariaga, R. (1976). Dynamics of an expanding circular fault. *Bull. Seism. Soc. Am.* **66**, 639–666.

McEvilly, T. V., W. H. Bakun, and K. B. Casaday (1967). The Parkfield, California earthquakes of 1966, *Bull. Seism. Soc. Am.* **57**, 1221-1244.

Moczo, P. (1989). Finite-difference technique for SH waves in 2-D media using irregular grids-Application to the seismic response problem, *Geophys. J. Int.* **99**, 321–329.

Moczo, P., J. Kristek, V. Vavryc̆uk, R. J. Archuleta, and L. Halada (2002). 3D heterogeneous staggered-grid finite-difference modeling of seismic motion with volume harmonic and arithmetic averaging of elastic moduli and densities, *Bull. Seism. Soc. Am.* **92**, 3042–3066.

Moczo, P., P. Labfik, J. Kristek, and F. Hron (1996). Amplification and differential motion due to an antiplane 2D resonance in the sediment valleys embedded in a layer over the half space, *Bull. Seism. Soc. Am.* **86**, 1434-1446.

Müller, G. (1969). Theoretical seismograms for some types of point-sources in layered media. Part III. Single force and dipole sources of arbitrary orientation, *Z. Geophys.* **35**, 347–371.

Niazy, A. (1975). An exact solution for a finite, two-dimensional moving dislocation in an elastic half-space, with application to the San Fernando earthquake of 1971, *Bull. Seism. Soc. Am.* **55**, 1797-1826.

Nielsen, S. B., and K. B. Olsen (2000). Constraints on stress and friction from dynamic rupture models of the 1994 Northridge, California, earthquake, *Pure Appl. Geophys.* **157**, 2029–2046.

Oakeshott G.B., Allen C. R., W. Smith, S. W., Pakiser, L. C., McEvilly, T. V., Cloud, W. K., and Steinbrugge, K. V. (1966). Parkfield earthquakes of June 27-29, 1966, Monterey and San Obispo Countries, California – Preliminary report, *Bull. Seism. Soc. Am.* **56**, 961-971.

Oglesby, D. D., and S. M. Day (2002). Stochastic fault stress: Implications for fault dynamics and ground motion, *Bull. Seism .Soc. Am.* **92**, no. 8, 3006–3021.

Ohminato, T., and B. Chouet (1997). A free surface boundary condition for including 3D topography in the finite-difference method, *Bull. Seism. Soc. Am.* **87**, 494–515.

Olsen, K. B. and R. J. Archuleta (1996). Three-dimensional simulation of earthquakes on the Los Angeles fault system, *Bull Seism. Soc. Am.* **86**, 575-596.

Olsen, K. B., and R. J. Archuleta (1996). Three-dimensional simulation of earthquakes on the Los Angeles Fault System, *Bull. Seism. Soc. Am.* **86**, 575–596.

Olsen, K. B., J. C. Pechmann, and G. T. Schuster (1995). Simulation of 3D elastic wave propagation in the Salt Lake Basin, *Bull. Seism. Soc. Am.* **85**, 1688–1710.

Papageorgiou, A. S. (1997). "Engineering Seismology," in Computer Analysis and Design of Earthquake Resistant Structures, edited by D. E. Beskos and S. A. Anagnostopoulos, *Computational Mechanics Publications*, September, 600 p

Peyrat, S., and K. B. Olsen (2004). Nonlinear dynamic rupture inversion of the 2000 western Tottori, Japan, earthquake, *Geophys. Res. Lett.* **31**, 1–4.

Pitarka, A. (1999). 3D elastic finite-difference modeling of seismic motion using staggered grids with nonuniform spacing, *Bull. Seism. Soc. Am.* **89**, 54–68.

Pitarka, A., and K. Irikura (1996a). Modeling 3D surface topography by a finite-difference method: Kobe–JMA station site, Japan, case study, *Geophys. Res. Lett.* **23**, 2729–2732.

Pitarka, A., and K. Irikura (1996b). Basin structure effects on long period strong motions in the San Fernando valley and the Los Angeles basin from the 1994 Northridge earthquake and aftershocks, *Bull. Seism. Soc. Am.* **86**, no. 18, S126–S137.

Pitarka, A., R. Graves, and P. Somerville (2004). Validation of a 3D velocity model of the Puget Sound region based on modeling ground motion from the 28 February 2001 Nisqually earthquake, *Bull. Seism. Soc. Am.* **94**, 1670–1689.

Ponce, D. A., R. W. Simpson, R. W. Graymer, and R. C. Jachens (2004). Gravity, magnetic, and high-precision relocated seismicity profiles suggest a connection between the Hayward and Calaveras faults, northern California, *Geochem. Geophys. Geosystems* (G3) 5, Q07004, doi10.1029/2003GC000684.

Randall, G. E. (1989). Efficient calculation of differential seismograms for lithospheric receiver functions, *Geophys. J. Int.* **99**, 469–481.

Richter, G. R. (1994). An explicit finite element method for the wave equation, *Appl. Num. Math.* **16**, 65-80.

Robertsson, J. O. A. (1996). A numerical free-surface condition for elastic/viscoelastic finite-difference modeling in the presence of topography, *Geophysics* **61**, 1921–1934.

Savage, J. C. (1966). Radiation from a realistic model of faulting, *Bull. Seism. Soc. Am.* **56**, 577-592.

Scholz, C. H. (1990). *The Mechanics of Earthquakes and Faulting*, Cambridge U Press, New York.

Tessmer, E., D. Kosloff, and A. Behle (1992). Elastic wave propagation simulation in the presence of surface topography, *Geophys. J. Int.* **108**, 621–632.

Toshinawa, T. and T. Ohmachi (1992). Love wave propagation in a three-dimensional sedimentary basin, *Bull. Seism. Soc. Am.* **82**, 1661-1677.

Trifunac, M. D. (1974). A three-dimensional dislocation model for the San Fernando, California, earthquake of February 9, 1971, *Bull. Seism. Soc. Am.* **64**, 149-172.

Trifunac, M. D. (2003). Nonlinear soil response as a natural passive isolation mechanism. Paper II. The 1933, Long Beach, California earthquake, *Soil Dyn. Earthq. Eng.* **23**, 549–562.

Trifunac, M. D. (2008). 75th Anniversary of strong motion observation — a historical review, *Soil Dyn. Earthq. Eng.* **29**, no. 4, doi 10.1016/j.soildyn.2008.05.011, 591–606.

Tsai, Y. B. and H. J. Patton (1972). Near field small earthquakes – dislocation motion, Semi-Annual Report 1, Texas Instr. Inc. (prep. for Air Force Off. Sci. Res., Contract F44620-72-C-0073).

Tsai, Yi-Ben and Patton, J. H. (1973). Interpretation of the strong-motion earthquake accelerograms using a moving dislocation model: II, The Parkfield, California earthquake of June 28, 1966, (Abstract), presented at the 68th Annual National Meeting of the Seismological Society of America.

Virieux, J. (1984). SH-wave propagation in heterogeneous media: velocity-stress finite-difference method, *Geophysics* **49**, 1933-1942.

Virieux, J. (1986). P-SV wave propagation in heterogeneous media: velocity-stress finite-difference method, *Geophysics* **51**, 889-901.

Waldhauser, F., and W. L. Ellsworth (2002). Fault structure and mechanics of the Hayward Fault, California, from double-difference earthquake locations, *J. Geophys. Res.* **107**.

Ward, S. N. and G. Valensise (1989). Fault parameters and slip distribution of the 1915, Avezzano, Italy earthquake derived from geodetic observations, *Bull. Seism. Soc. Am.* **79**, 690-710.

Wiggins, R. A., J. Sweet, and G. A. Frazier (1977). The Parkfield earthquake of 1966 – a study of the dislocation parameters based on a complete modeling of elastic wave propagation (abstract), EOS, *Trans. Am. Geophys. Union* **58**, 1193.

Williams, R. A., R. W. Simpson, R. C. Jachens, W. J. Stephenson, J. K. Odum, and D. A. Ponce (2005). Seismic reflection evidence for a northeast-dipping Hayward fault near Fremont, California: Implications for seismic hazard, *Geophys. Res. Lett.* **32**, L13301, doi10.1029/2005GL023113.

Yang, D. H., J. W. Teng, Z. J. Zhang, and E. Liu (2003). A nearly-analytic discrete method for acoustic and elastic wave equations in anisotropic media, *Bull. Seism. Soc. Am.* **93**, 882–890.

Appendix

A1. Observed waveforms

Here presented observed seismograms from three channels of 6 near-field broad-band stations, filtered (<1.4 Hz), decimated and cut up to 15 seconds from first arrival (plus 2 seconds before). These seismograms were used as reference signals and synthetic seismograms were calculated for sites of their location. Observed waveforms that were used in this work are presented for each of six seismic stations on the figures from A1-1 to A1-6
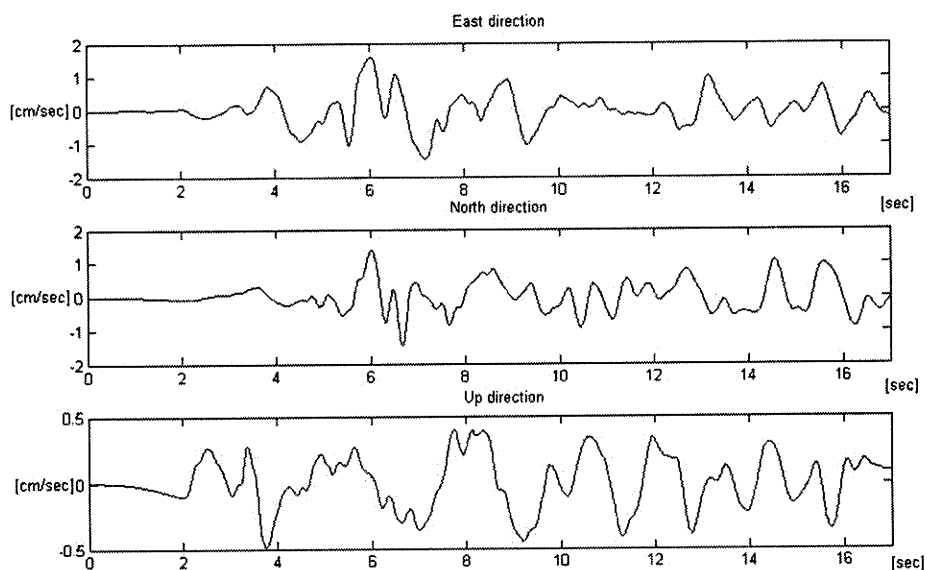
Fig. A1-1. Observed waveforms from the broad-band near-field seismic station 57950
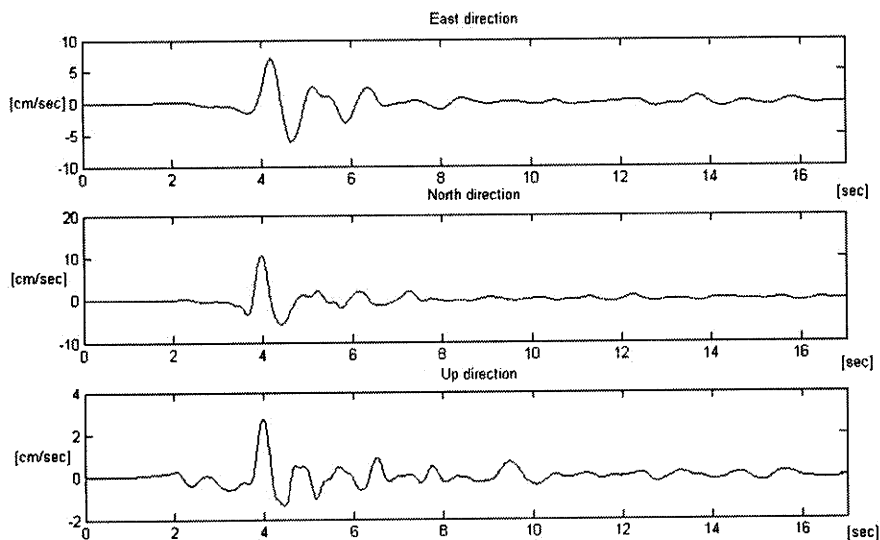
Fig. A1-2. Observed waveforms from the broad-band near-field seismic station CHR

70
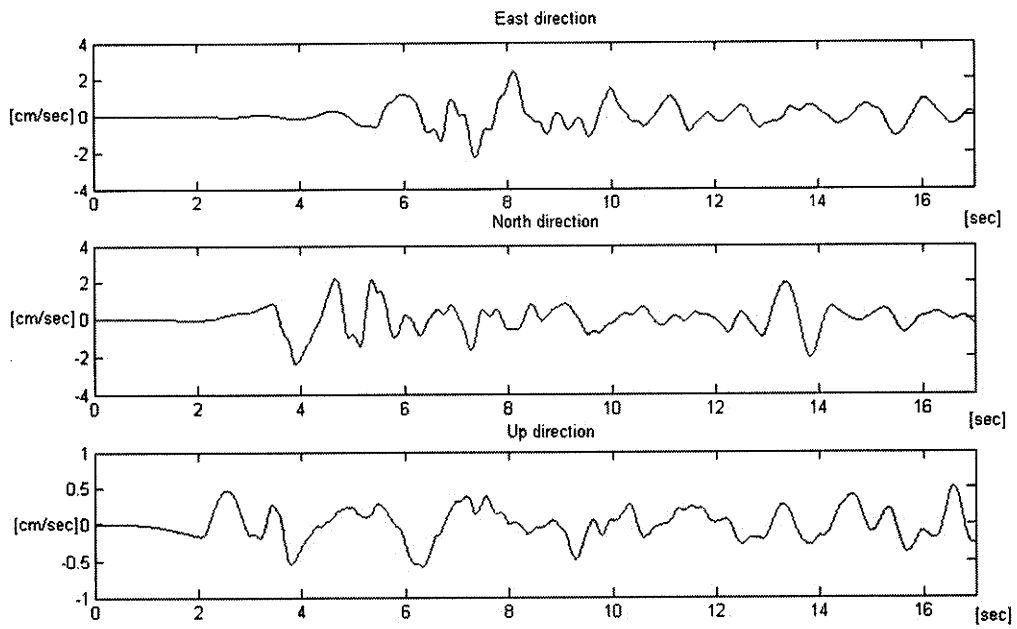
Fig. A1-3. Observed waveforms from the broad-band near-field seismic station MP3
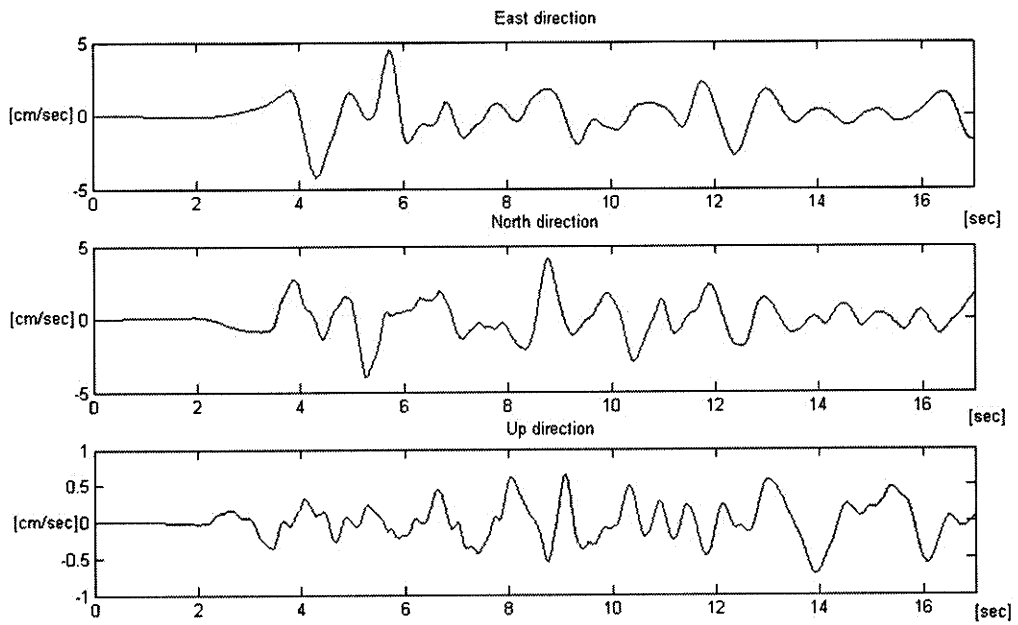
Fig. A1-4. Observed waveforms from the broad-band near-field seismic station Q32
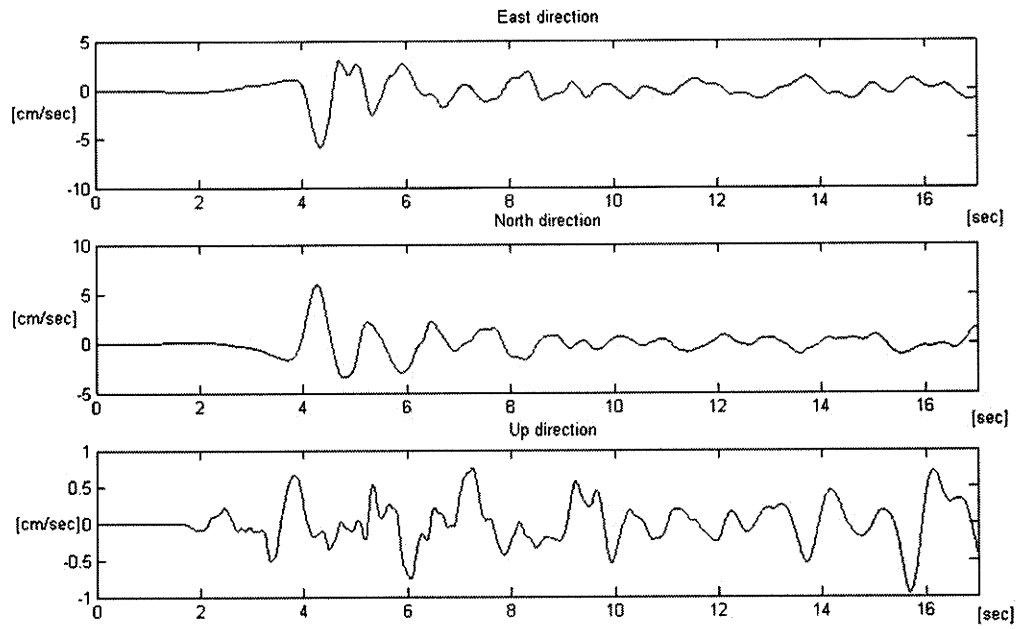
Fig. A1-5. Observed waveforms from the broad-band near-field seismic station ROC
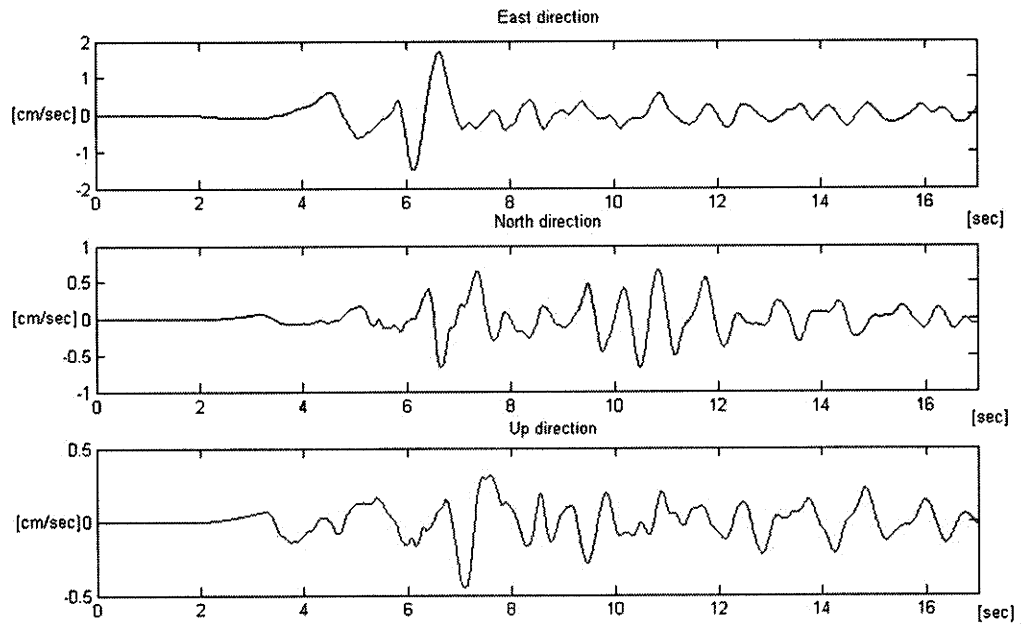
Fig. A1-6. Observed waveforms from the broad-band near-field seismic station 1684

A2. E3D input files

a. Input file of the original model

#Original model   //name of the input file

grid   z=25 x=80 y=60 dh=0.15 active=0 //grid parameters

time dt=0.005 t=4000 //time settings

block   p=2.40 s=1.10 r=2.30 z2=0.2   //description of the blocks of velocity model

block   p=3.00 s=1.40 r=2.45 z1=0.2 z2=0.5

block   p=3.60 s=1.95 r=2.50 z1=0.5 z2=1.

block   p=4.20 s=2.30 r=2.55 z1=1. z2=1.5

block   p=4.80 s=2.80 r=2.60 z1=1.5 z2=2.5

block   p=5.25 s=3.00 r=2.62 z1=2.5 z2=3.

block   p=5.60 s=3.25 r=2.65 z1=3. z2=5.

block   p=5.90 s=3.41 r=2.70 z1=5. z2=7.

block   p=6.15 s=3.55 r=2.75 z1=7. z2=9.

block   p=6.35 s=3.62 r=2.85 z1=9. z2=17.

block   p=7.00 s=4.10 r=3.00 z1=17. z2=25.

source   type=7 x=39.10 y=31.20 depth=8. strike=323 dip=90 rake=180 length=1.5 width=1.5 d0=0.75 s0=0 amp=9.37E+19 v=3. file=stf.sac t0=0.52   //description of finite fault source as sequence of multiple sources

source   type=7 x=40. y=30. depth=8. strike=323 dip=90 rake=180 length=1.5 width=1.5 d0=1.2 s0=0 amp=2.47E+20 v=3. file=stf.sac t0=0

source   type=7 x=40.9 y=28.8 depth=8. strike=323 dip=90 rake=180 length=1.5 width=1.5 d0=0.75 s0=0 amp=2.02E+20 v=3. file=stf.sac t0=0.52

source   type=7 x=41.8 y=27.6 depth=8. strike=323 dip=90 rake=180 length=1.5 width=1.5 d0=0.75 s0=0 amp=0. v=3. file=stf.sac t0=1.01

source   type=7 x=42.7 y=26.4 depth=8. strike=323 dip=90 rake=180 length=1.5 width=1.5 d0=0.75 s0=0 amp=0. v=3. file=stf.sac t0=1.51

source   type=7 x=43.6 y=25.2 depth=8. strike=323 dip=90 rake=180 length=1.5 width=1.5 d0=0.75 s0=0 amp=0. v=3. file=stf.sac t0=2.01

source   type=7 x=39.10 y=31.20 depth=9.5 strike=323 dip=90 rake=180 length=1.5 width=1.5 d0=0.75 s0=0 amp=2.63E+20 v=3. file=stf.sac t0=0.61

source   type=7 x=40. y=30. depth=9.5 strike=323 dip=90 rake=180 length=1.5 width=1.5 d0=0.75 s0=0 amp=8.63E+21 v=3. file=stf.sac t0=0.35

source   type=7 x=40.9 y=28.8 depth=9.5 strike=323 dip=90 rake=180 length=1.5 width=1.5 d0=0.75 s0=0 amp=7.51E+20 v=3. file=stf.sac t0=0.61

source   type=7 x=41.8 y=27.6 depth=9.5 strike=323 dip=90 rake=180 length=1.5 width=1.5 d0=0.75 s0=0 amp=1.12E+20 v=3. file=stf.sac t0=1.06

source   type=7 x=42.7 y=26.4 depth=9.5 strike=323 dip=90 rake=180 length=1.5 width=1.5 d0=0.75 s0=0 amp=0. v=3. file=stf.sac t0=1.54

source   type=7 x=43.6 y=25.2 depth=9.5 strike=323 dip=90 rake=180 length=1.5 width=1.5 d0=0.75 s0=0 amp=0. v=3. file=stf.sac t0=2.03

source   type=7 x=39.10 y=31.20 depth=11. strike=323 dip=90 rake=180 length=1.5 width=1.5 d0=0.75 s0=0 amp=1.12E+20 v=3. file=stf.sac t0=0.99

source   type=7 x=40. y=30. depth=11. strike=323 dip=90 rake=180 length=1.5 width=1.5 d0=0.75 s0=0 amp=9.00E+20 v=3. file=stf.sac t0=0.85

source   type=7 x=40.9 y=28.8 depth=11. strike=323 dip=90 rake=180 length=1.5 width=1.5 d0=0.75 s0=0 amp=1.27E+21 v=3. file=stf.sac t0=0.99

source   type=7 x=41.8 y=27.6 depth=11. strike=323 dip=90 rake=180 length=1.5 width=1.5 d0=0.75 s0=0 amp=8.63E+20 v=3. file=stf.sac t0=1.31

source   type=7 x=42.7 y=26.4 depth=11. strike=323 dip=90 rake=180 length=1.5 width=1.5 d0=0.75 s0=0 amp=4.51E+20 v=3. file=stf.sac t0=1.72

source   type=7 x=43.6 y=25.2 depth=11. strike=323 dip=90 rake=180 length=1.5 width=1.5 d0=0.75 s0=0 amp=4.17E+20 v=3. file=stf.sac t0=2.17

source   type=7 x=39.10 y=31.20 depth=12.5 strike=323 dip=90 rake=180 length=1.5 width=1.5 d0=0.75 s0=0 amp=3.00E+20 v=3. file=stf.sac t0=1.44

source   type=7 x=40. y=30. depth=12.5 strike=323 dip=90 rake=180 length=1.5 width=1.5 d0=0.75 s0=0 amp=6.75E+20 v=3. file=stf.sac t0=1.35

source   type=7 x=40.9 y=28.8 depth=12.5 strike=323 dip=90 rake=180 length=1.5 width=1.5 d0=0.75 s0=0 amp=7.51E+20 v=3. file=stf.sac t0=1.44

source   type=7 x=41.8 y=27.6 depth=12.5 strike=323 dip=90 rake=180 length=1.5 width=1.5 d0=0.75 s0=0 amp=7.12E+20 v=3. file=stf.sac t0=1.68

source   type=7 x=42.7 y=26.4 depth=12.5 strike=323 dip=90 rake=180 length=1.5 width=1.5 d0=0.75 s0=0 amp=6.30E+20 v=3. file=stf.sac t0=2.02

source   type=7 x=43.6 y=25.2 depth=12.5 strike=323 dip=90 rake=180 length=1.5 width=1.5 d0=0.75 s0=0 amp=5.63E+20 v=3. file=stf.sac t0=2.4

sac x=23.65 z=0. y=34.34 file="sac.fremont" //description of output parameters

sac x=32.66 z=0. y=25.00 file="sac.sanjoseres"

sac x=30.00 z=0. y=23.33 file="sac.sanjoseap"

sac x=27.66 z=0. y=28.44 file="sac.milpitas"

sac x=34.44 z=0. y=39.45 file="sac.sunol"

sac x=41.22 z=0. y=23.66 file="sac.mthamilton"

parallel nx=2 ny=2 nz=4   //parallelization of calculations

b. Input files of the models with modified dip angle

#Dip NE 80

grid z=25 x=80 y=60 dh=0.15 active=0

time dt=0.005 t=4000

block   p=2.40 s=1.10 r=2.30 z2=0.2
block   p=3.00 s=1.40 r=2.45 z1=0.2 z2=0.5
block   p=3.60 s=1.95 r=2.50 z1=0.5 z2=1.
block   p=4.20 s=2.30 r=2.55 z1=1. z2=1.5
block   p=4.80 s=2.80 r=2.60 z1=1.5 z2=2.5
block   p=5.25 s=3.00 r=2.62 z1=2.5 z2=3.
block   p=5.60 s=3.25 r=2.65 z1=3. z2=5.
block   p=5.90 s=3.41 r=2.70 z1=5. z2=7.
block   p=6.15 s=3.55 r=2.75 z1=7. z2=9.
block   p=6.35 s=3.62 r=2.85 z1=9. z2=17.
block   p=7.00 s=4.10 r=3.00 z1=17. z2=25.

source   type=7 x=39.10 y=31.20 depth=8. strike=323 dip=80 rake=180 length=1.5 width=1.5 d0=0.75 s0=0 amp=9.51E+19 v=3. file=stf.sac t0=0.52

source   type=7 x=40. y=30. depth=8. strike=323 dip=80 rake=180 length=1.5 width=1.5 d0=1.2 s0=0 amp=2.51E+20 v=3. file=stf.sac t0=0

source   type=7 x=40.9 y=28.8 depth=8. strike=323 dip=80 rake=180 length=1.5 width=1.5 d0=0.75 s0=0 amp=2.05E+20 v=3. file=stf.sac t0=0.52

source   type=7 x=41.8 y=27.6 depth=8. strike=323 dip=80 rake=180 length=1.5 width=1.5 d0=0.75 s0=0 amp=0. v=3. file=stf.sac t0=1.01

source   type=7 x=42.7 y=26.4 depth=8. strike=323 dip=80 rake=180 length=1.5 width=1.5 d0=0.75 s0=0 amp=0. v=3. file=stf.sac t0=1.51

source   type=7 x=43.6 y=25.2 depth=8. strike=323 dip=80 rake=180 length=1.5 width=1.5 d0=0.75 s0=0 amp=0. v=3. file=stf.sac t0=2.01

source   type=7 x=39.3084 y=31.3563 depth=9.4772 strike=323 dip=80 rake=180 length=1.5 width=1.5 d0=0.75 s0=0 amp=2.66E+20 v=3. file=stf.sac t0=0.61

source   type=7 x=40.2084 y=30.1563 depth=9.4772 strike=323 dip=80 rake=180 length=1.5 width=1.5 d0=0.75 s0=0 amp=8.75E+21 v=3. file=stf.sac t0=0.35

source   type=7 x=41.1084 y=28.9563 depth=9.4772 strike=323 dip=80 rake=180 length=1.5 width=1.5 d0=0.75 s0=0 amp=7.61E+20 v=3. file=stf.sac t0=0.61

source   type=7 x=42.0084 y=27.7563 depth=9.4772 strike=323 dip=80 rake=180 length=1.5 width=1.5 d0=0.75 s0=0 amp=1.14E+20 v=3. file=stf.sac t0=1.06

source   type=7 x=42.9084 y=26.5563 depth=9.4772 strike=323 dip=80 rake=180 length=1.5 width=1.5 d0=0.75 s0=0 amp=0. v=3. file=stf.sac t0=1.54

source   type=7 x=43.8084 y=25.3563 depth=9.4772 strike=323 dip=80 rake=180 length=1.5 width=1.5 d0=0.75 s0=0 amp=0. v=3. file=stf.sac t0=2.03

source   type=7 x=39.5168 y=31.5126 depth=10.9544 strike=323 dip=80 rake=180 length=1.5 width=1.5 d0=0.75 s0=0 amp=1.14E+20 v=3. file=stf.sac t0=0.99

source   type=7 x=40.4168 y=30.3126 depth=10.9544 strike=323 dip=80 rake=180 length=1.5 width=1.5 d0=0.75 s0=0 amp=9.13E+20 v=3. file=stf.sac t0=0.85

source   type=7 x=41.3168 y=29.1126 depth=10.9544 strike=323 dip=80 rake=180 length=1.5 width=1.5 d0=0.75 s0=0 amp=1.29E+21 v=3. file=stf.sac t0=0.99

source   type=7 x=42.2168 y=27.9126 depth=10.9544 strike=323 dip=80 rake=180 length=1.5 width=1.5 d0=0.75 s0=0 amp=8.75E+20 v=3. file=stf.sac t0=1.31

source   type=7 x=43.1168 y=26.7126 depth=10.9544 strike=323 dip=80 rake=180 length=1.5 width=1.5 d0=0.75 s0=0 amp=4.57E+20 v=3. file=stf.sac t0=1.72

source   type=7 x=44.0168 y=25.5126 depth=10.9544 strike=323 dip=80 rake=180 length=1.5 width=1.5 d0=0.75 s0=0 amp=4.23E+20 v=3. file=stf.sac t0=2.17

source   type=7 x=39.7251 y=31.6689 depth=12.4316 strike=323 dip=80 rake=180 length=1.5 width=1.5 d0=0.75 s0=0 amp=3.04E+20 v=3. file=stf.sac t0=1.44

source   type=7 x=40.6251 y=30.4689 depth=12.4316 strike=323 dip=80 rake=180 length=1.5 width=1.5 d0=0.75 s0=0 amp=6.84E+20 v=3. file=stf.sac t0=1.35

source   type=7 x=41.5251 y=29.2689 depth=12.4316 strike=323 dip=80 rake=180 length=1.5 width=1.5 d0=0.75 s0=0 amp=7.61E+20 v=3. file=stf.sac t0=1.44

source   type=7 x=42.4251 y=28.0689 depth=12.4316 strike=323 dip=80 rake=180 length=1.5 width=1.5 d0=0.75 s0=0 amp=7.22E+20 v=3. file=stf.sac t0=1.68

source   type=7 x=43.3251 y=26.4689 depth=12.4316 strike=323 dip=80 rake=180 length=1.5 width=1.5 d0=0.75 s0=0 amp=6.39E+20 v=3. file=stf.sac t0=2.02

source   type=7 x=44.2251 y=25.6689 depth=12.4316 strike=323 dip=80 rake=180 length=1.5 width=1.5 d0=0.75 s0=0 amp=5.71E+20 v=3. file=stf.sac t0=2.4

sac x=23.65 z=0. y=34.34 file="sac.fremont"
sac x=32.66 z=0. y=25.00 file="sac.sanjoseres"
sac x=30.00 z=0. y=23.33 file="sac.sanjoseap"
sac x=27.66 z=0. y=28.44 file="sac.milpitas"
sac x=34.44 z=0. y=39.45 file="sac.sunol"
sac x=41.22 z=0. y=23.66 file="sac.mthamilton"

parallel nx=2 ny=2 nz=4

#Dip SW 80

grid   z=25 x=80 y=60 dh=0.15 active=0

time dt=0.005 t=4000

block   p=2.40 s=1.10 r=2.30 z2=0.2

block p=3.00 s=1.40 r=2.45 z1=0.2 z2=0.5

block p=3.60 s=1.95 r=2.50 z1=0.5 z2=1.

block p=4.20 s=2.30 r=2.55 z1=1. z2=1.5

block p=4.80 s=2.80 r=2.60 z1=1.5 z2=2.5

block p=5.25 s=3.00 r=2.62 z1=2.5 z2=3.

block p=5.60 s=3.25 r=2.65 z1=3. z2=5.

block p=5.90 s=3.41 r=2.70 z1=5. z2=7.

block p=6.15 s=3.55 r=2.75 z1=7. z2=9.

block p=6.35 s=3.62 r=2.85 z1=9. z2=17.

block p=7.00 s=4.10 r=3.00 z1=17. z2=25.

source   type=7 x=39.10 y=31.20 depth=8. strike=143 dip=80 rake=0 length=1.5 width=1.5 d0=0.75 s0=0 amp=9.51E+19 v=3. file=stf.sac t0=0.52

source   type=7 x=40. y=30. depth=8. strike=143 dip=80 rake=0 length=1.5 width=1.5 d0=1.2 s0=0 amp=2.51E+20 v=3. file=stf.sac t0=0

source   type=7 x=40.9 y=28.8 depth=8. strike=143 dip=80 rake=0 length=1.5 width=1.5 d0=0.75 s0=0 amp=2.05E+20 v=3. file=stf.sac t0=0.52

source   type=7 x=41.8 y=27.6 depth=8. strike=143 dip=80 rake=0 length=1.5 width=1.5 d0=0.75 s0=0 amp=0. v=3. file=stf.sac t0=1.01

source   type=7 x=42.7 y=26.4 depth=8. strike=143 dip=80 rake=0 length=1.5 width=1.5 d0=0.75 s0=0 amp=0. v=3. file=stf.sac t0=1.51

source   type=7 x=43.6 y=25.2 depth=8. strike=143 dip=80 rake=0 length=1.5 width=1.5 d0=0.75 s0=0 amp=0. v=3. file=stf.sac t0=2.01

source   type=7 x=38.8916 y=31.0437 depth=9.4772 strike=143 dip=80 rake=0 length=1.5 width=1.5 d0=0.75 s0=0 amp=2.66E+20 v=3. file=stf.sac t0=0.61

source   type=7 x=39.7916 y=29.8437 depth=9.4772 strike=143 dip=80 rake=0 length=1.5 width=1.5 d0=0.75 s0=0 amp=8.75E+21 v=3. file=stf.sac t0=0.35

source   type=7 x=40.6916 y=28.6437 depth=9.4772 strike=143 dip=80 rake=0 length=1.5 width=1.5 d0=0.75 s0=0 amp=7.61E+20 v=3. file=stf.sac t0=0.61

source   type=7 x=41.5916 y=27.4437 depth=9.4772 strike=143 dip=80 rake=0 length=1.5 width=1.5 d0=0.75 s0=0 amp=1.14E+20 v=3. file=stf.sac t0=1.06

source   type=7 x=42.4916 y=26.2437 depth=9.4772 strike=143 dip=80 rake=0 length=1.5 width=1.5 d0=0.75 s0=0 amp=0. v=3. file=stf.sac t0=1.54

source   type=7 x=43.3916 y=25.0437 depth=9.4772 strike=143 dip=80 rake=0 length=1.5 width=1.5 d0=0.75 s0=0 amp=0. v=3. file=stf.sac t0=2.03

source   type=7 x=38.6832 y=30.8874 depth=10.9544 strike=143 dip=80 rake=0 length=1.5 width=1.5 d0=0.75 s0=0 amp=1.14E+20 v=3. file=stf.sac t0=0.99

source   type=7 x=39.5832 y=29.6874 depth=10.9544 strike=143 dip=80 rake=0 length=1.5 width=1.5 d0=0.75 s0=0 amp=9.13E+20 v=3. file=stf.sac t0=0.85

source   type=7 x=40.4832 y=28.4874 depth=10.9544 strike=143 dip=80 rake=0 length=1.5 width=1.5 d0=0.75 s0=0 amp=1.29E+21 v=3. file=stf.sac t0=0.99

source   type=7 x=41.3832 y=27.2874 depth=10.9544 strike=143 dip=80 rake=0 length=1.5 width=1.5 d0=0.75 s0=0 amp=8.75E+20 v=3. file=stf.sac t0=1.31

source   type=7 x=42.2832 y=26.0874 depth=10.9544 strike=143 dip=80 rake=0 length=1.5 width=1.5 d0=0.75 s0=0 amp=4.57E+20 v=3. file=stf.sac t0=1.72

source   type=7 x=43.1832 y=24.8874 depth=10.9544 strike=143 dip=80 rake=0 length=1.5 width=1.5 d0=0.75 s0=0 amp=4.23E+20 v=3. file=stf.sac t0=2.17

source   type=7 x=38.4749 y=30.7311 depth=12.4316 strike=143 dip=80 rake=0 length=1.5 width=1.5 d0=0.75 s0=0 amp=3.04E+20 v=3. file=stf.sac t0=1.44

source   type=7 x=39.9749 y=29.5311 depth=12.4316 strike=143 dip=80 rake=0 length=1.5 width=1.5 d0=0.75 s0=0 amp=6.84E+20 v=3. file=stf.sac t0=1.35

source   type=7 x=40.2749 y=28.3311 depth=12.4316 strike=143 dip=80 rake=0 length=1.5 width=1.5 d0=0.75 s0=0 amp=7.61E+20 v=3. file=stf.sac t0=1.44

source   type=7 x=41.1749 y=27.1311 depth=12.4316 strike=143 dip=80 rake=0 length=1.5 width=1.5 d0=0.75 s0=0 amp=7.22E+20 v=3. file=stf.sac t0=1.68

source   type=7 x=42.0749 y=25.9311 depth=12.4316 strike=143 dip=80 rake=0 length=1.5 width=1.5 d0=0.75 s0=0 amp=6.39E+20 v=3. file=stf.sac t0=2.02

source   type=7 x=42.9749 y=24.7311 depth=12.4316 strike=143 dip=80 rake=0 length=1.5 width=1.5 d0=0.75 s0=0 amp=5.71E+20 v=3. file=stf.sac t0=2.4

sac x=23.65 z=0. y=34.34 file="sac.fremont"
sac x=32.66 z=0. y=25.00 file="sac.sanjoseres"
sac x=30.00 z=0. y=23.33 file="sac.sanjoseap"
sac x=27.66 z=0. y=28.44 file="sac.milpitas"
sac x=34.44 z=0. y=39.45 file="sac.sunol"
sac x=41.22 z=0. y=23.66 file="sac.mthamilton"

parallel nx=2 ny=2 nz=4

c. Input files of the models with modified strike angle

#Strike 308^0

grid   z=25 x=80 y=60 dh=0.15 active=0

time dt=0.005 t=4000

block   p=2.40 s=1.10 r=2.30 z2=0.2
block   p=3.00 s=1.40 r=2.45 z1=0.2 z2=0.5
block   p=3.60 s=1.95 r=2.50 z1=0.5 z2=1.
block   p=4.20 s=2.30 r=2.55 z1=1. z2=1.5
block   p=4.80 s=2.80 r=2.60 z1=1.5 z2=2.5
block   p=5.25 s=3.00 r=2.62 z1=2.5 z2=3.
block   p=5.60 s=3.25 r=2.65 z1=3. z2=5.
block   p=5.90 s=3.41 r=2.70 z1=5. z2=7.
block   p=6.15 s=3.55 r=2.75 z1=7. z2=9.
block   p=6.35 s=3.62 r=2.85 z1=9. z2=17.
block   p=7.00 s=4.10 r=3.00 z1=17. z2=25.

source   type=7 x=38.82 y=30.93 depth=8. strike=308 dip=90 rake=180 length=1.5 width=1.5 d0=0.75
s0=0 amp=9.51E+19 v=3. file=stf.sac t0=0.52
source   type=7 x=40. y=30. depth=8. strike=308 dip=90 rake=180 length=1.5 width=1.5 d0=1.2 s0=0
amp=2.51E+20 v=3. file=stf.sac t0=0
source   type=7 x=41.18 y=29.07 depth=8. strike=308 dip=90 rake=180 length=1.5 width=1.5 d0=0.75
s0=0 amp=2.05E+20 v=3. file=stf.sac t0=0.52
source   type=7 x=42.36 y=28.15 depth=8. strike=308 dip=90 rake=180 length=1.5 width=1.5 d0=0.75
s0=0 amp=0. v=3. file=stf.sac t0=1.01
source   type=7 x=43.54 y=27.22 depth=8. strike=308 dip=90 rake=180 length=1.5 width=1.5 d0=0.75
s0=0 amp=0. v=3. file=stf.sac t0=1.51
source   type=7 x=44.72 y=26.30 depth=8. strike=308 dip=90 rake=180 length=1.5 width=1.5 d0=0.75
s0=0 amp=0. v=3. file=stf.sac t0=2.01
source   type=7 x=38.82 y=30.93 depth=9.5 strike=308 dip=90 rake=180 length=1.5 width=1.5 d0=0.75
s0=0 amp=2.67E+20 v=3. file=stf.sac t0=0.61
source   type=7 x=40. y=30. depth=9.5 strike=308 dip=90 rake=180 length=1.5 width=1.5 d0=0.75 s0=0
amp=8.76E+20 v=3. file=stf.sac t0=0.35
source   type=7 x=41.18 y=29.07 depth=9.5 strike=308 dip=90 rake=180 length=1.5 width=1.5 d0=0.75
s0=0 amp=7.62E+20 v=3. file=stf.sac t0=0.61
source   type=7 x=42.36 y=28.15 depth=9.5 strike=308 dip=90 rake=180 length=1.5 width=1.5 d0=0.75
s0=0 amp=1.14E+20 v=3. file=stf.sac t0=1.06
source   type=7 x=43.54 y=27.22 depth=9.5 strike=308 dip=90 rake=180 length=1.5 width=1.5 d0=0.75
s0=0 amp=0. v=3. file=stf.sac t0=1.54
source   type=7 x=44.72 y=26.30 depth=9.5 strike=308 dip=90 rake=180 length=1.5 width=1.5 d0=0.75
s0=0 amp=0. v=3. file=stf.sac t0=2.03

source   type=7 x=38.82 y=30.93 depth=11. strike=308 dip=90 rake=180 length=1.5 width=1.5 d0=0.75 s0=0 amp=1.14E+20 v=3. file=stf.sac t0=0.99

source   type=7 x=40. y=30. depth=11. strike=308 dip=90 rake=180 length=1.5 width=1.5 d0=0.75 s0=0 amp=9.14E+21 v=3. file=stf.sac t0=0.85

source   type=7 x=41.18 y=29.07 depth=11. strike=308 dip=90 rake=180 length=1.5 width=1.5 d0=0.75 s0=0 amp=1.29E+21 v=3. file=stf.sac t0=0.99

source   type=7 x=42.36 y=28.15 depth=11. strike=308 dip=90 rake=180 length=1.5 width=1.5 d0=0.75 s0=0 amp=8.76E+21 v=3. file=stf.sac t0=1.31

source   type=7 x=43.54 y=27.22 depth=11. strike=308 dip=90 rake=180 length=1.5 width=1.5 d0=0.75 s0=0 amp=4.57E+20 v=3. file=stf.sac t0=1.72

source   type=7 x=44.72 y=26.30 depth=11. strike=308 dip=90 rake=180 length=1.5 width=1.5 d0=0.75 s0=0 amp=4.23E+20 v=3. file=stf.sac t0=2.17

source   type=7 x=38.82 y=30.93 depth=12.5 strike=308 dip=90 rake=180 length=1.5 width=1.5 d0=0.75 s0=0 amp=3.05E+20 v=3. file=stf.sac t0=1.44

source   type=7 x=40. y=30. depth=12.5 strike=308 dip=90 rake=180 length=1.5 width=1.5 d0=0.75 s0=0 amp=6.85E+20 v=3. file=stf.sac t0=1.35

source·   type=7 x=41.18 y=29.07 depth=12.5 strike=308 dip=90 rake=180 length=1.5 width=1.5 d0=0.75 s0=0 amp=7.62E+20 v=3. file=stf.sac t0=1.44

source   type=7 x=42.36 y=28.15 depth=12.5 strike=308 dip=90 rake=180 length=1.5 width=1.5 d0=0.75 s0=0 amp=7.23E+20 v=3. file=stf.sac t0=1.68

source   type=7 x=43.54 y=27.22 depth=12.5 strike=308 dip=90 rake=180 length=1.5 width=1.5 d0=0.75 s0=0 amp=6.40E+20 v=3. file=stf.sac t0=2.02

source   type=7 x=44.72 y=26.30 depth=12.5 strike=308 dip=90 rake=180 length=1.5 width=1.5 d0=0.75 s0=0 amp=5.71E+20 v=3. file=stf.sac t0=2.4

sac x=23.65 z=0. y=34.34 file="sac.fremont"

sac x=32.66 z=0. y=25.00 file="sac.sanjoseres"

sac x=30.00 z=0. y=23.33 file="sac.sanjoseap"

sac x=27.66 z=0. y=28.44 file="sac.milpitas"

sac x=34.44 z=0. y=39.45 file="sac.sunol"

sac x=41.22 z=0. y=23.66 file="sac.mthamilton"

parallel nx=2 ny=2 nz=4

#Strike 338[0]

grid   z=25 x=80 y=60 dh=0.15 active=0

time dt=0.005 t=4000

block   p=2.40 s=1.10 r=2.30 z2=0.2

block   p=3.00 s=1.40 r=2.45 z1=0.2 z2=0.5

block   p=3.60 s=1.95 r=2.50 z1=0.5 z2=1.

block p=4.20 s=2.30 r=2.55 z1=1. z2=1.5

block p=4.80 s=2.80 r=2.60 z1=1.5 z2=2.5

block p=5.25 s=3.00 r=2.62 z1=2.5 z2=3.

block p=5.60 s=3.25 r=2.65 z1=3. z2=5.

block p=5.90 s=3.41 r=2.70 z1=5. z2=7.

block p=6.15 s=3.55 r=2.75 z1=7. z2=9.

block p=6.35 s=3.62 r=2.85 z1=9. z2=17.

block p=7.00 s=4.10 r=3.00 z1=17. z2=25.

source   type=7 x=39.44 y=31.39 depth=8. strike=338 dip=90 rake=180 length=1.5 width=1.5 d0=0.75
s0=0 amp=8.22E+19 v=3. file=stf.sac t0=0.52

source   type=7 x=40. y=30. depth=8. strike=338 dip=90 rake=180 length=1.5 width=1.5 d0=1.2 s0=0
amp=2.17E+20 v=3. file=stf.sac t0=0

source   type=7 x=40.56 y=28.61 depth=8. strike=338 dip=90 rake=180 length=1.5 width=1.5 d0=0.75
s0=0 amp=1.77E+20 v=3. file=stf.sac t0=0.52

source   type=7 x=41.12 y=27.22 depth=8. strike=338 dip=90 rake=180 length=1.5 width=1.5 d0=0.75
s0=0 amp=0. v=3. file=stf.sac t0=1.01

source   type=7 x=41.68 y=25.82 depth=8. strike=338 dip=90 rake=180 length=1.5 width=1.5 d0=0.75
s0=0 amp=0. v=3. file=stf.sac t0=1.51

source   type=7 x=42.24 y=24.43 depth=8. strike=338 dip=90 rake=180 length=1.5 width=1.5 d0=0.75
s0=0 amp=0. v=3. file=stf.sac t0=2.01

source   type=7 x=39.44 y=31.39 depth=9.5 strike=338 dip=90 rake=180 length=1.5 width=1.5 d0=0.75
s0=0 amp=2.30E+20 v=3. file=stf.sac t0=0.61

source   type=7 x=40. y=30. depth=9.5 strike=338 dip=90 rake=180 length=1.5 width=1.5 d0=0.75 s0=0
amp=7.56E+20 v=3. file=stf.sac t0=0.35

source   type=7 x=40.56 y=28.61 depth=9.5 strike=338 dip=90 rake=180 length=1.5 width=1.5 d0=0.75
s0=0 amp=6.58E+20 v=3. file=stf.sac t0=0.61

source   type=7 x=41.12 y=27.22 depth=9.5 strike=338 dip=90 rake=180 length=1.5 width=1.5 d0=0.75
s0=0 amp=9.83E+19 v=3. file=stf.sac t0=1.06

source   type=7 x=41.68 y=25.82 depth=9.5 strike=338 dip=90 rake=180 length=1.5 width=1.5 d0=0.75
s0=0 amp=0. v=3. file=stf.sac t0=1.54

source   type=7 x=42.24 y=24.43 depth=9.5 strike=338 dip=90 rake=180 length=1.5 width=1.5 d0=0.75
s0=0 amp=0. v=3. file=stf.sac t0=2.03

source   type=7 x=39.44 y=31.39 depth=11. strike=338 dip=90 rake=180 length=1.5 width=1.5 d0=0.75
s0=0 amp=9.83E+19 v=3. file=stf.sac t0=0.99

source   type=7 x=40. y=30. depth=11. strike=338 dip=90 rake=180 length=1.5 width=1.5 d0=0.75 s0=0
amp=7.89E+21 v=3. file=stf.sac t0=0.85

source   type=7 x=40.56 y=28.61 depth=11. strike=338 dip=90 rake=180 length=1.5 width=1.5 d0=0.75
s0=0 amp=1.12E+21 v=3. file=stf.sac t0=0.99

source   type=7 x=41.12 y=27.22 depth=11. strike=338 dip=90 rake=180 length=1.5 width=1.5 d0=0.75
s0=0 amp=7.56E+20 v=3. file=stf.sac t0=1.31

source   type=7 x=41.68 y=25.82 depth=11. strike=338 dip=90 rake=180 length=1.5 width=1.5 d0=0.75
s0=0 amp=3.95E+20 v=3. file=stf.sac t0=1.72

source   type=7 x=42.24 y=24.43 depth=11. strike=338 dip=90 rake=180 length=1.5 width=1.5 d0=0.75 s0=0 amp=3.66E+20 v=3. file=stf.sac t0=2.17

source   type=7 x=39.44 y=31.39 depth=12.5 strike=338 dip=90 rake=180 length=1.5 width=1.5 d0=0.75 s0=0 amp=2.63E+20 v=3. file=stf.sac t0=1.44

source   type=7 x=40. y=30. depth=12.5 strike=338 dip=90 rake=180 length=1.5 width=1.5 d0=0.75 s0=0 amp=5.91E+20 v=3. file=stf.sac t0=1.35

source   type=7 x=40.56 y=28.61 depth=12.5 strike=338 dip=90 rake=180 length=1.5 width=1.5 d0=0.75 s0=0 amp=6.58E+20 v=3. file=stf.sac t0=1.44

source   type=7 x=41.12 y=27.22 depth=12.5 strike=338 dip=90 rake=180 length=1.5 width=1.5 d0=0.75 s0=0 amp=6.24E+20 v=3. file=stf.sac t0=1.68

source   type=7 x=41.68 y=25.82 depth=12.5 strike=338 dip=90 rake=180 length=1.5 width=1.5 d0=0.75 s0=0 amp=5.53E+20 v=3. file=stf.sac t0=2.02

source   type=7 x=42.24 y=24.43 depth=12.5 strike=338 dip=90 rake=180 length=1.5 width=1.5 d0=0.75 s0=0 amp=4.93E+20 v=3. file=stf.sac t0=2.4

sac x=23.65 z=0. y=34.34 file="sac.fremont"
sac x=32.66 z=0. y=25.00 file="sac.sanjoseres"
sac x=30.00 z=0. y=23.33 file="sac.sanjoseap"
sac x=27.66 z=0. y=28.44 file="sac.milpitas"
sac x=34.44 z=0. y=39.45 file="sac.sunol"
sac x=41.22 z=0. y=23.66 file="sac.mthamilton"

parallel nx=2 ny=2 nz=4

d. Input file of the model with modified fault plane length

#Length 13.5 km

grid   z=25 x=80 y=60 dh=0.15 active=0

time dt=0.005 t=4000

block   p=2.40 s=1.10 r=2.30 z2=0.2
block   p=3.00 s=1.40 r=2.45 z1=0.2 z2=0.5
block   p=3.60 s=1.95 r=2.50 z1=0.5 z2=1.
block   p=4.20 s=2.30 r=2.55 z1=1. z2=1.5
block   p=4.80 s=2.80 r=2.60 z1=1.5 z2=2.5
block   p=5.25 s=3.00 r=2.62 z1=2.5 z2=3.
block   p=5.60 s=3.25 r=2.65 z1=3. z2=5.
block   p=5.90 s=3.41 r=2.70 z1=5. z2=7.
block   p=6.15 s=3.55 r=2.75 z1=7. z2=9.
block   p=6.35 s=3.62 r=2.85 z1=9. z2=17.
block   p=7.00 s=4.10 r=3.00 z1=17. z2=25.

source   type=7 x=37.30 y=33.60 depth=8. strike=323 dip=90 rake=180 length=1.5 width=1.5 d0=0.75 s0=0 amp=0. v=3. file=stf.sac t0=1.5075
source   type=7 x=38.20 y=32.40 depth=8. strike=323 dip=90 rake=180 length=1.5 width=1.5 d0=0.75 s0=0 amp=0. v=3. file=stf.sac t0=1.0112
source   type=7 x=39.10 y=31.20 depth=8. strike=323 dip=90 rake=180 length=1.5 width=1.5 d0=0.75 s0=0 amp=8.53E+19 v=3. file=stf.sac t0=0.52
source   type=7 x=40. y=30. depth=8. strike=323 dip=90 rake=180 length=1.5 width=1.5 d0=1.2 s0=0 amp=2.25E+20 v=3. file=stf.sac t0=0
source   type=7 x=40.90 y=28.80 depth=8. strike=323 dip=90 rake=180 length=1.5 width=1.5 d0=0.75 s0=0 amp=1.84E+20 v=3. file=stf.sac t0=0.52
source   type=7 x=41.80 y=27.60 depth=8. strike=323 dip=90 rake=180 length=1.5 width=1.5 d0=0.75 s0=0 amp=0. v=3. file=stf.sac t0=1.0112
source   type=7 x=42.70 y=26.40 depth=8. strike=323 dip=90 rake=180 length=1.5 width=1.5 d0=0.75 s0=0 amp=0. v=3. file=stf.sac t0=1.5075
source   type=7 x=43.60 y=25.20 depth=8. strike=323 dip=90 rake=180 length=1.5 width=1.5 d0=0.75 s0=0 amp=0. v=3. file=stf.sac t0=2.0056
source   type=7 x=44.50 y=24.00 depth=8. strike=323 dip=90 rake=180 length=1.5 width=1.5 d0=0.75 s0=0 amp=0. v=3. file=stf.sac t0=2.5045
source   type=7 x=37.30 y=33.60 depth=9.5 strike=323 dip=90 rake=180 length=1.5 width=1.5 d0=0.75 s0=0 amp=0. v=3. file=stf.sac t0=1.5403
source   type=7 x=38.20 y=32.40 depth=9.5 strike=323 dip=90 rake=180 length=1.5 width=1.5 d0=0.75 s0=0 amp=0. v=3. file=stf.sac t0=1.0595
source   type=7 x=39.10 y=31.20 depth=9.5 strike=323 dip=90 rake=180 length=1.5 width=1.5 d0=0.75 s0=0 amp=2.39E+20 v=3. file=stf.sac t0=0.6103

source   type=7 x=40. y=30. depth=9.5 strike=323 dip=90 rake=180 length=1.5 width=1.5 d0=0.75 s0=0 amp=7.84E+20 v=3. file=stf.sac t0=0.35

source   type=7 x=40.90 y=28.80 depth=9.5 strike=323 dip=90 rake=180 length=1.5 width=1.5 d0=0.75 s0=0 amp=6.82E+20 v=3. file=stf.sac t0=0.6103

source   type=7 x=41.80 y=27.60 depth=9.5 strike=323 dip=90 rake=180 length=1.5 width=1.5 d0=0.75 s0=0 amp=1.02E+20 v=3. file=stf.sac t0=1.0595

source   type=7 x=42.70 y=26.40 depth=9.5 strike=323 dip=90 rake=180 length=1.5 width=1.5 d0=0.75 s0=0 amp=0. v=3. file=stf.sac t0=1.5403

source   type=7 x=43.60 y=25.20 depth=9.5 strike=323 dip=90 rake=180 length=1.5 width=1.5 d0=0.75 s0=0 amp=0. v=3. file=stf.sac t0=2.0304

source   type=7 x=44.50 y=24.00 depth=9.5 strike=323 dip=90 rake=180 length=1.5 width=1.5 d0=0.75 s0=0 amp=0. v=3. file=stf.sac t0=2.5244

source   type=7 x=37.30 y=33.60 depth=11. strike=323 dip=90 rake=180 length=1.5 width=1.5 d0=0.75 s0=0 amp=1.36E+20 v=3. file=stf.sac t0=1.7241

source   type=7 x=38.20 y=32.40 depth=11. strike=323 dip=90 rake=180 length=1.5 width=1.5 d0=0.75 s0=0 amp=0. v=3. file=stf.sac t0=1.3124

source   type=7 x=39.10 y=31.20 depth=11. strike=323 dip=90 rake=180 length=1.5 width=1.5 d0=0.75 s0=0 amp=1.02E+20 v=3. file=stf.sac t0=0.9862

source   type=7 x=40. y=30. depth=11. strike=323 dip=90 rake=180 length=1.5 width=1.5 d0=0.75 s0=0 amp=8.19E+20 v=3. file=stf.sac t0=0.85

source   type=7 x=40.90 y=28.80 depth=11. strike=323 dip=90 rake=180 length=1.5 width=1.5 d0=0.75 s0=0 amp=1.16E+21 v=3. file=stf.sac t0=0.9862

source   type=7 x=41.80 y=27.60 depth=11. strike=323 dip=90 rake=180 length=1.5 width=1.5 d0=0.75 s0=0 amp=7.84E+20 v=3. file=stf.sac t0=1.3124

source   type=7 x=42.70 y=26.40 depth=11. strike=323 dip=90 rake=180 length=1.5 width=1.5 d0=0.75 s0=0 amp=4.09E+20 v=3. file=stf.sac t0=1.7241

source   type=7 x=43.60 y=25.20 depth=11. strike=323 dip=90 rake=180 length=1.5 width=1.5 d0=0.75 s0=0 amp=3.79E+20 v=3. file=stf.sac t0=2.1731

source   type=7 x=44.50 y=24.00 depth=11. strike=323 dip=90 rake=180 length=1.5 width=1.5 d0=0.75 s0=0 amp=1.36E+20 v=3. file=stf.sac t0=2.6405

source   type=7 x=37.30 y=33.60 depth=12.5 strike=323 dip=90 rake=180 length=1.5 width=1.5 d0=0.75 s0=0 amp=3.42E+20 v=3. file=stf.sac t0=2.0180

source   type=7 x=38.20 y=32.40 depth=12.5 strike=323 dip=90 rake=180 length=1.5 width=1.5 d0=0.75 s0=0 amp=3.42E+20 v=3. file=stf.sac t0=1.6800

source   type=7 x=39.10 y=31.20 depth=12.5 strike=323 dip=90 rake=180 length=1.5 width=1.5 d0=0.75 s0=0 amp=2.73E+20 v=3. file=stf.sac t0=1.4396

source   type=7 x=40. y=30. depth=12.5 strike=323 dip=90 rake=180 length=1.5 width=1.5 d0=0.75 s0=0 amp=6.14E+20 v=3. file=stf.sac t0=1.35

source   type=7 x=40.90 y=28.80 depth=12.5 strike=323 dip=90 rake=180 length=1.5 width=1.5 d0=0.75 s0=0 amp=6.82E+20 v=3. file=stf.sac t0=1.4396

source   type=7 x=41.80 y=27.60 depth=12.5 strike=323 dip=90 rake=180 length=1.5 width=1.5 d0=0.75 s0=0 amp=6.48E+20 v=3. file=stf.sac t0=1.6800

source   type=7 x=42.70 y=26.40 depth=12.5 strike=323 dip=90 rake=180 length=1.5 width=1.5
d0=0.75 s0=0 amp=5.73E+20 v=3. file=stf.sac t0=2.0180

source   type=7 x=43.60 y=25.20 depth=12.5 strike=323 dip=90 rake=180 length=1.5 width=1.5
d0=0.75 s0=0 amp=5.12E+20 v=3. file=stf.sac t0=2.4130

source   type=7 x=44.50 y=24.00 depth=12.5 strike=323 dip=90 rake=180 length=1.5 width=1.5
d0=0.75 s0=0 amp=3.07E+20 v=3. file=stf.sac t0=2.8412

sac x=23.65 z=0. y=34.34 file="sac.fremont"

sac x=32.66 z=0. y=25.00 file="sac.sanjoseres"

sac x=30.00 z=0. y=23.33 file="sac.sanjoseap"

sac x=27.66 z=0. y=28.44 file="sac.milpitas"

sac x=34.44 z=0. y=39.45 file="sac.sunol"

sac x=41.22 z=0. y=23.66 file="sac.mthamilton"

parallel nx=2 ny=2 nz=4

e. Input files of the models with modified rupture velocity

#Rupture velocity 2.8 km/sec

grid   z=25 x=80 y=60 dh=0.15 active=0

time dt=0.005 t=4000

block   p=2.40 s=1.10 r=2.30 z2=0.2
block   p=3.00 s=1.40 r=2.45 z1=0.2 z2=0.5
block   p=3.60 s=1.95 r=2.50 z1=0.5 z2=1.
block   p=4.20 s=2.30 r=2.55 z1=1. z2=1.5
block   p=4.80 s=2.80 r=2.60 z1=1.5 z2=2.5
block   p=5.25 s=3.00 r=2.62 z1=2.5 z2=3.
block   p=5.60 s=3.25 r=2.65 z1=3. z2=5.
block   p=5.90 s=3.41 r=2.70 z1=5. z2=7.
block   p=6.15 s=3.55 r=2.75 z1=7. z2=9.
block   p=6.35 s=3.62 r=2.85 z1=9. z2=17.
block   p=7.00 s=4.10 r=3.00 z1=17. z2=25.

source   type=7 x=39.10 y=31.20 depth=8. strike=323 dip=90 rake=180 length=1.5 width=1.5 d0=0.75 s0=0 amp=9.37E+19 v=2.8 file=stf2.8.sac t0=0.5593

source   type=7 x=40. y=30. depth=8. strike=323 dip=90 rake=180 length=1.5 width=1.5 d0=1.2 s0=0 amp=2.47E+20 v=2.8 file=stf2.8.sac t0=0

source   type=7 x=40.9 y=28.8 depth=8. strike=323 dip=90 rake=180 length=1.5 width=1.5 d0=0.75 s0=0 amp=2.02E+20 v=2.8 file=stf2.8.sac t0=0.5593

source   type=7 x=41.8 y=27.6 depth=8. strike=323 dip=90 rake=180 length=1.5 width=1.5 d0=0.75 s0=0 amp=0. v=2.8 file=stf2.8.sac t0=1.0834

source   type=7 x=42.7 y=26.4 depth=8. strike=323 dip=90 rake=180 length=1.5 width=1.5 d0=0.75 s0=0 amp=0. v=2.8 file=stf2.8.sac t0=1.6151

source   type=7 x=43.6 y=25.2 depth=8. strike=323 dip=90 rake=180 length=1.5 width=1.5 d0=0.75 s0=0 amp=0. v=2.8 file=stf2.8.sac t0=2.1489

source   type=7 x=39.10 y=31.20 depth=9.5 strike=323 dip=90 rake=180 length=1.5 width=1.5 d0=0.75 s0=0 amp=2.63E+20 v=2.8 file=stf2.8.sac t0=0.6539

source   type=7 x=40. y=30. depth=9.5 strike=323 dip=90 rake=180 length=1.5 width=1.5 d0=0.75 s0=0 amp=8.63E+20 v=2.8 file=stf2.8.sac t0=0.357

source   type=7 x=40.9 y=28.8 depth=9.5 strike=323 dip=90 rake=180 length=1.5 width=1.5 d0=0.75 s0=0 amp=7.51E+20 v=2.8 file=stf2.8.sac t0=0.6539

source   type=7 x=41.8 y=27.6 depth=9.5 strike=323 dip=90 rake=180 length=1.5 width=1.5 d0=0.75 s0=0 amp=1.12E+20 v=2.8 file=stf2.8.sac t0=1.1351

source   type=7 x=42.7 y=26.4 depth=9.5 strike=323 dip=90 rake=180 length=1.5 width=1.5 d0=0.75 s0=0 amp=0. v=2.8 file=stf2.8.sac t0=1.6503

source   type=7 x=43.6 y=25.2 depth=9.5 strike=323 dip=90 rake=180 length=1.5 width=1.5 d0=0.75 s0=0 amp=0. v=2.8 file=stf2.8.sac t0=2.1754

source   type=7 x=39.10 y=31.20 depth=11. strike=323 dip=90 rake=180 length=1.5 width=1.5 d0=0.75 s0=0 amp=1.12E+20 v=2.8 file=stf2.8.sac t0=1.0566

source   type=7 x=40. y=30. depth=11. strike=323 dip=90 rake=180 length=1.5 width=1.5 d0=0.75 s0=0 amp=9.00E+20 v=2.8 file=stf2.8.sac t0=0.9107

source   type=7 x=40.9 y=28.8 depth=11. strike=323 dip=90 rake=180 length=1.5 width=1.5 d0=0.75 s0=0 amp=1.27E+21 v=2.8 file=stf2.8.sac t0=1.05669

source   type=7 x=41.8 y=27.6 depth=11. strike=323 dip=90 rake=180 length=1.5 width=1.5 d0=0.75 s0=0 amp=8.63E+20 v=2.8 file=stf2.8.sac t0=1.4062

source   type=7 x=42.7 y=26.4 depth=11. strike=323 dip=90 rake=180 length=1.5 width=1.5 d0=0.75 s0=0 amp=4.51E+20 v=2.8 file=stf2.8.sac t0=1.8472

source   type=7 x=43.6 y=25.2 depth=11. strike=323 dip=90 rake=180 length=1.5 width=1.5 d0=0.75 s0=0 amp=4.17E+20 v=2.8 file=stf2.8.sac t0=2.3284

source   type=7 x=39.10 y=31.20 depth=12.5 strike=323 dip=90 rake=180 length=1.5 width=1.5 d0=0.75 s0=0 amp=3.00E+20 v=2.8 file=stf2.8.sac t0=1.5424

source   type=7 x=40. y=30. depth=12.5 strike=323 dip=90 rake=180 length=1.5 width=1.5 d0=0.75 s0=0 amp=6.75E+20 v=2.8 file=stf2.8.sac t0=1.4464

source   type=7 x=40.9 y=28.8 depth=12.5 strike=323 dip=90 rake=180 length=1.5 width=1.5 d0=0.75 s0=0 amp=7.51E+20 v=2.8 file=stf2.8.sac t0=1.5424

source   type=7 x=41.8 y=27.6 depth=12.5 strike=323 dip=90 rake=180 length=1.5 width=1.5 d0=0.75 s0=0 amp=7.12E+20 v=2.8 file=stf2.8.sac t0=1.8000

source   type=7 x=42.7 y=26.4 depth=12.5 strike=323 dip=90 rake=180 length=1.5 width=1.5 d0=0.75 s0=0 amp=6.30E+20 v=2.8 file=stf2.8.sac t0=2.1622

source   type=7 x=43.6 y=25.2 depth=12.5 strike=323 dip=90 rake=180 length=1.5 width=1.5 d0=0.75 s0=0 amp=5.63E+20 v=2.8 file=stf2.8.sac t0=2.5853

sac x=23.65 z=0. y=34.34 file="sac.fremont"

sac x=32.66 z=0. y=25.00 file="sac.sanjoseres"

sac x=30.00 z=0. y=23.33 file="sac.sanjoseap"

sac x=27.66 z=0. y=28.44 file="sac.milpitas"

sac x=34.44 z=0. y=39.45 file="sac.sunol"

sac x=41.22 z=0. y=23.66 file="sac.mthamilton"

parallel nx=2 ny=2 nz=4

Rupture velocity 3.1 km/sec

grid   z=25 x=80 y=60 dh=0.15 active=0

time dt=0.005 t=4000

block p=2.40 s=1.10 r=2.30 z2=0.2

block p=3.00 s=1.40 r=2.45 z1=0.2 z2=0.5

block p=3.60 s=1.95 r=2.50 z1=0.5 z2=1.

block   p=4.20 s=2.30 r=2.55 z1=1. z2=1.5

block   p=4.80 s=2.80 r=2.60 z1=1.5 z2=2.5

block   p=5.25 s=3.00 r=2.62 z1=2.5 z2=3.

block   p=5.60 s=3.25 r=2.65 z1=3. z2=5.

block   p=5.90 s=3.41 r=2.70 z1=5. z2=7.

block   p=6.15 s=3.55 r=2.75 z1=7. z2=9.

block   p=6.35 s=3.62 r=2.85 z1=9. z2=17.

block   p=7.00 s=4.10 r=3.00 z1=17. z2=25.

source   type=7 x=39.10 y=31.20 depth=8. strike=323 dip=90 rake=180 length=1.5 width=1.5 d0=0.75 s0=0 amp=9.37E+19 v=3.1 file=stf3.1.sac t0=0.5051

source   type=7 x=40. y=30. depth=8. strike=323 dip=90 rake=180 length=1.5 width=1.5 d0=1.2 s0=0 amp=2.47E+20 v=3.1 file=stf3.1.sac t0=0

source   type=7 x=40.9 y=28.8 depth=8. strike=323 dip=90 rake=180 length=1.5 width=1.5 d0=0.75 s0=0 amp=2.02E+20 v=3.1 file=stf3.1.sac t0=0.5051

source   type=7 x=41.8 y=27.6 depth=8. strike=323 dip=90 rake=180 length=1.5 width=1.5 d0=0.75 s0=0 amp=0. v=3.1 file=stf3.1.sac t0=0.9785

source   type=7 x=42.7 y=26.4 depth=8. strike=323 dip=90 rake=180 length=1.5 width=1.5 d0=0.75 s0=0 amp=0. v=3.1 file=stf3.1.sac t0=1.4588

source   type=7 x=43.6 y=25.2 depth=8. strike=323 dip=90 rake=180 length=1.5 width=1.5 d0=0.75 s0=0 amp=0. v=3.1 file=stf3.1.sac t0=1.9409

source   type=7 x=39.10 y=31.20 depth=9.5 strike=323 dip=90 rake=180 length=1.5 width=1.5 d0=0.75 s0=0 amp=2.63E+20 v=3.1 file=stf3.1.sac t0=0.5906

source   type=7 x=40. y=30. depth=9.5 strike=323 dip=90 rake=180 length=1.5 width=1.5 d0=0.75 s0=0 amp=8.63E+20 v=3.1 file=stf3.1.sac t0=0.3387

source   type=7 x=40.9 y=28.8 depth=9.5 strike=323 dip=90 rake=180 length=1.5 width=1.5 d0=0.75 s0=0 amp=7.51E+20 v=3.1 file=stf3.1.sac t0=0.5906

source   type=7 x=41.8 y=27.6 depth=9.5 strike=323 dip=90 rake=180 length=1.5 width=1.5 d0=0.75 s0=0 amp=1.12E+20 v=3.1 file=stf3.1.sac t0=1.0253

source   type=7 x=42.7 y=26.4 depth=9.5 strike=323 dip=90 rake=180 length=1.5 width=1.5 d0=0.75 s0=0 amp=0. v=3.1 file=stf3.1.sac t0=1.4906

source   type=7 x=43.6 y=25.2 depth=9.5 strike=323 dip=90 rake=180 length=1.5 width=1.5 d0=0.75 s0=0 amp=0. v=3.1 file=stf3.1.sac t0=1.9648

source   type=7 x=39.10 y=31.20 depth=11. strike=323 dip=90 rake=180 length=1.5 width=1.5 d0=0.75 s0=0 amp=1.12E+20 v=3.1 file=stf3.1.sac t0=0.9543

source   type=7 x=40. y=30. depth=11. strike=323 dip=90 rake=180 length=1.5 width=1.5 d0=0.75 s0=0 amp=9.00E+20 v=3.1 file=stf3.1.sac t0=0.8225

source   type=7 x=40.9 y=28.8 depth=11. strike=323 dip=90 rake=180 length=1.5 width=1.5 d0=0.75 s0=0 amp=1.27E+21 v=3.1 file=stf3.1.sac t0=0.9543

source   type=7 x=41.8 y=27.6 depth=11. strike=323 dip=90 rake=180 length=1.5 width=1.5 d0=0.75 s0=0 amp=8.63E+20 v=3.1 file=stf3.1.sac t0=1.2701

source   type=7 x=42.7 y=26.4 depth=11. strike=323 dip=90 rake=180 length=1.5 width=1.5 d0=0.75 s0=0 amp=4.51E+20 v=3.1 file=stf3.1.sac t0=1.6684

source   type=7 x=43.6 y=25.2 depth=11. strike=323 dip=90 rake=180 length=1.5 width=1.5 d0=0.75 s0=0 amp=4.17E+20 v=3.1 file=stf3.1.sac t0=2.1030

source   type=7 x=39.10 y=31.20 depth=12.5 strike=323 dip=90 rake=180 length=1.5 width=1.5 d0=0.75 s0=0 amp=3.00E+20 v=3.1 file=stf3.1.sac t0=1.3931

source   type=7 x=40. y=30. depth=12.5 strike=323 dip=90 rake=180 length=1.5 width=1.5 d0=0.75 s0=0 amp=6.75E+20 v=3.1 file=stf3.1.sac t0=1.3064

source   type=7 x=40.9 y=28.8 depth=12.5 strike=323 dip=90 rake=180 length=1.5 width=1.5 d0=0.75 s0=0 amp=7.51E+20 v=3.1 file=stf3.1.sac t0=1.3931

source   type=7 x=41.8 y=27.6 depth=12.5 strike=323 dip=90 rake=180 length=1.5 width=1.5 d0=0.75 s0=0 amp=7.12E+20 v=3.1 file=stf3.1.sac t0=1.6258

source   type=7 x=42.7 y=26.4 depth=12.5 strike=323 dip=90 rake=180 length=1.5 width=1.5 d0=0.75 s0=0 amp=6.30E+20 v=3.1 file=stf3.1.sac t0=1.9529

source   type=7 x=43.6 y=25.2 depth=12.5 strike=323 dip=90 rake=180 length=1.5 width=1.5 d0=0.75 s0=0 amp=5.63E+20 v=3.1 file=stf3.1.sac t0=2.3351

sac x=23.65 z=0. y=34.34 file="sac.fremont"
sac x=32.66 z=0. y=25.00 file="sac.sanjoseres"
sac x=30.00 z=0. y=23.33 file="sac.sanjoseap"
sac x=27.66 z=0. y=28.44 file="sac.milpitas"
sac x=34.44 z=0. y=39.45 file="sac.sunol"
sac x=41.22 z=0. y=23.66 file="sac.mthamilton"

parallel nx=2 ny=2 nz=4

f. Input file of the model with alternative velocity model

#Waldhauser & Ellsworth velocity model

grid   z=25 x=80 y=60 dh=0.15 active=0

time dt=0.005 t=4000

block   p=3.75 s=2.17 r=2.36 z2=1.0
block   p=4.64 s=2.68 r=2.48 z1=1.0 z2=3.0
block   p=5.34 s=3.08 r=2.59 z1=3.0 z2=6.0
block   p=5.75 s=3.32 r=2.67 z1=6.0 z2=14.0
block   p=6.22 s=3.59 r=2.77 z1=14.0 z2=20.0
block   p=7.98 s=4.61 r=3.28 z1=20.0 z2=25.0

source   type=7 x=39.10 y=31.20 depth=8. strike=323 dip=90 rake=180 length=1.5 width=1.5 d0=0.75 s0=0 amp=9.37E+19 v=3. file=stf.sac t0=0.52

source   type=7 x=40. y=30. depth=8. strike=323 dip=90 rake=180 length=1.5 width=1.5 d0=1.2 s0=0 amp=2.47E+20 v=3. file=stf.sac t0=0

source   type=7 x=40.9 y=28.8 depth=8. strike=323 dip=90 rake=180 length=1.5 width=1.5 d0=0.75 s0=0 amp=2.02E+20 v=3. file=stf.sac t0=0.52

source   type=7 x=41.8 y=27.6 depth=8. strike=323 dip=90 rake=180 length=1.5 width=1.5 d0=0.75 s0=0 amp=0. v=3. file=stf.sac t0=1.01

source   type=7 x=42.7 y=26.4 depth=8. strike=323 dip=90 rake=180 length=1.5 width=1.5 d0=0.75 s0=0 amp=0. v=3. file=stf.sac t0=1.51

source   type=7 x=43.6 y=25.2 depth=8. strike=323 dip=90 rake=180 length=1.5 width=1.5 d0=0.75 s0=0 amp=0. v=3. file=stf.sac t0=2.01

source   type=7 x=39.10 y=31.20 depth=9.5 strike=323 dip=90 rake=180 length=1.5 width=1.5 d0=0.75 s0=0 amp=2.63E+20 v=3. file=stf.sac t0=0.61

source   type=7 x=40. y=30. depth=9.5 strike=323 dip=90 rake=180 length=1.5 width=1.5 d0=0.75 s0=0 amp=8.63E+20 v=3. file=stf.sac t0=0.35

source   type=7 x=40.9 y=28.8 depth=9.5 strike=323 dip=90 rake=180 length=1.5 width=1.5 d0=0.75 s0=0 amp=7.51E+20 v=3. file=stf.sac t0=0.61

source   type=7 x=41.8 y=27.6 depth=9.5 strike=323 dip=90 rake=180 length=1.5 width=1.5 d0=0.75 s0=0 amp=1.12E+20 v=3. file=stf.sac t0=1.06

source   type=7 x=42.7 y=26.4 depth=9.5 strike=323 dip=90 rake=180 length=1.5 width=1.5 d0=0.75 s0=0 amp=0. v=3. file=stf.sac t0=1.54

source   type=7 x=43.6 y=25.2 depth=9.5 strike=323 dip=90 rake=180 length=1.5 width=1.5 d0=0.75 s0=0 amp=0. v=3. file=stf.sac t0=2.03

source   type=7 x=39.10 y=31.20 depth=11. strike=323 dip=90 rake=180 length=1.5 width=1.5 d0=0.75 s0=0 amp=1.12E+20 v=3. file=stf.sac t0=0.99

source   type=7 x=40. y=30. depth=11. strike=323 dip=90 rake=180 length=1.5 width=1.5 d0=0.75 s0=0 amp=9.00E+20 v=3. file=stf.sac t0=0.85

source   type=7 x=40.9 y=28.8 depth=11. strike=323 dip=90 rake=180 length=1.5 width=1.5 d0=0.75
s0=0 amp=1.27E+21 v=3. file=stf.sac t0=0.99

source   type=7 x=41.8 y=27.6 depth=11. strike=323 dip=90 rake=180 length=1.5 width=1.5 d0=0.75
s0=0 amp=8.63E+20 v=3. file=stf.sac t0=1.31

source   type=7 x=42.7 y=26.4 depth=11. strike=323 dip=90 rake=180 length=1.5 width=1.5 d0=0.75
s0=0 amp=4.51E+20 v=3. file=stf.sac t0=1.72

source   type=7 x=43.6 y=25.2 depth=11. strike=323 dip=90 rake=180 length=1.5 width=1.5 d0=0.75
s0=0 amp=4.17E+20 v=3. file=stf.sac t0=2.17

source   type=7 x=39.10 y=31.20 depth=12.5 strike=323 dip=90 rake=180 length=1.5 width=1.5
d0=0.75 s0=0 amp=3.00E+20 v=3. file=stf.sac t0=1.44

source   type=7 x=40. y=30. depth=12.5 strike=323 dip=90 rake=180 length=1.5 width=1.5 d0=0.75
s0=0 amp=6.75E+20 v=3. file=stf.sac t0=1.35

source   type=7 x=40.9 y=28.8 depth=12.5 strike=323 dip=90 rake=180 length=1.5 width=1.5 d0=0.75
s0=0 amp=7.51E+20 v=3. file=stf.sac t0=1.44

source   type=7 x=41.8 y=27.6 depth=12.5 strike=323 dip=90 rake=180 length=1.5 width=1.5 d0=0.75
s0=0 amp=7.12E+20 v=3. file=stf.sac t0=1.68

source   type=7 x=42.7 y=26.4 depth=12.5 strike=323 dip=90 rake=180 length=1.5 width=1.5 d0=0.75
s0=0 amp=6.30E+20 v=3. file=stf.sac t0=2.02

source   type=7 x=43.6 y=25.2 depth=12.5 strike=323 dip=90 rake=180 length=1.5 width=1.5 d0=0.75
s0=0 amp=5.63E+20 v=3. file=stf.sac t0=2.4

sac x=23.65 z=0. y=34.34 file="sac.fremont"
sac x=32.66 z=0. y=25.00 file="sac.sanjoseres"
sac x=30.00 z=0. y=23.33 file="sac.sanjoseap"
sac x=27.66 z=0. y=28.44 file="sac.milpitas"
sac x=34.44 z=0. y=39.45 file="sac.sunol"
sac x=41.22 z=0. y=23.66 file="sac.mthamilton"

parallel nx=2 ny=2 nz=4

A3. Synthetic waveforms obtained using original model

Simulated long-period (up to 1.4 Hz) waveforms were calculated for the time of 20 seconds from the initial time of rupture for locations of six broad-band near-field seismic stations.
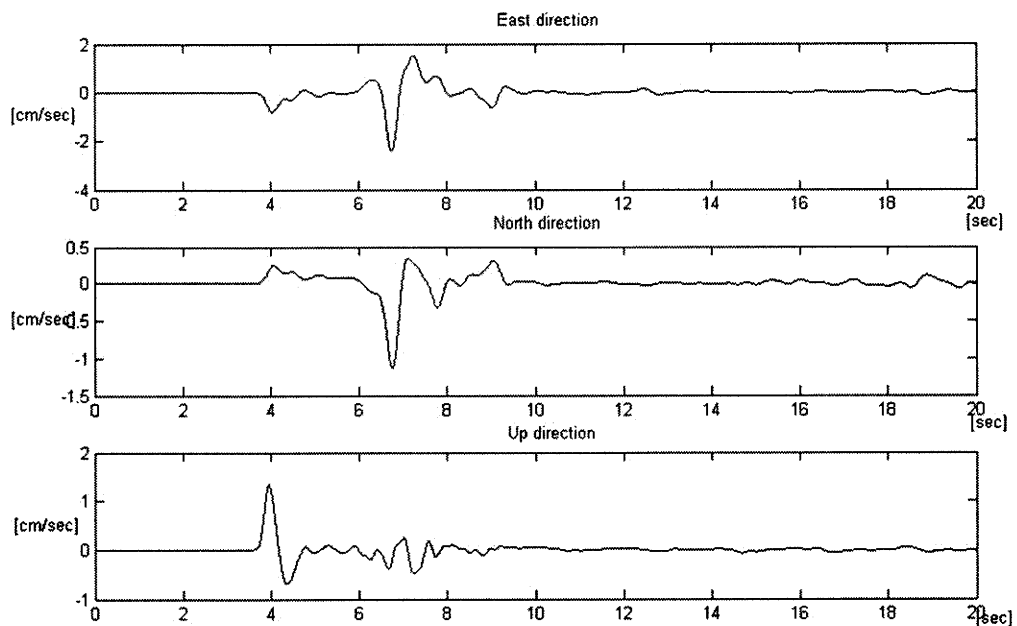
Fig. A3-1. Synthetic waveforms for the three channels of the station 57950
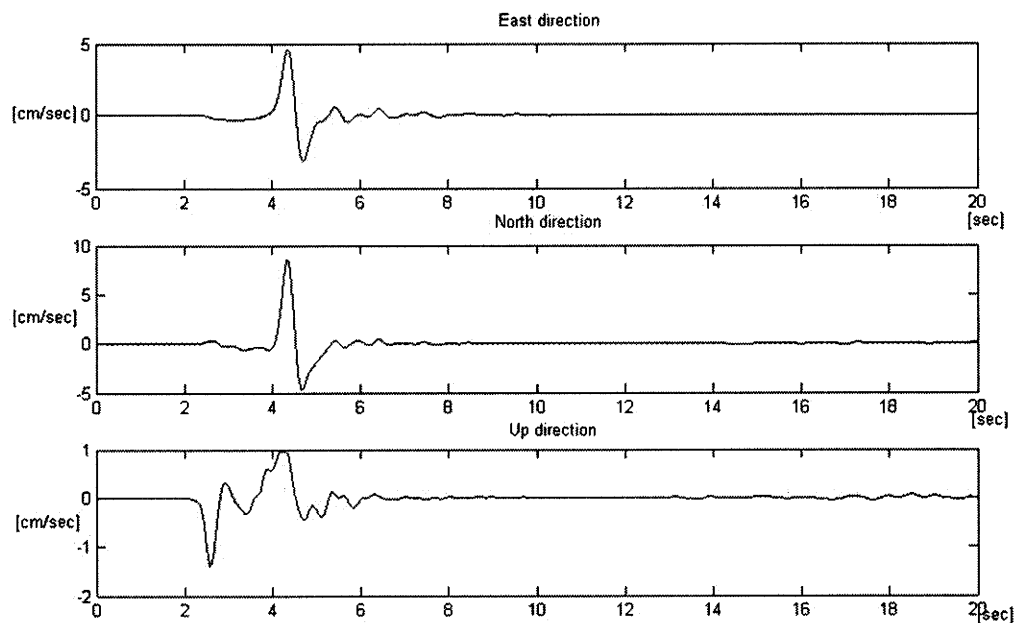
Fig. A3-2. Synthetic waveforms for the three channels of the station CHR
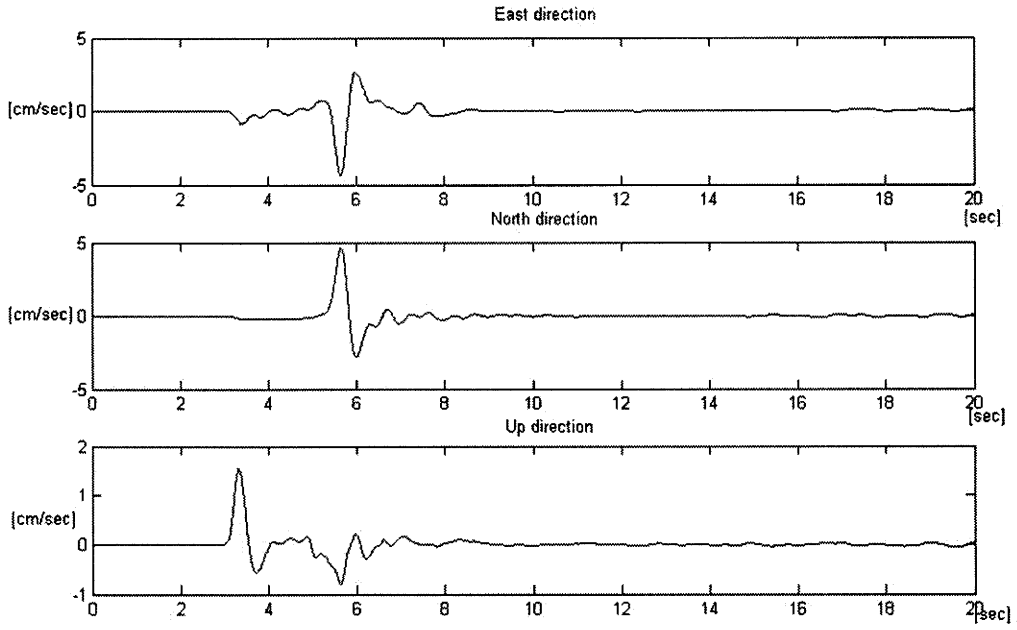
Fig. A3-3. Synthetic waveforms for the three channels of the station MP3
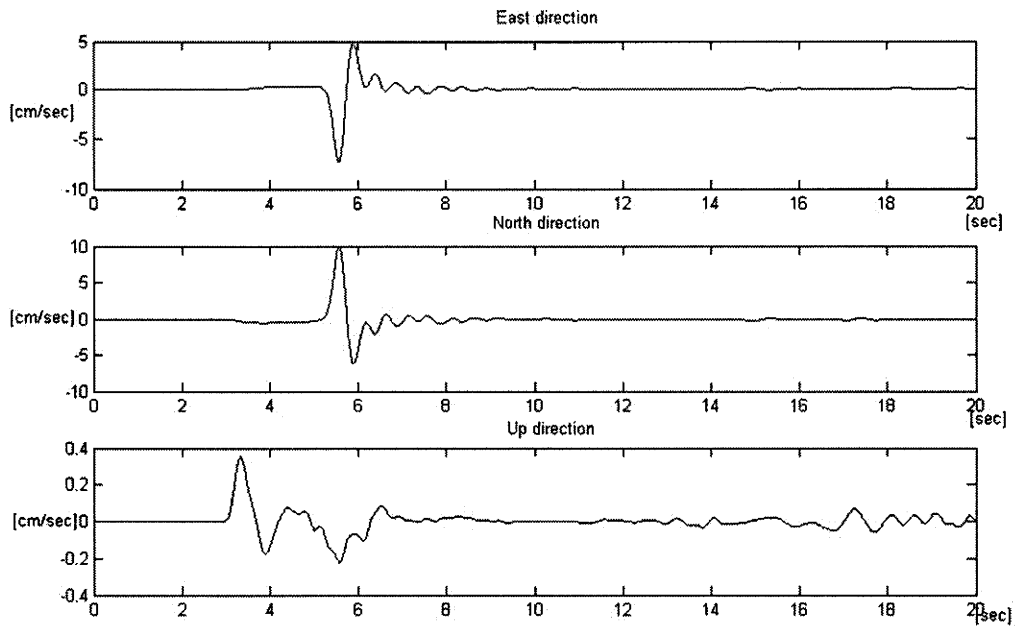
Fig. A3-4. Synthetic waveforms for the three channels of the station Q32
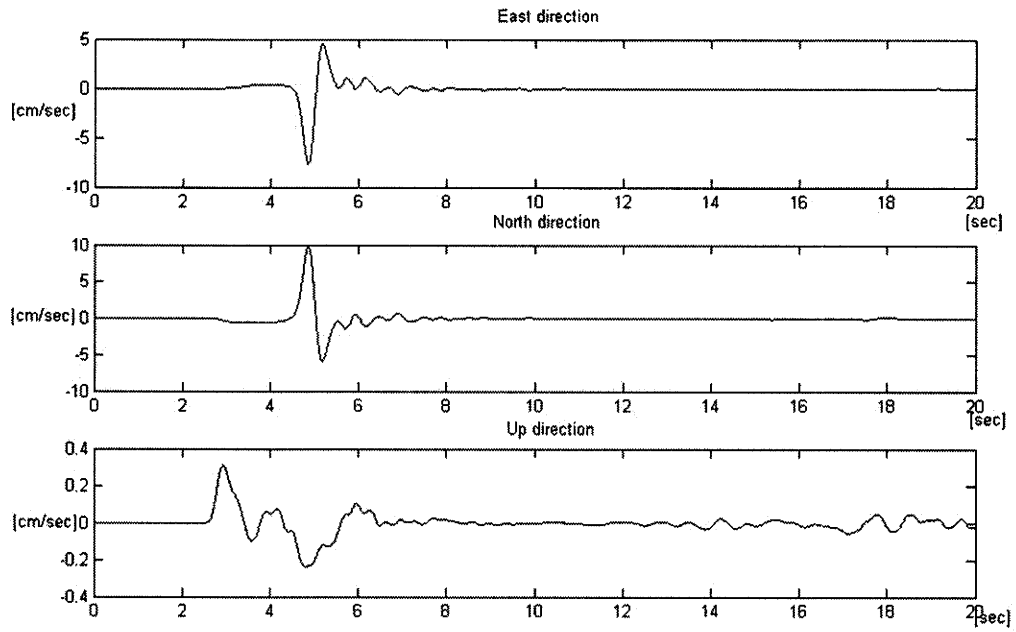
Fig. A3-5. Synthetic waveforms for the three channels of the station ROC
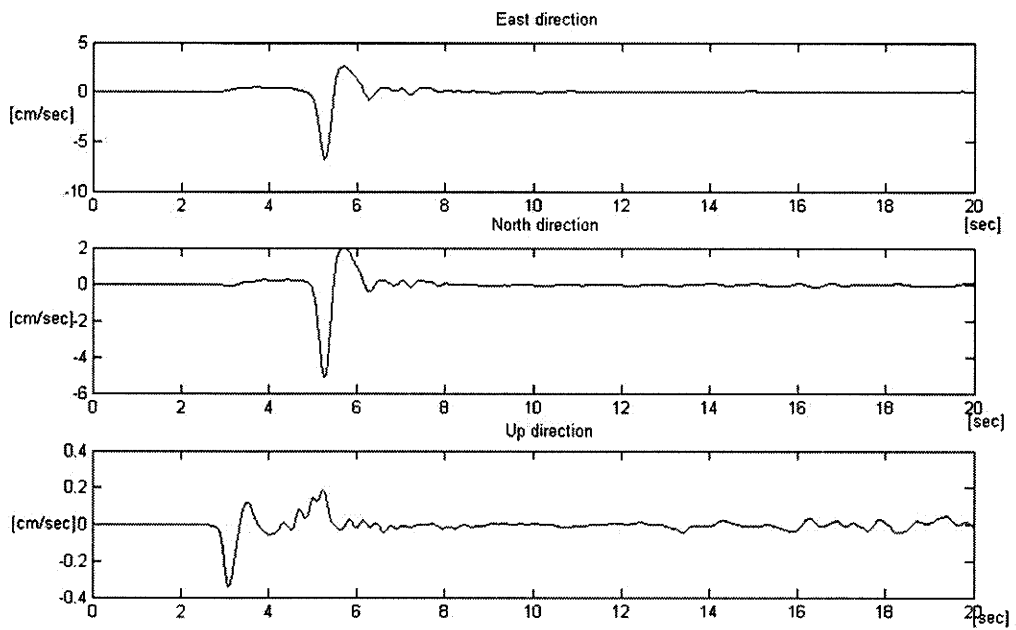
Fig. A3-6. Synthetic waveforms for the three channels of the station 1684

A4. Time-frequency misfit computation algorithm

```
clear

[data_ref, header_ref]=sac2mat('file name of reference signal');

S_ref=data_ref';

[data, header]=sac2mat('file name of comparable signal');

S=(data(1:length(S_ref))');

t_delta=header_ref(1:1);//sampling rate

t_min=0;//initial time

t_max=(length (S_ref)*t_delta)-t_delta;//end time

t=[t_min:t_delta:t_max];

amin=0.01;

amax=250;

adelta=(amax-amin)/100;

a=[amin:adelta:amax];//sacle parameter

TFR_ref=cwt(S_ref, a, 'cmor1-1.5'); //complex wavelet transform, time frequency representation of the reference signal

TFR=cwt(S, a, 'cmor1-1.5'); // complex wavelet transform, time frequency representation of thesignal that is to be compared with the reference signal

delta_E=abs(TFR)-abs(TFR_ref); //envelope difference

delta_P=(abs(TFR_ref).*(angle(TFR)-angle(TFR_ref)))/pi; //phase difference

TFEM=delta_E/max(max(abs(TFR_ref))); //time frequency envelope misfit (normalized difference)

TFPM=delta_P/max(max(abs(TFR_ref))); //time frequency phase misfit (normalized difference)

figure (1); subplot(3,1,1), imagesc (TFEM), colorbar, xlabel ('time [sec]'), ylabel ('scaling parameter a');

subplot(3,1,2), plot (t, S_ref, 'red', t, S, 'green'), xlabel ('time [sec]'), ylabel ('V [cm/sec]');

subplot(3,1,3), imagesc (TFPM), colorbar, xlabel ('time [sec]'), ylabel ('scaling parameter a');
```

A5. Results of quantitative comparison of observed and synthetic waveforms

a)

b)

c)
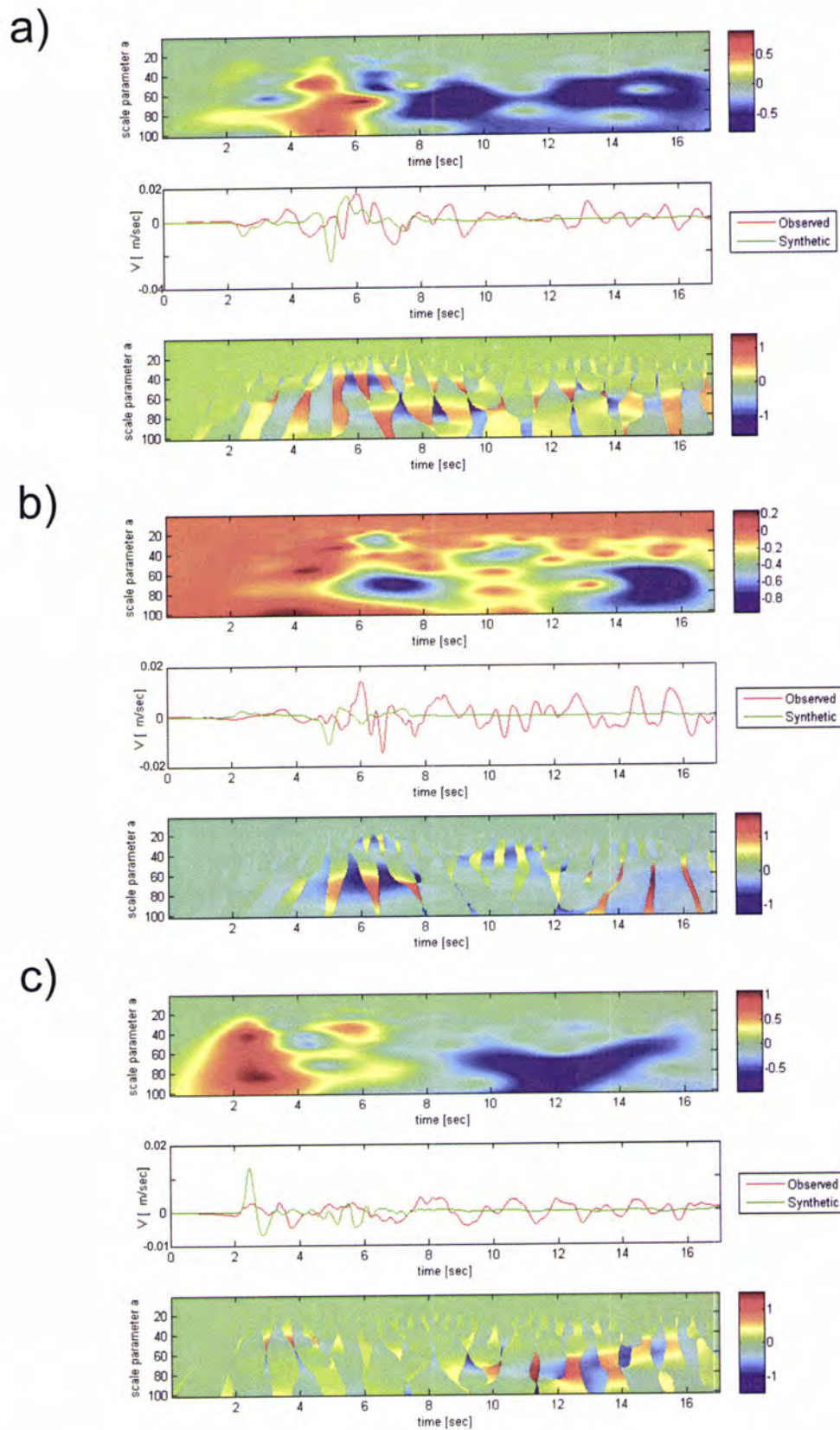
Fig. A5-1.Time-frequency envelope misfit (top), comparison of observed and synthetic waveforms (middle) and time-frequency phase misfit (bottom) for the three channels (a – East, b – North, c - Up) of the station 57950
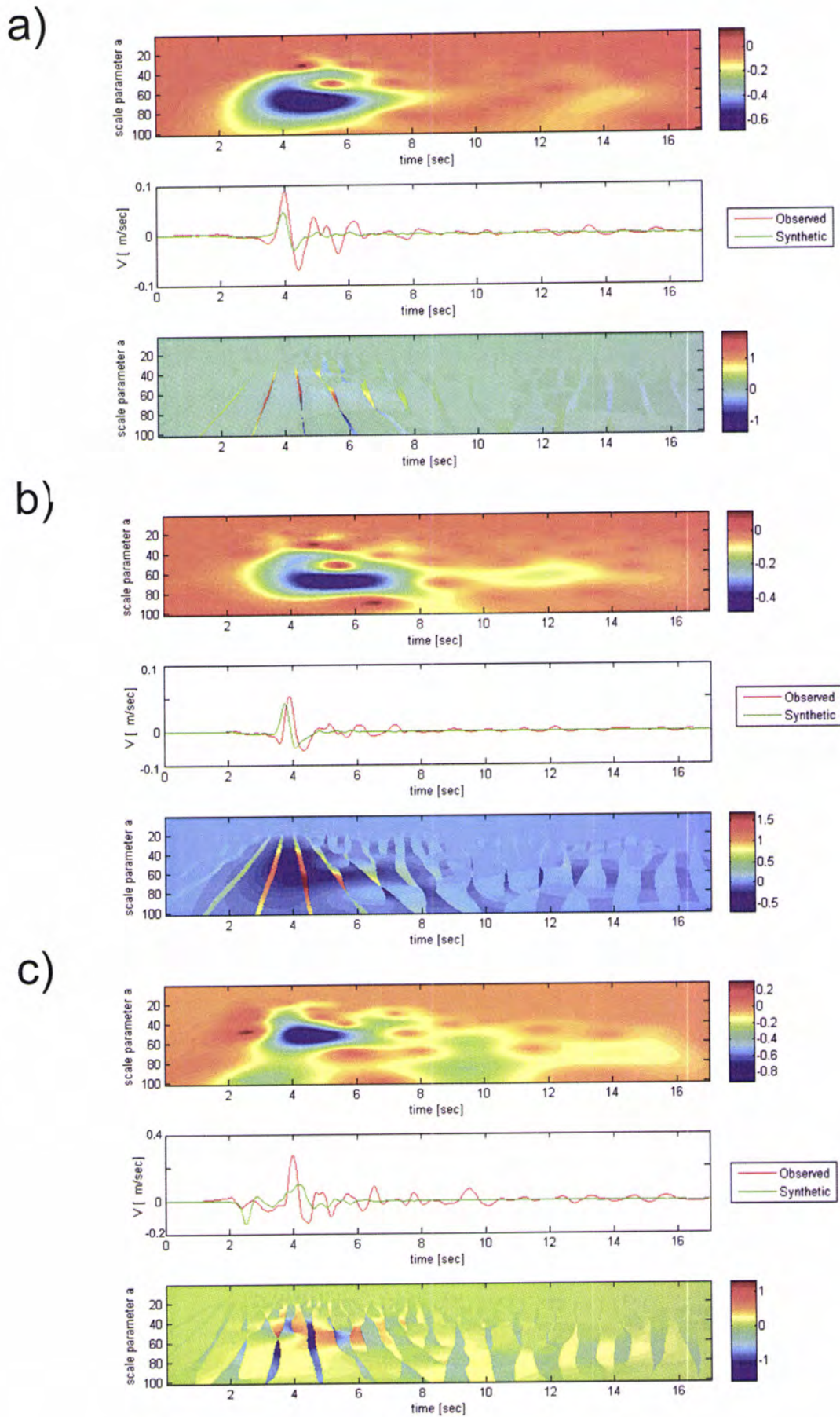
Fig. A5-2.Time-frequency envelope misfit (top), comparison of observed and synthetic waveforms (middle) and time-frequency phase misfit (bottom) for the three channels (a – East, b – North, c - Up) of the station CHR
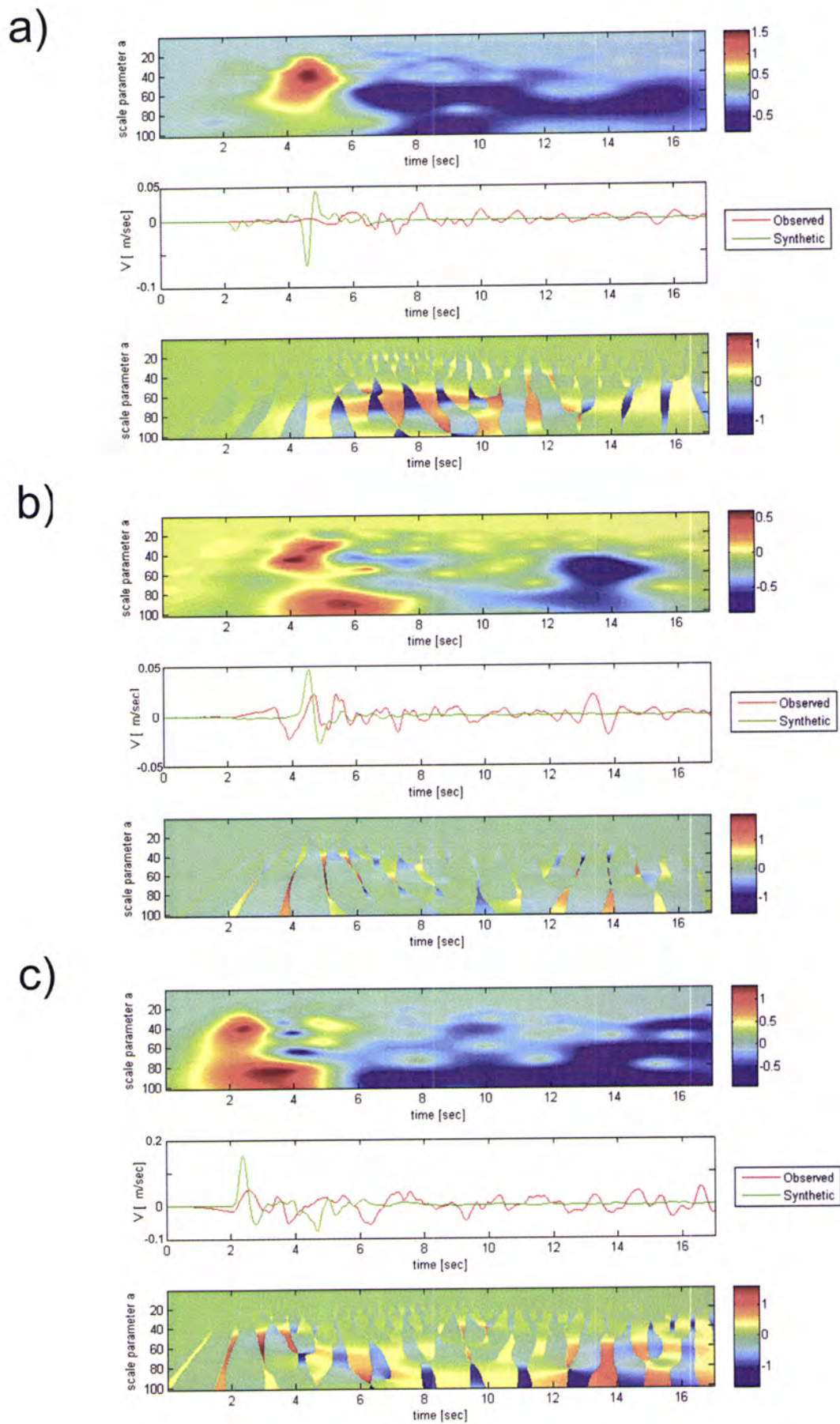
Fig. A5-3.Time-frequency envelope misfit (top), comparison of observed and synthetic waveforms (middle) and time-frequency phase misfit (bottom) for the three channels (a – East, b – North, c - Up) of the station MP3

98
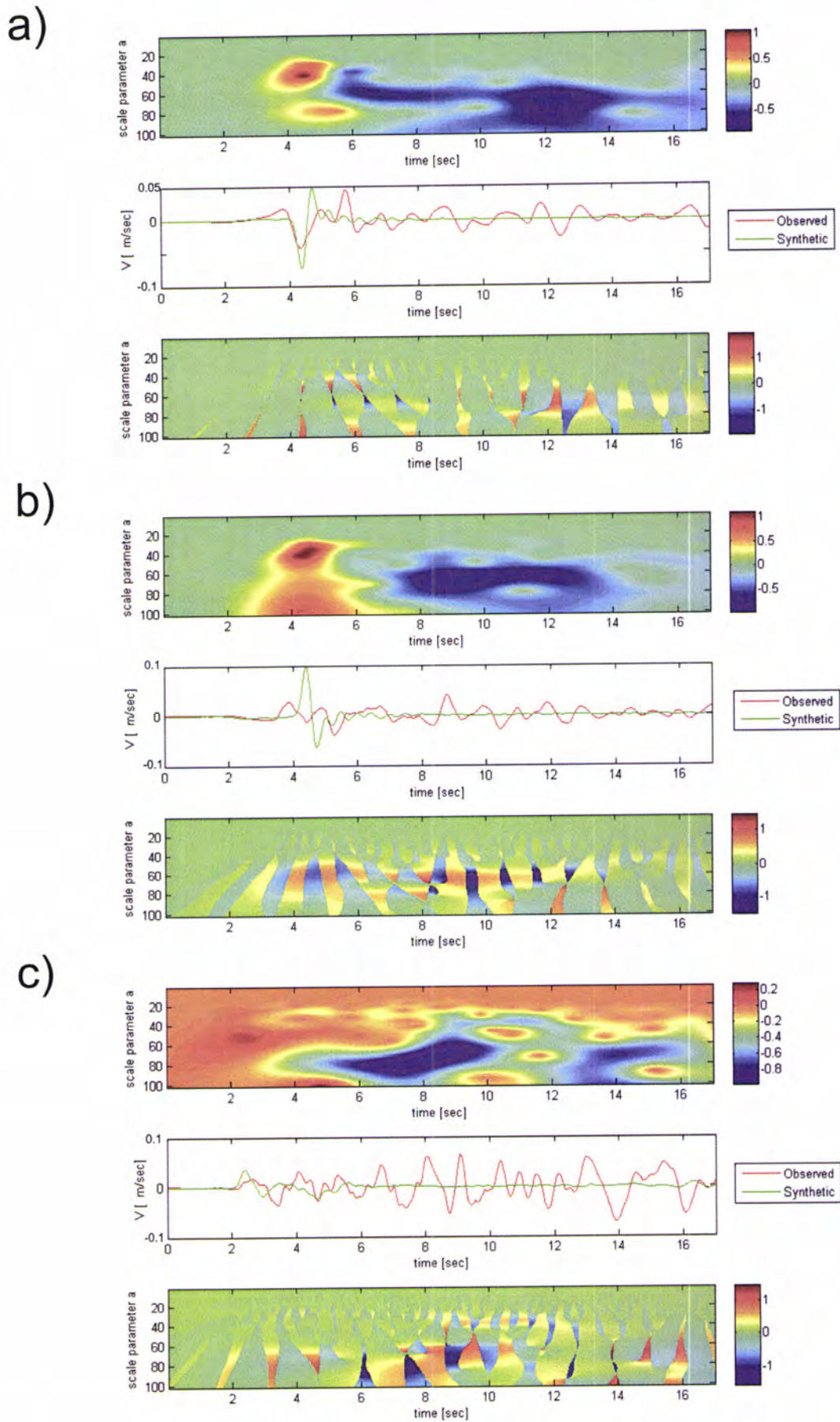
Fig. A5-4.Time-frequency envelope misfit (top), comparison of observed and synthetic waveforms (middle) and time-frequency phase misfit (bottom) for the three channels (a – East, b – North, c - Up) of the station Q32

99
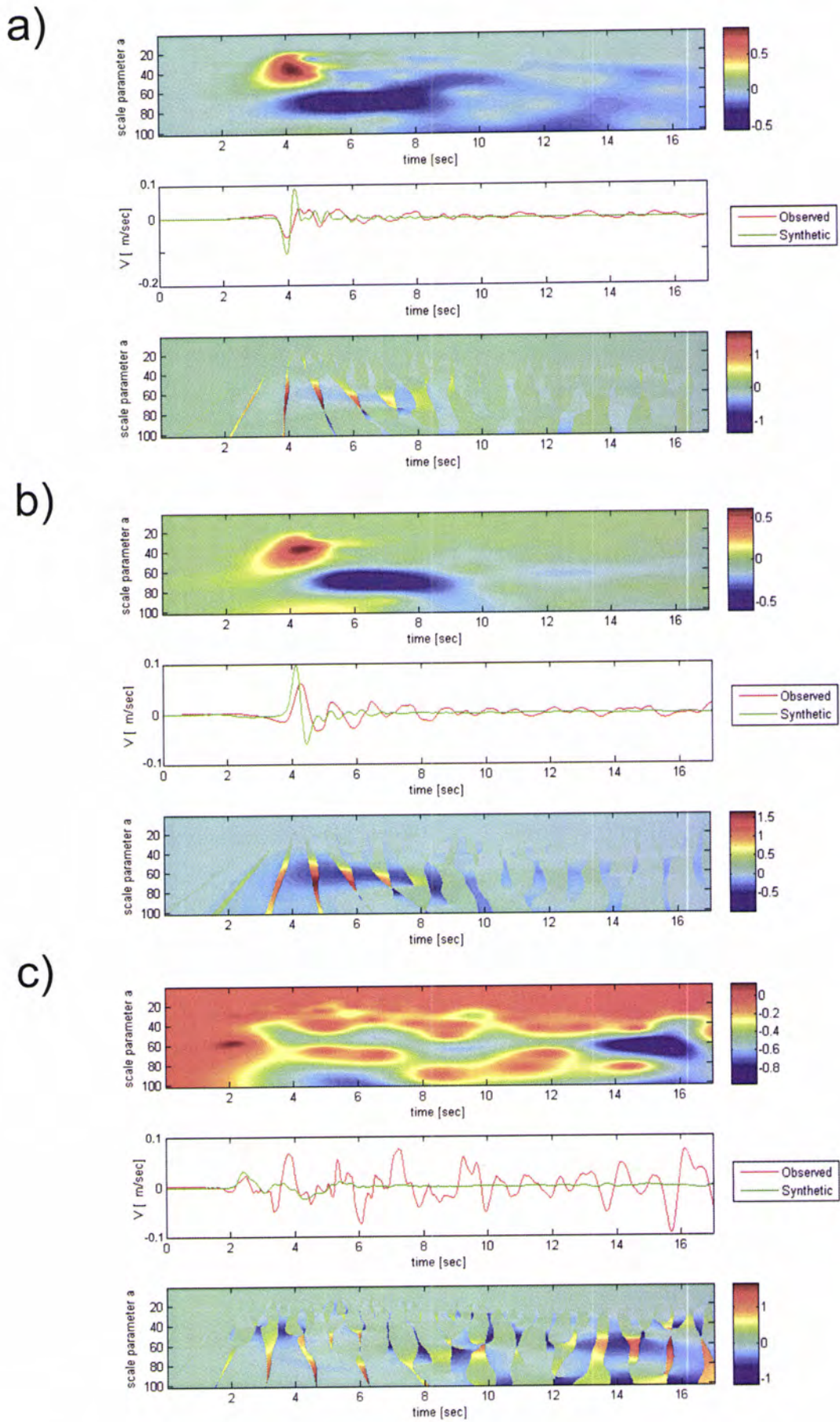
Fig. A5-5.Time-frequency envelope misfit (top), comparison of observed and synthetic waveforms (middle) and time-frequency phase misfit (bottom) for the three channels (a – East, b – North, c - Up) of the station ROC

100
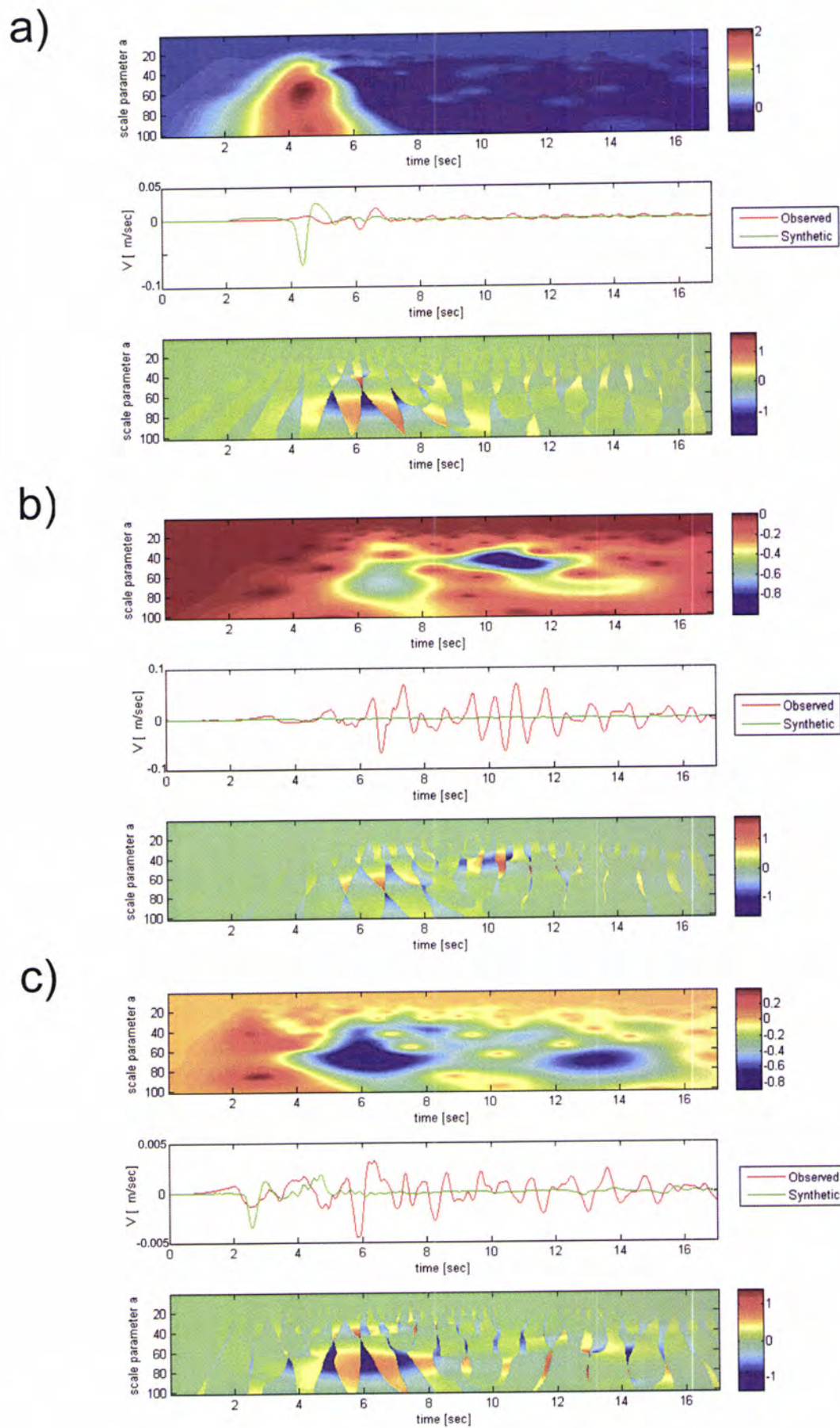
Fig. A5-6.Time-frequency envelope misfit (top), comparison of observed and synthetic waveforms (middle) and time-frequency phase misfit (bottom) for the three channels (a – East, b – North, c - Up) of the station 1684
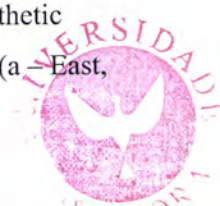
A6. Results of quantitative comparison of originally synthesized waveforms with waveforms obtained using models with independently modified parameters

a. Comparison of originally synthesized waveforms with waveforms obtained using models with modified dip angle

i. Reference model: dip angle – 90^0

Modified model: dip angle – 80^0 dipping in the north-east direction
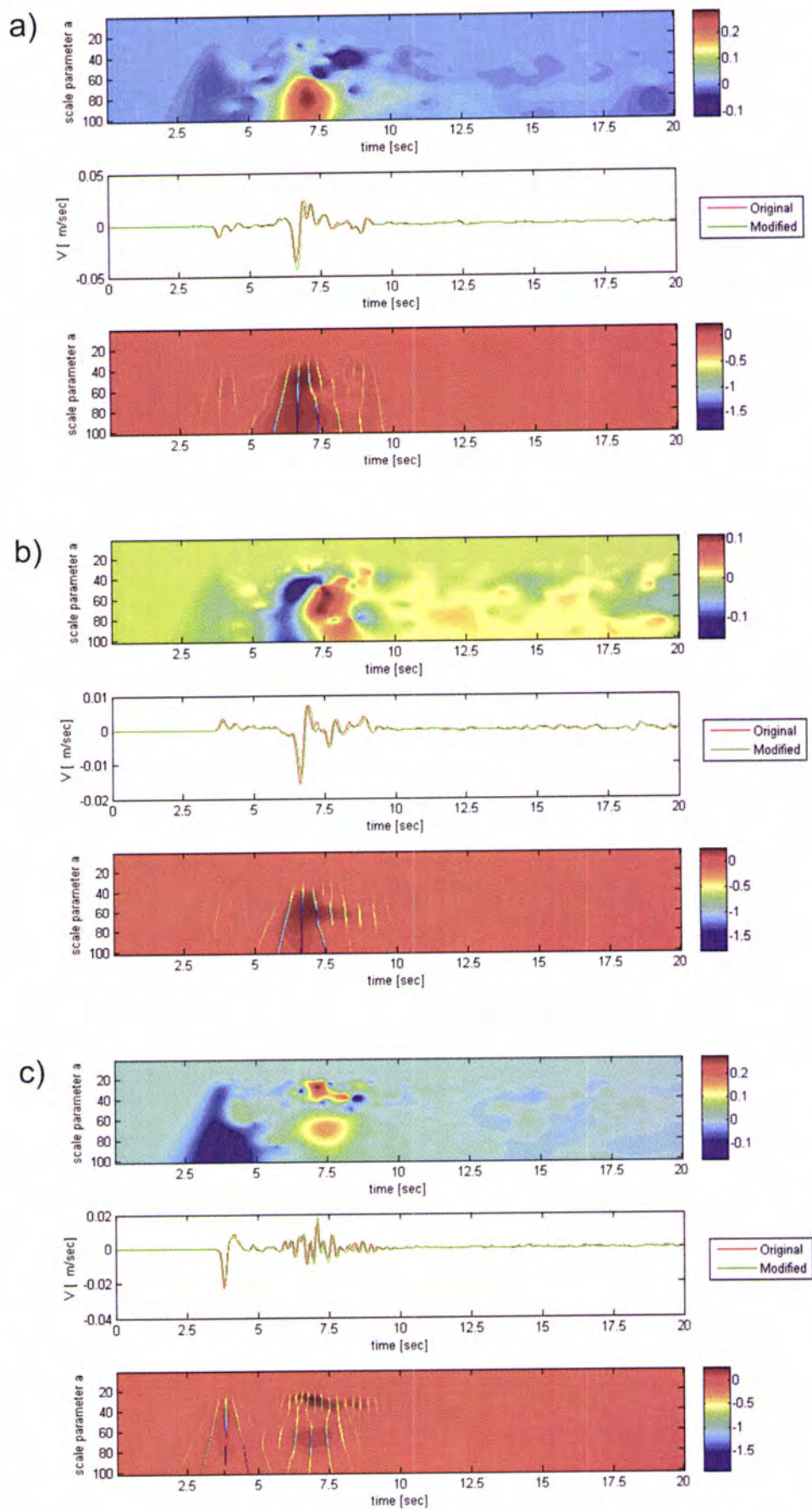
Fig. A6-a-i-1. Time-frequency envelope misfit (top), reference and comparison signals (middle) and time-frequency phase misfit (bottom) for the three channels (a – East, b – North, c – Up) of the station 57950

103
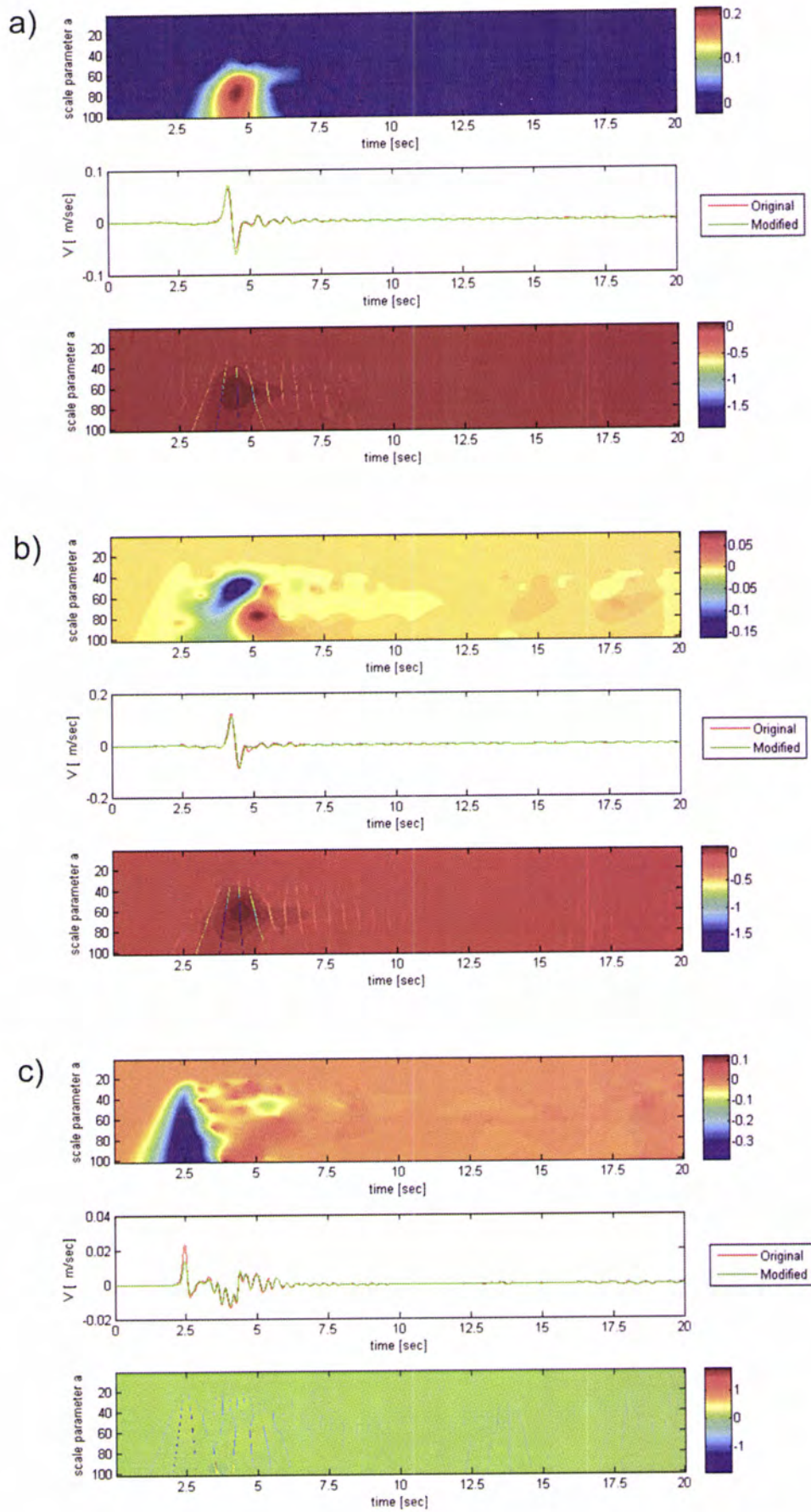
Fig. A6-a-i-2. Time-frequency envelope misfit (top), reference and comparison signals (middle) and time-frequency phase misfit (bottom) for the three channels (a – East, b – North, c – Up) of the station CHR
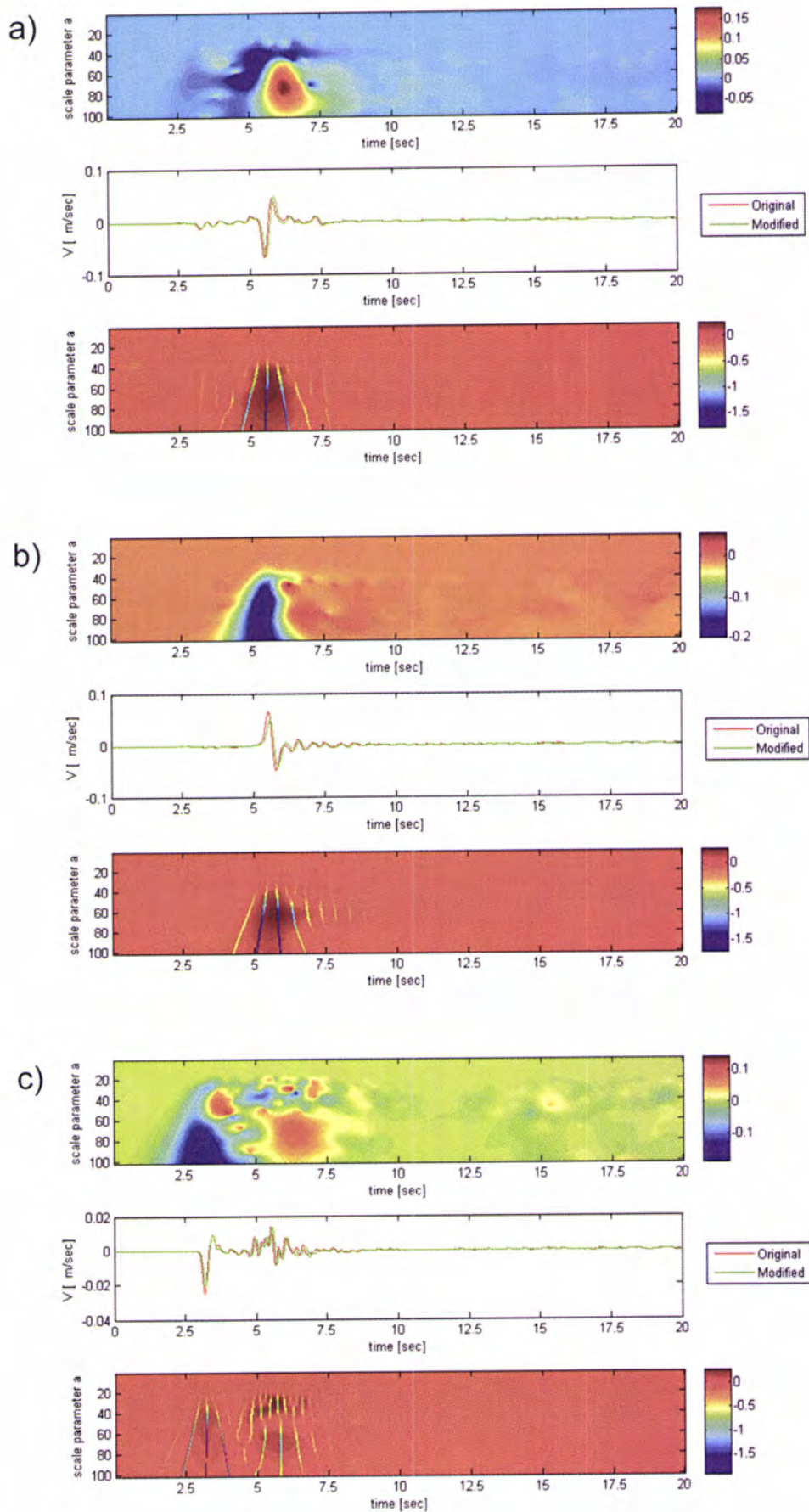
Fig. A6-a-i-3.Time-frequency envelope misfit (top), reference and comparison signals (middle) and time-frequency phase misfit (bottom) for the three channels (a – East, b – North, c – Up) of the station MP3
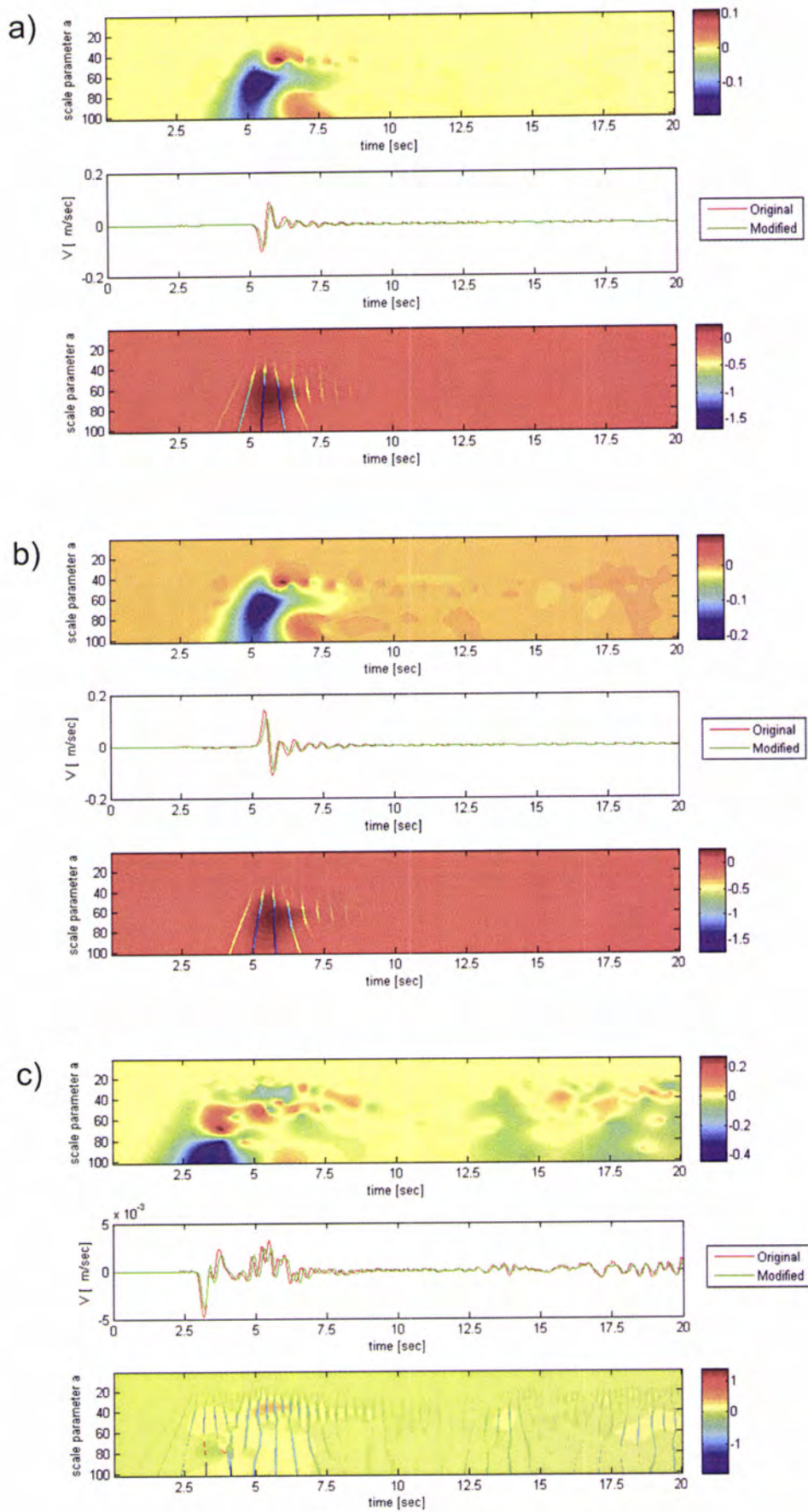
Fig. A6-a-i-4.Time-frequency envelope misfit (top), reference and comparison signals (middle) and time-frequency phase misfit (bottom) for the three channels (a – East, b – North, c – Up) of the station Q32
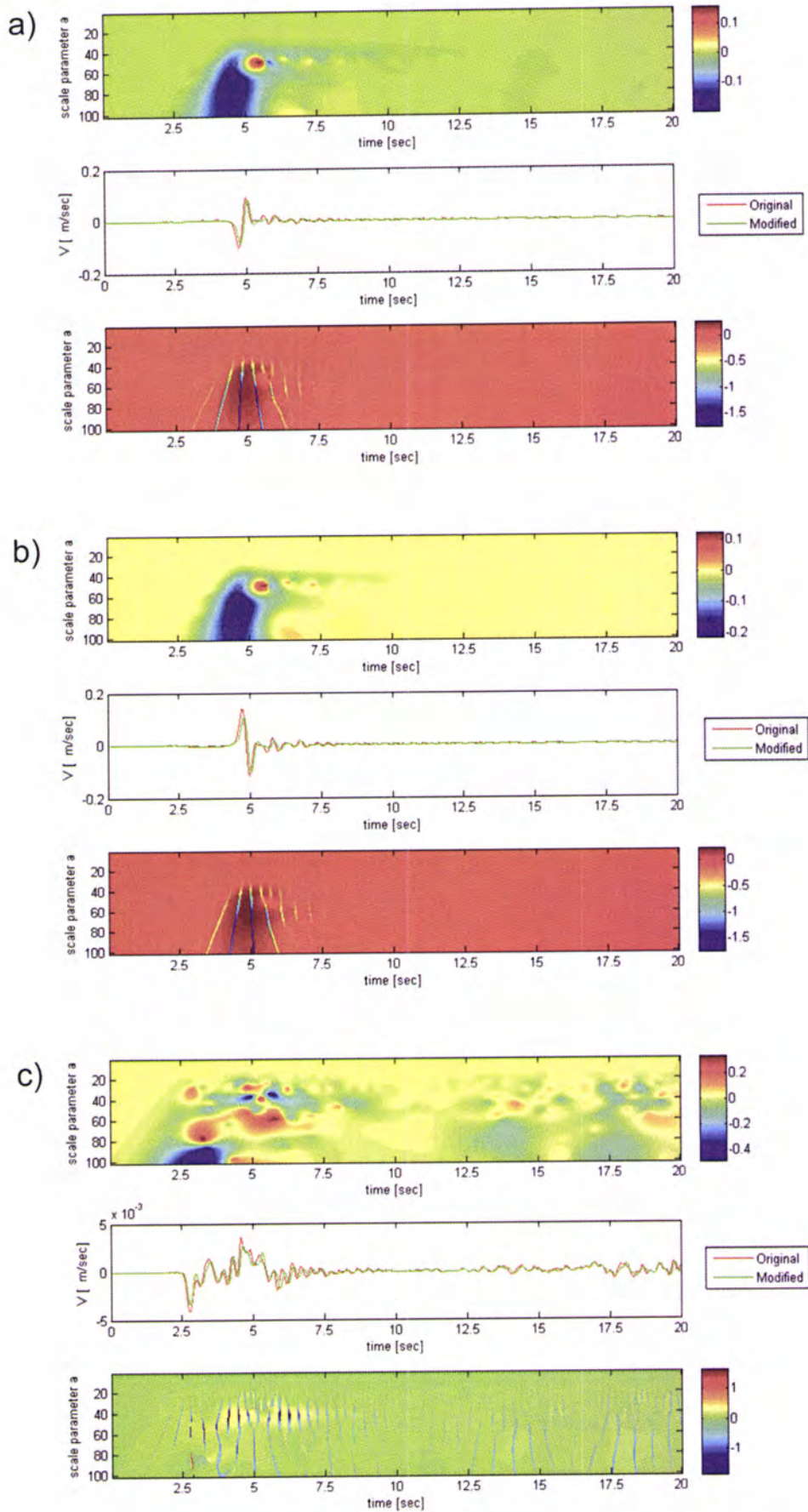
Fig. A6-a-i-5.Time-frequency envelope misfit (top), reference and comparison signals (middle) and time-frequency phase misfit (bottom) for the three channels (a – East, b – North, c – Up) of the station ROC

107
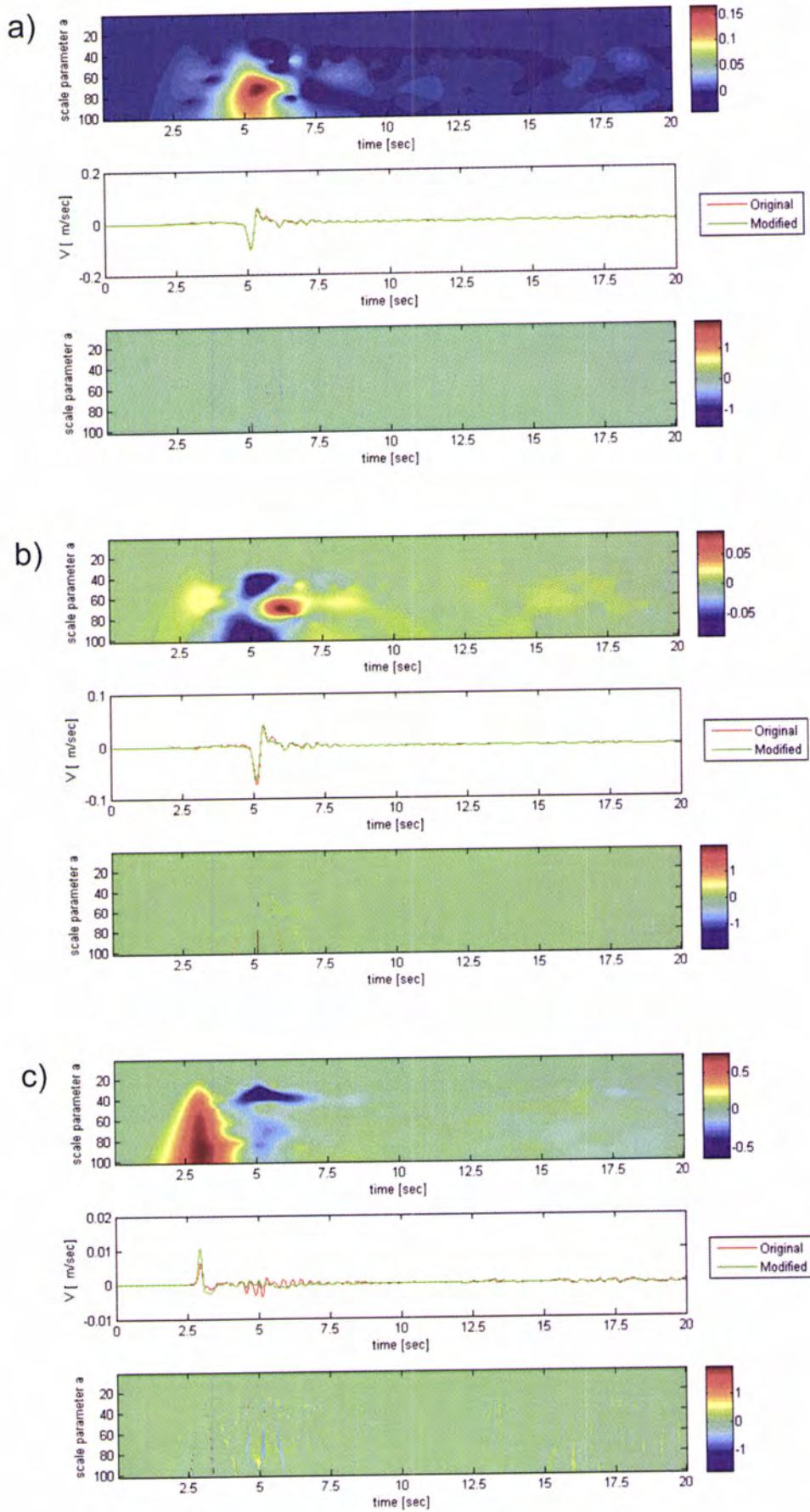
Fig. A6-a-i-6.Time-frequency envelope misfit (top), reference and comparison signals (middle) and time-frequency phase misfit (bottom) for the three channels (a – East, b – North, c – Up) of the station 1684

ii. Reference model: dip angle – 90^0, strike angle – 323^0

Modified model: dip angle – 80^0 dipping in the south-west direction, strike angle – 143^0, rake angle – 0^0
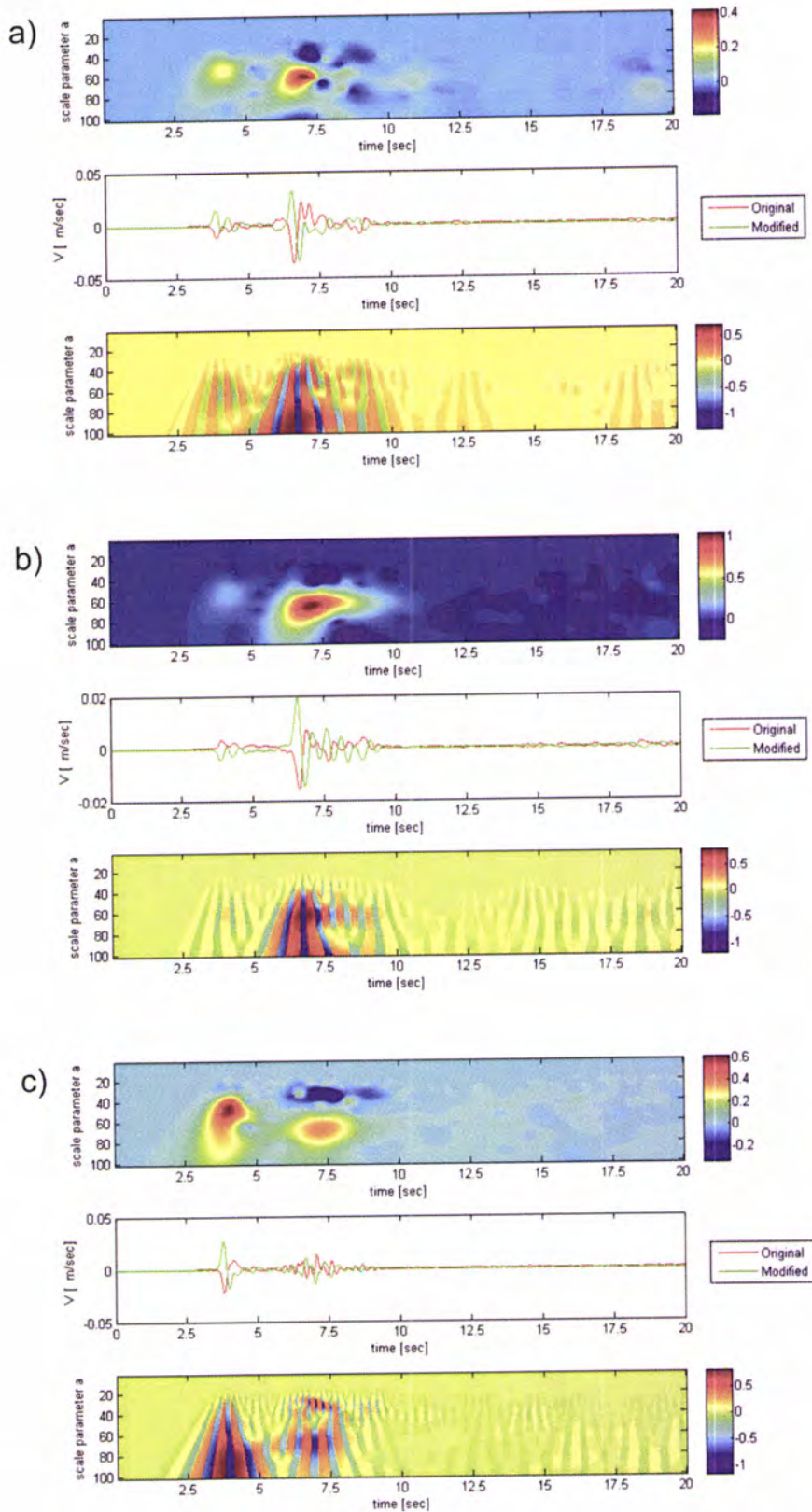
Fig. A6-a-ii-1.Time-frequency envelope misfit (top), reference and comparison signals (middle) and time-frequency phase misfit (bottom) for the three channels (a – East, b – North, c – Up) of the station 57950
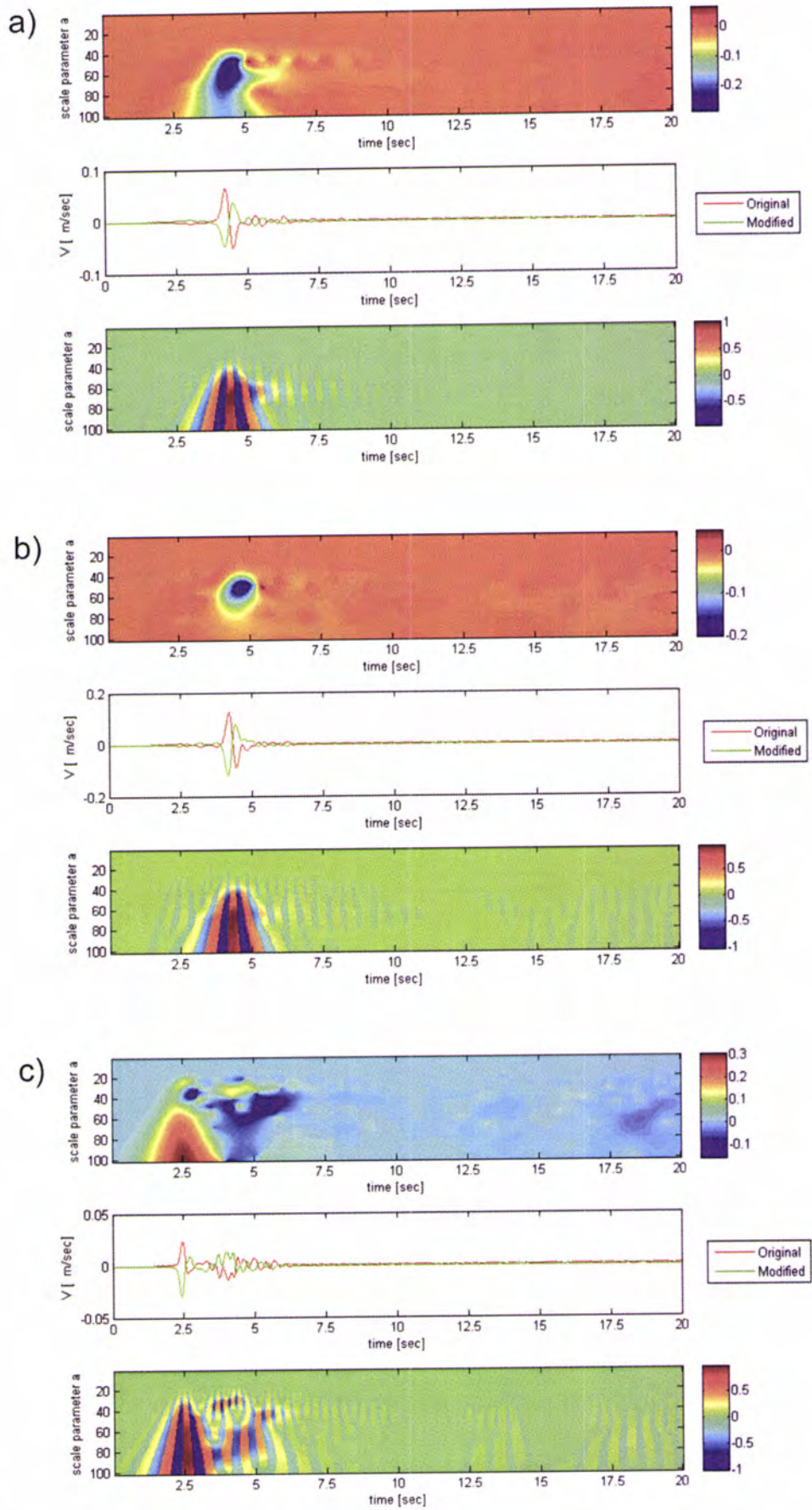
Fig. A6-a-ii-2.Time-frequency envelope misfit (top), reference and comparison signals (middle) and time-frequency phase misfit (bottom) for the three channels (a – East, b – North, c – Up) of the station CHR

110
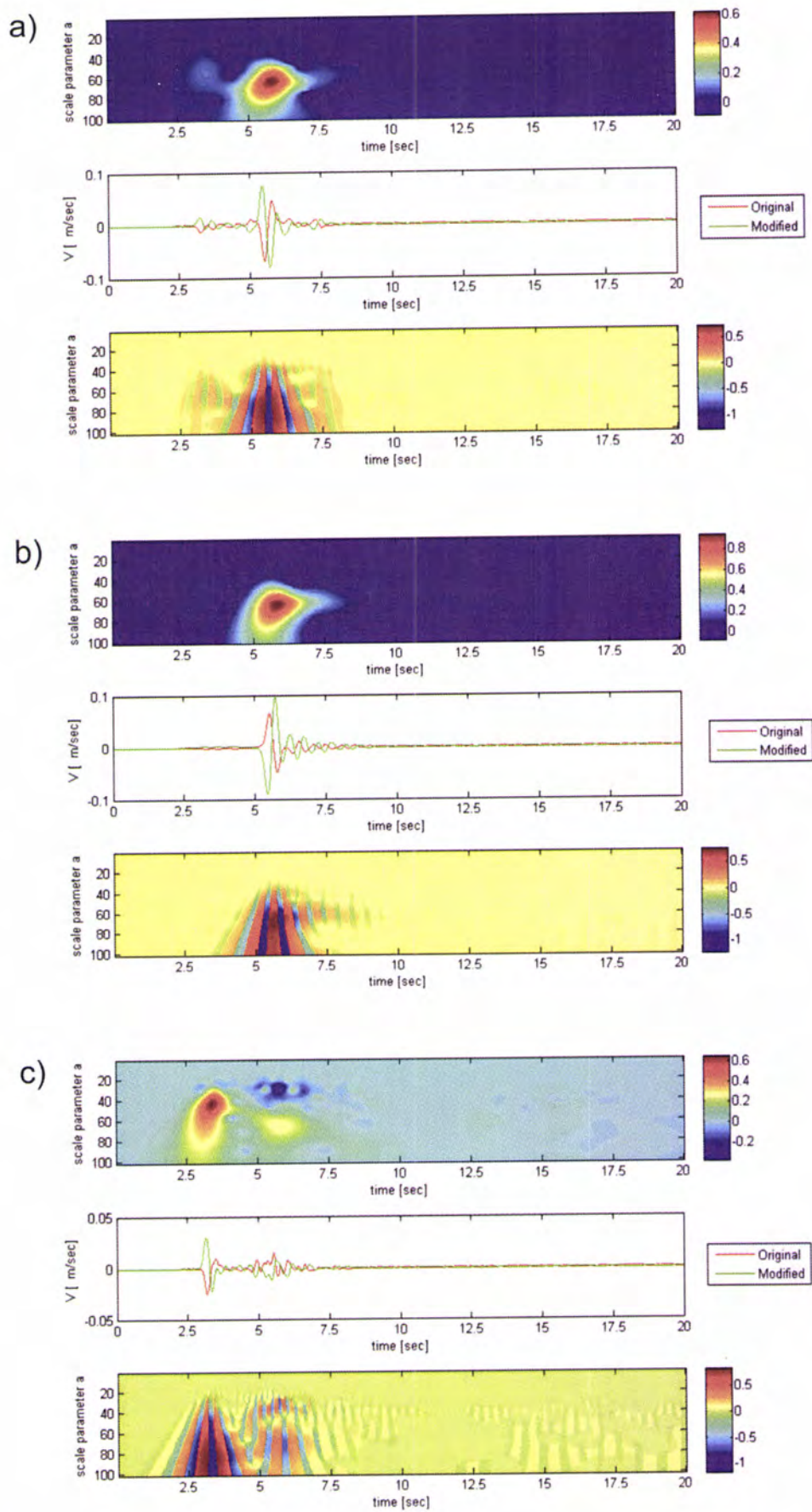
Fig. A6-a-ii-3.Time-frequency envelope misfit (top), reference and comparison signals (middle) and time-frequency phase misfit (bottom) for the three channels (a – East, b – North, c – Up) of the station MP3

111
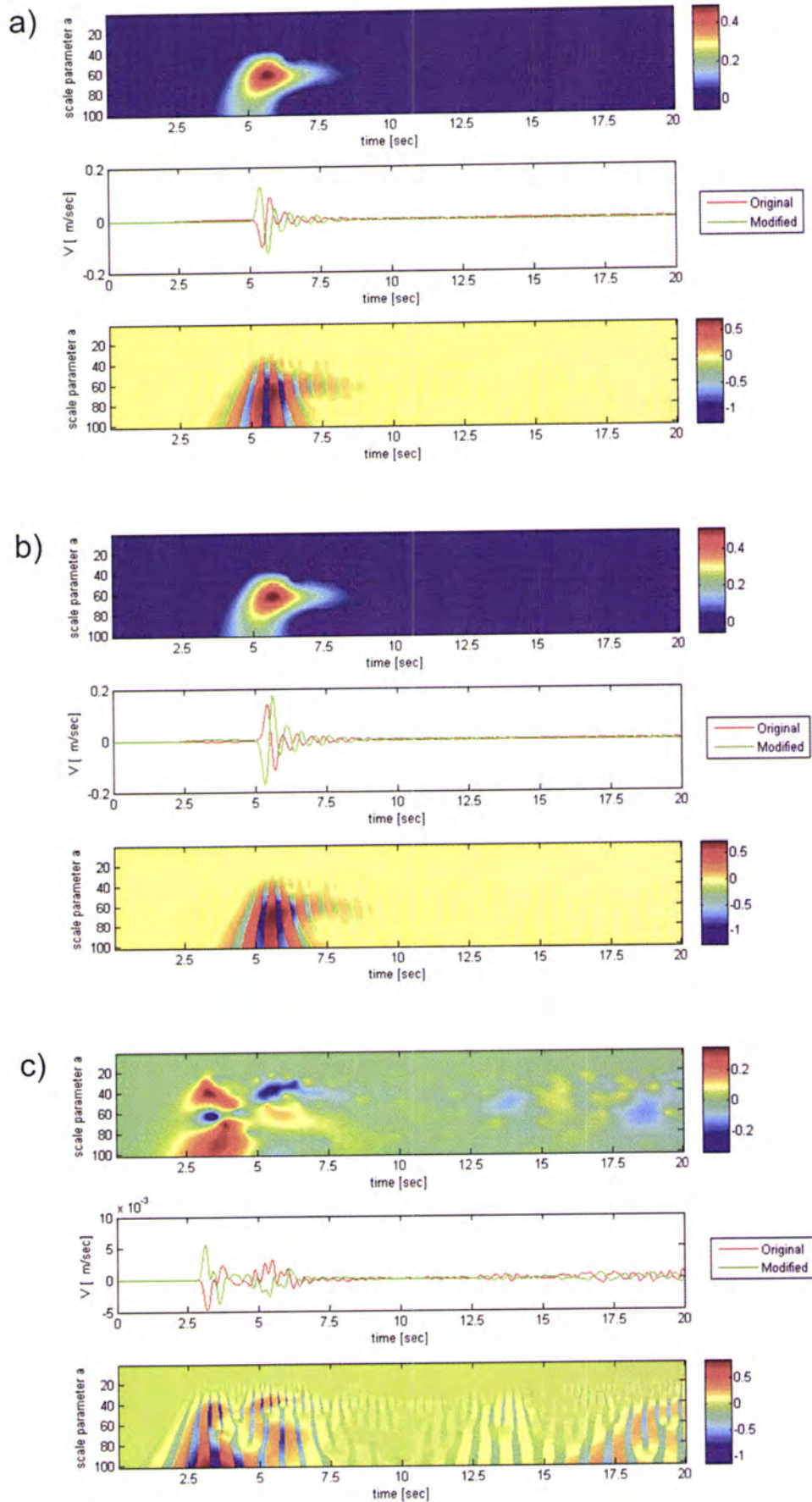
Fig. A6-a-ii-4.Time-frequency envelope misfit (top), reference and comparison signals (middle) and time-frequency phase misfit (bottom) for the three channels (a – East, b – North, c – Up) of the station Q32

112
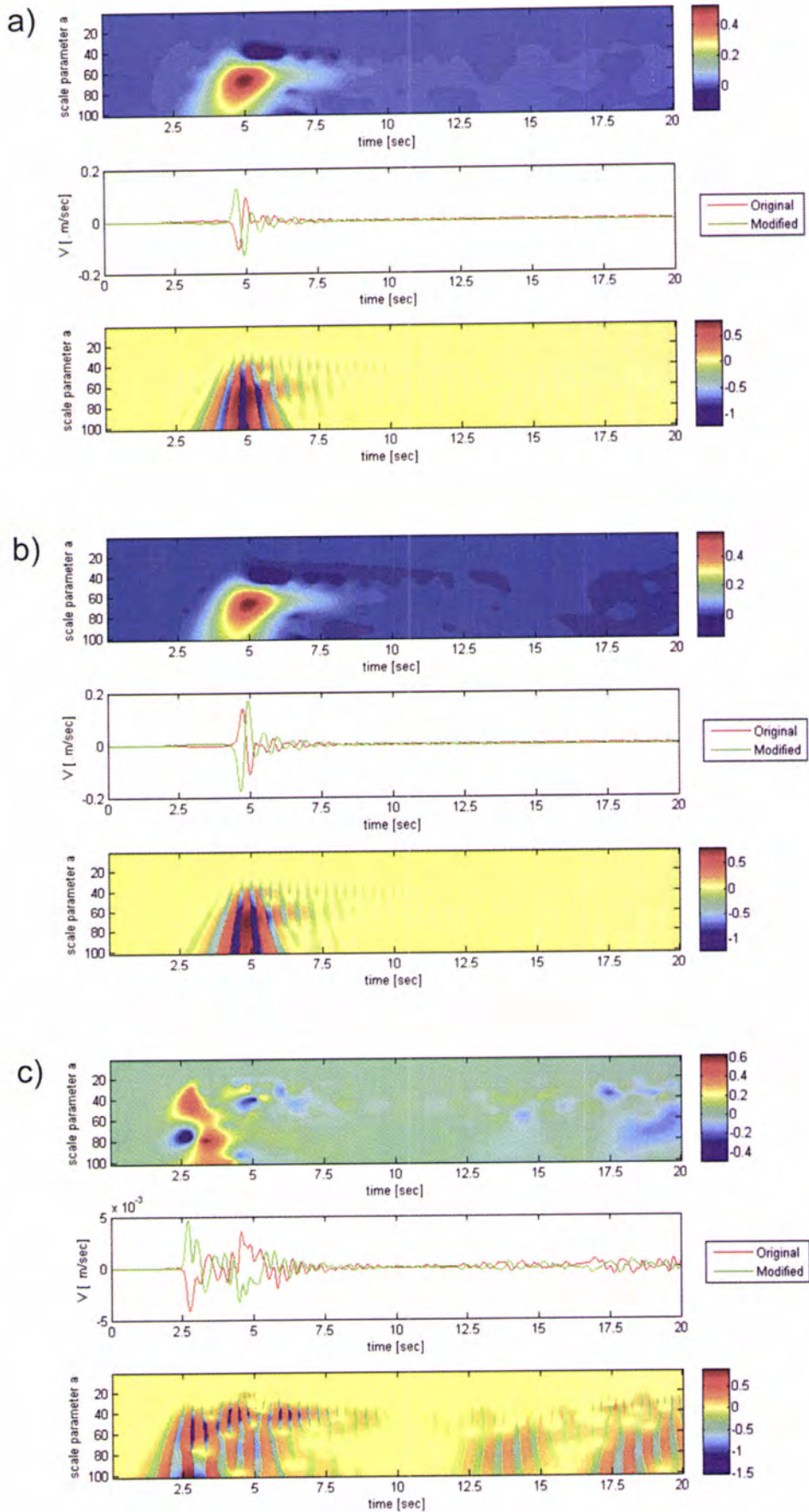
Fig. A6-a-ii-5.Time-frequency envelope misfit (top), reference and comparison signals (middle) and time-frequency phase misfit (bottom) for the three channels (a – East, b – North, c – Up) of the station ROC
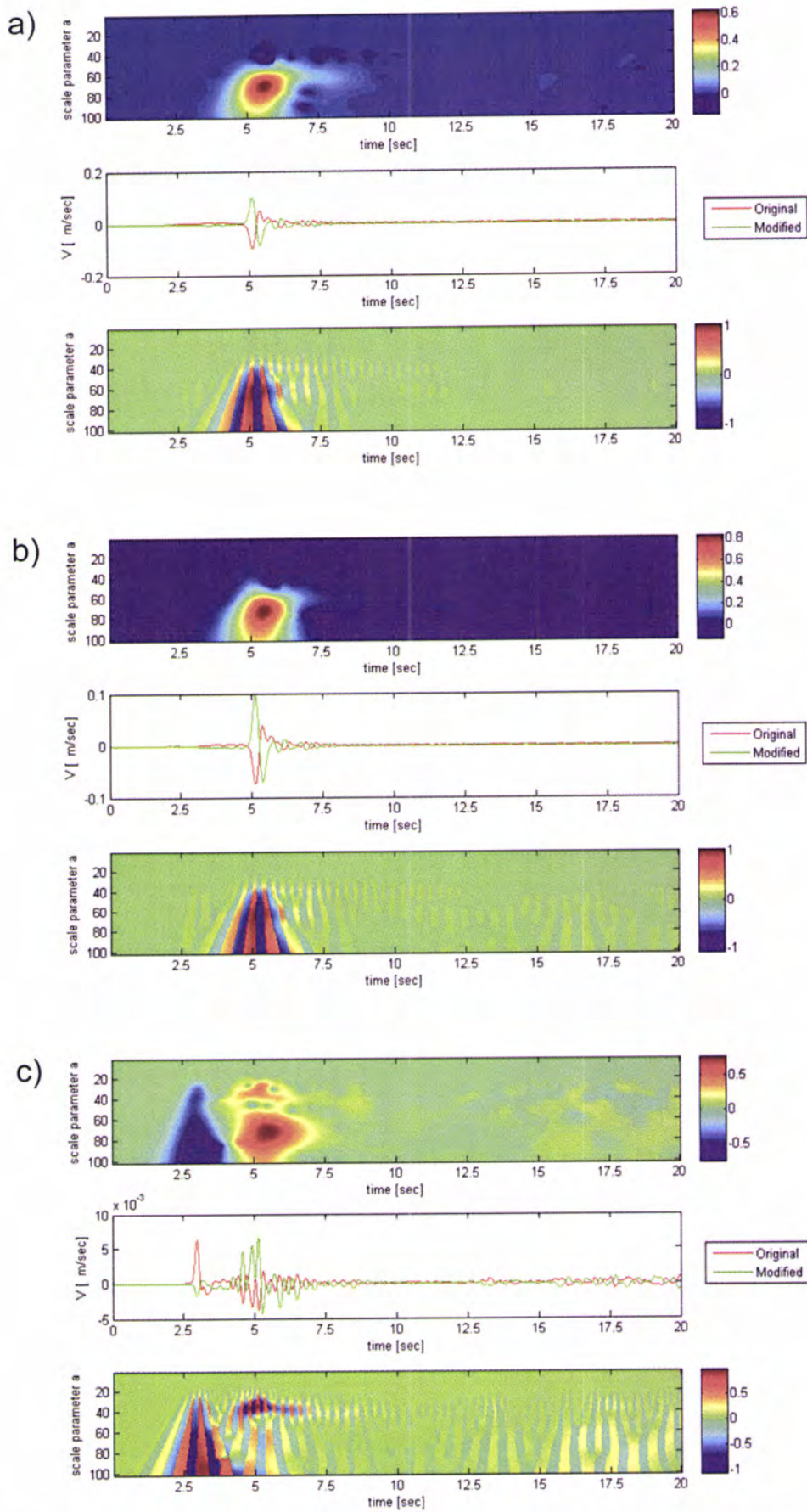
Fig. A6-a-ii-6.Time-frequency envelope misfit (top), reference and comparison signals (middle) and time-frequency phase misfit (bottom) for the three channels (a – East, b – North, c – Up) of the station 1684

i.   Reference model: strike angle – 323^0

Modified model: strike angle –308^0
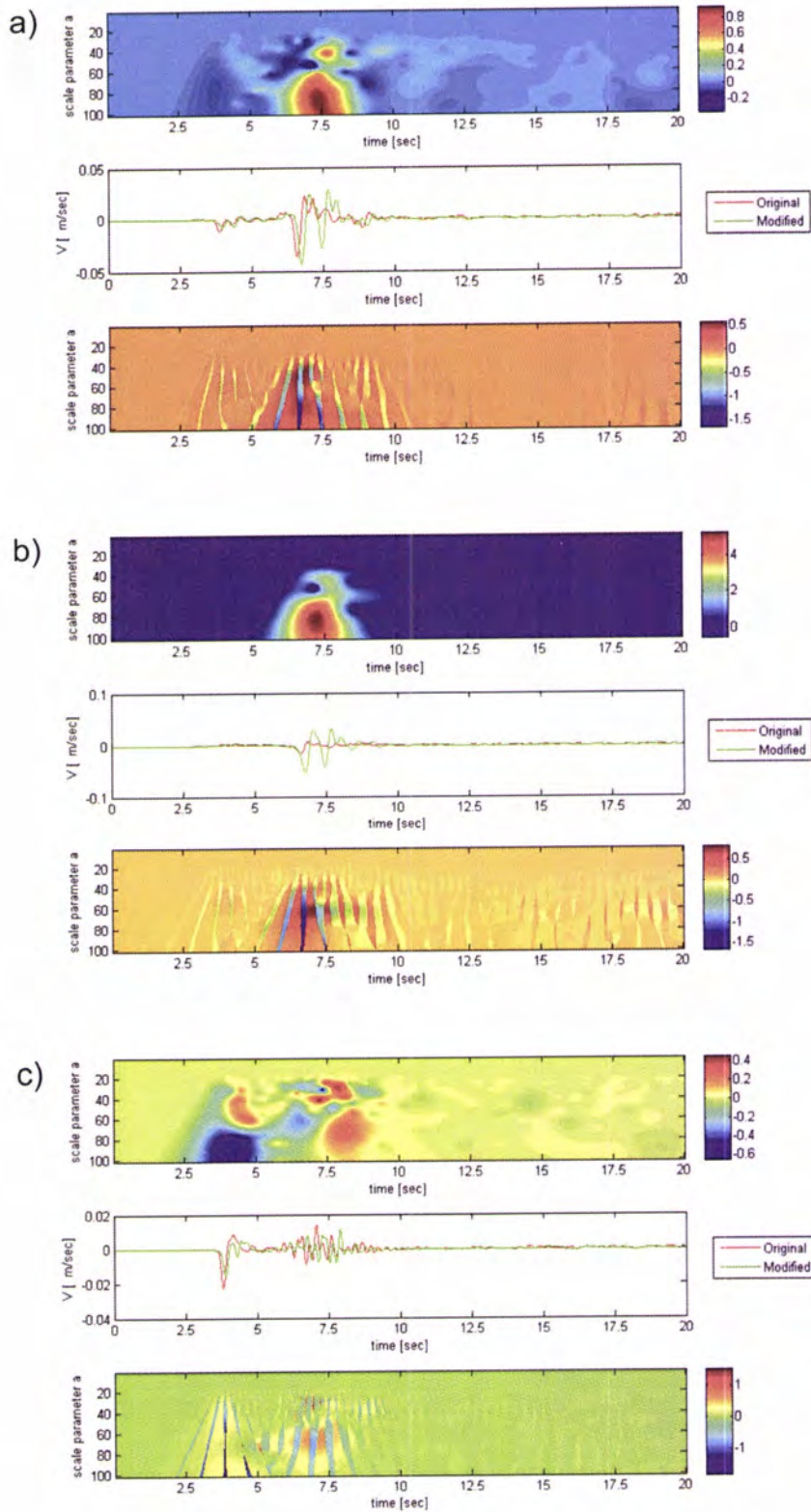
Fig. A6-b-i-1.Time-frequency envelope misfit (top), reference and comparison signals (middle) and time-frequency phase misfit (bottom) for the three channels (a – East, b – North, c – Up) of the station 57950

115
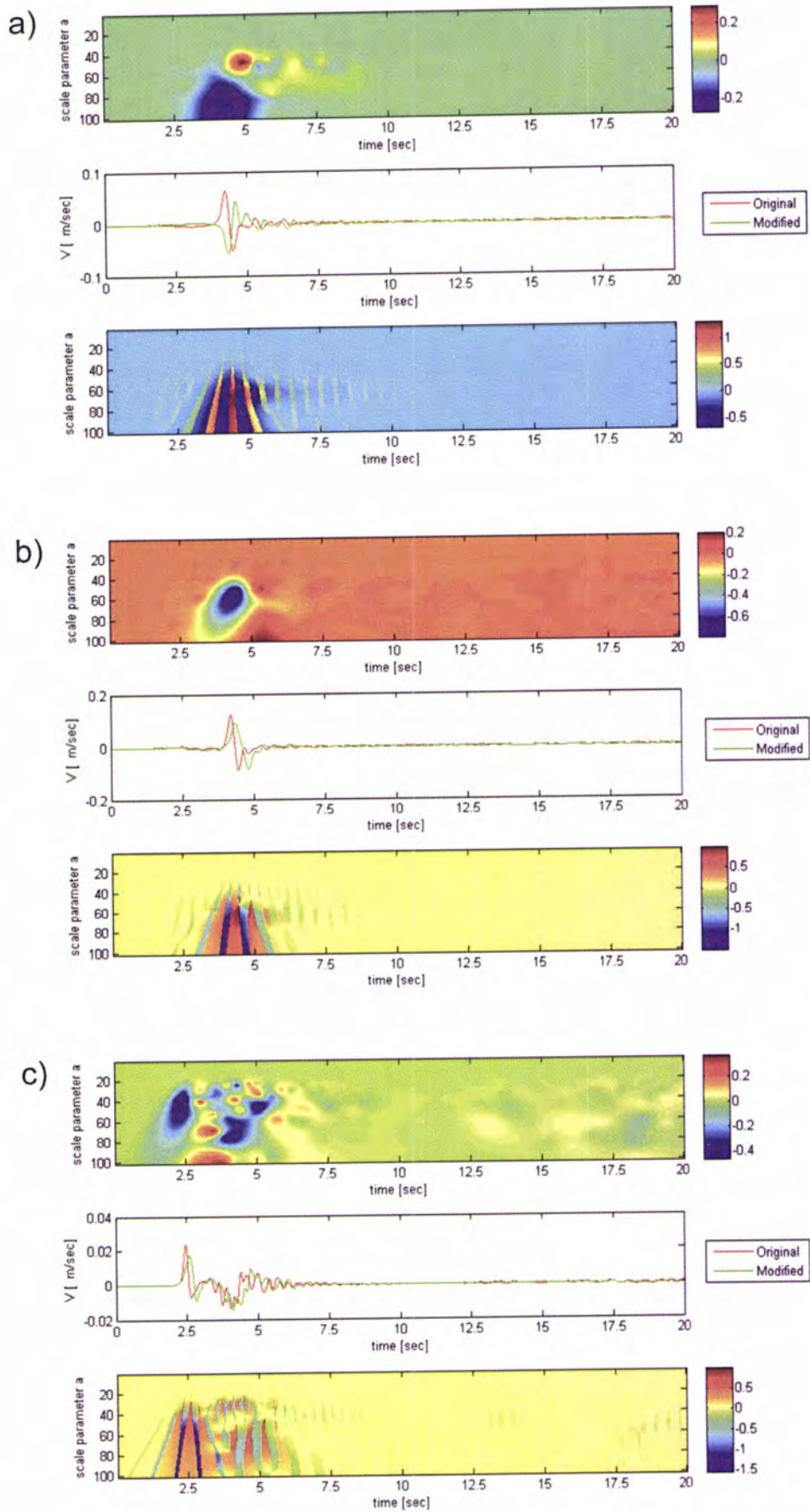
Fig. A6-b-i-2.Time-frequency envelope misfit (top), reference and comparison signals (middle) and time-frequency phase misfit (bottom) for the three channels (a – East, b – North, c – Up) of the station CHR
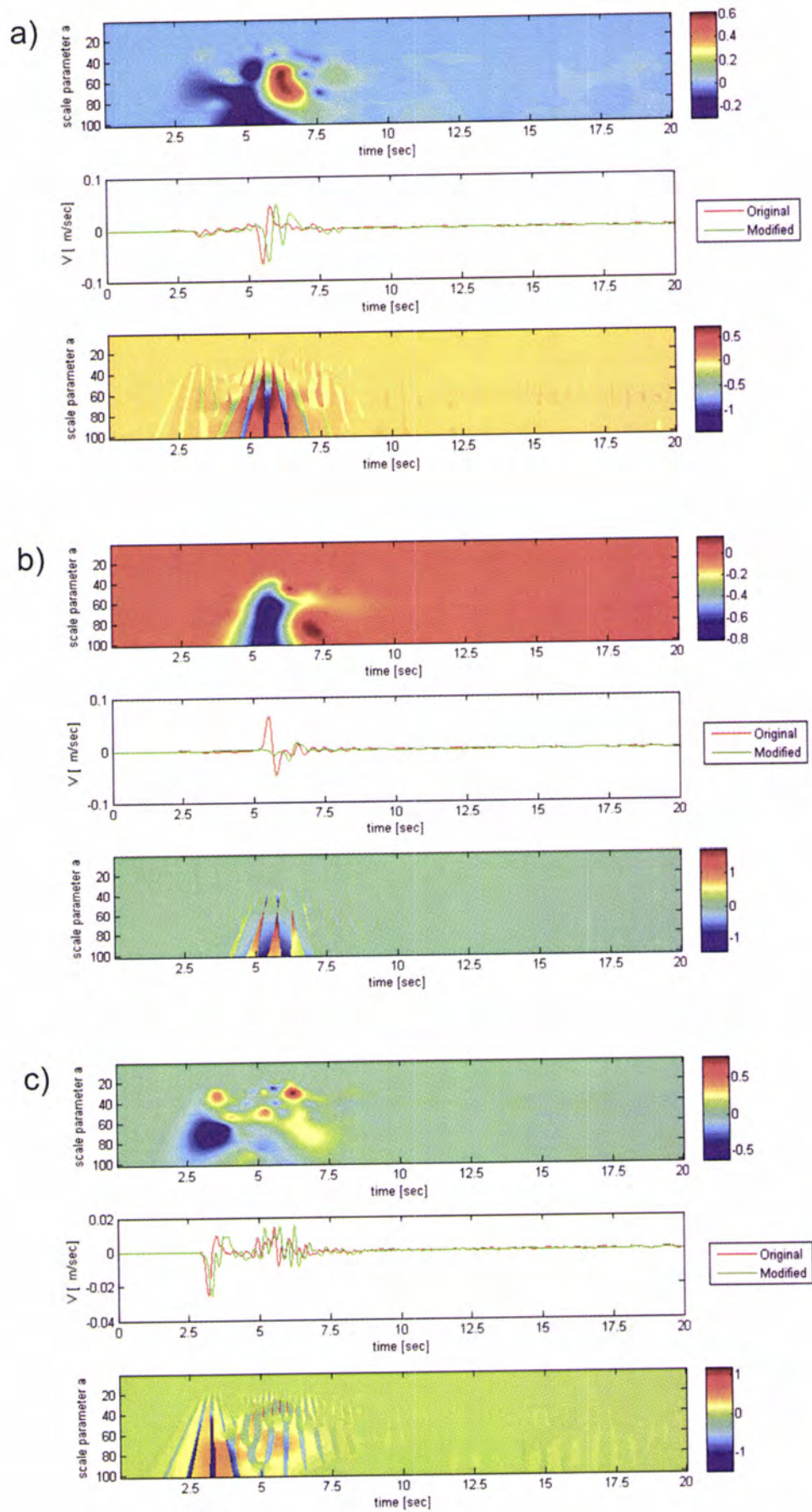
Fig. A6-b-i-3.Time-frequency envelope misfit (top), reference and comparison signals (middle)
and time-frequency phase misfit (bottom) for the three channels (a – East, b – North, c – Up) of
the station MP3

117
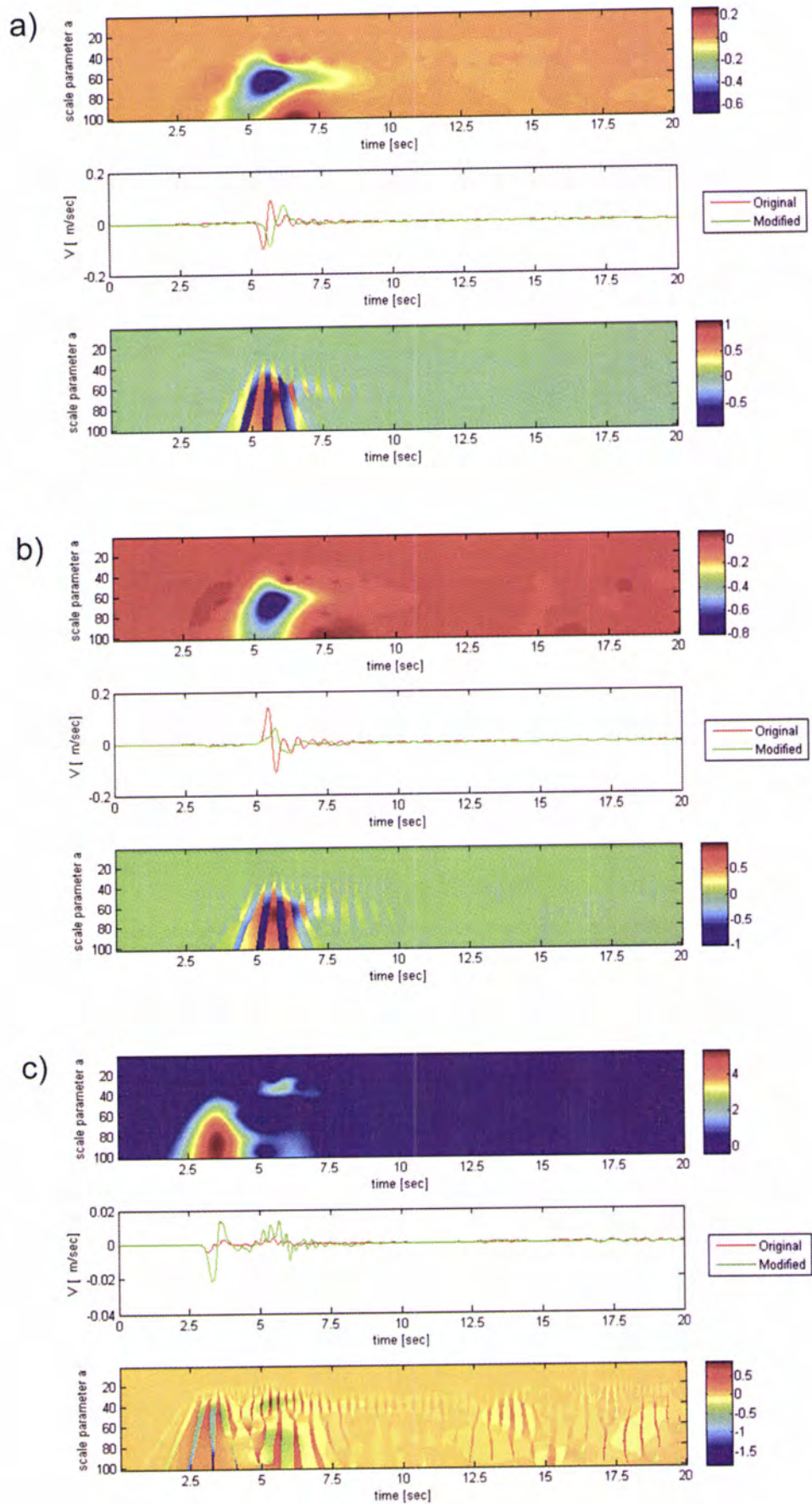
Fig. A6-b-i-4.Time-frequency envelope misfit (top), reference and comparison signals (middle) and time-frequency phase misfit (bottom) for the three channels (a – East, b – North, c – Up) of the station Q32

118
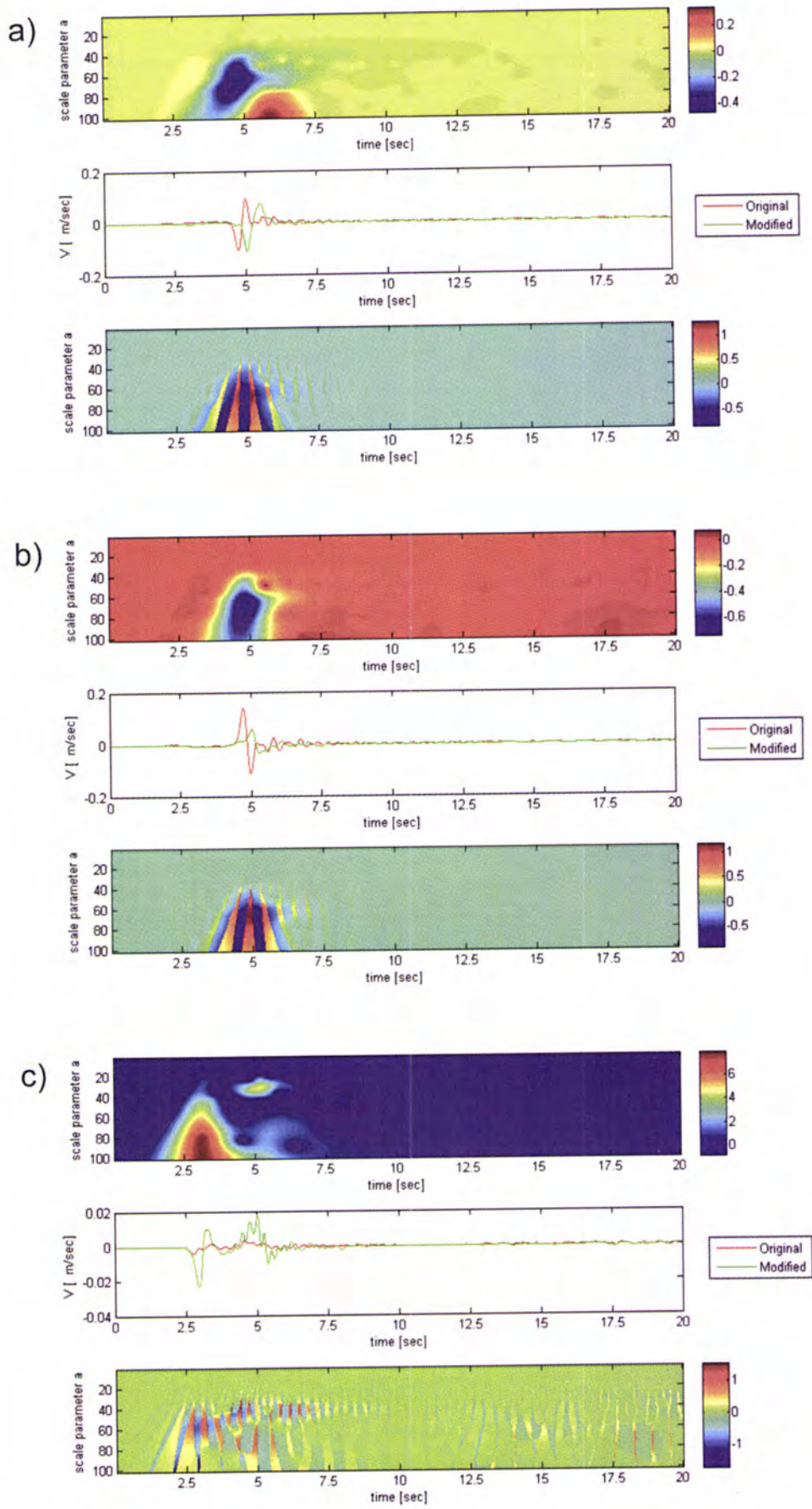
Fig. A6-b-i-5.Time-frequency envelope misfit (top), reference and comparison signals (middle)
and time-frequency phase misfit (bottom) for the three channels (a – East, b – North, c – Up) of
the station ROC

119
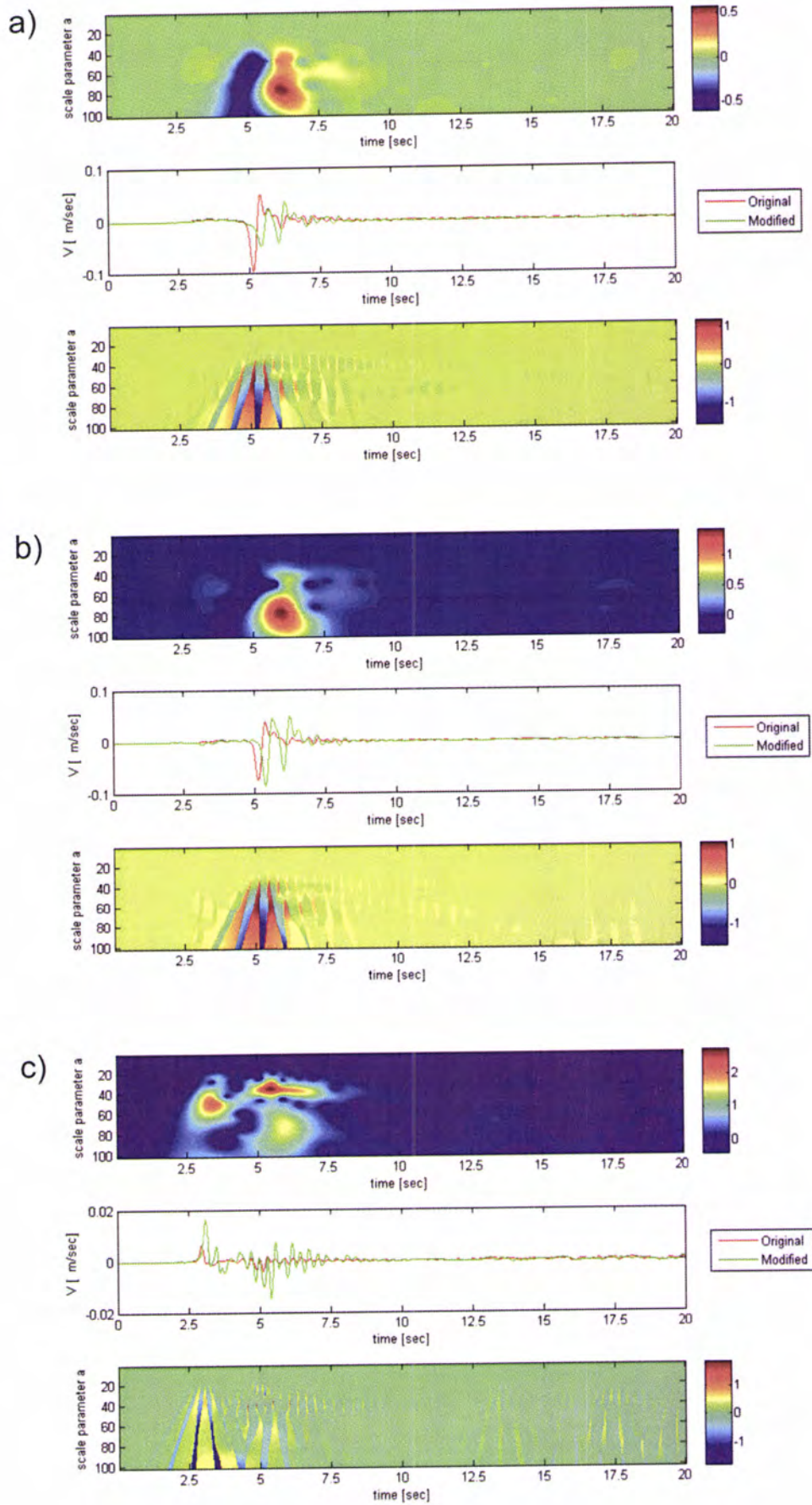
Fig. A6-b-i-6.Time-frequency envelope misfit (top), reference and comparison signals (middle) and time-frequency phase misfit (bottom) for the three channels (a – East, b – North, c – Up) of the station 1684

Fig. A6-b-ii-1.Time-frequency envelope misfit (top), reference and comparison signals (middle) and time-frequency phase misfit (bottom) for the three channels (a – East, b – North, c – Up) of the station 57950

121
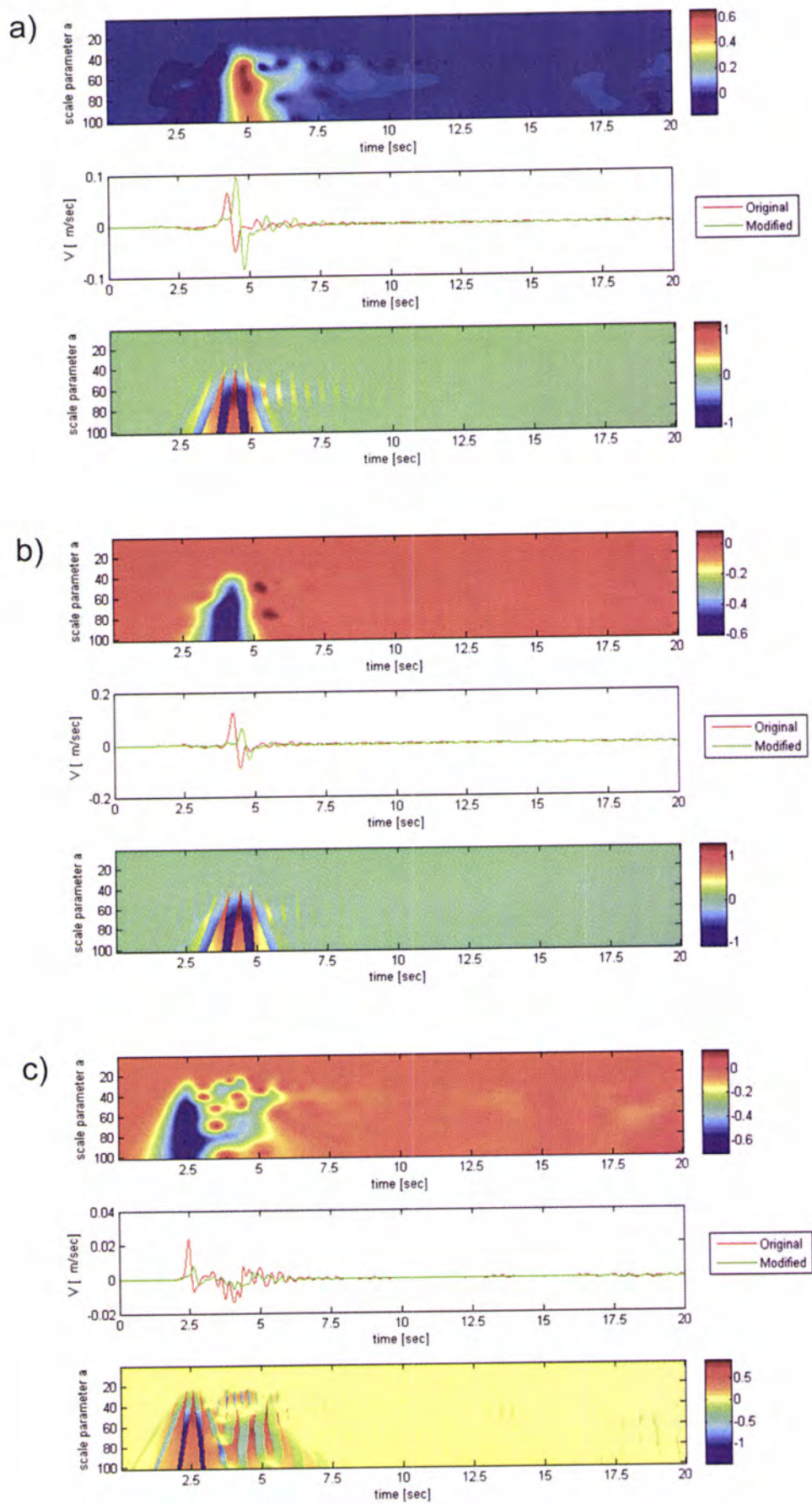
Fig. A6-b-ii-2.Time-frequency envelope misfit (top), reference and comparison signals (middle) and time-frequency phase misfit (bottom) for the three channels (a – East, b – North, c – Up) of the station CHR
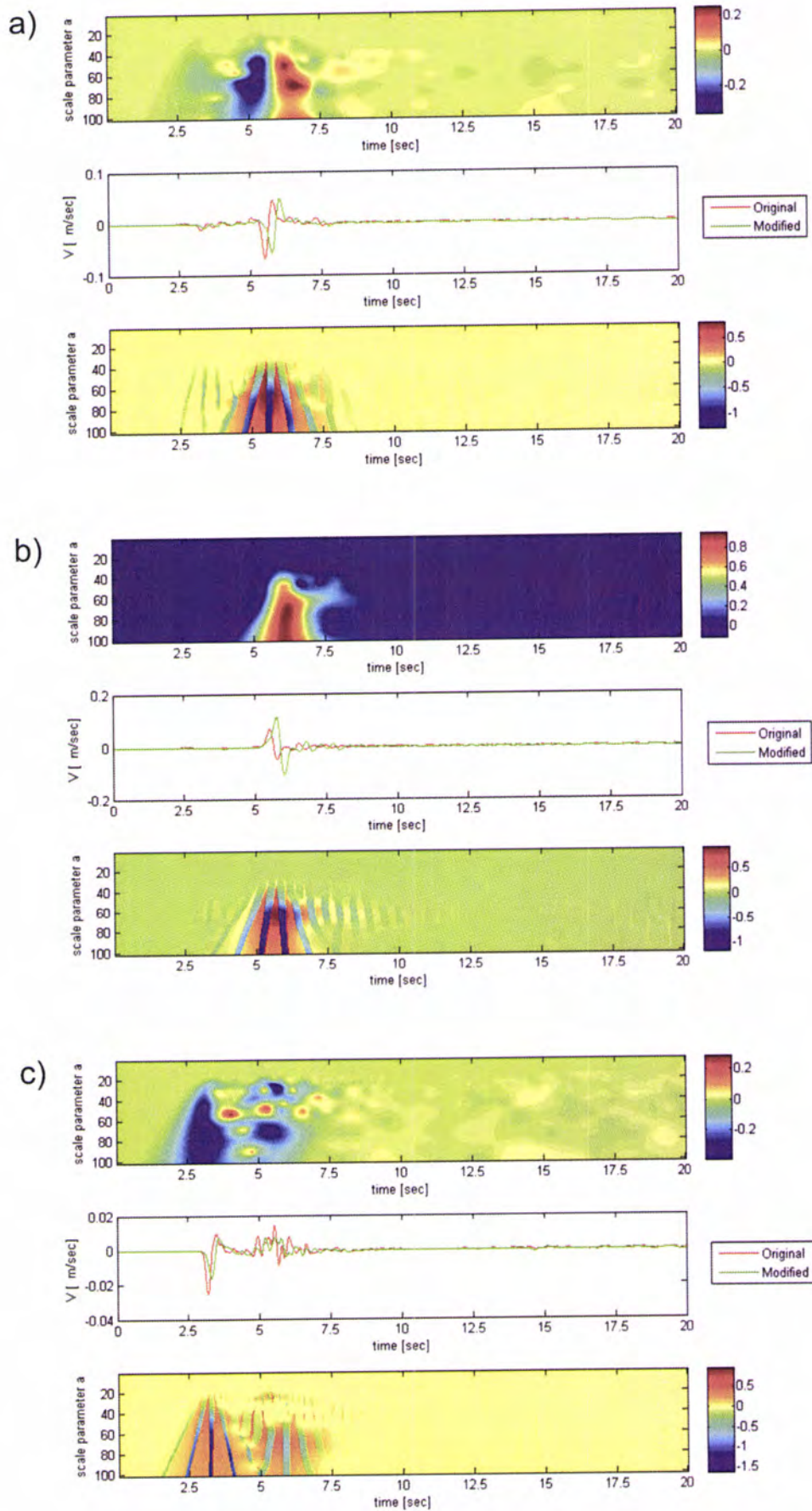
Fig. A6-b-ii-3.Time-frequency envelope misfit (top), reference and comparison signals (middle) and time-frequency phase misfit (bottom) for the three channels (a – East, b – North, c – Up) of the station MP3
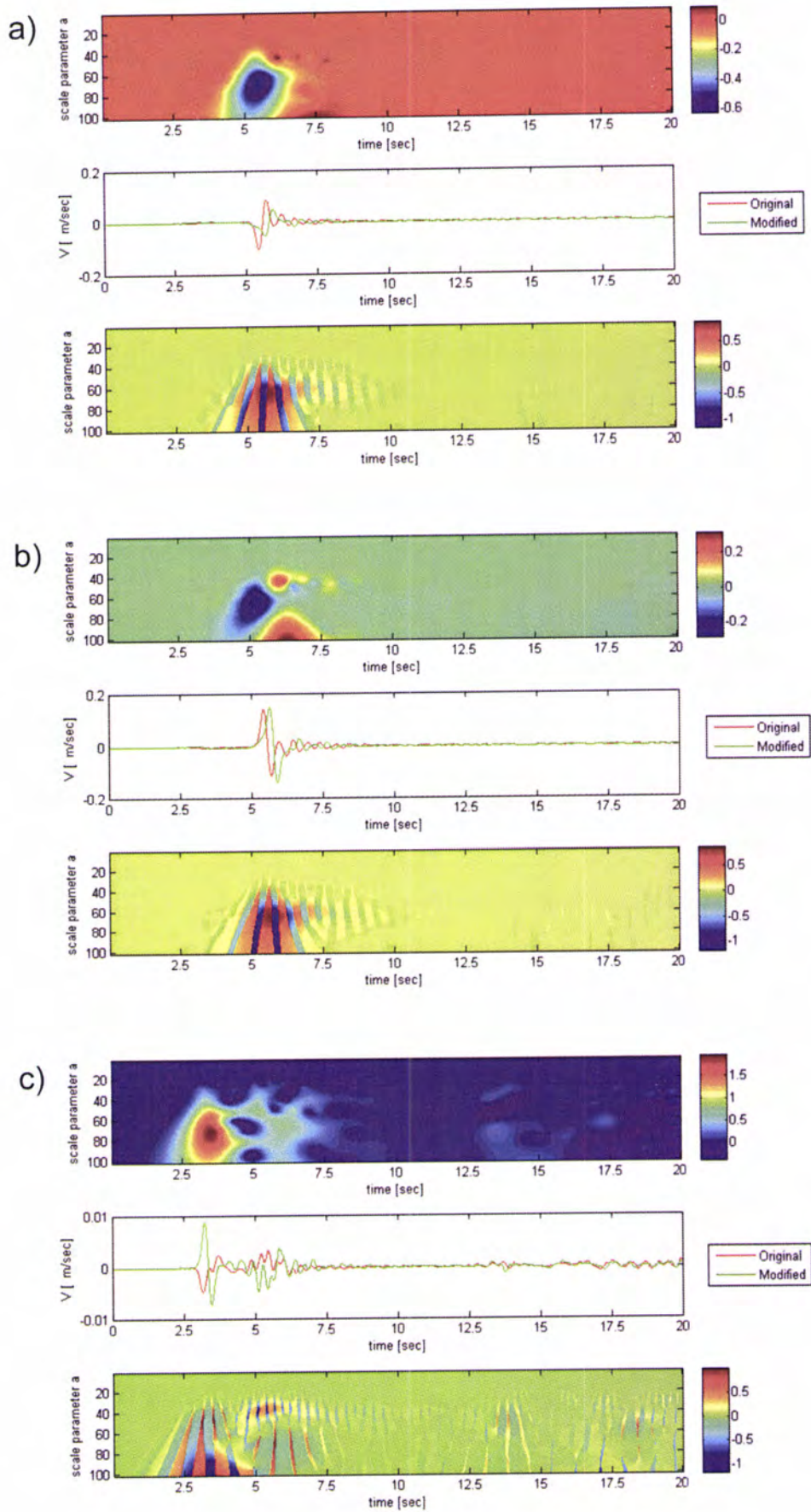
Fig. A6-b-ii-4.Time-frequency envelope misfit (top), reference and comparison signals (middle) and time-frequency phase misfit (bottom) for the three channels (a – East, b – North, c – Up) of the station Q32
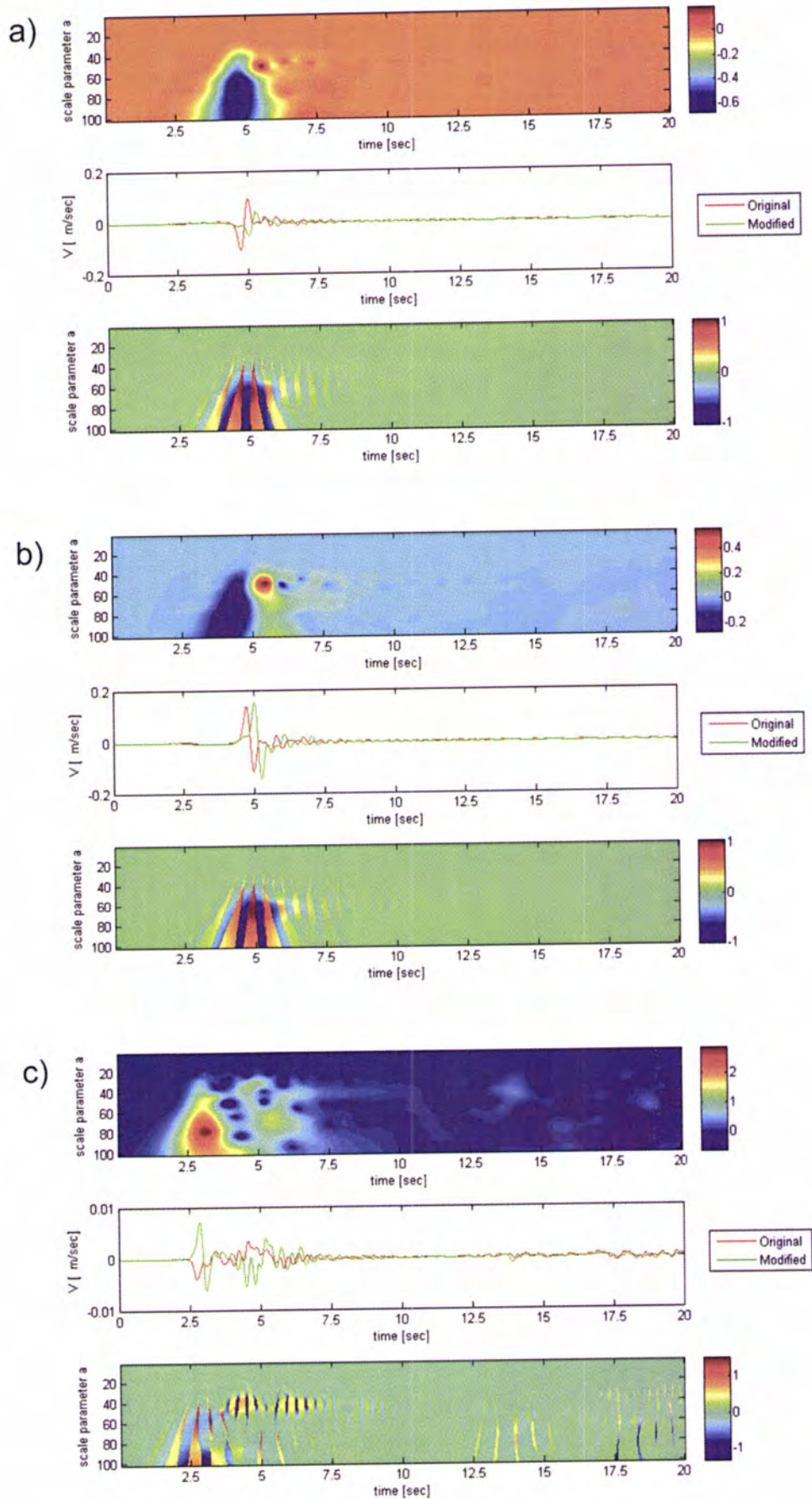
Fig. A6-b-ii-5.Time-frequency envelope misfit (top), reference and comparison signals (middle) and time-frequency phase misfit (bottom) for the three channels (a – East, b – North, c – Up) of the station ROC

125
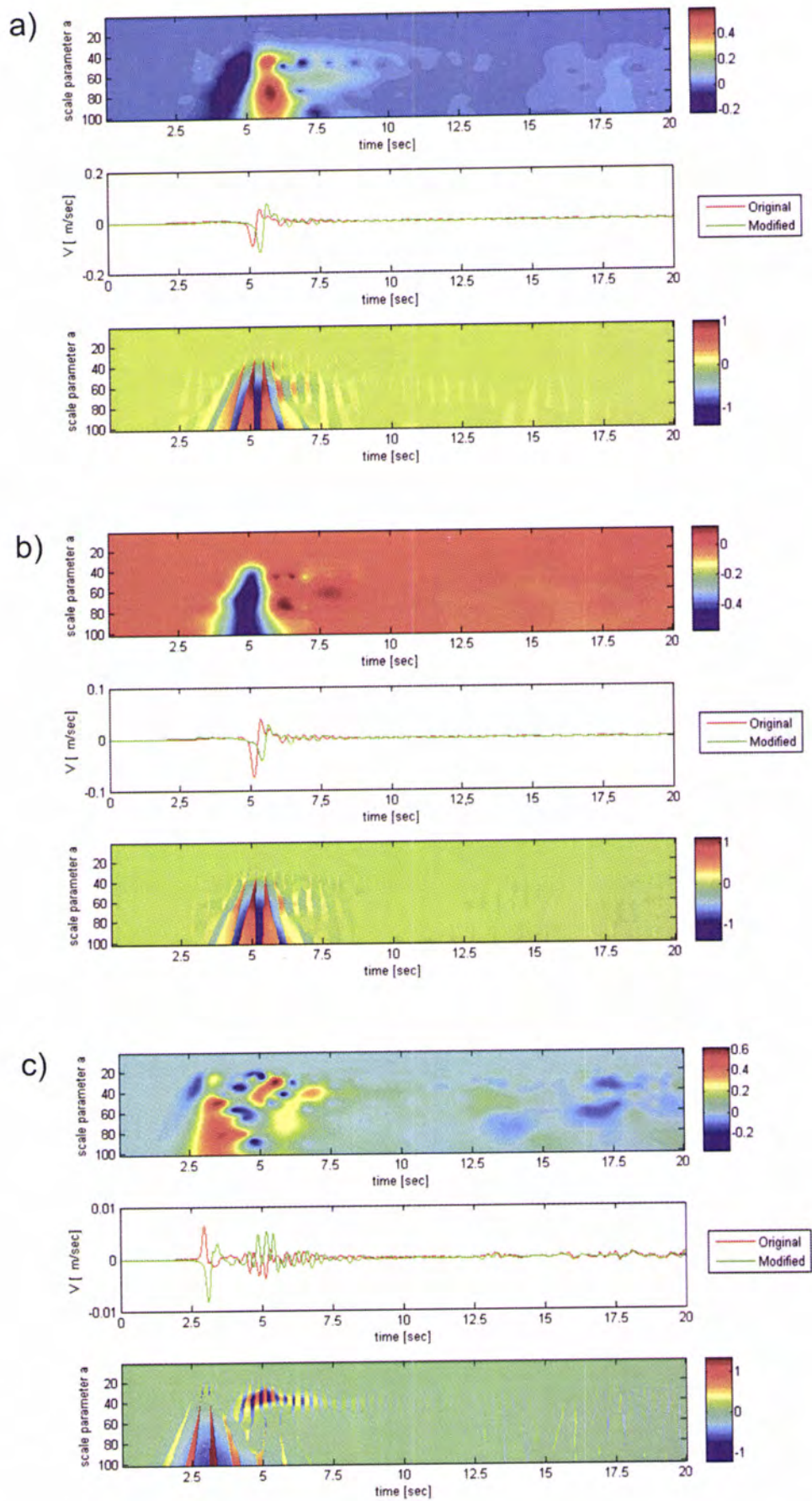
Fig. A6-b-ii-6.Time-frequency envelope misfit (top), reference and comparison signals (middle) and time-frequency phase misfit (bottom) for the three channels (a – East, b – North, c – Up) of the station 1684

126

c. Comparison of originally synthesized waveforms with waveforms obtained using model with modified fault plane length

Reference model: fault plane length–9 km

Modified model: fault plane length–13.5 km
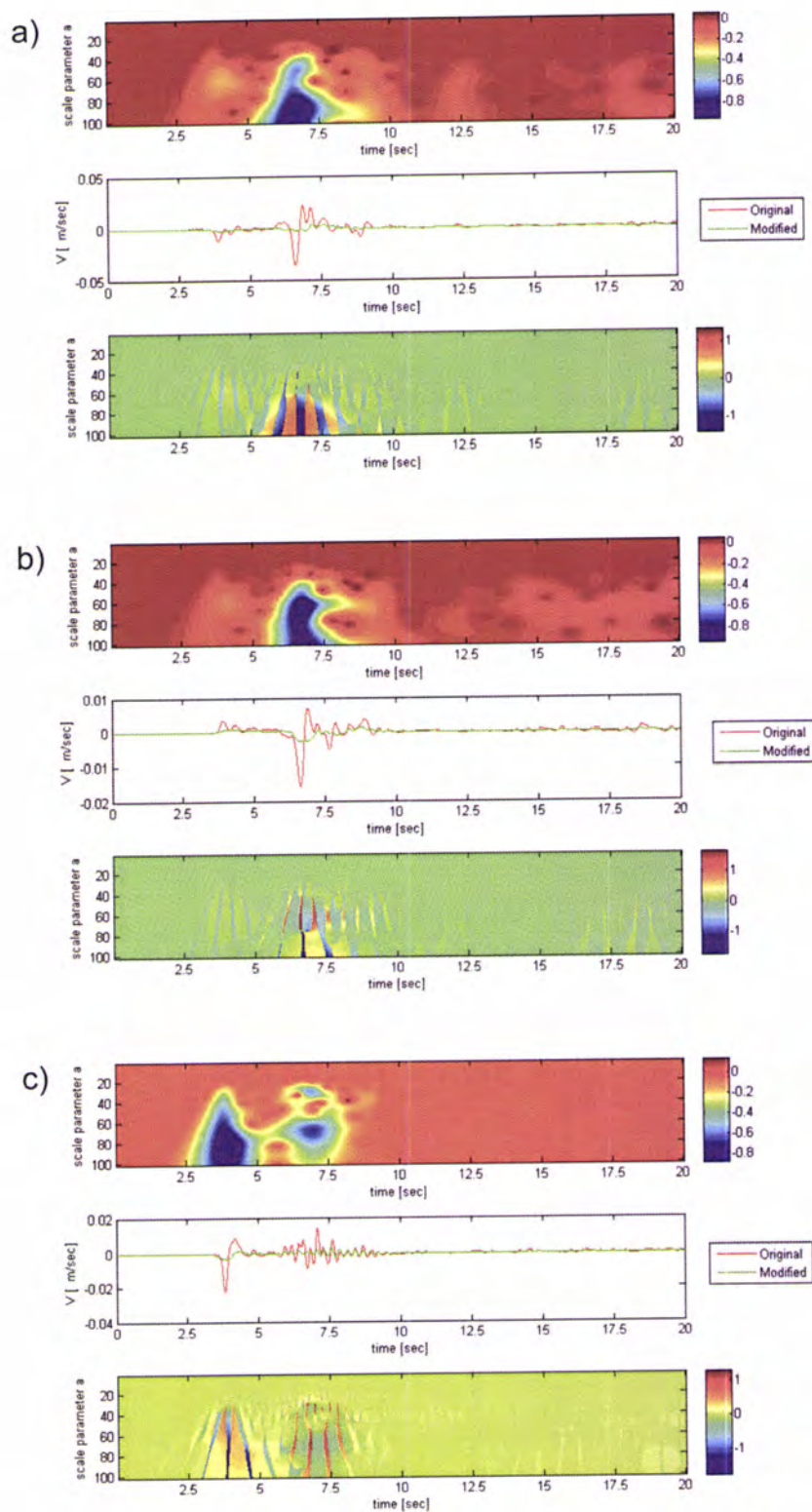
Fig. A6-c-1.Time-frequency envelope misfit (top), reference and comparison signals (middle) and time-frequency phase misfit (bottom) for the three channels (a – East, b – North, c –Up) of the station 57950
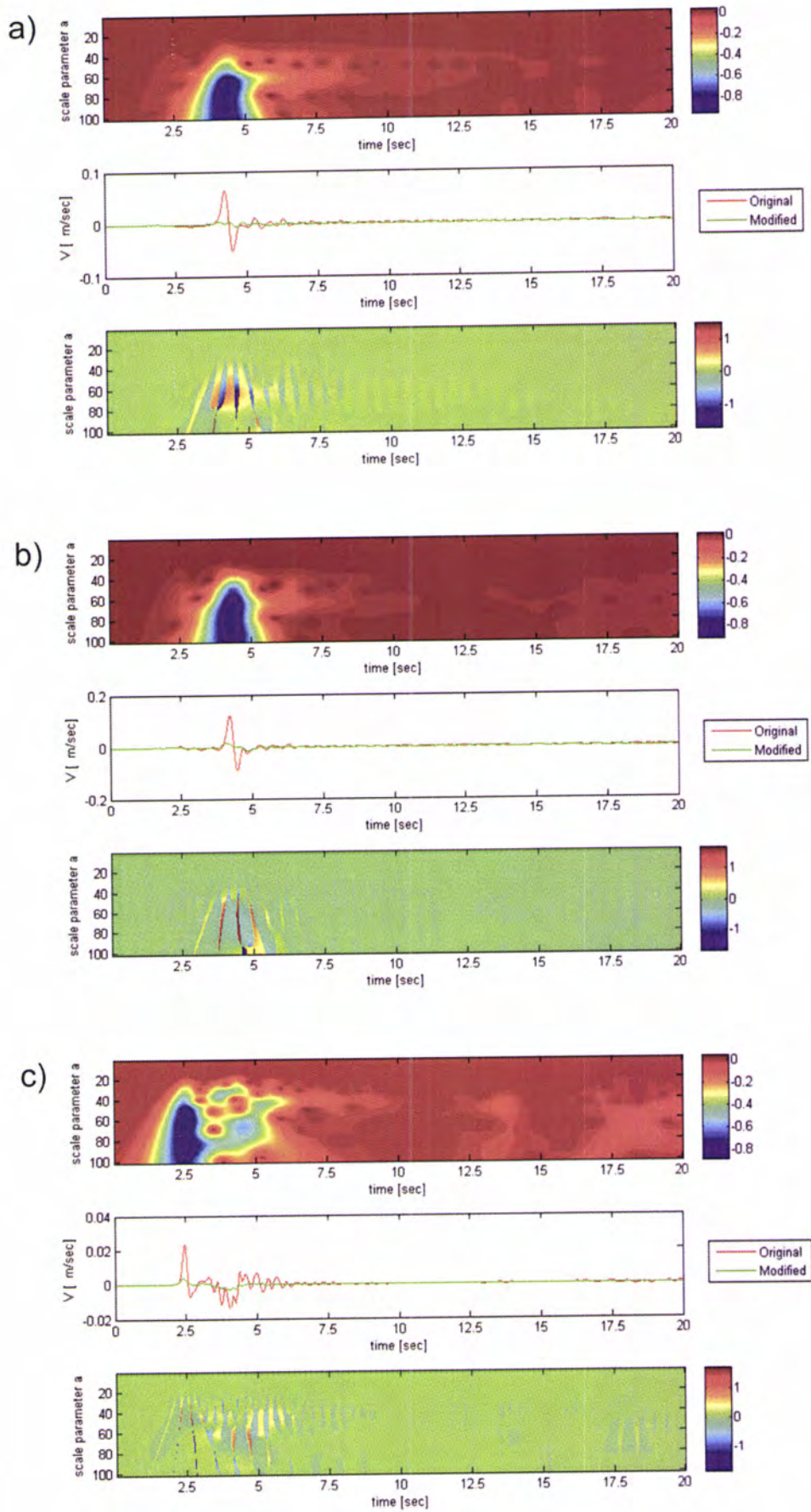
Fig. A6-c-2.Time-frequency envelope misfit (top), reference and comparison signals (middle) and time-frequency phase misfit (bottom) for the three channels (a – East, b – North, c – Up) of the station CHR

128
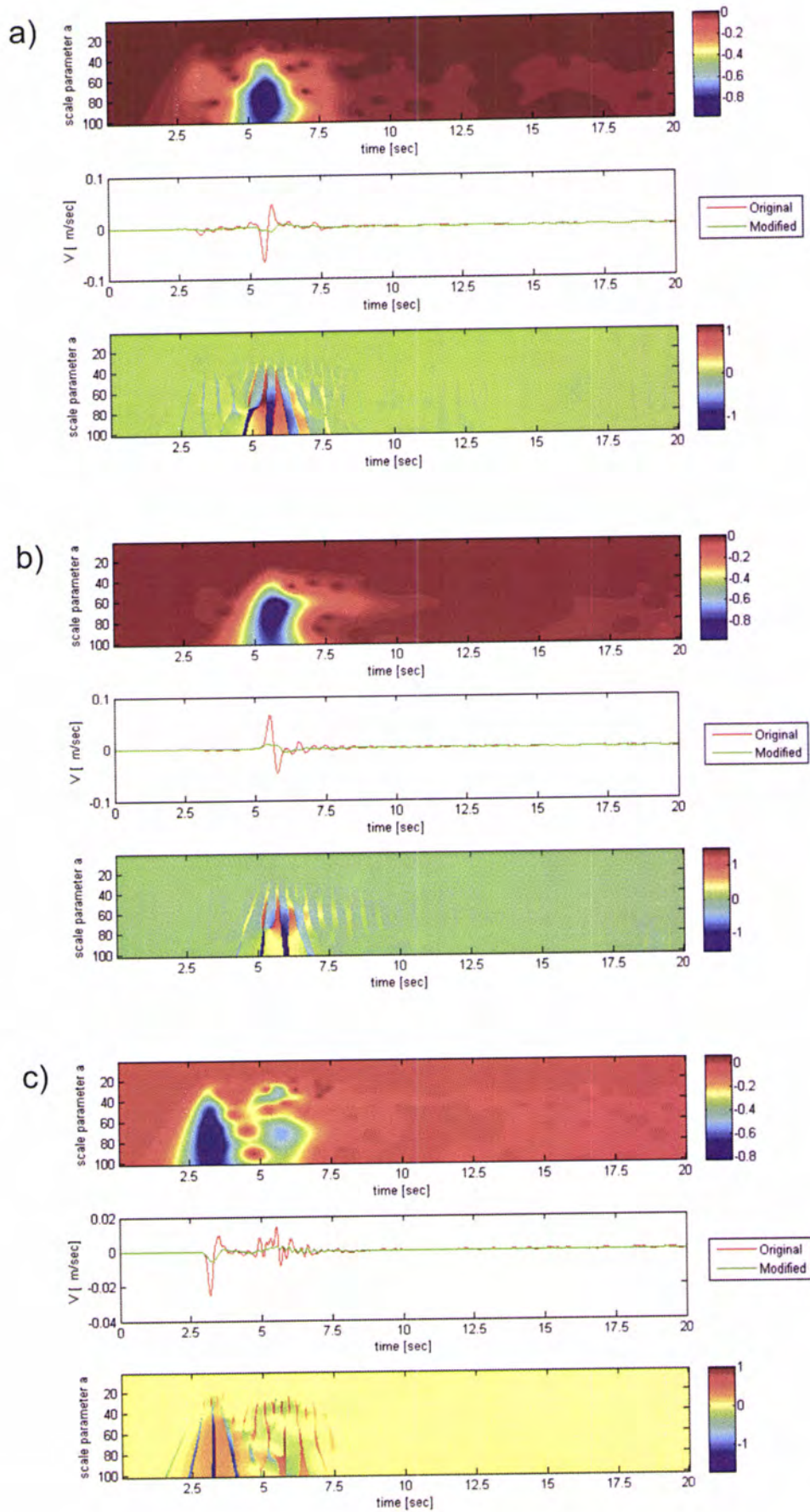
Fig. A6-c-3.Time-frequency envelope misfit (top), reference and comparison signals (middle) and time-frequency phase misfit (bottom) for the three channels (a – East, b – North, c – Up) of the station MP3

129
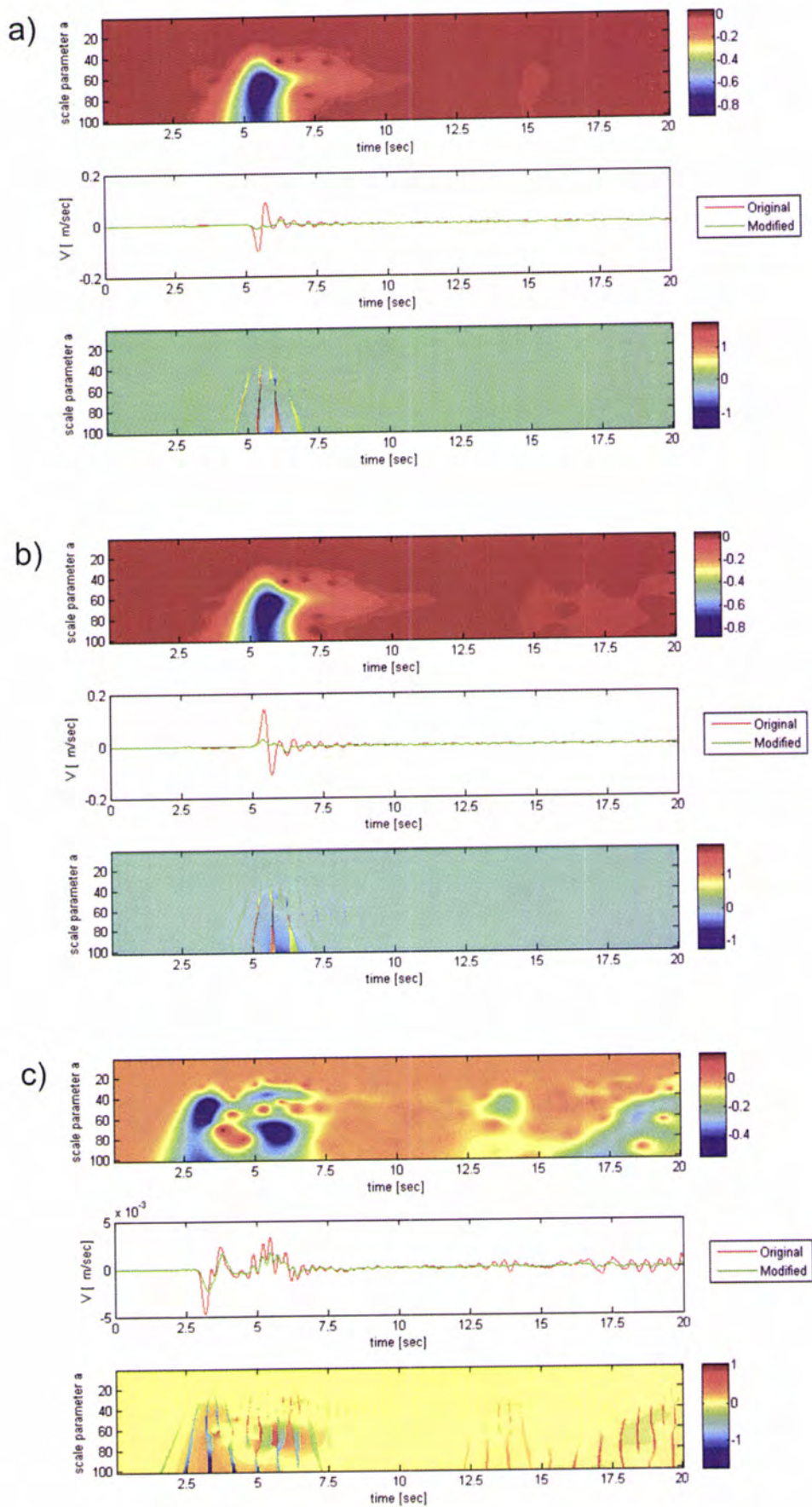
Fig. A6-c-4.Time-frequency envelope misfit (top), reference and comparison signals (middle) and time-frequency phase misfit (bottom) for the three channels (a – East, b – North, c – Up) of the station Q32
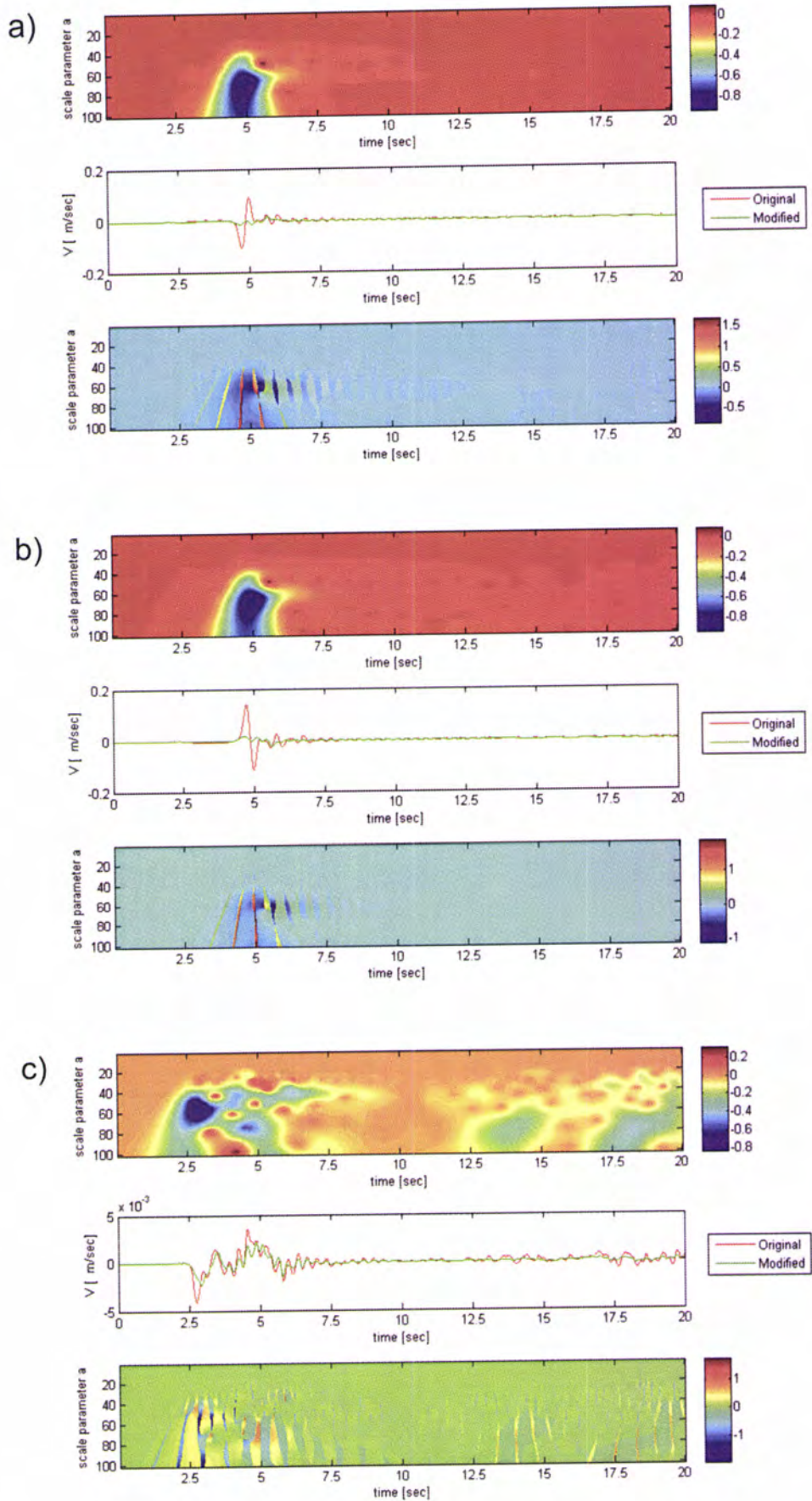
Fig. A6-c-5.Time-frequency envelope misfit (top), reference and comparison signals (middle) and time-frequency phase misfit (bottom) for the three channels (a – East, b – North, c – Up) of the station ROC

131
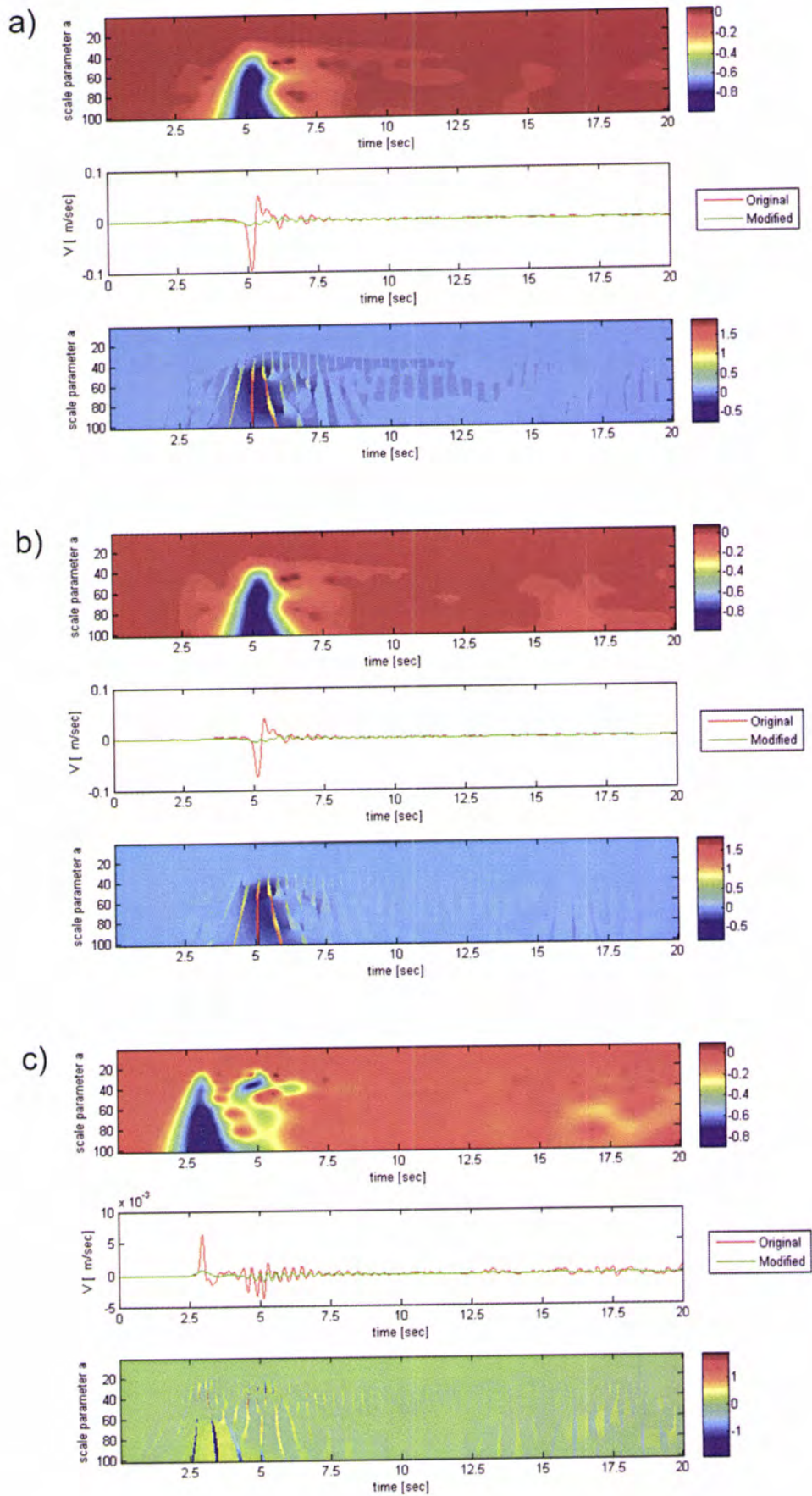
Fig. A6-c-6.Time-frequency envelope misfit (top), reference and comparison signals (middle) and time-frequency phase misfit (bottom) for the three channels (a – East, b – North, c – Up) of the station 1684

132

d. **Comparison of originally synthesized waveforms with waveforms obtained using models with modified rupture velocity**

i.   Reference model: rupture velocity – 3.0 km/sec

     Modified model: rupture velocity – 2.8 km/sec
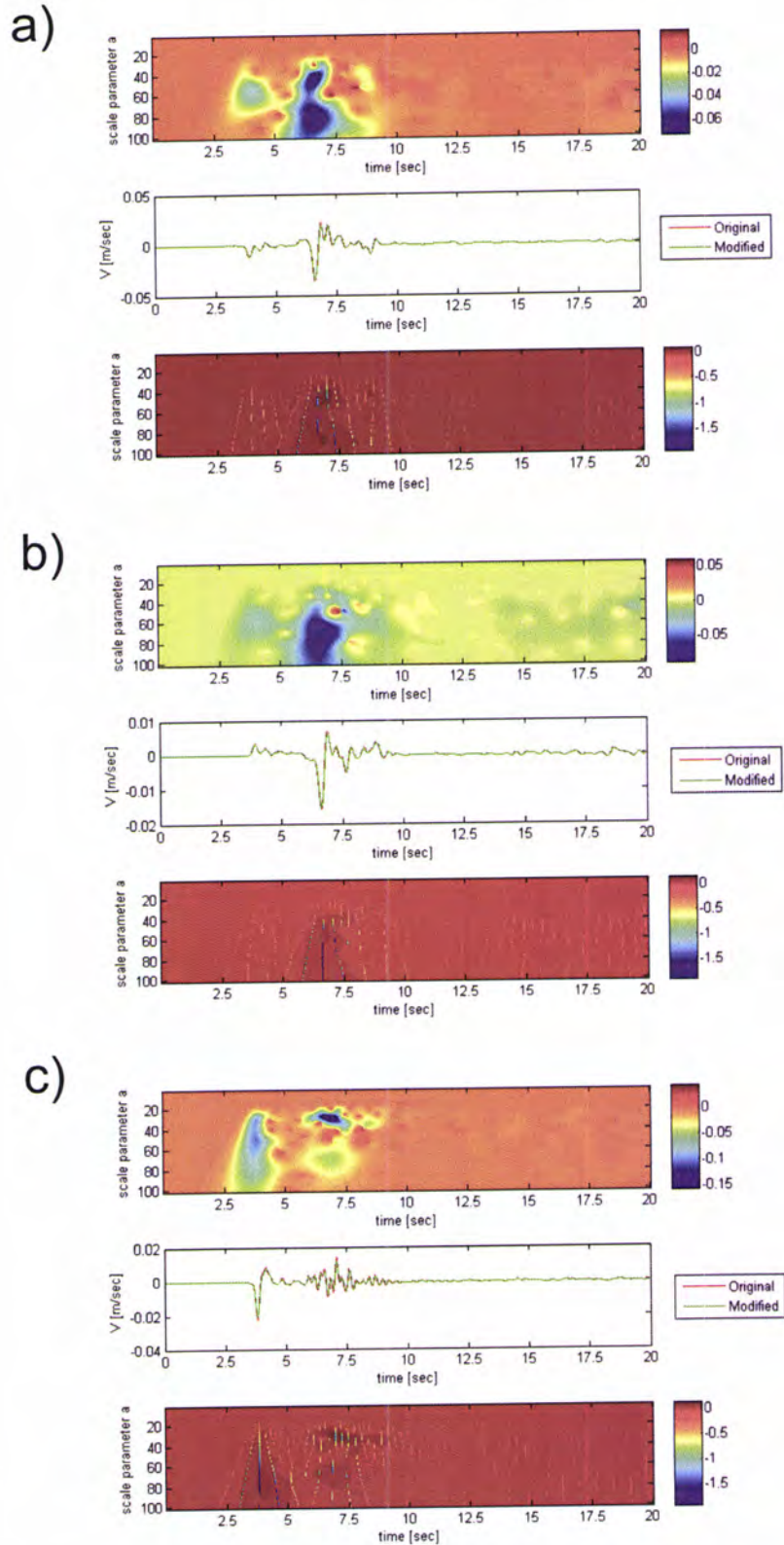
Fig. A6-d-i-1. Time-frequency envelope misfit (top), reference and comparison signals (middle) and time-frequency phase misfit (bottom) for the three channels (a – East, b – North, c – Up) of the station 57950
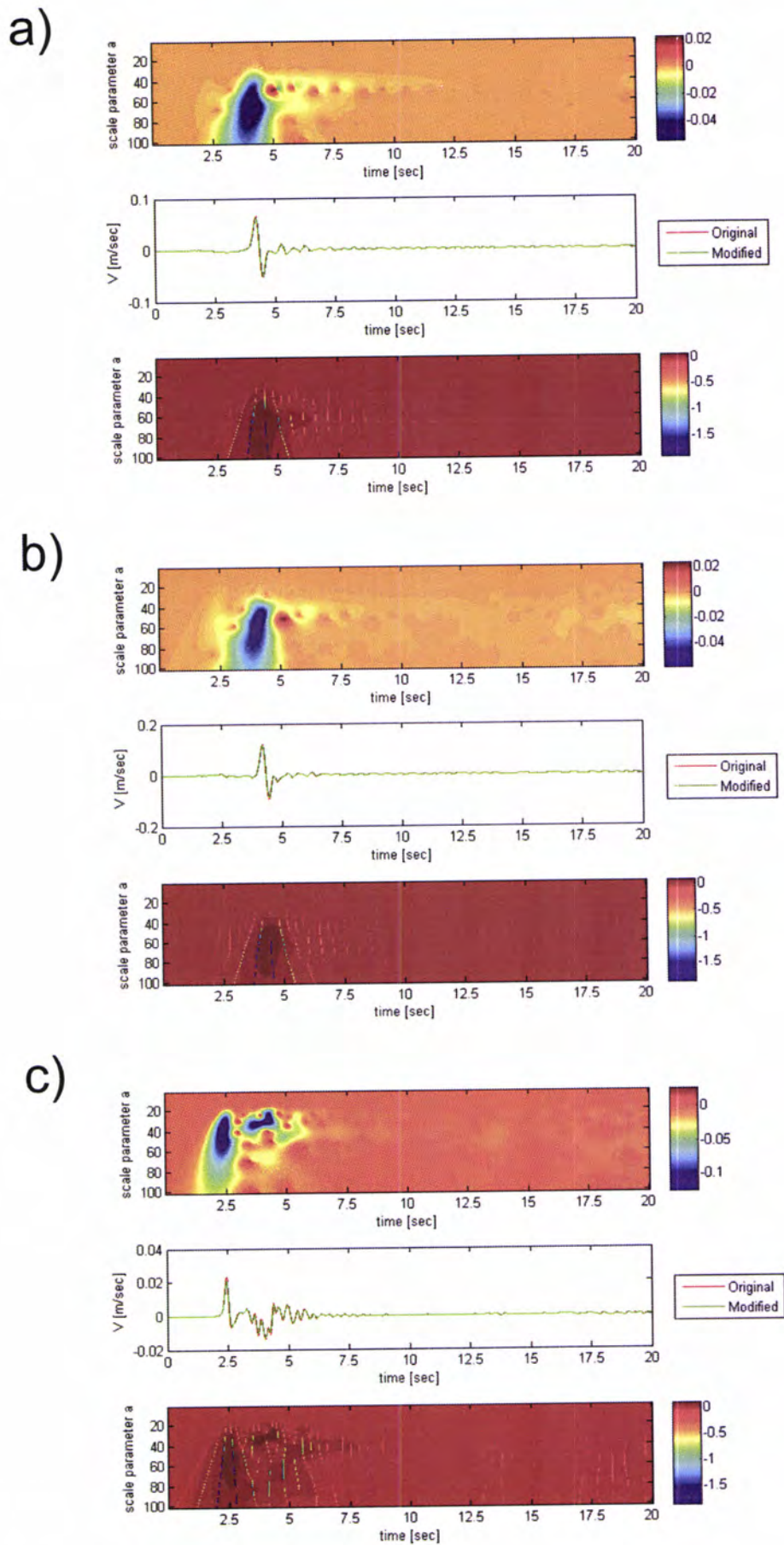
Fig. A6-d-i-2. Time-frequency envelope misfit (top), reference and comparison signals (middle) and time-frequency phase misfit (bottom) for the three channels (a – East, b – North, c – Up) of the station CHR
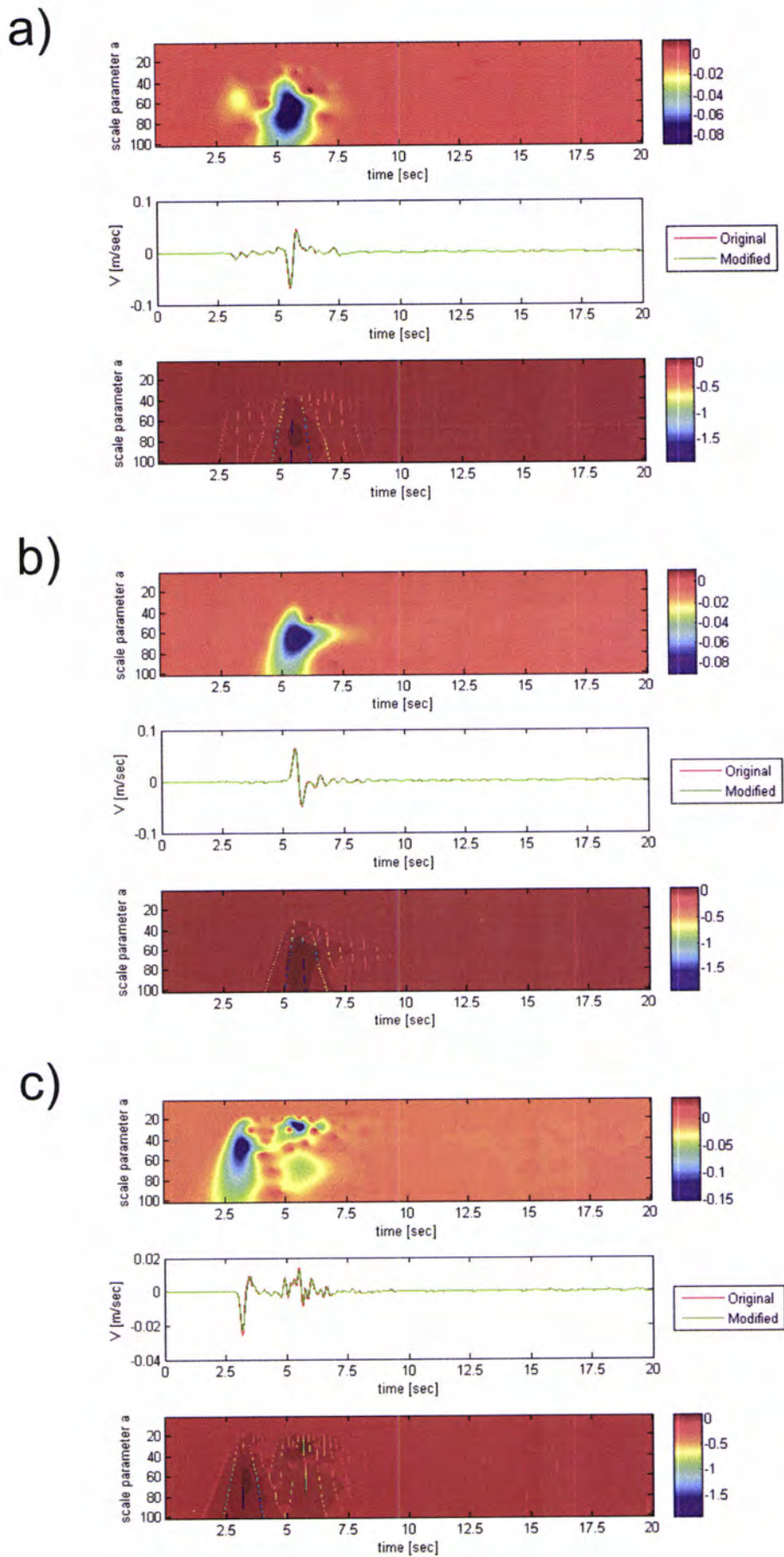
Fig. A6-d-i-3. Time-frequency envelope misfit (top), reference and comparison signals (middle) and time-frequency phase misfit (bottom) for the three channels (a – East, b – North, c – Up) of the station MP3
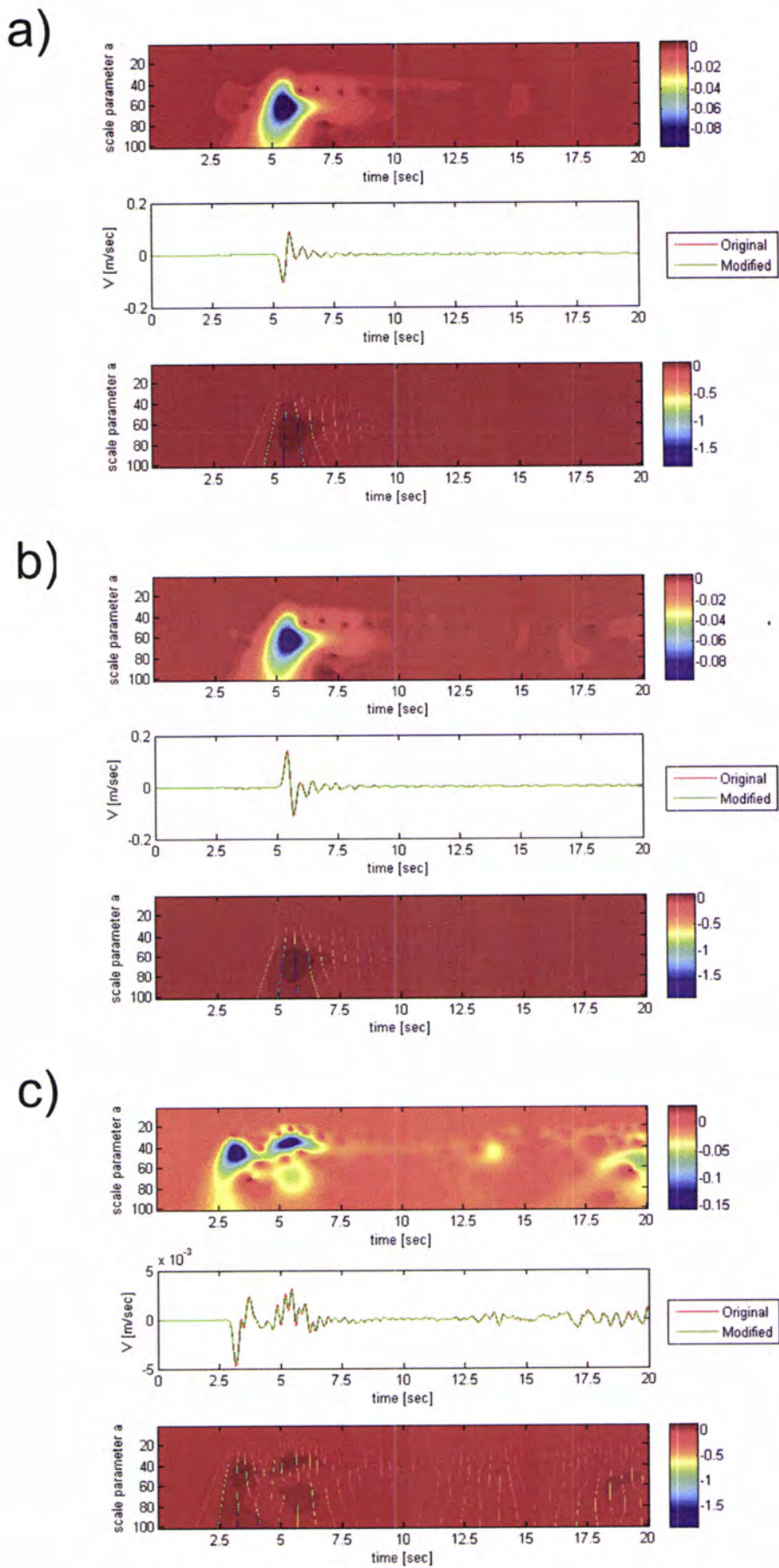
Fig. A6-d-i-4. Time-frequency envelope misfit (top), reference and comparison signals (middle) and time-frequency phase misfit (bottom) for the three channels (a – East, b – North, c – Up) of the station Q32

136
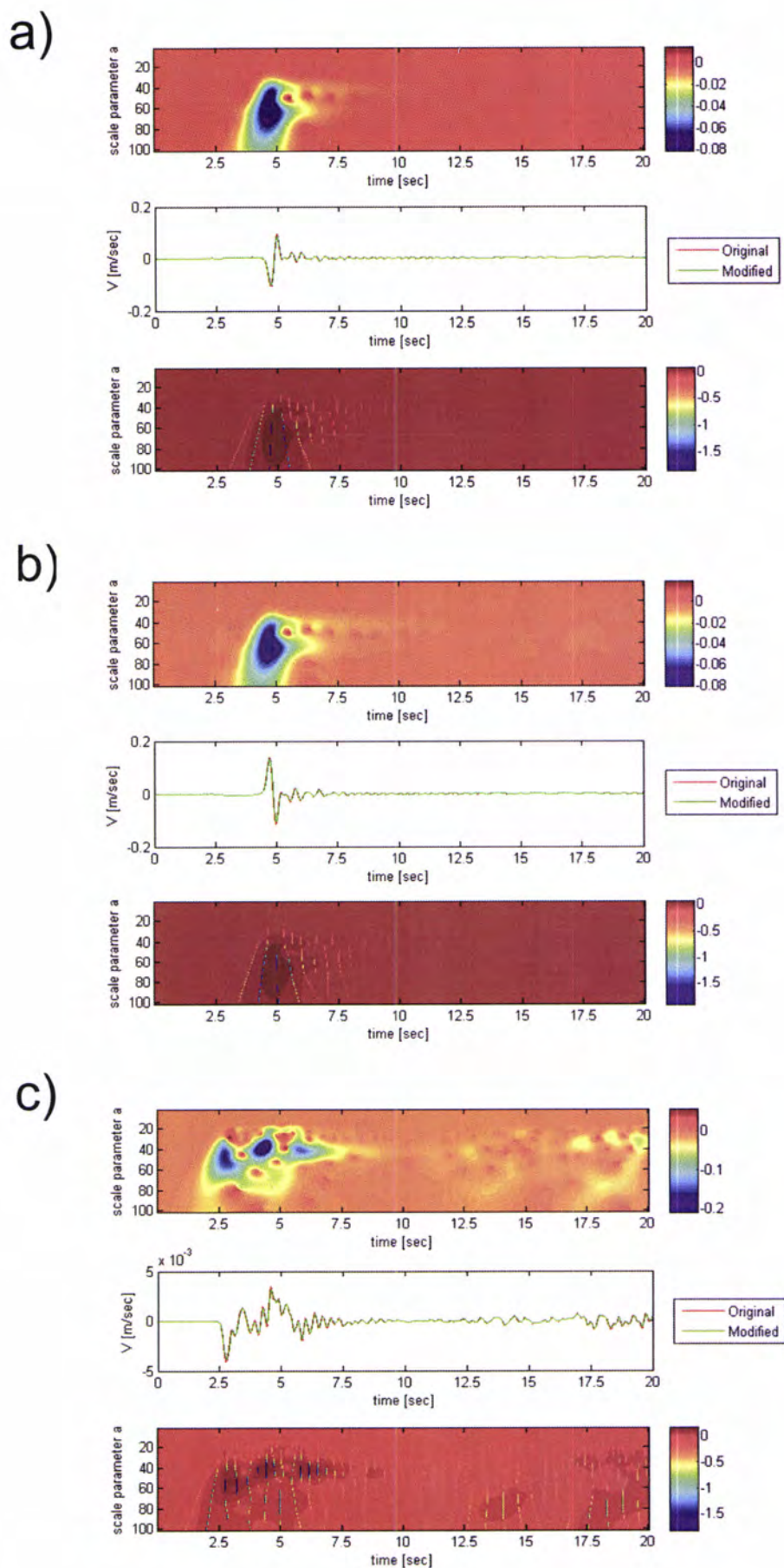
Fig. A6-d-i-5. Time-frequency envelope misfit (top), reference and comparison signals (middle) and time-frequency phase misfit (bottom) for the three channels (a – East, b – North, c – Up) of the station ROC

137
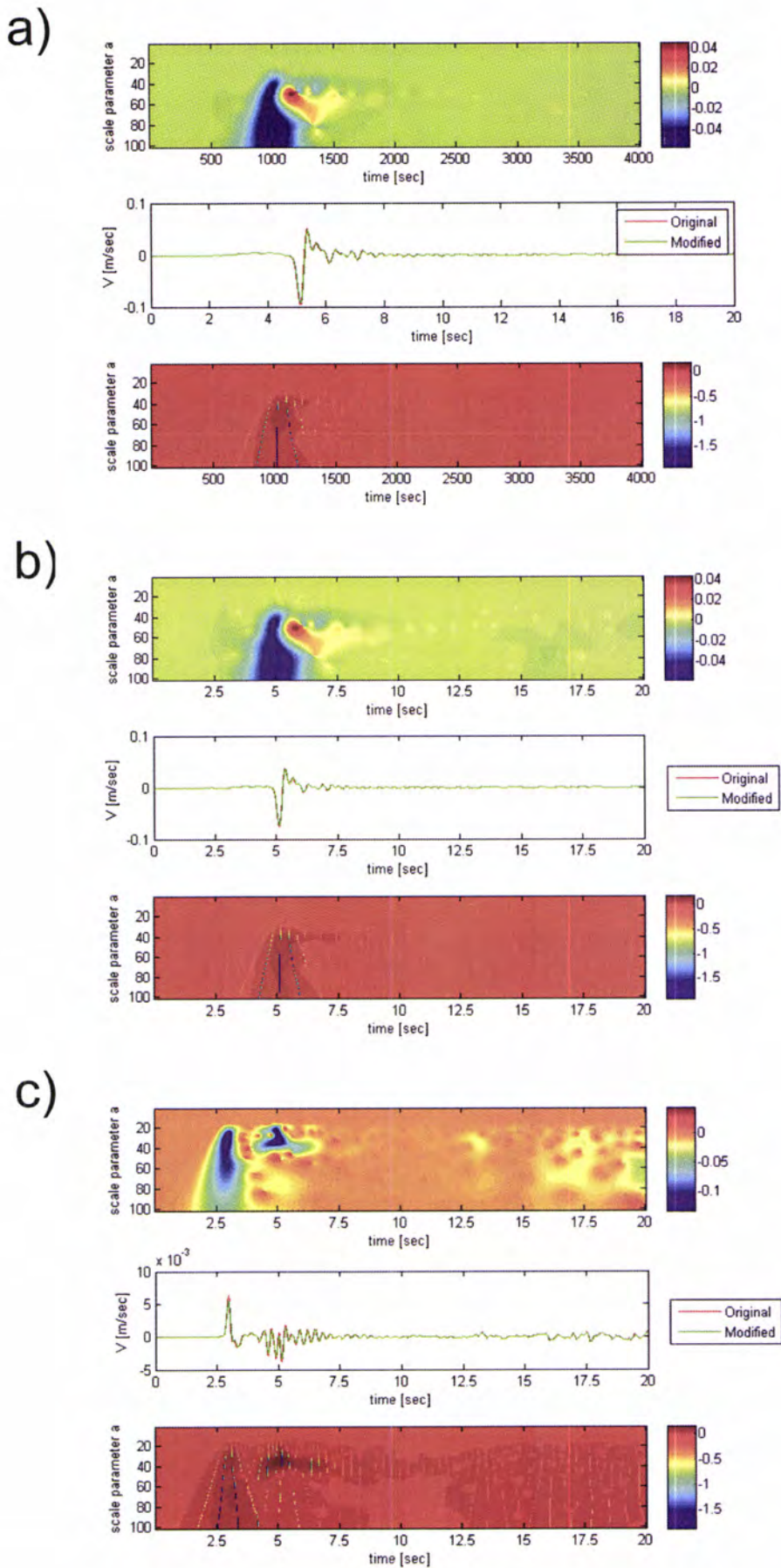
Fig. A6-d-i-6. Time-frequency envelope misfit (top), reference and comparison signals (middle) and time-frequency phase misfit (bottom) for the three channels (a – East, b – North, c – Up) of the station 1684

Modified model: rupture velocity – 3.1 km/sec

a)

b)

c)

Fig. A6-d-ii-1. Time-frequency envelope misfit (top), reference and comparison signals
(middle) and time-frequency phase misfit (bottom) for the three channels (a – East, b – North, c
– Up) of the station 57950
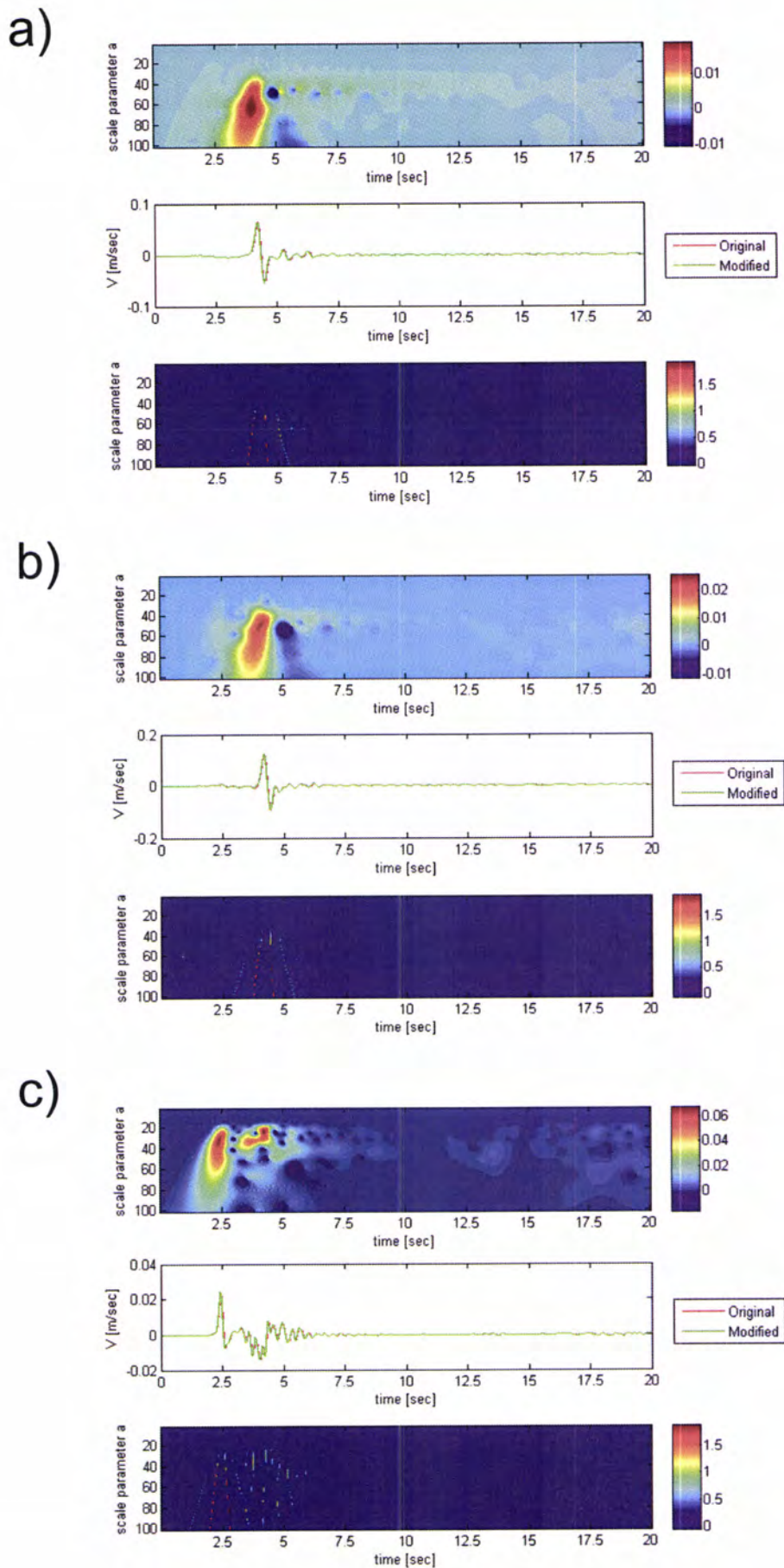
Fig. A6-d-ii-2. Time-frequency envelope misfit (top), reference and comparison signals (middle) and time-frequency phase misfit (bottom) for the three channels (a – East, b – North, c – Up) of the station CHR

140
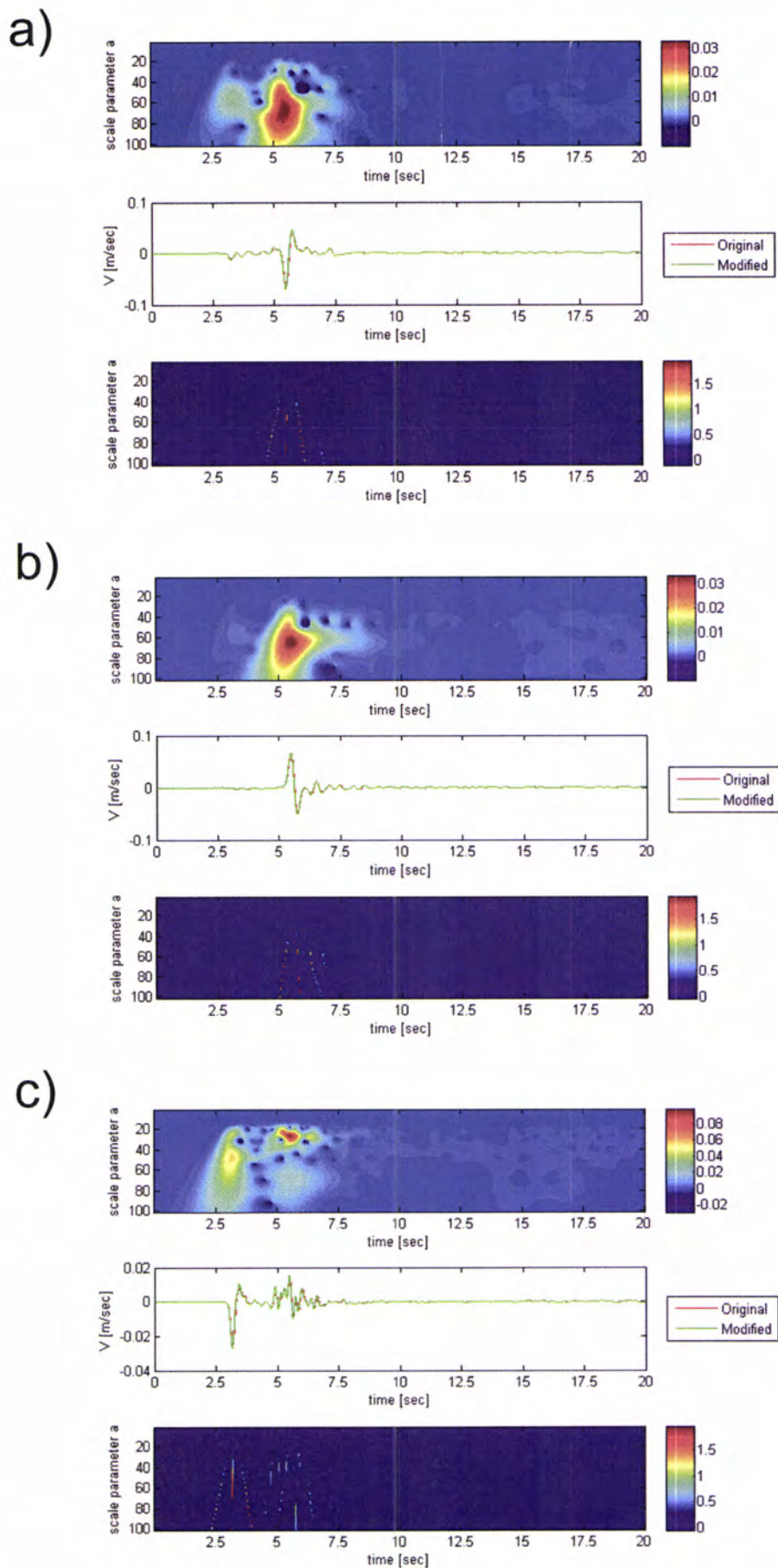
Fig. A6-d-ii-3. Time-frequency envelope misfit (top), reference and comparison signals (middle) and time-frequency phase misfit (bottom) for the three channels (a – East, b – North, c – Up) of the station MP3

141
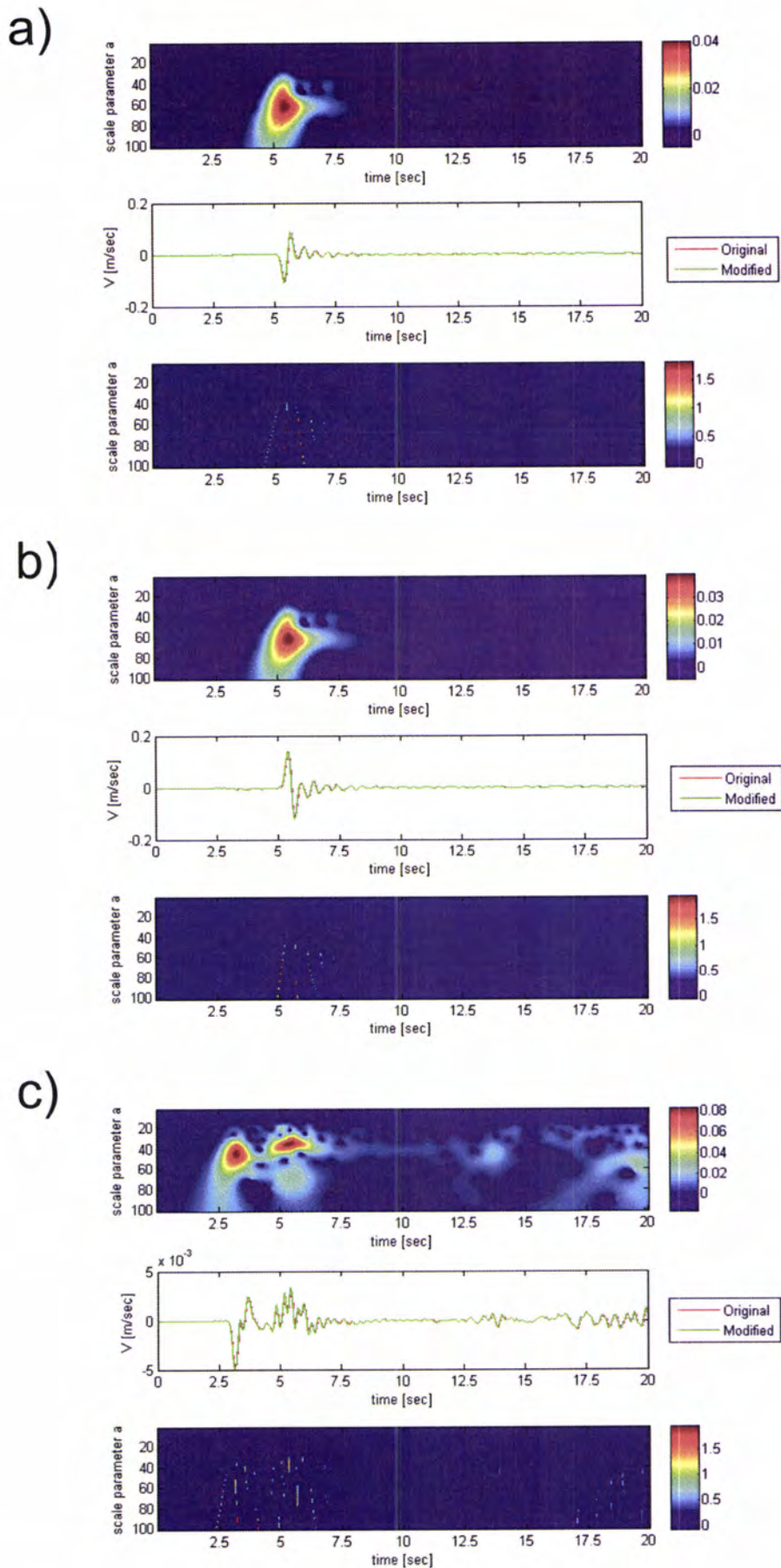
Fig. A6-d-ii-4. Time-frequency envelope misfit (top), reference and comparison signals (middle) and time-frequency phase misfit (bottom) for the three channels (a – East, b – North, c – Up) of the station Q32

142
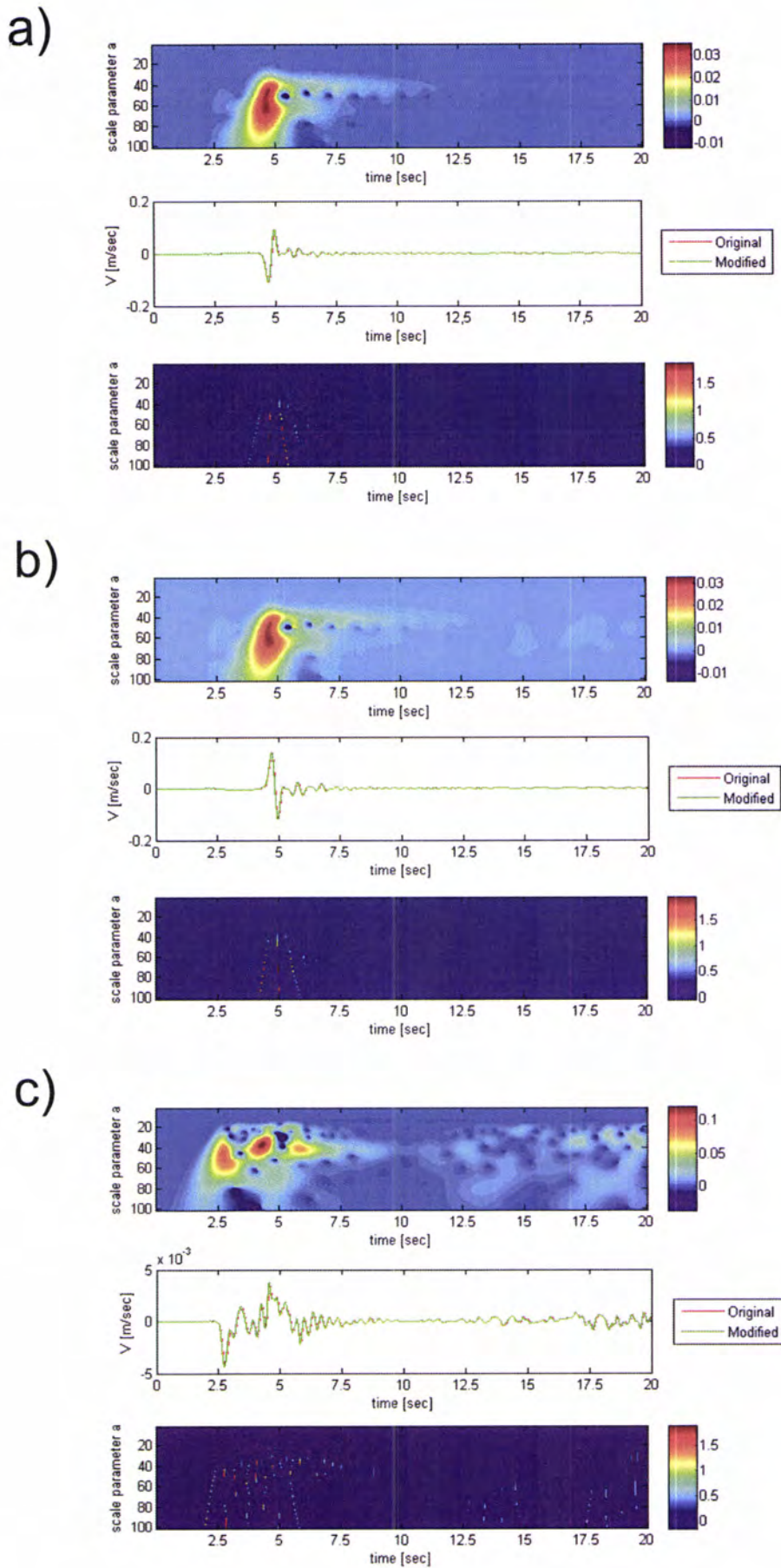
Fig. A6-d-ii-5. Time-frequency envelope misfit (top), reference and comparison signals (middle) and time-frequency phase misfit (bottom) for the three channels (a – East, b – North, c – Up) of the station ROC

143
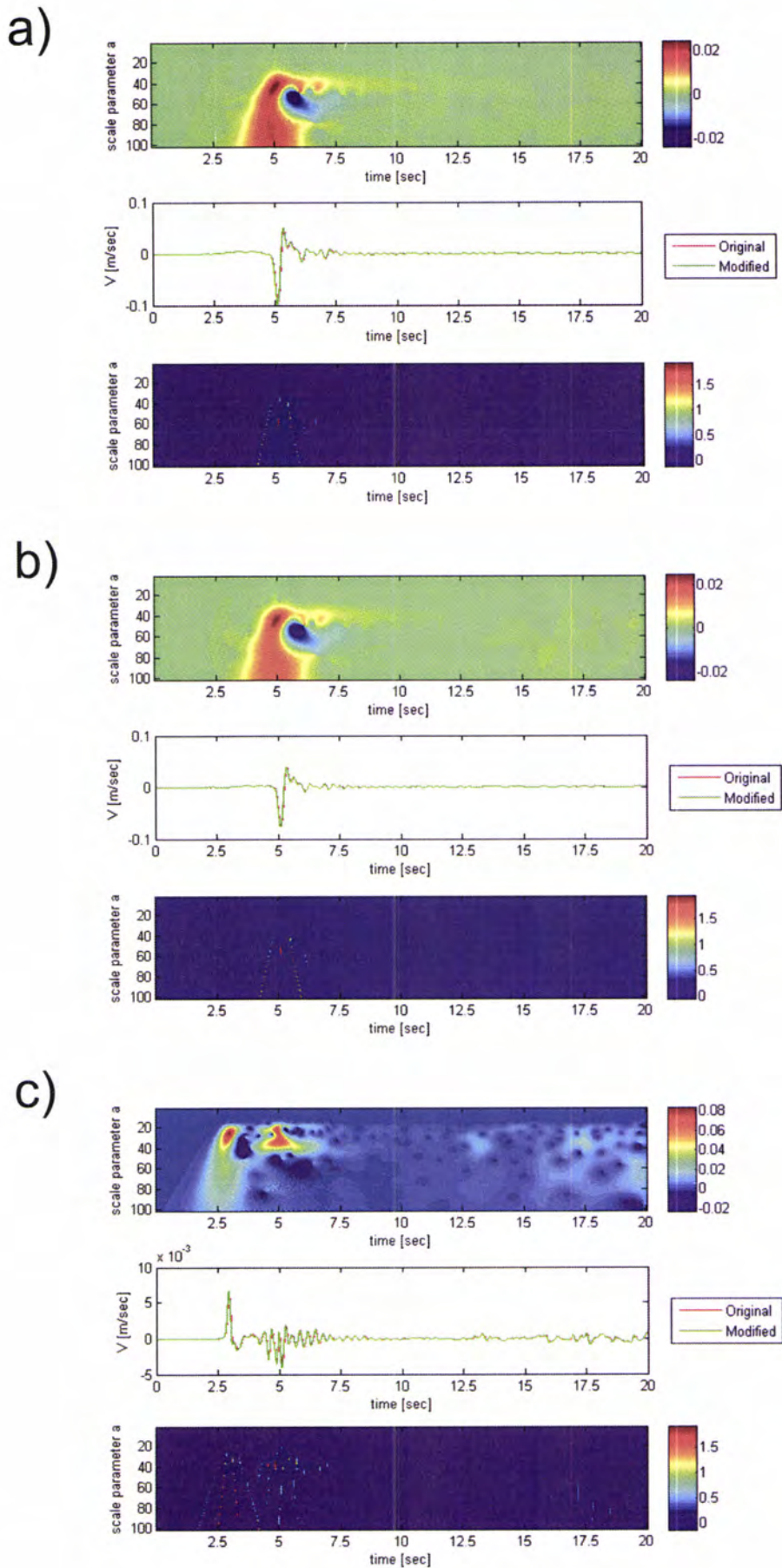
Fig. A6-d-ii-6. Time-frequency envelope misfit (top), reference and comparison signals (middle) and time-frequency phase misfit (bottom) for the three channels (a – East, b – North, c – Up) of the station 1684

144

Reference model: velocity model – Aagaard et al, 2008

Modified model: velocity model – Waldhauser & Ellsworth, 2002
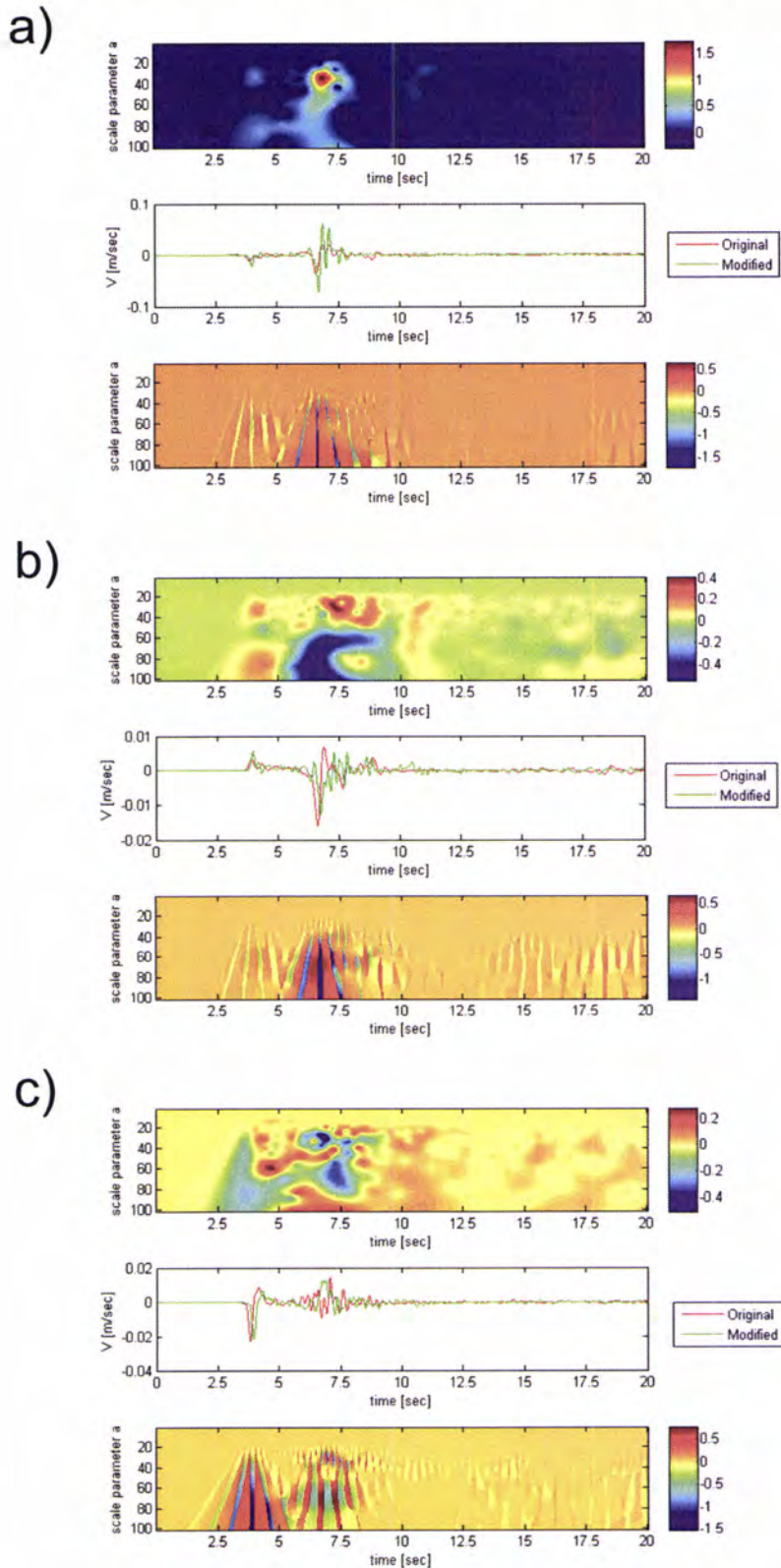
Fig. A6-e-1. Time-frequency envelope misfit (top), reference and comparison signals (middle) and time-frequency phase misfit (bottom) for the three channels (a – East, b – North, c – Up) of the station 57950
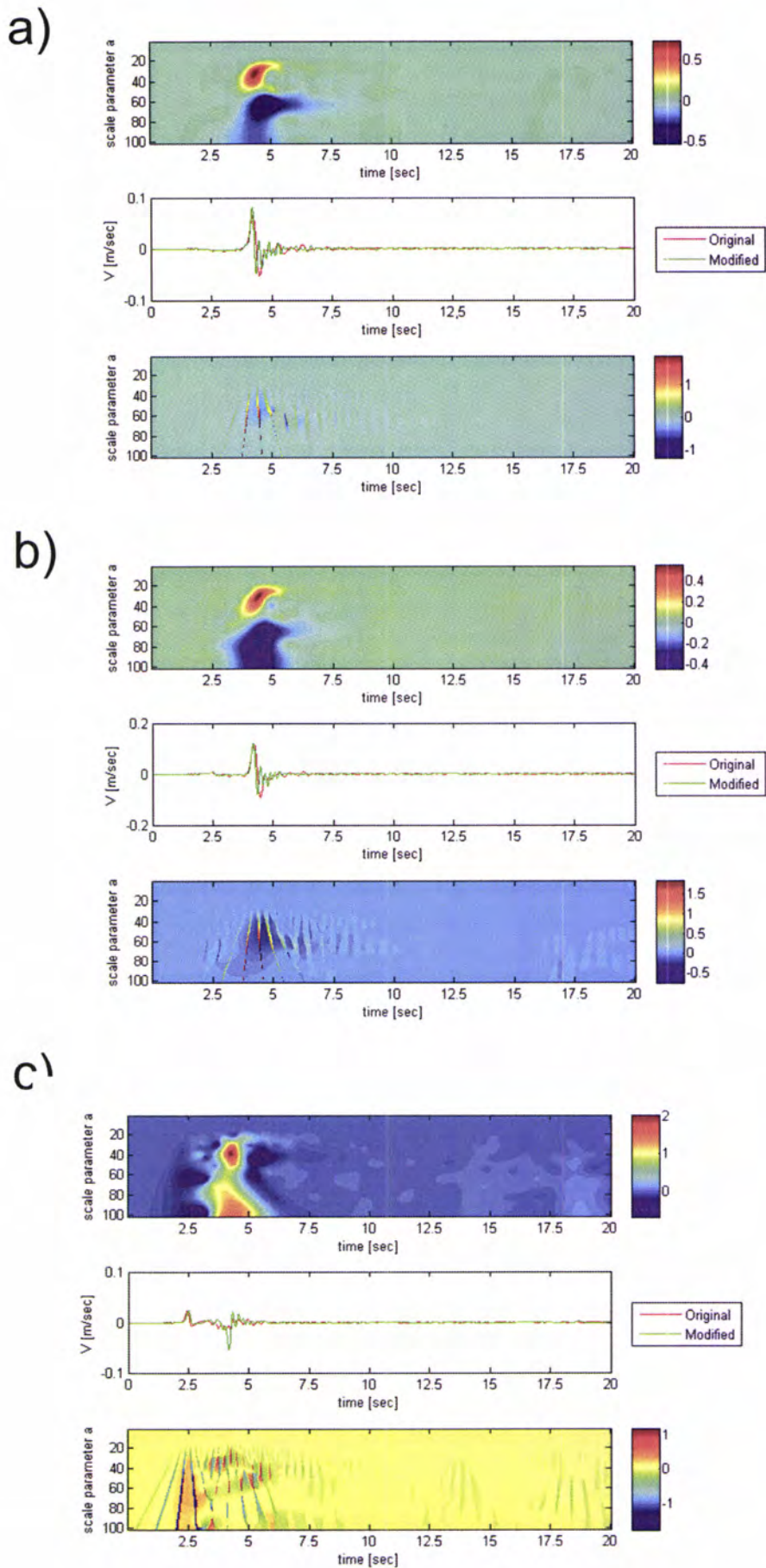
Fig. A6-e-2. Time-frequency envelope misfit (top), reference and comparison signals (middle) and time-frequency phase misfit (bottom) for the three channels (a – East, b – North, c – Up) of the station CHR
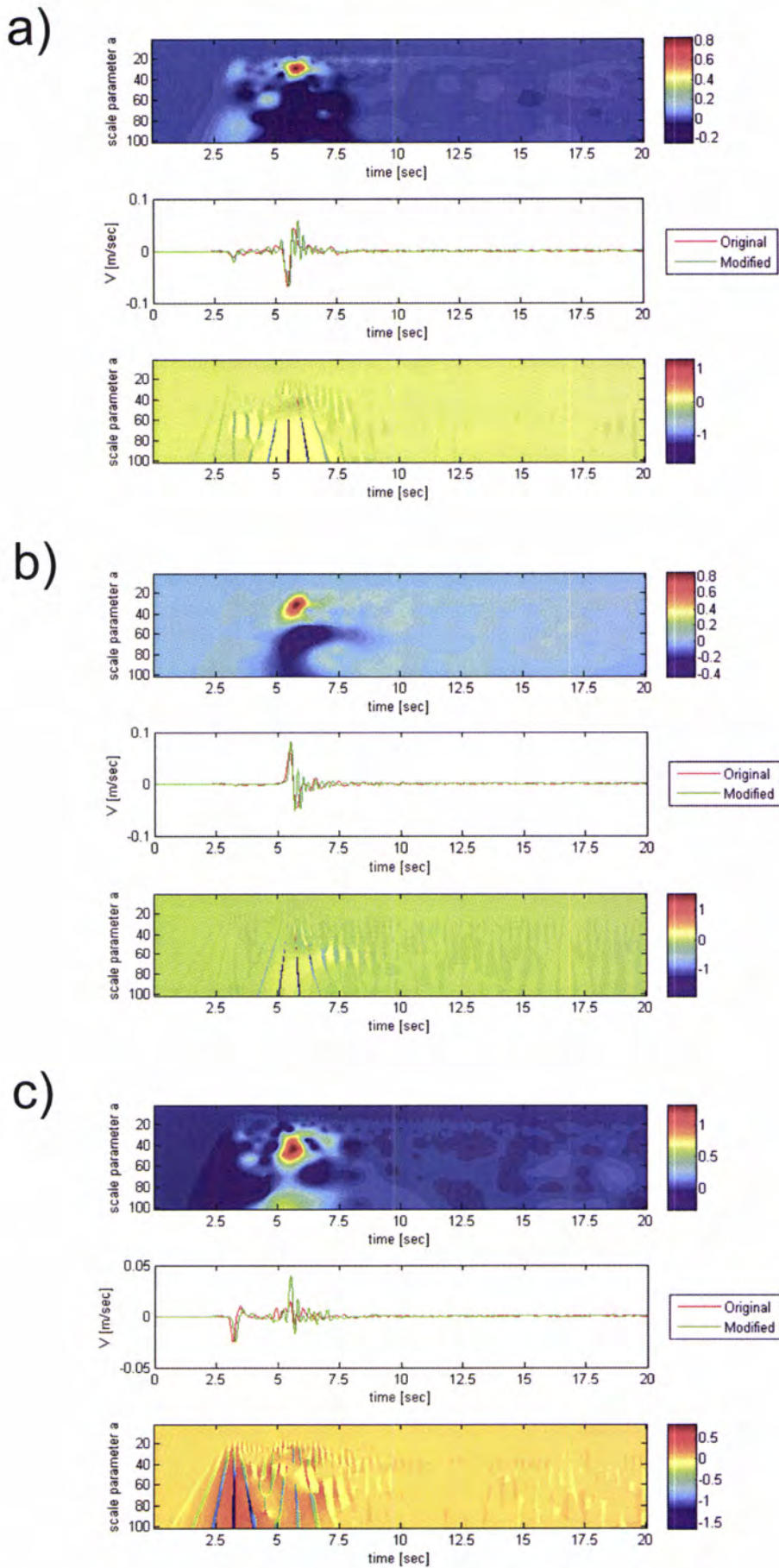
Fig. A6-e-3. Time-frequency envelope misfit (top), reference and comparison signals (middle)
and time-frequency phase misfit (bottom) for the three channels (a – East, b – North, c – Up) of
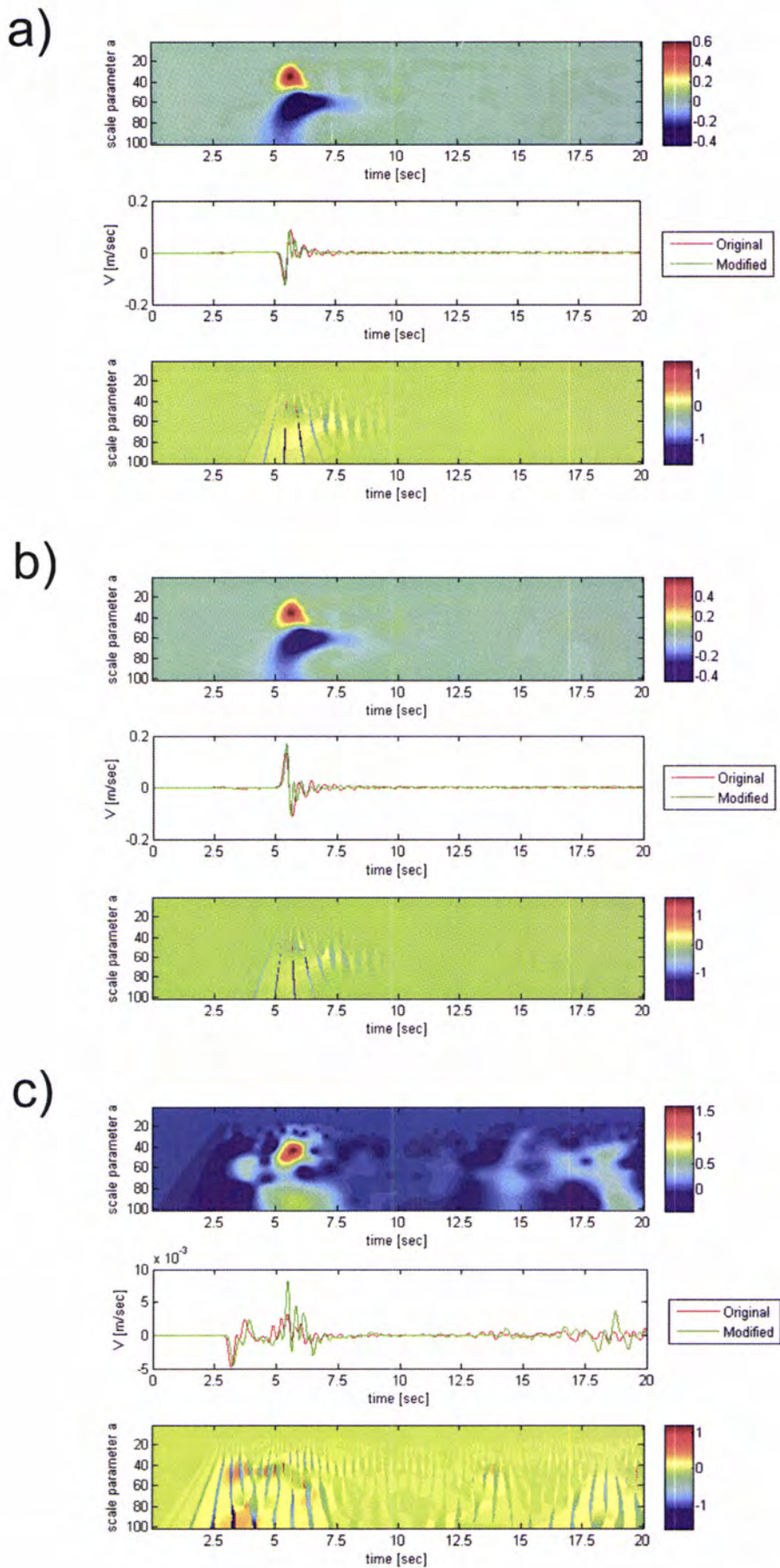
the station MP3

Fig. A6-e-4. Time-frequency envelope misfit (top), reference and comparison signals (middle) and time-frequency phase misfit (bottom) for the three channels (a – East, b – North, c – Up) of the station Q32
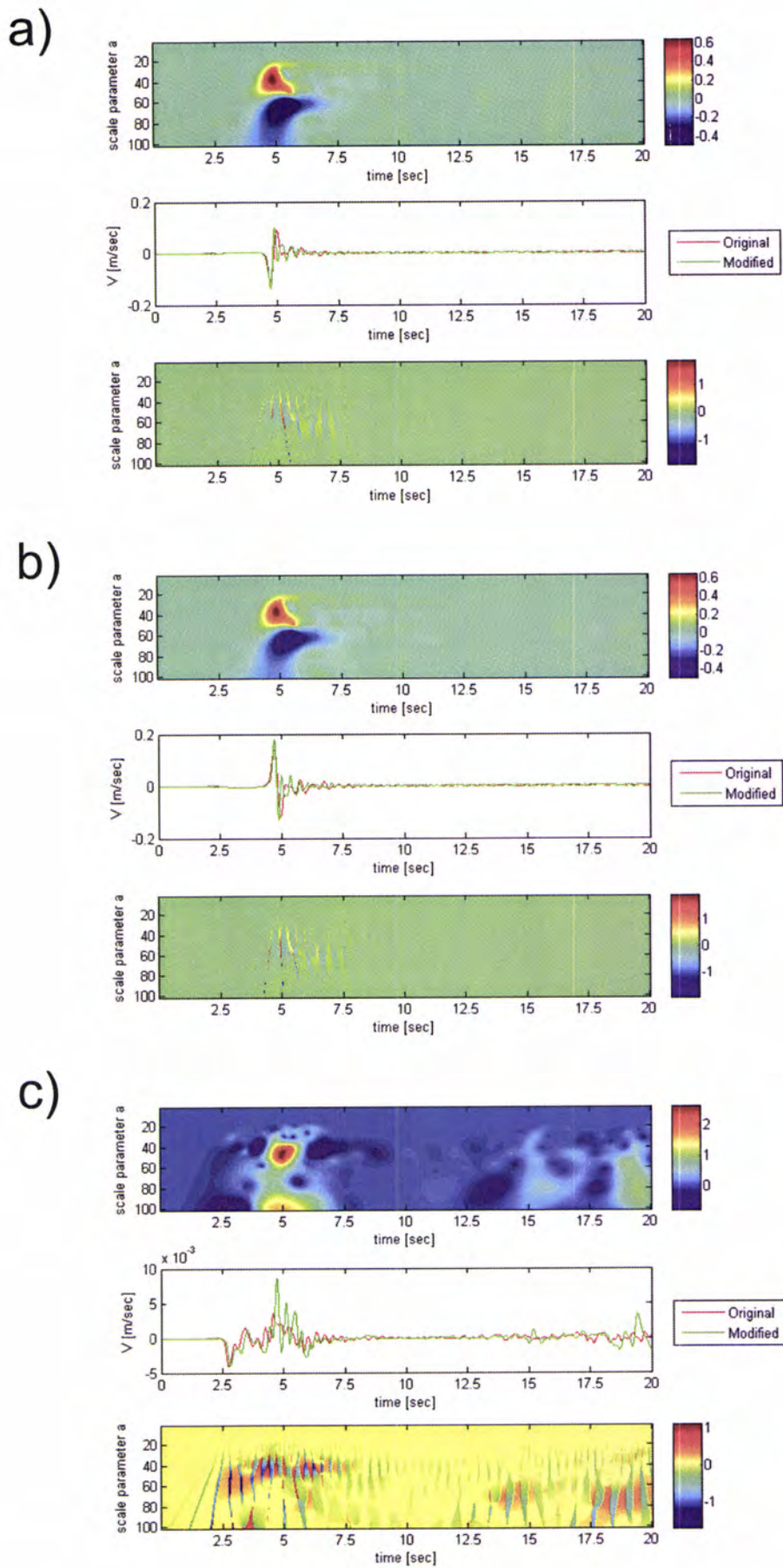
Fig. A6-e-5. Time-frequency envelope misfit (top), reference and comparison signals (middle) and time-frequency phase misfit (bottom) for the three channels (a – East, b – North, c – Up) of the station ROC
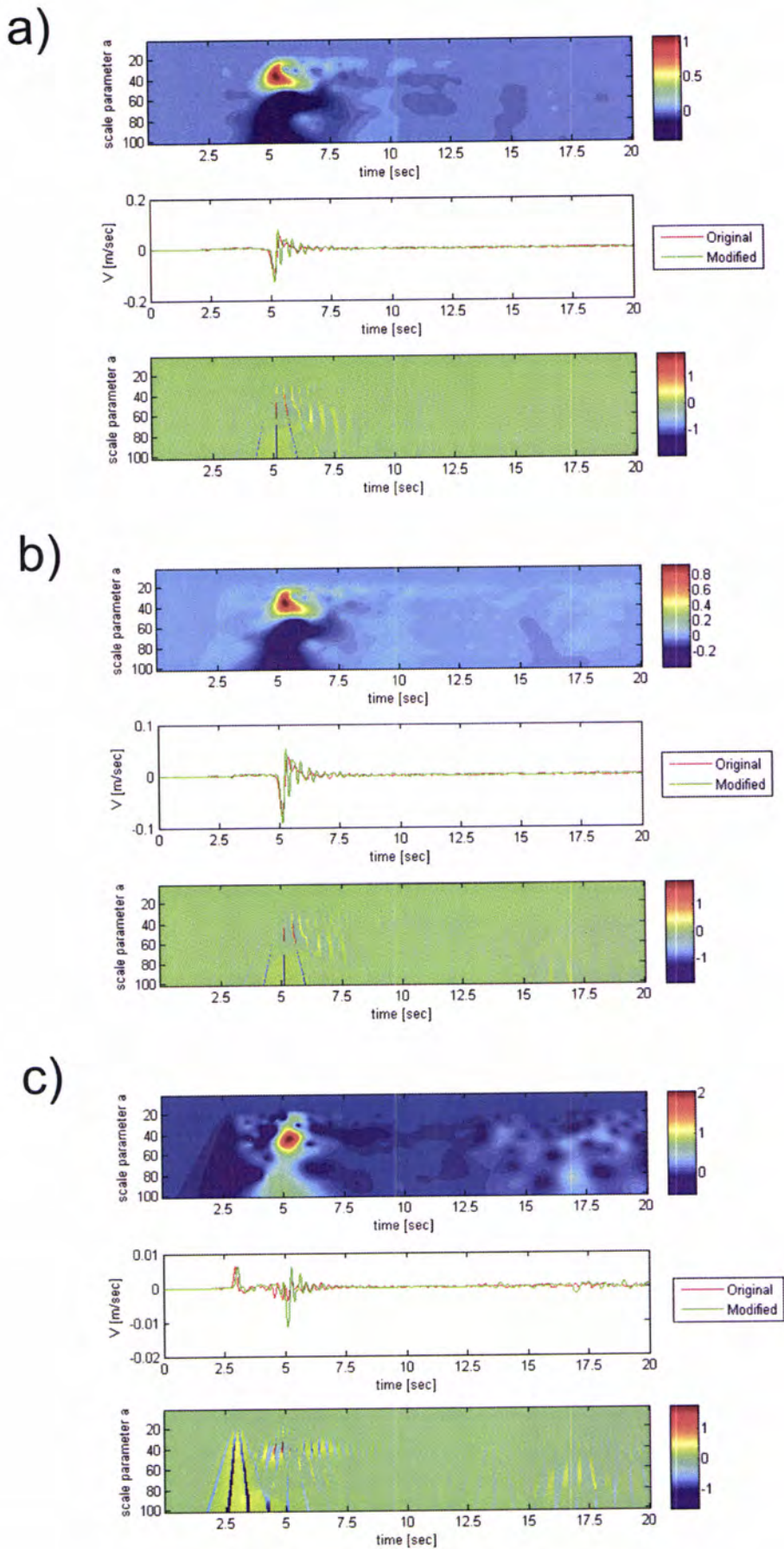
Fig. A6-e-6. Time-frequency envelope misfit (top), reference and comparison signals (middle) and time-frequency phase misfit (bottom) for the three channels (a – East, b – North, c – Up) of the station 1684

For notes